Testing and modeling of sheet pile reinforced dikes on organic soils
Insights from the Eemdijk full-scale failure test

Lengkeek, H.J.

Important note
To cite this publication, please use the final published version (if applicable).
Please check the document version above.

Testing and modeling of sheet pile reinforced dikes on organic soils
Insights from the Eemdijk full-scale failure test

Lengkeek, H.J.

DOI
10.4233/uuid:78df5e2b-740e-4268-a821-ed0ccaae93e5

Important note
To cite this publication, please use the final published version (if applicable).
Please check the document version above.

Testing and modeling
of sheet pile reinforced dikes
on organic soils

Insights from the Eemdijk full-scale failure test

Testing and modeling
of sheet pile reinforced dikes
on organic soils

Insights from the Eemdijk full-scale failure test

Proefschrift

ter verkrijging van de graad van doctor
aan de Technische Universiteit Delft,
op gezag van de Rector Magnificus prof.dr.ir. T.H.J.J. van der Hagen,
voorzitter van het college voor Promoties,
in het openbaar te verdedigen
op vrijdag 17 juni 2022 om 15:00 uur

door

Henri John LENGKEEK

Civiel ingenieur, Technische Universiteit Delft, Nederland
Geboren te Raesfeld, Duitsland

Dit proefschrift is goedgekeurd door:

Prof.dr.ir. S.N. Jonkman	promotor
Dr.ir. R.B.J. Brinkgreve	copromotor

Samenstelling promotiecommissie:

Rector Magnificus	voorzitter
Prof.dr.ir. S.N. Jonkman	Technische Universiteit Delft
Dr.ir. R.B.J. Brinkgreve	Technische Universiteit Delft

Onafhankelijke leden:

Prof.dr. C. Jommi	Technische Universiteit Delft, Politecnico di Milano
Prof. P. Mayne	Georgia Tech - School of Civil and Environmental Engineering
Prof.dr.ir. M. Kok	Technische Universiteit Delft
Ir. H. van Hemert	STOWA, Rijkswaterstaat
Dr. P.J. Vardon	Technische Universiteit Delft, reservelid

An electronic version of this dissertation is available at:
http://repository.tudelft.nl

SUMMARY

The Netherlands is inherently challenged by water, as a large part of the country lies below sea level and several major rivers in North-western Europe cross the country. The most prevalent form of protection from coastal and river floods in the Netherlands includes approximately 22,000 km of earthen dikes, of which 3800 km are primary flood defenses (i.e., the first line of defense against high water). Subsidence, sea level rise, and the increase of rain intensity and river discharge due to climate change further challenge existing flood defenses to maintain required levels of safety. To do so, the top elevation of existing earthen dikes is often incrementally raised over time. However, raising a dike requires an extension of its base, which is frequently restricted by the presence of existing buildings and other spatial constraints. These dikes can be reinforced by alternative means such as a sheet pile wall.

Another specific challenge regarding dike reinforcement in the Netherlands includes the presence of soft subsoil conditions at many dikes. These soft soils often consist of organic clays and peats. Such soils have a low stiffness and continue to deform over time; their strength is not well understood and often underestimated. Furthermore, organic soils are often not properly identified from Cone Penetration Tests (CPTs) using common interpretation methods, while CPT is the main testing method in the Netherlands.

This research focuses on improving two aspects of the global stability assessment of dikes in the Netherlands: the modeling challenges of organic soil and dike reinforcement using sheet piles. Chapter 2 of this dissertation addresses the empirical relations for organic soils. The CPT-based correlation to derive the soil unit weight (Lengkeek et al. 2018) is validated and improved. Furthermore, new CPT-based correlations for organic soils are obtained by relating the soil state parameters to the cone resistance and the unique soil type properties to the friction ratio. An adjustment to Robertson (2010) CPT-based classification is proposed. In the improved SBT classification, organic soils (SBT=2) are redefined and subdivided into peat, organic clay, and mineral clay with organic matter.

In chapter 3 the new Critical Stress Ratio (CSR) model is presented, which classifies as 'Simplified Critical State Soil Mechanics'. The CSR model can be seen as a theoretical version of the SHANSEP equation, providing a link between effective stress parameters, obtained from common laboratory tests, and the undrained shear strength. The model can be implemented in LEM for ultimate limit state stability analysis.

The CSR model provides the state dependent undrained shear strength for each stress point. The CSR model does not require to determine the exact yield contour as in a constitutive FEM model, this is taken into account by a variable spacing ratio, called the 'Critical Stress Ratio'. This parameter of the CSR model can be regarded as the over-consolidation ratio at which no net excess pore pressures occurs, a parameter which can be fitted based on a few CAUC tests. Furthermore, the CSR model contains methods to obtain other model parameters for existing constitutive models used in the finite element method, such as the Poisson's ratio which determines the horizontal and isotropic stress in unloading.

Chapter 4 presents the set-up, results, and evaluation of the full-scale failure test. (In Dutch: 'Eemdijk damwandproef'), initiated by the Dutch Flood Protection Programme. The Eemdijk full-scale failure tests involves separate tests on (1) sheet pile panels, (2) on a ground dike, as well as a combined test (3) on a ground dike with sheet pile reinforcement. The Eemdijk full-scale failure tests provides valuable insights through a detailed analysis of the deformations of dikes leading up to and beyond failure. Furthermore, the soil investigation is re-examined and parameters are determined for multiple constitutive models applied in FEM back-analyses. Finally, both the CPT-based methods, the CSR model and the SHANSEP-NGI-ADP model are validated at the Eemdijk test site.

The back-analysis of the pull-over tests (PO-test) confirmed that the cross-section class 2 sheet piles (AZ26) reached the full plastic bending moment capacity and the cross-section class 3 sheet piles (AZ13-700 and GU8N) reached at least the elastic bending moment capacity. Furthermore, from the analysis of the SAAF measurements it is concluded that the stiffness of only the side sheet piles of panels should be reduced due to edge effects.

The ground dike test (GD-test) and sheet pile reinforced dike test (SPD-test) allowed for a unique comparison and provided insight in the critical deformation rate prior to progressive failure. This criterion is useful in the assessment of unstable slopes. The GD-test illustrates the importance of high density of soil investigations and the importance of high quality CPTs (ISO class 1) and proper CPT based classification.

The sheet pile reinforced dike test (SDP-test) shows that a continuous sheet pile, with sufficient length and embedment, makes an important contribution to the robustness of the dike after failure. Even after structural failure due to a plastic hinge, all sheet piles remained intact and interlocked. The failed sheet piles functioned as a weir and ultimately prevented breaching.

Based on a careful examination of the Triaxial (CAUC) test it is recommended to use the 15% axial strain value as a basis for the ultimate value and to apply additional criteria to prevent unrealistic high or low values for the undrained shear strength, and to re-examine the applied geometrical corrections.

Based on the performed variation analysis it is recommended to use average stiffness parameters in a SLS or ULS dike design analysis, when performed with advanced constitutive models in FEM.

The alternative approaches to dike assessment presented in this research are expected to result in a more economic and better understood dike design and assessment based on improved field data interpretation (chapter 2,) undrained shear strength and modeling procedures (chapter 3) and takeaways from the full-scale tests and back analyses (chapter 4).

SAMENVATTING

Nederland ligt midden in een delta van drie grote rivieren, op land dat voor een groot deel onder het gemiddeld zeeniveau ligt. Een groot gedeelte van Nederland wordt daarom bedreigd door het water. De meest voorkomende vorm van bescherming tegen overstromingen in Nederland omvat ongeveer 22000 km gronddijken, waarvan 3800 km primaire waterkeringen langs de kust en grote rivieren. Bodemdaling, zeespiegelstijging en de toename van regenval en rivierafvoer als gevolg van klimaatverandering vormen een uitdaging voor bestaande waterkeringen om het vereiste veiligheidsniveau te handhaven. Hiervoor wordt het niveau van bestaande gronddijken in de loop van de tijd vaak stapsgewijs verhoogd. Voor het ophogen van een dijk is echter een verbreding van de basis nodig, die vaak wordt beperkt door de aanwezigheid van bestaande bebouwing en naastgelegen bestemmingen. Deze dijken kunnen worden versterkt met alternatieve middelen zoals een damwand. Dergelijke doorlopende damwandschermen worden veelal aangeduid als langsconstructies.

Een andere specifieke uitdaging op het gebied van dijkversterking in Nederland is de aanwezigheid van een slappe ondergrond bij veel dijken, vaak bestaande uit organische klei en veen. Dergelijke organische grondsoorten hebben een lage stijfheid en blijven na verloop van tijd vervormen; de sterkte is niet altijd eenduidig te bepalen en wordt vaak onderschat in het geval van veen. Bovendien worden organische grondsoorten vaak niet goed geïdentificeerd met internationaal gangbare interpretatiemethoden op basis van sonderingen (CPT's), terwijl dit de belangrijkste testmethode in Nederland is.

Dit onderzoek richt zich op het verbeteren van twee aspecten van de globale stabiliteitsbeoordeling van dijken in Nederland: de modellering van organische grondsoorten en dijkversterking met behulp van damwand langsconstructies. Hoofdstuk 2 van dit proefschrift behandelt de empirische relaties voor organische grondsoorten. De CPT correlatie voor volume gewicht van grond (Lengkeek et al. 2018) is gevalideerd en verbeterd. Verder zijn nieuwe CPT correlaties voor organische grondsoorten bepaald door de toestandsparameters te relateren aan de conusweerstand en de unieke grondeigenschappen aan het wrijvingsgetal. Ook is er een aanpassing van de 'Soil Behaviour Type' (SBT) classificatie van Robertson (2010) voorgesteld. In deze verbeterde SBT-classificatie worden organische grondsoorten (SBT=2) opnieuw gedefinieerd en onderverdeeld in veen, organische klei en minerale klei met organische stof.

In hoofdstuk 3 wordt het nieuwe Critical Stress Ratio (CSR) model gepresenteerd, dat geclassificeerd kan worden als 'Simplified Critical State Soil Mechanics'. Het CSR-model kan worden gezien als een theoretische versie van de SHANSEP-vergelijking, die een verband legt tussen effectieve spanningsparameters, verkregen uit in de praktijk gangbare laboratoriumproeven en de ongedraineerde schuifsterkte. Het model kan worden geïmplementeerd in een glijvlakmodel (LEM) voor een stabiliteitsanalyse op basis van de ongedraineerde schuifsterkte.

Met het CSR model kan de ongedraineerde schuifsterkte worden bepaald voor elk spanningspunt, met inachtname van de belastingshistorie. Het is niet nodig de volledige vloeicontour te bepalen zoals bij een constitutief FEM model, dit is middels een variabele

'spacing ratio' genaamd de 'Critical Stress Ratio' verdisconteerd. Deze parameter in het CSR model kan worden gezien als de overconsolidatieratio waar bij belasten geen netto wateroverspanningen ontstaan en kan worden gefit op basis van een aantal CUAC proeven, vergelijkbaar met de 'SHANSEP' procedure. Tenslotte, het CSR model geeft procedures voor de bepaling van andere parameters voor bestaande constitutive modellen, zoals de dwarscontractiecoëfficiënt die bepalend is voor de horizontale en isotrope spanning bij ontlasten.

Hoofdstuk 4 presenteert de condities, de meetresultaten en de evaluatie van de full-scale bezwijkproeven te Eemdijk. De 'Eemdijk damwandproef', geïnitieerd door het Hoogwaterbeschermingsprogramma (HWBP), bestaat uit (1) afzonderlijke bezwijkproeven op damwandpanelen, (2) een gronddijk en (3) een dijk versterkt met een damwand langsconstructie. Verder is het grondonderzoek geanalyseerd en zijn parameters bepaald voor meerdere constitutieve modellen die zijn toegepast in de FEM postdictie. Ten slotte zijn de CPT correlaties en classificatie, het CSR-model en het SHANSEP-NGI-ADP-model gevalideerd op de Eemdijk testlocatie.

De postdictie van de pull-over tests (PO-test) bevestigt dat de dwarsdoorsnede klasse 2 damwanden (AZ26) de volledige capaciteit van het plastisch weerstandmoment bereikten en de dwarsdoorsnede klasse 3 damwanden (AZ13-700 en GU8N) bereikten ten minste de capaciteit van het elastisch weerstandmoment. Verder is uit de analyse van de SAAF-metingen geconcludeerd dat de stijfheid van enkel de damwanden aan de zijkant van panelen gereduceerd hoeven te worden vanwege randeffecten.

De proeven op de gronddijk (GD-test) en de damwand versterkte dijk (SPD-test) maken een unieke vergelijking mogelijk en geven inzicht in de kritische vervormingssnelheid voorafgaand aan progressief bezwijken. Dit criterium is nuttig bij de beoordeling van instabiele dijken. De GD-test illustreert het belang van een hoge dichtheid van bodemonderzoeken en het belang van hoogwaardige sonderingen (ISO klasse 1) en correcte classificatie.

Uit de proef op de damwand versterkte dijk (SDP-proef) blijkt dat een doorlopende damwand, met voldoende lengte en verankering, een belangrijke bijdrage levert aan de robuustheid van de dijk na bezwijken. Ook na constructief falen door een plastisch scharnier bleven alle damwanden intact en verbonden in de sloten. De bezweken doorlopende damwand fungeerde als overlaat en verhinderde een volledige ontwikkeling van een bres.

Op basis van de analyse van de triaxiaalproeven (CAUC) wordt aanbevolen om de 15% axiale rek te gebruiken als basis voor de 'ultimate' waarde, in combinatie met twee aanvullende criteria om onrealistische hoge of lage waarden voor de ongedraineerde schuifsterkte te voorkomen. Op basis van de uitgevoerde variatiestudies wordt aanbevolen om gemiddelde stijfheidsparameters te gebruiken in een SLS en ULS berekeningen, indien deze worden uitgevoerd met geavanceerde constitutieve modellen in FEM.

De benaderingen die in dit onderzoek worden gepresenteerd, zullen naar verwachting resulteren in een meer economisch ontwerp en een beter inzicht in het faalmechanisme macro-stabiliteit van dijken, met en zonder damwand langsconstructies.

ACKNOWLEDGEMENTS

I express my gratitude to my promotor Prof. Bas Jonkman, the freedom you gave me to shape the contents of my PhD, as well as the support to finalize it in a timely manner.

Special thanks to Dr. Ronald Brinkgreve. The frequent teams meeting we had in the last years were crucial. I really acknowledge your scientific writing skills, accurate reviews and of course the shared enthusiasm for soil mechanics and constitutive modeling.

I would like to thank the POVM, established in 2015 by Water Authorities in the Netherlands, who initiated and financed the "Eemdijk damwandproef". With a team of colleagues from Witteveen+Bos and Deltares; Thomas, Huub, Joost, Mark, Dennis and many others, we had a great cooperation which resulted in a successful full-scale failure test, and above all a lifetime memory.

Although Delft is far from home, it was always nice to meet my fellow researchers Chris, Wouter Jan, Mark and Joost in room 3.58 at the TU. Thanks for the good discussions, the tips and tricks and the laughs. I am certainly proud of all of your research output. I also like to thank Prof. Matthijs Kok and Dr. Wim Kanning for setting up the All-risk programme and creating such a great atmosphere and the nice All-risk book[1].

Witteveen+Bos has been really supportive throughout these years. I would really like to thank Egbert, Robert and Dirk-Jan for their trust in me, even before I started my PhD. I also would like to thank my colleagues; Floris, Stan, Friso, Jasper, Osco, Esther, Jos, Bart and many others, for their help with drawings, programming, project management, English writing, and the technical discussions at the coffee corner. I am looking forward to work with you on other projects again.

Dad en mam, bedankt voor het vertrouwen dat jullie altijd uitspraken, vroeger op school en nu nog. Matteo en Laudi, mooi om tegelijk met jullie te studeren, de één net klaar en de ander bijna, trots op jullie. En hoe leuk was het om samen een Android app (ShansApp) te ontwikkelen om soil tests te simuleren. Nina, jij was er altijd voor mij en ons gezin en wist telkens weer een gezond perspectief te schetsen. Stress smelt als ijs door jouw zonnestralen.

---

[1] https://kbase.ncr-web.org/all-risk/

'The summit is what drives us, but the climb itself is what matters' - Conrad Anker.

This is true for all the epic trail adventures I had in the Alps, but certainly also for this PhD. I really enjoyed the research and to deepen my understanding of soil mechanics, to contribute to geotechnical and dike engineering.

CONTENTS

1
Introduction

1.1   Background

The Netherlands is inherently challenged by the sea as a major part of the country lies below average sea level. The protection against flooding has therefore always been and will continue to be top priority. The Delta Plan was initiated in response to the North Sea Flood in Zeeland in 1953. The goal of the Delta Plan was to protect the western part of the Netherlands against flooding using dikes, dams and other types of barriers. The execution of the Delta Plan took several decades to complete. This contributed to the internationally renowned expertise of the Netherlands in the field of hydraulic engineering.

In addition to being coastal, the Netherlands is also a deltaic country. Several major rivers in Northwestern Europe cross the country, finding their way to the sea. In times of high river discharges that occur after the melting of snow and ice in spring or in periods of heavy rainfall, the high river water levels threaten the people living behind river dikes. In 1993 and 1995, high water levels in the Rhine and Meuse rivers led to local flooding in the south and to a critical situation in middle of the country (1995) whereby 250,000 people were evacuated out of precaution.

In response to these extreme events, the necessary reinforcement of the primary flood protection structures was organized in 2014 by the Dutch Ministry of Infrastructure and Water management and the Regional Water Authorities in the Dutch Flood Protection Programme (in Dutch: 'Hoogwaterbeschermingsprogramma', abbreviated as 'HWBP'). Flood protection from then on not only involved dike reinforcements, but also the creation of dedicated areas to allow more space for rivers in times of extreme water discharges. This concept is known as 'Room for the River' (in Dutch: 'Ruimte voor de rivier').

The 'National Water Plan' is the Netherlands' flood risk management plan for the four basins of the Rhine, Meuse, Schelde and Ems River. The flood risk management plan uses a risk-based approach (Jonkman and Schweckendiek 2015; Jorissen et al. 2016). The approach requires that the greater the risk (probability of flood occurrence times potential consequences), the stricter the standards. In addition, these standards consider the probability of flooding rather than the probability of exceedance of a hydraulic load (i.e., water level). The flood risk management plan offers everyone living behind the flood defenses in the Netherlands a tolerable yearly risk level of 1/100,000. Additional protection is offered to areas where there may be (1) potentially large group of victims, (2) major economic damage, or (3) serious damage as a result of the failure of vital and vulnerable infrastructure of national importance.

The by far most prevalent form of flood protection in the Netherlands is the approximately 22,000 km of earthen dikes, of which 3800 km are primary flood defenses. The vastness of the

network and age of the dikes result in the need for continuous evaluation and reinforcement. One specific challenge regarding dike reinforcement in the Netherlands is introduced by the presence of soft subsoil conditions at many of the dikes. These soft soils in polder areas and along rivers often consist of organic clays and peats. Such soils have a low stiffness and continue to deform over time; however, their strength is often underestimated. Organic soils are neither easily nor properly identified from Cone Penetration Tests (CPTs) using existing interpretation methods.

Subsidence, sea level rise, and the increase of rain intensity and river discharge due to climate change all lead to additional challenges to dike reinforcement. To maintain required levels of safety, the top elevation of earthen dikes is incrementally raised over time with soil to compensate for sea level rise, increased flood intensities and subsidence. However, raising a dike requires an extension of its base, which is sometimes restricted by the presence of existing buildings. These dikes can be reinforced by alternative means such as a sheet pile wall. This research is focused on the global stability assessment of dikes, addressing both the modeling challenges of organic soil and dike reinforcement using sheet piles.

1.2   Dike reinforcement practice and challenges in the Netherlands

The flood risk management plan comprises of new flood protection standards to address the safety of flood defenses in deltaic areas in the Netherlands. These standards are based on the estimated probability of flooding and the expected impact of the flooding (e.g., casualties, damages, disruption). The dikes must be inspected and their level of safety re-assessed every decennial. This is done to verify adverse local conditions with respect to geometry, strength and recent changes in loads and failure mechanisms. The design lifetime of dikes is typically 50 years and accounts for recent changes in risk assessment of the protected properties and inhabitants, and long-term changes in environmental conditions such as flood intensities, sea level rise and subsidence.

Efforts are also being made to identify opportunities for synergy between flood risk management, spatial economics, nature development, and cultural heritage. Traditional reinforcement by base widening and crest raising is not always possible due to the ongoing urbanization throughout many areas in the Netherlands. Urbanization changes greenfield areas to brownfield areas, which introduces multiple new functions and stakeholders. Hence, new reinforcement methods with sheet pile stability walls as shown in Figure 1.1 have become more popular because they strengthen the dike without increasing its base.

The application of sheet piles started after the flooding of the Waal, Maas, and Rhine in 1995 and continues to increase for dike reinforcement projects. In densely populated areas, such as the city Den Oever, dikes are often reinforced with sheet piles over the full length. In sparsely populated areas with villages, like the project 'Nederbetuwe' along the main branch of the river Rhine (In Dutch: 'Waal'), dikes are often reinforced by sheet piles over a portion of the length (e.g., 5 km of the 20 km at 'Nederbetuwe'). The direct costs of sheet piles are typically a factor 2 higher compared to conventional widening and raising with soil. Engineering costs and asset management costs also increase, as well as the CO_2 emissions. The percentage of length reinforced with sheet piles is expected to increase in future dike projects due to constraints from other functions and stakeholders. The total length of installed sheet piles is expected to grow to

hundreds of kilometers in the next 50 years. This thesis is an attempt to improve the design and assessment of dikes reinforced with sheet piles.
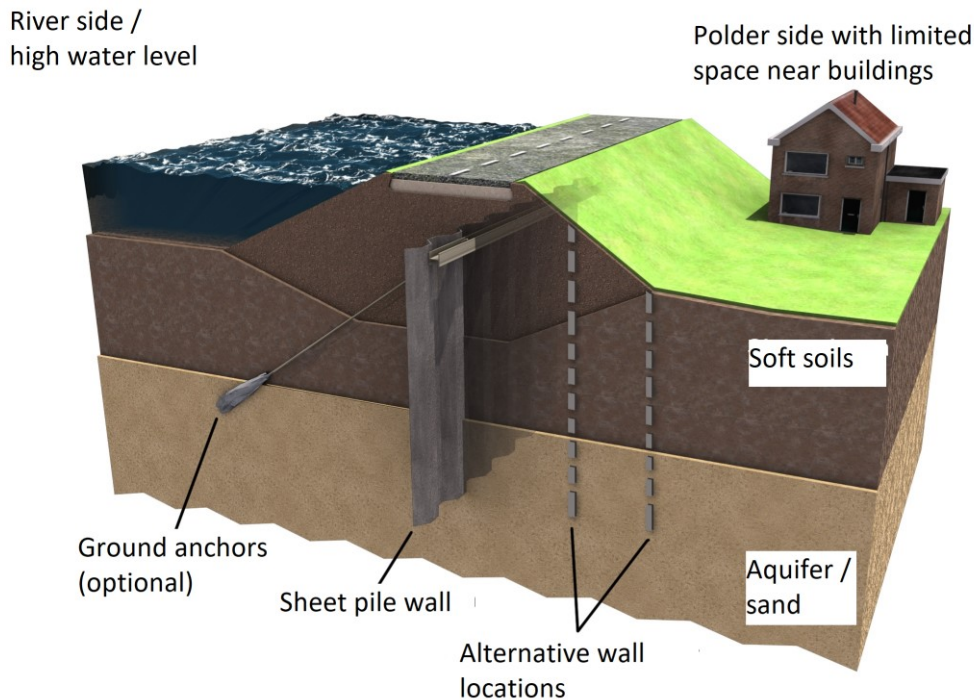
Figure 1.1 Sketch of dike with sheet pile reinforcement [Figure courtesy https://www.hwbp.nl/kennisbank/pov-macrostabiliteit]

1.3   Knowledge gaps

The assessment of the macro-stability of earthen dikes is traditionally performed with limit equilibrium methods (LEM). These methods have been effectively applied for slope stability assessment and can include non-circular failure surfaces and uplift conditions. LEM models only consider the soil's fully plastic shear strength, independent from the amount of deformation. Therefore, the mobilization of strength and deformations are not considered. Additionally, such methods cannot be applied to dikes with sheet pile stability walls because soil-structure interaction (SSI) is not included. SSI requires the use of more advanced numerical methods, such as the finite element method (FEM), which includes structural properties and stiffness and strength parameters for soil. Although experience with FEM and SSI exists for other types of infrastructure since the 1990s (Jardine et al. 1986; Bourne-Webb et al. 2011; Gaba et al. 2017), the application in dikes on organic soils is different and challenging because of the following aspects:

- The required safety levels are very strict. The acceptable probability of flooding for a dike section in the new safety standards range from 1/300 to 1/100,000 per year, depending on the dike section. The target probability for geotechnical failure in a specific cross-section is even more strict and the associated hydraulic conditions are beyond any experience. Such design conditions completely rely on models.
- The stability assessment of dikes considers global failure, which leads to breaching and flooding. It is based on the critical state strength of the soil, associated with large strains and ongoing irreversible displacements. Sheet piles are stiff structures compared to the soft

organic soils present. The SSI effects the mobilization of strength along the failure surface, which introduces a modeling challenge.
- The determination of properties for organic soils and the translation to constitutive model parameters for stability assessment with FEM is different than from that of mineral soils and it is not well captured in existing research.
- There are more types of failure mechanisms of a wall in an earthen embankment compared to a retaining wall alone or embankment alone. The combined failure mechanism of soil and wall cannot be captured by either a simple active-passive wedge or slip circle analysis.

The challenges associated with the above aspects has led to the study presented herein.

1.4 Aim of this thesis and research questions

The aim of this thesis is to improve the geotechnical stability assessment of river dikes under high water conditions, in particular dikes with sheet pile reinforcement. To steer the research towards the primary goal of this thesis, the following main research question and sub-questions have been formulated:

How does a dike on organic soil reinforced by a sheet pile wall perform under high water conditions, and how can this be modeled?

The sub-questions are divided in two categories: dikes in general and dikes reinforced by sheet piles.

Dikes in general
How can the stability assessment be improved by:
1. advanced CPT-based classification methods and correlations for organic soils?
2. linking effective strength parameters to undrained strength parameters using Critical State Soil Mechanics theory?
3. re-examination of ultimate strength criteria, standardized procedures and numerical simulations to determine constitutive model parameters?

Dikes reinforced by sheet piles
The following sub-questions are formulated related to the Eemdijk full-scale failure test that has been studied in detail as part of this research.
4. How does a dike with sheet pile reinforcement perform leading up to and beyond failure in a full-scale failure experiment and how does this compare to an earthen dike?
5. What is the performance of the sheet piles leading up to and beyond failure?
6. How can the complex soil-structure interaction and failure mechanism of a sheet pile reinforced dike be analyzed and explained by means of the finite element method?
7. How can the results of this research be used to improve the dike engineering practice?

1.5 Research method

The following research activities have been undertaken to address the research aim and questions.

Firstly, CPTs and boreholes that were performed in proximity of each other were selected from several different dike engineering projects throughout the Netherlands. Laboratory test results

and CPT measurements taken at the same depth were paired and processed into a regional database. The data was analyzed and existing and new CPT-based methods were explored. This allowed for the development of improved CPT-based methods for organic soils, such as classification and correlations (Research question 1).

Secondly, a new CSR model classified as "Simplified Critical State Soil Mechanics" was developed. This new theoretical model was formulated to define the undrained shear strength in Triaxial test conditions based on the critical state friction angle, the vertical effective stresses and stiffness based on oedometric loading conditions. The CSR model can be used in a stability analysis and for evaluation of the undrained shear strength (Research question 2 and 3).

Thirdly, the Dutch Flood Protection Programme initiated a full-scale failure test on a dike reinforced by a sheet pile wall in Eemdijk (Breedeveld et al. 2019). This experiment was focused on the soil-structure interaction leading up to and beyond failure of a sheet pile reinforced dike on soft soil conditions. The activities consisted of setting up and performing the experiment in 2018 in collaboration with Deltares and Witteveen+Bos as part of the POVM programme[2].

The full-scale failure test was used in this study to analyze the measurements and compare results with back-analyses. The Eemdijk full-scale failure test consists of three tests (Lengkeek et al. 2019a; Lengkeek et al. 2019b):
- Sheet pile pull-over test (PO-test)
- Ground dike test (GD-test)
- Sheet pile reinforced dike test (SPD-test)

The GD-test and SPD-test were performed on a newly constructed embankment. The embankment consisted of two parallel sections of 60 m length with a maximum height of 5.5 m. The core material consisted of sand and the cover layer consisted of firm clay. The center area of the embankment contains a clay cut-off wall to create two compartments with controllable water levels. The focus of the Eemdijk full-scale failure test is on the SPD-test. The GD-test is used as reference case and to optimize the SPD-test conditions. The PO-test is used to investigate the sheet pile properties and the soil structure interaction up to and beyond failure.

This research provides additional insights through a detailed analysis of the deformations of dikes leading up to and beyond failure. Furthermore, the soil investigation was re-examined and parameters are determined for multiple constitutive models applied in FEM back-analyses of the Eemdijk full-scale tests. Finally, both the CPT-based methods and CSR model are validated for the Eemdijk test site (Research question 3 to 7).

Reduction of unnecessary conservatism in a design approach can be reached through physical and numerical experiments. Numerical models, such as the finite element method, can be used to model the deformations until failure. Numerical models can also be used to model soil-structure interaction. The Eemdijk experiment involves a combination all of these.

1.6   Outline
This thesis is structured around the research topics as mentioned in Section 1.4. Following this Introduction, Chapter 2 presents a new CPT-based classification method for soft organic soils as

---

[2] https://www.hwbp.nl/kennisbank/pov-macrostabiliteit

well as pairwise established CPT-based correlations to estimate geotechnical properties (Research question 1).

Chapter 3 presents the elaboration and formulation of a new model called the CSR model, which enables a link between effective strength parameters and undrained strength parameters. It also describes the methods to obtain parameters for existing constitutive models used in the finite element method (Research question 2 and 3).

Chapter 4 presents the results and evaluation of the Eemdijk full-scale failure test ("Eemdijk damwandproef" in Dutch). It includes a description of the test lay-out, the geotechnical investigations, the instrumentation, the construction and loading scheme and the test results. This chapter also includes the results of back-analyses and conclusions of the applicability of the proposed CPT-based methods (Research question 4). Lastly, this chapter presents the investigation of how the complex soil-structure interaction and failure mechanism of a sheet pile reinforced dike can be analyzed and explained by means of the finite element method (Research question 6).

Chapter 5 presents the conclusions on the various subjects. Recommendations are presented identifying how the research outcomes and the proposed methods can be integrated and used for the assessment of (reinforced) dikes under design high water conditions in the engineering practice. The relations between the chapters in this thesis are illustrated in Figure 1.2.
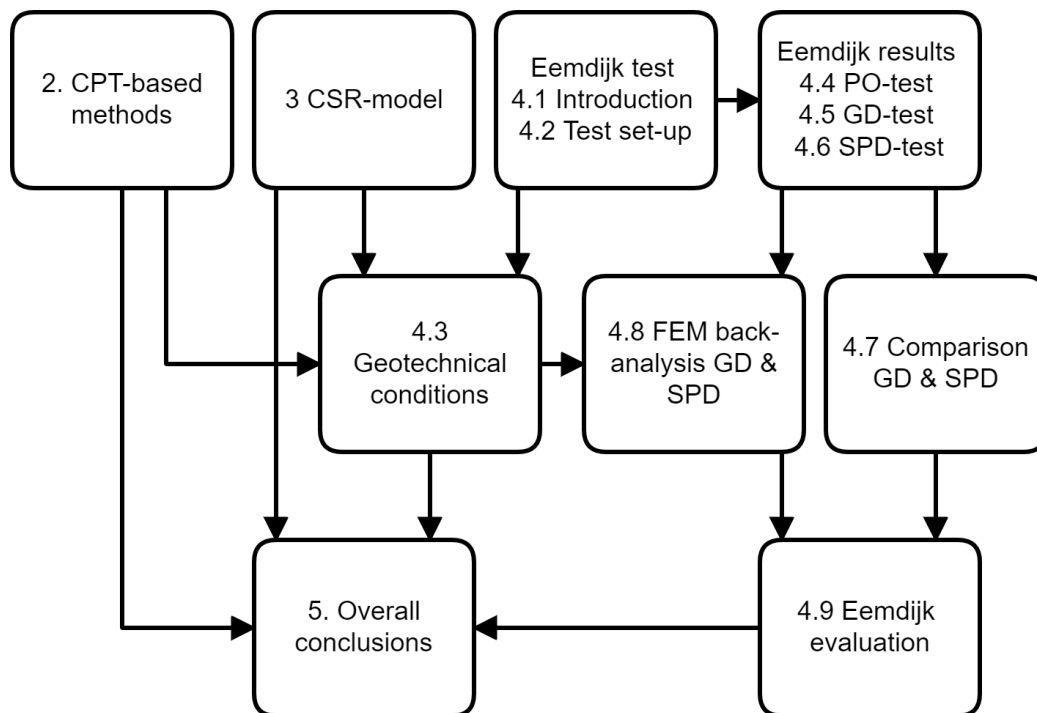
Figure 1.2 Flowchart illustrating the relations within this thesis

1.7   All-Risk research programme

This thesis is part of the All-Risk project, which was initiated in 2017 to support the Dutch Flood Protection Programme in its implementation of a new probabilistic risk-based approach to the management of flood defenses. The All-Risk project provides research categorized by five themes (A to E) to:

- Improve risk assessment by reducing the uncertainty of the estimated flood probabilities (theme A) through the understanding of the spatial and temporal hydraulic loads (theme B), subsoil characteristics (theme C), and the strength of flood defenses (theme D).
- Evaluate the design of innovative reinforcement measures throughout entire dike sections for improving the ecological benefits and landscape utilization (themes A to D).
- Develop legal and governance arrangements that clarify responsibilities and legal rights of local stakeholders to support the implementation (theme E).

This research is part of theme D, Reliability of flood defenses. The work in this thesis focuses on a better understanding of failure mechanisms, models and reinforcement techniques, to reduce the conservative estimates that are often encountered in current models and standards. The other research as part of theme D which are not included in this thesis are:

- Residual dike resistance
- Time dependency and interactions
- Incorporating past performance
- Overtopping flow and cover erosion
- Berms and roughness elements and their effect on overtopping

CPT-based methods for organic soils

2.1 Introduction

To successfully plan, design and construct a geotechnical project, various types of investigative techniques to obtain a broad spectrum of information, such as topographic, geological, geotechnical, geo-hydrological, and structural are required. Geotechnical field investigations generally comprises of borehole with sampling, and of in-situ cone penetration tests, performed with a friction cone penetrometer (CPT) or with a piezocone penetrometer (CPTU). In early stages of a project CPTs are used for profiling and setting out additional investigation for special soils and at varying conditions. In later stages CPTs are considered together with boreholes and laboratory tests to determine site specific classification and correlations based on paired data in the cross sections. In the design stages this can be used for CPT-based parameter determination along the whole dike, an example of such a design method is the 'Dijken op Veen' (peat dikes) method by Zwanenburg and Jardine (2015).

This chapter presents a new CPT-based classification method for soft organic soils as well as pairwise established CPT-based correlations to estimate geotechnical properties, addressing research question 1 of this thesis. The research is focused on levee projects in the Netherlands, but is more broadly applicable to other geotechnical projects where organic soils are involved.

2.1.1 Application of CPTs for dike projects in the Netherlands

The use of Cone Penetration Tests (CPT) in the design of dikes in the Netherlands has intensified over the years. On a typical dike project of certain kilometers length, CPTs are performed typically every 100 m along the center line, supplemented with 3 CPTs and 1 borehole along a cross section every 200 m. The number of CPTs is typically 5 times greater than the number of boreholes. This is related to the relative costs and the increased possibilities associated with the use of CPTs.

With the increase of automated processed CPT data in engineering (Brinkgreve 2019; Van Berkom et al. 2022), it is required to have an accurate classification of soils and estimation of soil unit weight, as this is the first and most important step in geotechnical parameter determination. This is relevant for organic soils which are not included in existing CPT-based methods. With thousands of kilometers of dikes and about 25 CPTs per kilometer of dike, there is an evident need and good opportunity for better classification and correlations. The term correlation is equivalent for trend, empirical relation or transformation model.

---

[3] Contents of this chapter has been accepted in two articles for CPT'22 conference (Lengkeek and Brinkgreve 2022a, 2022b).

2.1.2 Application of CPTs in organic soils

Cone penetration testing (CPT) has become increasingly popular as the preferred in-situ test method as it can be used for soil classification, estimation of geotechnical parameters and in empirical methods. The initial soil texture-based classifications were based on direct measurement of cone resistance(q_c) and sleeve friction (f_s) e.g. Begemann (1965). The current CPT-based classification systems are based on behavior characteristics and are often referred to as a Soil Behavior Type (SBT) classification (Robertson 2009, 2010, 2016). These classification systems are based on normalized cone parameters, include pore pressure measurements from CPTU tests and possibly the shear wave velocity from seismic CPTs. Examples of CPT-based empirical methods can be found in the Eurocode (EN1997-1 2005; EN1997-2 2007), where the cone resistance is used for the estimation of soil strength. In addition, there is a wide range of publications on CPT-based estimation of geotechnical parameters. A comprehensive overview can be found in Kulhawy and Mayne (1990); (Lunne et al. 2002; Mayne 2014).

To date, most published research is on mineral soils. Existing CPT-based correlations for mineral clays do not accurately capture the behavior of soft organic clays and peats compared to other soils (Mayne et al. 2020). The properties of peats have been investigated and extensively published (Den Haan and Kruse 2007; Mesri and Ajlouni 2007). However, limited attention has been devoted to the whole range of slightly organic clay to peat, and how this relates to CPT measurements. These organic soft soils are frequently present within the Holocene deposits in the Netherlands and in other deltaic areas worldwide. Organic soils are characterized by a low unit weight and high compressibility. Organic soils can be identified by a high organic content and high CPT friction ratio and low CPT pore pressure. In contrast to other soft soils, the strength is not necessarily low.

The aim of this research is to improve the applicability of CPTs for organic soils. To achieve this, results from soil investigations from dike reinforcement projects across the Netherlands have been collected. CPTs and boreholes that were performed in proximity of each other have been selected. The laboratory test results and CPT measurements are taken at the same depth, paired, and processed into a regional database. By presenting and analyzing the measurements from this large database of soft organic soils a better understanding of the typical behavior of organic soft soils is achieved. In this section, three improvements for CPT-based methods for organic soils are proposed:
- Updated unit weight correlation
- Adjustment of SBT classification for organic soils
- Correlations for organic soil properties

2.1.3 Research approach and databases

This research combines an existing database Lengkeek et al. (2018) and a new compiled database for organic soil properties, referred to as the 2021 database. Both datasets consist of pairs of soil samples and CPT measurements. The 2018 database includes the sample unit weight and Class 2 CPTs of Holocene and Pleistocene sedimentary deposits in the Netherlands. This database is used for the unit weight correlation that is applicable for the whole range of soils, from sand to peat.

The 2021 database includes the classification, strength and compression laboratory test results and ISO class 1 CPTs of Holocene organic clays and peats in the Netherlands. This database is used to derive new CPT-based correlations for organic soils. The combined database is used to validate and update the unit weight correlation, and to propose an adjustment to the CPT-based classification to include organic soils. Figure 2.1 presents the overview of these databases and primary goals. The databases are available in the Delft University of Technology repository[4] (Lengkeek 2022).

Section 2.2 presents an overview of existing classification methods, section 2.3 presents an overview of the properties of organic soils and the research methodology is presented in section 2.4. Section 2.5 presents an updated unit weight correlation for organic soils and mineral soils, section 2.6 presents an adjustment to the existing SBT classification to account for organic soils and section 2.7 presents new CPT-based correlations for the whole range of organic clays and peats. The conclusions are presented in section 2.8.

2018 database
- Unit weight correlation sedimentary soils of Holocene and Pleistocene deposits in NL

2021 database
- Correlations organic soils from deltaic Holocene deposits in NL

Combined database
- Validation and update unit weight correlation for organic soils
- Adjustment SBT and SBTn classification for organic soils
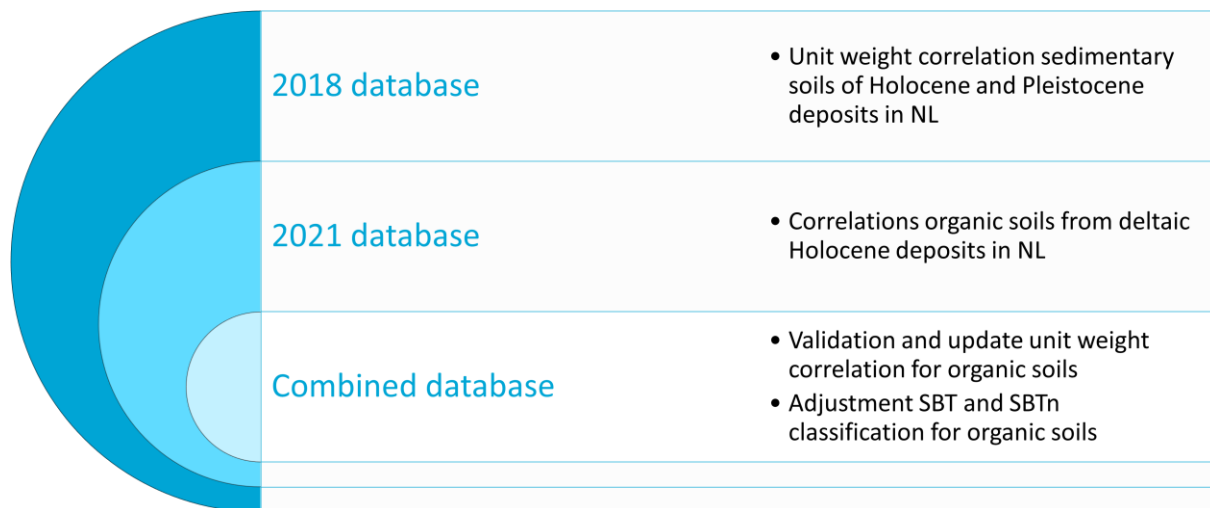
Figure 2.1 Overview of databases and research output

2.2   Classification methods
This section presents an overview of existing laboratory and CPT-based classification methods.

2.2.1   Laboratory classification
Existing classification systems are based on geomorphology, topography, botanical origin, genetic processes, chemical properties or physical characteristics. From a geotechnical engineering perspective, the physical characterization is the most relevant. Several classification systems for organic soils are used in various countries and are based on similar grounds. In many cases, a certain degree of humification (Von Post 1922; Landva 2007) is used for the classification of peat, together with the normal geotechnical parameters, such as water content, Atterberg limits, organic content, bulk density etc. Understanding of the stratification and properties in a soil profile is made easier if the geological history and the environmental conditions at deposition of the sediments are known.

Examples of classifications for geotechnical engineering can be found in MacFarlane (1969); (Landva and Pheeney 1980; Andrejko et al. 1983; Jarrett 1983; Landva et al. 1983; NEN5104 1989; Wüst et al. 2003; Huang et al. 2009; O'Kelly 2016; ISO14688-1 2017; ISO14688-2 2017). Both the term Organic content and Ash content are used to identify organic soils. The classification systems differ, in particular for the organic content in the range [20, 50] %, where peats and organic clays overlap.

The identification and description of soils are currently specified in the international standard ISO14688-1 (2017). The identification of fine-grained soil is based on the plasticity of the soil. The identification of soils rich in organic matter is summarized in Table 2 of ISO14688-1 (2017). These include Peats (amorphous to fibrous type), Humus, Gyttja and Dy. Following identification and description, ISO14688-2 (2017) gives the means by which soils can be classified into groups of similar composition and geotechnical properties. Classification uses the results of laboratory tests. The laboratory tests are carried out in accordance with ISO14475-1 (2016) and subsequent parts. Classification places soils into groups based on their nature which is the composition only, irrespective of the water content, considering the following characteristics: particle size distribution, plasticity, organic content, chemical constituents, and origin of the deposit.

2.2.2   CPT-based classification methods

CPT-based classification methods provide two-dimensional charts for soil type classification based on the CPT measurements. These charts were developed through direct correlation between the CPT data and the corresponding soil type determined from adjacent borings. The initial soil texture-based classifications were based on direct measurement of cone resistance and sleeve friction (Begemann 1965; Schmertmann 1978; Douglas 1981).

Robertson et al. (1986) developed a non-normalized soil behavior-based classification, initially with 12 zones. In Robertson (2010) this is updated to 9 zones based on dimensionless cone parameters (q_t/p_a, R_f) and the non-normalized SBT-index I_{SBT}. Robertson (1990) presented the normalized soil behavior classification for 9 zones, based on the linear normalized cone parameters (Q_{t1}, F_r, B_q). The soil behavior type index I_{c1} is added to this in Robertson and Wride (1998). In (Zhang et al. 2002); Robertson (2009); (Robertson 2012) the classification system SBTn is adjusted with a variable stress exponent n and nonlinear normalized cone resistance Q_{tn} and nonlinear SBT-index I_{cn}. The definition of these cone parameters is presented in Appendix A.

Since 1990, more CPT soil behavior-type charts have been developed including (Been and Jefferies 1993; Eslami and Fellenius 1997; Schneider et al. 2008). In Robertson (2016) a modified SBT classification system is presented with 7 zones and charts based on Q_{tn} versus the small-strain rigidity index I_G and versus the normalized pore pressure U_2. Additionally, a new hyperbolic shaped modified SBT-index I_B is introduced.

Existing CPT-based classifications generally relate to mineral soils due to the international application. The major disadvantage of existing CPT-based classification methods is that the classification of organic soils is inaccurate. In many cases a peat layer is classified as clay (SBT=3) instead of organic soils (SBT=2). Furthermore, it does not distinguish between peats and organic clays. This will be elaborated in the next section. Engineering of dike projects in the Netherlands, where peat is often present, is therefore mostly based on local experience or the non-stress

normalized q_t/p_a-R$_f$ chart of Robertson (2010). The reasons why pore pressure classification charts and stress normalization are not preferred will be elaborated further on.

2.3   Organic soils
This section presents an overview of the properties of organic soils.

2.3.1   Formation of organic soils
The term 'organic soils' has often been a concept with various meanings in geotechnical engineering and the rules for classification are rather diffuse. Apart from purely organic forms of peat and gyttja, there are many mixed soils from organic to mineral soils. Organic soils can be identified by their loss on ignition (LOI), the percentage of weight loss after burning in the oven. They are formed during the decomposition of dead organic substances i.e., remnants of plants and animals. This process takes place in different ways, mainly through bacterial activity, intensified by temperature and oxygen.

Peatland (Muskeg) soils can be divided into two groups, sedimentary and sedentary (Von Post 1922). Peats accumulated *in-situ* in a wetland are generally of low density. Another type of sediment with a highly variable organic content are the flood-plain sediments, which are deposited when streams at high water overflowed natural embankments. In northern Europe, the deposition of Holocene clay started at a time when large parts of the land were submerged under the sea. At the same time as the inland ice retreated, the temperature rose and thereby the biological activity increased. This increased the amount of plant and animal remains in the sediment deposits. In some areas, the lakes were overgrown and became swamps (fens) where different types of peat were formed. Such areas were also created in higher regions by topographical conditions leading to high ground water levels and marshes. An extensive description of the formation of peat is presented in Hobbs (1986); (Hartlén and Wolski 1996).

2.3.2   Properties of organic soils
The geo-mechanical behavior of peats is characterized by high initial porosity, high initial permeability, high compressibility, high creep rate, high degree of fibers and by changes in these characteristics with time and applied pressure. The behavior of organic clays depends strongly on the organic content. The loss on ignition (expressed as a percentage of the oven-dry weight) is often quoted as an index property of peats. The following definitions are used by Skempton and Petley (1970):

$$N = 100\% - AC \qquad\qquad (2\text{-}1)$$

$$OC = 100\% - MC \qquad\qquad (2\text{-}2)$$

Where N is loss on ignition, AC is ash content, OC is organic content and MC is mineral content; all units in percent (%). The specific gravity of the soil particles (G_s) and N are closely correlated by the expressions:

$$G_s = \frac{G_m G_o}{(G_m - G_o)\left(\frac{1.04N}{100\%} - 0.04\right) + G_o} \qquad\qquad (2\text{-}3)$$

$$\frac{1}{G_s} = \frac{N}{1.354} + \frac{1-N}{2.746} \tag{2-4}$$

Where $G_m = 2.7$ and $G_o = 1.4$ as specific gravity of mineral matter and organic matter. An extensive overview of peat properties versus the main index parameter N and a simplified equation for the Specific gravity is presented in Den Haan and Kruse (2007), Eq.(2-4).

The coefficient of earth pressure at-rest for normally consolidated ($K_{0;nc}$) peats is typically lower than for mineral soils, caused by the fibre content. The use of the constant volume effective friction angle from a Triaxial compression test (TX) in Jaky's equation (Jaky 1944) for the ratio of lateral over vertical effective stress in a state of normal consolidation would lead to $K_{0;nc}$ values significantly less than those directly measured. Hence, Mesri and Ajlouni (2007) proposed to use the friction angle defined at the phase transition point, where during shear the response changes from contractive to dilative.

The compression behavior of organic clays and peat shows large similarities with mineral soft soils. Organic soils have a high rate of creep. Settlement calculations are mostly performed with isotache type of models (Bjerrum 1967; Leroueil et al. 1985; Yin and Graham 1994; Den Haan 1996; Yin and Feng 2016). These models incorporate linear or natural strain and logarithm of stress. The viscous (creep) behavior of soft soils is modeled by assuming a unique relationship between vertical effective stress, strain, and rate of creep strain. The creep rate is related to the intrinsic time, which would indicate the geological age.

Peats possess a very high initial permeability. Upon compression, the permeability of fibrous peats decreases significantly. Mesri and Ajlouni (2007) report an empirical correlation for the strain dependent permeability coefficient normalized by the void ratio (C_k), which is half the value compared to mineral clays. A smaller value means a large decrease in permeability upon compression.

2.3.3   Strength of organic soils

Landva and La Rochelle (1983); (Yamaguchi et al. 1985) discuss the importance of internal reinforcement provided by fibers in fibrous peats and explained the rather high effective friction angles reported by various investigators and anisotropic behavior. They concluded that the shearing resistance would vary depending on the orientation of the failure plane relative to the general alignment of the fibers.

In an extensive overview of data, Edil and Wang (2000) concludes that the Triaxial test constant volume effective friction angle ($\phi'_{cv;tx}$) for normally consolidated peats shows a dependency with the organic content. It varies between 35° and 45° and for organic clays and up to 65° for peats. The constant volume normalized undrained shear strength (S-ratio) based on a normally consolidated Triaxial test, defined as $S_{cv,tx} = \left[\frac{s_u}{\sigma'_{v,con}}\right]_{nc}$, varies between 0.4 to 0.6 for organic clay and up to 0.7 for peats, with the higher values at lower consolidation stress. Furthermore, the considered classification border between organic clay and peat equals $N = 25\%$, based on geotechnical considerations.

The generation of excess pore water pressures in undrained Triaxial test can be as large as the effective radial stress, resulting in the occurrence of water between membrane and sample

(Boulanger et al. 1998; Edil and Wang 2000; Cola and Cortellazzo 2005; Cheng et al. 2007; Den Haan and Kruse 2007; Zwanenburg et al. 2012). At low confining stress the shear failure line can coincide with the tension cut-off criterium. Boulanger et al. (1998) concludes that the high pore pressures for conventional rates of loading ($15\%/hr$) on peat specimens is possibly caused by the high compressibility. The specimen's continued resistance to shear while the confining stress is zero, demonstrates that the reinforcing effects of the organic fibers are extremely important under compressive loading. The measured values however become meaningless once the tension cut-off is reached in compression. The same applies for necking in extension.

The Direct simple shear (DSS) test generally provides a lower S-ratio and ϕ' than Triaxial tests. Zwanenburg et al. (2012) conclude that the observed failure of their test embankment corresponds with failure calculated with the parameter values derived from DSS test measurements for peat. The DSS undrained shear strength corresponds best to the average undrained shear strength of the combined Active, Direct simple shear and Passive stress path in a slope stability analysis.

2.4   Research methodology organic soils

This section discusses the research methodology for the interpretation of the laboratory tests and correlations with CPT data.

2.4.1   2018 database all soils

The research approach is based on pairing unit weight from laboratory tests with CPT measurements. The CPT data are taken from the same depth as the samples, with a maximum distance between borehole and CPT of 1 meter. For the 2018 database reference is made to Lengkeek et al. (2018), consisting of 231 pairs of Holocene and Pleistocene sedimentary deposits. Most of the CPTs are ISO class 2 (ISO22476-1 2012) and include pore pressure measurement.

2.4.2   2021 database organic soils

Soil investigations from various dike reinforcement projects across the Netherlands have been collected under the same pairing conditions. These soil investigations are performed in the period 2010-2020. Recently, the Dutch Water Authorities required that all new soil investigations be performed according to a dedicated protocol for dikes, summarized in a standardized STOWA Excel sheet (www.helpdeskwater.nl). The CPTs are standardized in GEF format. These standardized formats are very useful and efficient to set up a comprehensive database. The laboratory tests results are derived from classifications tests, compression tests and undrained shear strength tests. An overview of the locations and number of CPTs and boreholes is presented in Figure 2.2. The total number of undisturbed samples is 464, the number of CPT pairs is 233 of which 211 include the unit weight, 136 include organic content and 109 include specific gravity.

Figure 2.2 Overview of 57 paired CPT-Borehole locations in the Netherlands

The 2021 database consists of the following measurements and the parameters are explained below:

- Classification parameters: $\gamma_{nat}\left(\frac{kN}{m^3}\right), \gamma_{dry}\left(\frac{kN}{m^3}\right), w_{nat}(\%), N(\%), G_s(-)$.
- Compression parameters: $CR\ (-), RR\ (-), C_\alpha(-), c_v\left(\frac{m^2}{s}\right), \sigma'_{v,y}(kPa)$.
- Shear strength parameters: $s_u(kPa), S\ (-), \phi'(°)$. The shear strength parameters follow from K₀-consolidated undrained Triaxial compression tests and DSS tests.
- CPT measurements: $q_c(kPa), f_s(kPa), u_2(kPa)$.

The protocol does not require Atterberg limit tests as they do not produce reliable results (w_L, w_P) for peats and highly organic soils, whereas the Organic content is measured in most cases. The saturated unit weight γ_{sat} is calculated based on the natural unit weight γ_{nat} corrected for saturation by the set of classification parameters. The OC is determined by the measured Loss on ignition (N) method without further correction, so all graphs and relations in this chapter are relative to N. For soils containing more than $10\%\ OC$ it was found that the MC dried at $105\ °C$ only loses about 4% by weight when ignited at $550\ °C$.

The compression parameters CR and C_α are taken at the load step beyond the vertical preconsolidation stress $\sigma'_{v,y}$. The RR is taken as average from unload-reload loops with a stress ratio close to 4. The consolidation coefficient c_v is taken at the load step between the in-situ effective vertical stress $\sigma'_{v,0}$ and $\sigma'_{v,y}$.

The protocol requires strength tests on both normally consolidated (NC) and overconsolidated (OC) samples. The NC-samples are consolidated beyond the $\sigma'_{v,y}$ and the OC-samples are consolidated at the in-situ stress. No SHANSEP preloading procedure is followed for the OC-samples at the in-situ stress. SHANSEP, 'the Stress History And Normalized Soil Engineering Properties', is a testing procedures for estimating the in situ undrained shear strength of clays developed at MIT (Ladd and Foott 1974).

The Dutch dike engineering guidelines requires that for peats DSS tests are used and for clays Triaxial tests. Both the peak strength and strength at ultimate strain level are recorded. The DSS-tests are performed as undrained constant height tests up to an ultimate shear strain level of 40%. The Triaxial tests are performed as anisotropic consolidated undrained compression (CAUC) tests up to an ultimate axial strain level of 25%. The normally consolidated samples are consolidated to $K_{0;nc}$ in the range [0.35, 0.50]. The overconsolidated samples are consolidated to $K_{0;oc}$ in the range $[K_{0;nc}, 1.0]$.

The peak s_u is defined as the maximum shear stress, and the ultimate s_u based on large strain, intending to approximate the critical state strength or constant volume strength. Only the ultimate values are reported here. The strength parameter ϕ' from the Triaxial test and DSS test on NC-samples is defined by the stresses at failure:

$$\sin \phi'_{tx} = \left[\frac{t}{s'}\right]_{nc} \quad ; \quad (t = s_u) \tag{2-5}$$

$$\sin \phi'_{dss} \cong \left[\frac{\tau}{\sigma'_v}\right]_{nc} \quad ; \quad (\tau = s_u) \tag{2-6}$$

The strength parameters S from the Triaxial test and DSS test on NC-samples is defined the undrained shear strength and vertical consolidation stress:

$$S_{tx} = \left[\frac{t}{\sigma'_{v,con}}\right]_{nc} \quad ; \quad (t = s_u) \tag{2-7}$$

$$S_{dss} = \left[\frac{\tau}{\sigma'_{v,con}}\right]_{nc} \quad ; \quad (\tau = s_u) \tag{2-8}$$

All tests are consolidated in the range $10 \leq \sigma'_{v,con} \leq 400 kPa$. Samples classified as clayey sand or clay with sand laminations have been excluded from the database as they tend to be dilative and give unrealistic high values in undrained tests. Samples with very high strength ($\sin \phi' > 0.8, S > 0.6$) are excluded from the regression analyses. These samples are either associated with peats that tend to reach the tension cut-off criteria, or include sand laminations which were not mentioned in the classification. The following criteria have been used for the selection of normally consolidated samples:
-   $\sigma'_{v,con} > \sigma'_{v,y}$
-   $\sigma'_{v,con} > 2\sigma'_{v,0}$

For the overconsolidated samples, the vertical consolidation stress should match the in-situ vertical effective stress. The following criteria have been used:
-   $\sigma'_{v,con} \leq \sigma'_{v,y}$

- $0.7\sigma'_{v,0} < \sigma'_{v,con} < 1.3\sigma'_{v,0}$

This 30% margin on the $\sigma'_{v;con}$ has been added to account for the uncertainty in unit weight and groundwater level. The protocol specifies ISO class 1 CPTs, including pore pressure measurements (ISO22476-1 2012). For each laboratory test sample the corresponding level in the CPT is selected; these are the pairs. The samples are typically $2 - 12\ cm$ high, and the corresponding CPT measurements have been averaged over $20\ cm$ (11 readings, one each $2\ cm$). Averaging over $20\ cm$ is selected as a practical approach to reduce noise in the CPT reading and is in line with the uncertainty of the exact level of a test sample taken from the sampler. In case the local variation was too high, or the level was at a transition between two distinct layers, the level was shifted, up to 10 cm, to match the sample characteristics and borehole description.

The starting points for stress normalization and normalized CPT parameters are based on Robertson (2009). The stress relation follows a power function. The stress exponent-n varies with I_{cn}. The stress normalization cut-off parameter $C_n = 1.7$ applied is in line with Boulanger and Idriss (2016). The groundwater level is estimated from the borehole log data and CPTU measurements. The parameters I_{cn}, Q_{tn}, n are determined in an iterative procedure (Robertson 2009; Mayne 2017), where stresses are calculated based on γ_{sat} according to Lengkeek et al. (2018).

2.5 Updated CPT-based unit weight correlation

This section presents an updated CPT-based correlations for the unit weight of organic soils and mineral soils as encountered in the Netherlands.

The improved unit weight correlation is based on the combined database. The 2018 database mainly consists of mineral soils whereas the 2021 database mainly consists of organic soils. The combined database allows for a validation and improvement of the correlation for unit weight. The CPT- based unit weight correlation of Lengkeek et al. (2018) is shown in Eq.(2-9).

$$\gamma_{sat} = \gamma_{sat,ref} - \beta \cdot \frac{\log\left(\frac{q_{t,ref}}{q_t}\right)}{\log\left(\frac{R_{f,ref}}{R_f}\right)} \tag{2-9}$$

The correlation is based on the corrected cone resistance q_t and friction ratio R_f, which are both normalized by a reference value. The reference unit weight, here 19.5 kN/m³, is the value when q_t equals $q_{t,ref}$. The parameter β is a fit factor. The updated variables based on the combined database of 427 pairs are presented in Table 2-1.

Table 2-1 Updated parameters for saturated unit weight correlation

Parameter	Value	Unit
$\gamma_{sat,ref}$	19.5	kN/m3
$q_{t,ref}$	9.0	MPa
$R_{f,ref}$	20	%
β	2.87	

Figure 2.3 presents all measured data per soil type combined with the lines of equal unit weight (e.g., 10, 11,.., 21 kN/m³). The results are plotted on the SBT template of Robertson (2010). From this figure it can be concluded that the lines of equal unit weight are reasonable aligned with the SBT zones of coarse-grained soils but less for the fine-grained soils. Coarse grained soils, SBT=5 and higher correspond to a saturated unit weight of 18 to 21 kN/m³. The variation in unit weight for fine grained soils is much larger and in particular at SBT=2. For that reason, an adjusted classification system is proposed which is presented in the next section.
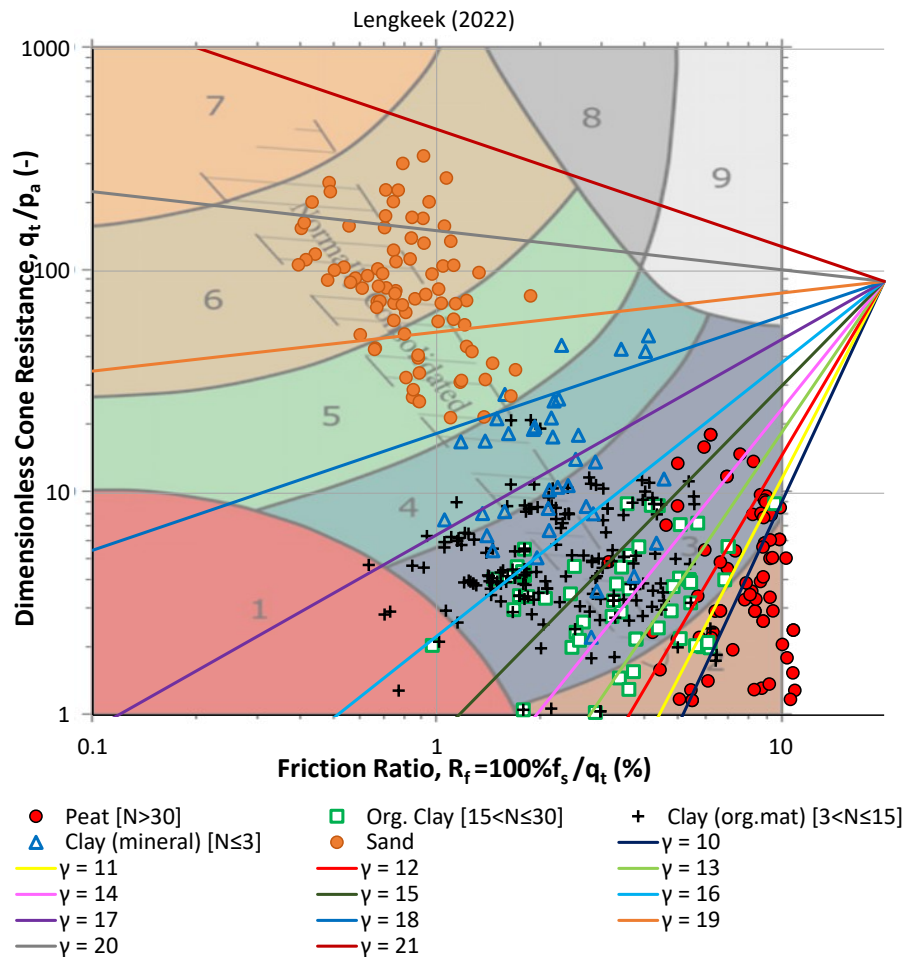
Figure 2.3 Unit weight measurements and lines of equal unit weight of the proposed improved correlation, presented on top of Robertson (2010) SBT template

Figure 2.4 shows the measured unit weight versus the predicted unit weight using the improved correlation. The database is subdivided in the soil types [Peat; Organic Clay; Clay with organic matter; Mineral Clay; Sand]. These soil types are based on the classification as will be elaborated in the next section. From this graph it can be seen that the trend follows the 1:1 line very well. The scatter is larger for lower unit weights and/or organic soils, however, for peats the results are close to 10 kN/m³, which is also the minimum value as applied.
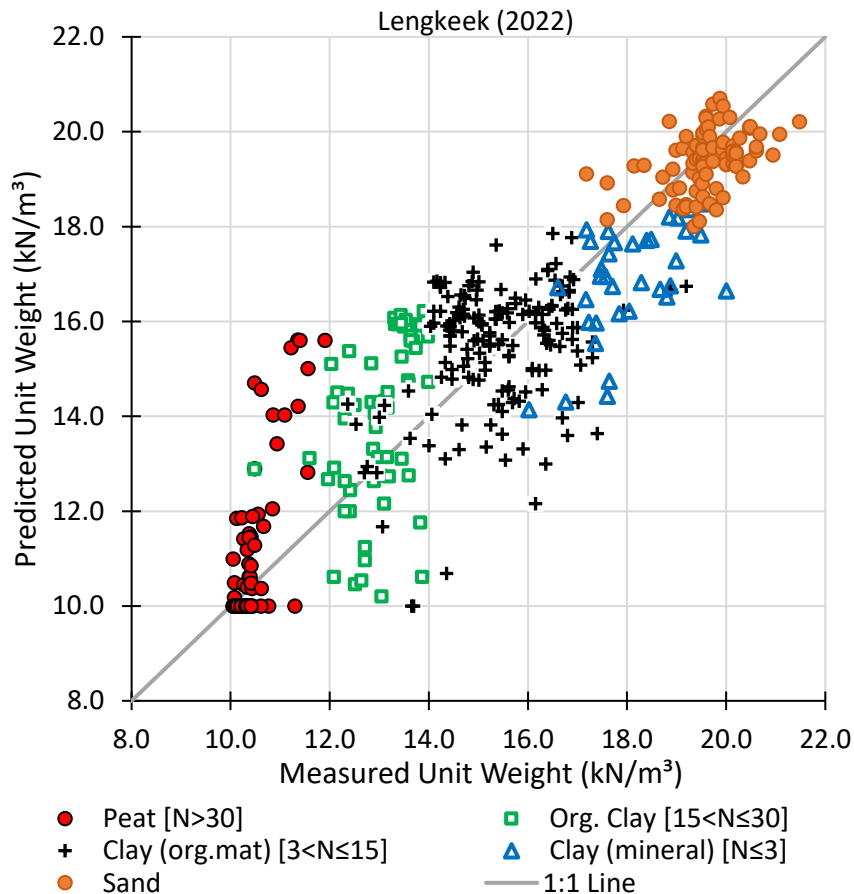
Figure 2.4 Measured versus predicted saturated unit weight, based on the updated correlation (Table 2-1)

The performance of the improved correlation can be expressed in statistical parameters, the Coefficient of determination (R^2), and the Standard deviation on regression (S_y) and the slope of the trendline through the origin [x=measured, y=predicted] in Figure 2.4. The comparison with other existing correlations (Robertson and Cabal 2010; Mayne 2014; Lengkeek et al. 2018) is presented in Table 2-2. The coefficient of determination (R^2) and standard deviation on regression (S_y) comply to Ordinary Least Squares (OLS) regression with free intercept. The slope complies with regression through the origin and is a measure for the bias. From this comparison it can be concluded that the new correlation performs better for all statistical parameters. The previous correlation results in slightly different values which confirms the validity to use the 2018 correlation in this research.

Table 2-2 Comparison of statistical results of considered unit weight correlations for the whole range of soils

Method	R^2	S_y	OLS slope [y:x]	Slope through origin [y:x]
updated correlation Table 2-1 (Lengkeek and Brinkgreve 2022b)	0.80	1.32	0.84	1.00
Lengkeek et al. (2018)	0.79	1.33	0.80	1.00
Robertson and Cabal (2010)	0.25	1.46	0.26	1.06
Mayne (2014)	0.12	1.68	0.20	1.03

2.6 Adjustment of the SBT classification for organic soils

This section presents an adjustment to the existing SBT classification to account for organic soils as encountered in the Netherlands.

2.6.1 Selected classification and soil types

Classification of laboratory samples is based on different methods. The relevant Standard for identification and description of soils is ISO14688-1 (2017); (ISO14688-2 2017). The identification of fine-grained soil is based on the plasticity of the soil. The identification of organic soils includes Peats (fibrous to amorphous type), Humus, Gyttja and Dy. In the former Dutch Standard (NEN5104 1989) the boundary between peat and organic clay consists of a transition zone of 15 to 35% Organic content measured by Loss on ignition (N), whereas the Dutch national annex (ISO14688-2 2017) uses N=30% as boundary.

To overcome the differences in classification methods, the method after Huang et al. (2009) is applied in for research. This classification method of the Federal Highway Association (FHWA) matches well with the other two methods and considers only four subcategories. The systems are very comparable as shown in Figure 2.5. The classification, based on organic content measured by the Loss on ignition (N), consists of the following soil categories:
- mineral fine-grained soils: $N \leq 3\%$
- mineral fine-grained soils with organic matter: $3 < N \leq 15\%$
- organic fine-grained soils: $15 < N \leq 30\%$
- peats: $N > 30\%$

The classification criteria and results for the combined database are presented in Table 2-3. For samples where the organic content is unknown, the classification is based on the unit weight, the secondary criteria presented in Table 2-3. The index parameters are generally well correlated and confirm the correlation by Den Haan (1997), see Figure B 3. The results are presented in the graphs in Appendix B. The names of the soil types in the table below and graphs are shortened for practical reasons.
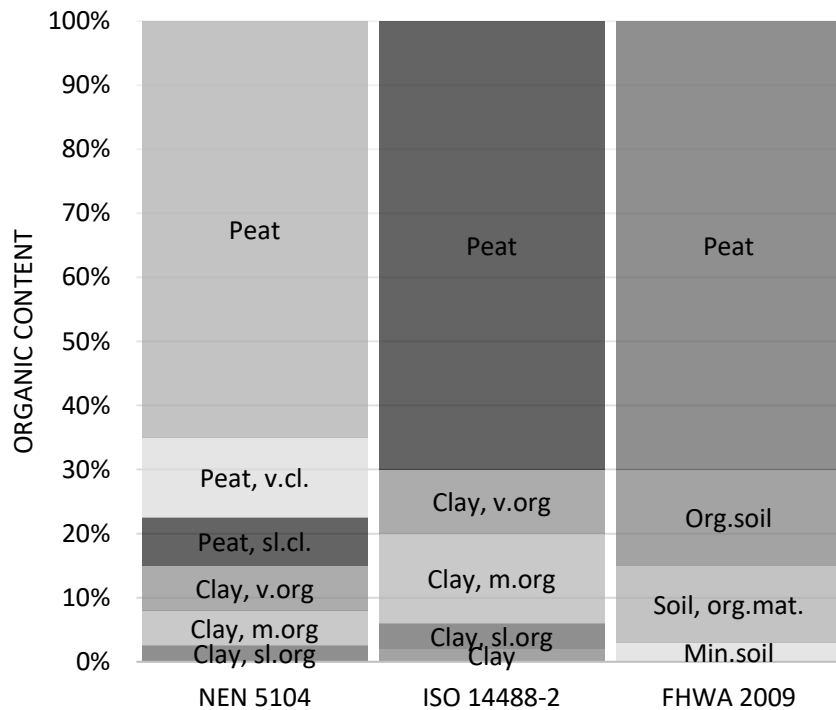
Figure 2.5 Comparison of classification systems for organic soils

Table 2-3 Classification criteria for organic soils and results per soil type

Soil type	Primary criterion	Secondary criterion	Results			
	N (%)	γ_{sat} (kN/m³)	# Tests (-)	Average N (%)	Range γ_{sat} (kN/m³)	Range Gs (-)
Peat	>30	≤12	118	79	10.1 - 13.1	1.4 - 2.0
Organic clay	15-30	12-14	55	22	11.6 - 14.0	1.9 - 2.4
Clay (org.matter)	3-15	14-17	242	8	12.4 - 19.2	2.3 - 2.7
Clay (mineral)	≤3	>17	49	2	15.6 - 20.0	2.6 - 2.7

2.6.2 Stress normalization at low stresses

The samples of the combined database are taken from 0.5 to 15 m depth and effective vertical stresses in the range of 5 to 150 kPa. For situations with the presence of peat layers and high-water tables, stresses are sometimes less than 20 kPa at 10 m depth. Therefore, care should be taken with CPT-based classification that includes stress normalization, as illustrated in the following example:

A peat layer below a dike with a high stress level of about 100 kPa is originally classified as SBT=2 (Robertson 2010) and SBTn=2 (Robertson 2009), but the same peat layer beside the dike with a low stress of 20 kPa moves up to SBTn=3 and will be classified as clay. This second classification is not correct as the soil type is the same, but only the stress state is different. Consequently, the soil profiling beside the dike can be incorrect, and the wrong parameters will be appointed to this layer. In this example the normalized cone resistance Q_{tn} is 5 times higher than Q_t. These high stress corrections are not included in the international databases where most of the stresses are typically in the range of 50 to 300 kPa.

For dike projects there is a second argument not to apply a large stress correction. The peat layers beside the dike are generally lightly overconsolidated by OCR of about 2, due to a combination of water level changes and aging. This corresponds to a Pre Overburden Pressure (POP) of 20 kPa. The POP is the difference between the preconsolidation stress and the initial vertical effective stress. The same peat layer below the dike, which has been raised periodically, is only slightly overconsolidated. As the cone resistance is related to the preconsolidation stress more than the vertical effective stress, the actual stress correction is expected be about 2 to reflect the state properties.

The proposed adjustments to the SBT charts, as will be presented in the next section, are valid for the non-stress normalized SBT chart (Robertson 2010) and the stress-normalized SBT chart (Robertson 2009) with the application of the stress normalization cut-off (C_n). In the 2021 database $C_n=1.7$ is applied in line with recommended practice by Boulanger and Idriss (2016). As upper limit a value of 2 is recommended.

2.6.3 Proposed SBT adjustment

This section presents the adjustment to the SBT classification for organic soils, such as those encountered in deltaic areas in the Netherlands. The pairs from the combined database are plotted on the Robertson (2010) template in Figure 2.6. The soil types consist of the four categories presented in Table 2-3 and one category for sand.

Figure 2.6 Combined database pairs and proposed SBT adjustment for organic soils, presented on top of Robertson (2010) SBT template

The data coincide to a large extent with Robertson (2010), as expected for the mineral soils. A few datapoints coincide with SBT=1 (sensitive soils) and no data points coincide with SBT=7, 8 and 9. Soils of SBT=7 can be present in Pleistocene sand deposits, and gravelly deposits which are present along the river Meuse in the South of the Netherlands. Soils of SBT=8 and 9 are not expected in a deltaic area down to 15 m depth.

There are major differences in for soils in SBT=2 and 3, where a significant amount of organic soils plot in SBT=3. The performance results based on the existing Robertson (2010) classification of organic fine grained soils are presented in Table 2-4. It is concluded that most of the organic soils, including most of the peats, plot in SBT=3 ($I_c \leq 3.6$). The performance is about the same for I_{cn} based on stress normalization including C_n=1.7. Without the C_n cut-off nearly all points plot outside of SBT=2.

Table 2-4 Performance results for organic soils based on existing Robertson (2010) SBT classification

SBT zone: Soil type	SBT=2 [Ic>3.6]	SBT=3, 4 [Ic≤3.6]
Peat [N>30]	35%	65%
Org. Clay [15<N≤30]	21%	79%
Clay (org.matter) [3<N≤15]	6%	94%
Clay (mineral) [N≤3]	0%	100%

The proposed adjustment is that SBT=2 is redefined and split up into SBT=2a (Peat), 2b (Organic Clay) and 2c (Mineral Clay, with organic matter). No adjustments are proposed to the boundaries between SBT=3, 4 and higher. This is also not possible as this database does not distinguish between silts and clays due to the lack of Atterberg limits tests. Most of the classified points plot in the correct SBT when using the proposed adjustment, however quite some points plot in the adjacent SBT. The selection of the boundaries is determined by maximizing the group of positives and minimizing the number of false positives and false negatives.

In addition, the boundaries are selected to separate overconsolidated organic soils from overconsolidated plastic clays, such as Pot clay and Boom clay encountered in the Netherlands. The maximum cone resistance occasionally measured in peats at high stress levels is about 2 MPa. The new boundaries are extended to a friction ratio of 20%, which is occasionally measured in peats at low stress levels.

The performance results are presented in Table 2-5. It is concluded that most of the classified points in SBT=2a and SBT=3, 4 are correct. For SBT=2b and 2c it is concluded that significant number of data points plot in the adjacent SBT but still the majority complies to the new SBT. The number of false positives outside of the adjacent SBT is less than 5%.

Table 2-5 Performance results for organic soils based on proposed adjustments to Robertson (2010) SBT classification

SBT zone: Soil type	SBT=2a	SBT=2b	SBT=2c	SBT=3, 4
Peat [N>30]	**78%**	15%	1%	4%
Org. Clay [15<N≤30]	16%	**42%**	40%	2%
Clay (org.matter) [3<N≤15]	3%	22%	**38%**	37%
Clay (mineral) [N≤3]	0%	11%	3%	**86%**

The formulation as shown in Eq.(2-10) for the new proposed boundaries is the same, the parameter values are shown in Table 2-6.

$$q_t/p_a = a_o\left(R_f - R_{f,min}\right)^{b_o}$$ (2-10)

Table 2-6 Parameter values for boundaries of proposed adjustments to Robertson SBT (2010) and SBTn (2009) classification

SBT & SBTn boundary: Parameter Eq.(2-10)	SBT=2a	SBT=2b	SBT=2c
a_o (-)	8.0	5.2	4.7
b_o (-)	0.50	0.62	0.64
$R_{f,min}$ (%)	5.2	2.3	0.60

The proposed boundaries are optimized such that they can also be applied as adjustment to Robertson (2009); (Robertson 2016), in combination with a stress normalization cut-off ($C_n \leq 2$). The parameters in Eq.(2-10) should then be replaced, Q_{tn} for q_t/p_a and F_r for R_f These boundaries for organic soils do not apply if there is no stress normalization cut-off applied. The results of the 2021 database are plotted in Figure 2.7 on top of the combined 2009 and 2016 template. The mineral clays and sands are not included, as not all stresses required for normalization are known. Most points plot in the CC zone 'contractive clays', although quite some points plot in the CCS zone 'contractive clays sensitive', which is larger than the SBT=1 (2009) zone. A few points plot in the CD zone 'dilative clays'. Those points correspond to the organic soils with high stresses or large overconsolidation.
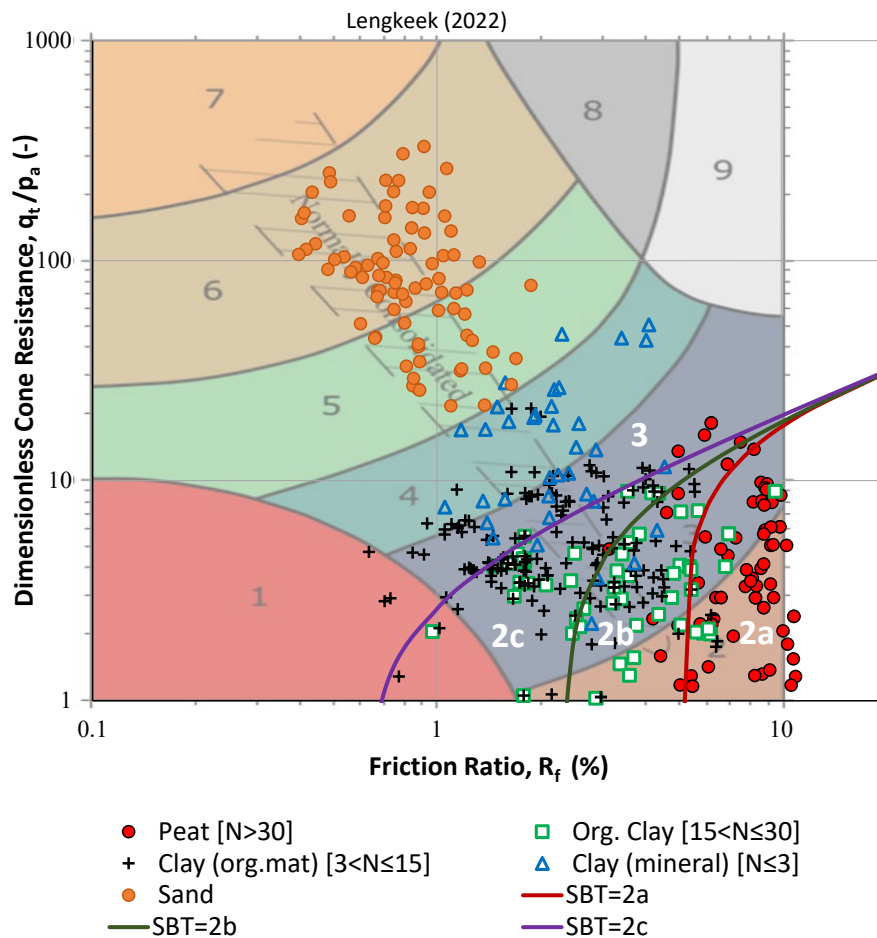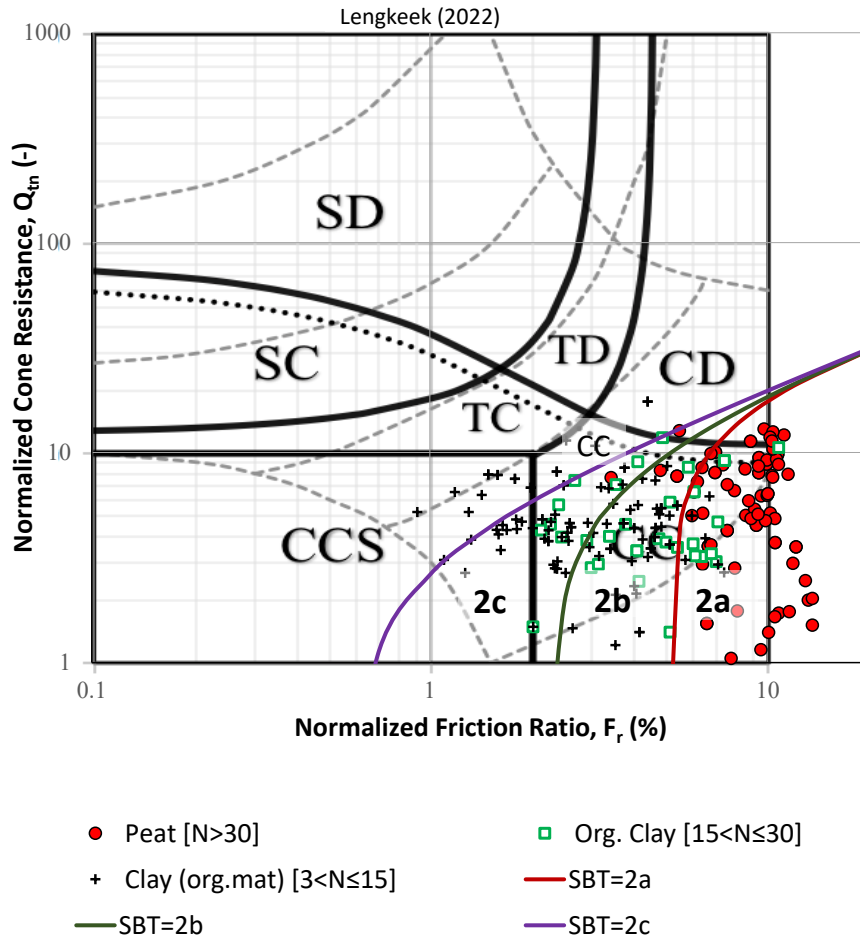
Figure 2.7 2021 database pairs and proposed SBT adjustment for organic soils, presented on top of Robertson (2009 & 2016) SBT template

2.7 CPT-based correlations for organic soils

2.7.1 Introduction

This section presents new pairwise established CPT-based correlations for the whole range of organic clays and peats between CPT measurements and index parameters such as unit weight, organic content and specific gravity. This is followed by various CPT-based correlations where the soil state parameters are correlated to the CPT cone resistance, and the unique soil type properties are correlated to the CPT friction ratio. The low CPT pore pressure measurements (u_2) are part of the key to identification of organic soils, that is their "signature". The u_2 readings for organic soils are however less reliable and therefor are not considered suitable for correlations.

The following CPT-based correlations are presented in this section:
- Saturated unit weight versus corrected cone resistance, for soils classified as peat: Eq.(2-11)
- Organic content versus CPT friction ratio, for organic to mineral soils: Appendix B.
- Compression ratio versus CPT friction ratio, for organic to mineral soils: Eq.(2-12)
- Swelling (recompression) ratio versus compression ratio, for organic to mineral soils: Eq.(2-13)
- Secondary compression (creep) ratio versus compression ratio, for organic to mineral soils: Eq.(2-14)

- Vertical preconsolidation stress versus CPT net cone resistance, for organic to mineral soils, excluding sandy clays: Eq.(2-15)
- Preconsolidation net cone factor versus CPT friction ratio, for organic to mineral soils, excluding sandy clays: Eq.(2-16)
- Undrained shear strength from at in-situ stress consolidated DSS tests versus CPT net cone resistance, for peats and organic clays, excluding mineral clays and sandy clays: (2-17)
- S-ratio from normally consolidated DSS tests versus friction ratio, for peats and organic clays, excluding mineral clays and sandy clays: Eq.(2-18)
- Undrained shear strength from at in-situ stress consolidated CAUC Triaxial tests versus CPT net cone resistance, for mineral clays and organic clays, excluding peats and sandy clays: Eq. (2-19)
- S-ratio from normally consolidated CAUC tests versus friction ratio, for mineral clays and organic clays, excluding peats and sandy clays: Eq.(2-20)

2.7.2 Relations between index parameters and CPT measurements

The CPT-based correlation for unit weight is presented in the previous section, as this one is based on the combined database. The relations and correlations in this section are based on the 2021 database, which focuses on organic soils and uses ISO class 1 CPTs.

The relations between the index properties only are presented in Appendix B. The Appendix B shows various graphs with the subcategories indicated in the legend, the trendline and the confidence intervals are indicated in the graphs and the statistical parameters are shown in the title. The regression methodology, determination of the statistical parameters and transformation uncertainties are described in Lengkeek et al. (2021). The main conclusion is that the existing relations between unit weight, natural water content, specific gravity and organic content comply to generally known trends. Furthermore, the organic content and specific gravity can be well correlated to the CPT friction ratio. These will not be discussed here further, as this is outside the scope of this research.

One CPT-based index correlations will be presented in this section, namely the unit weight specifically for soils that are classified as peats, as shown in Figure 2.8 and Eq.(2-11). This figure illustrates a linear relation where the range is [10, 12] kN/m^3, the R^2 is moderate and the standard deviation on regression S_y=0.265 kN/m^3. This correlation cannot be used for organic clays.
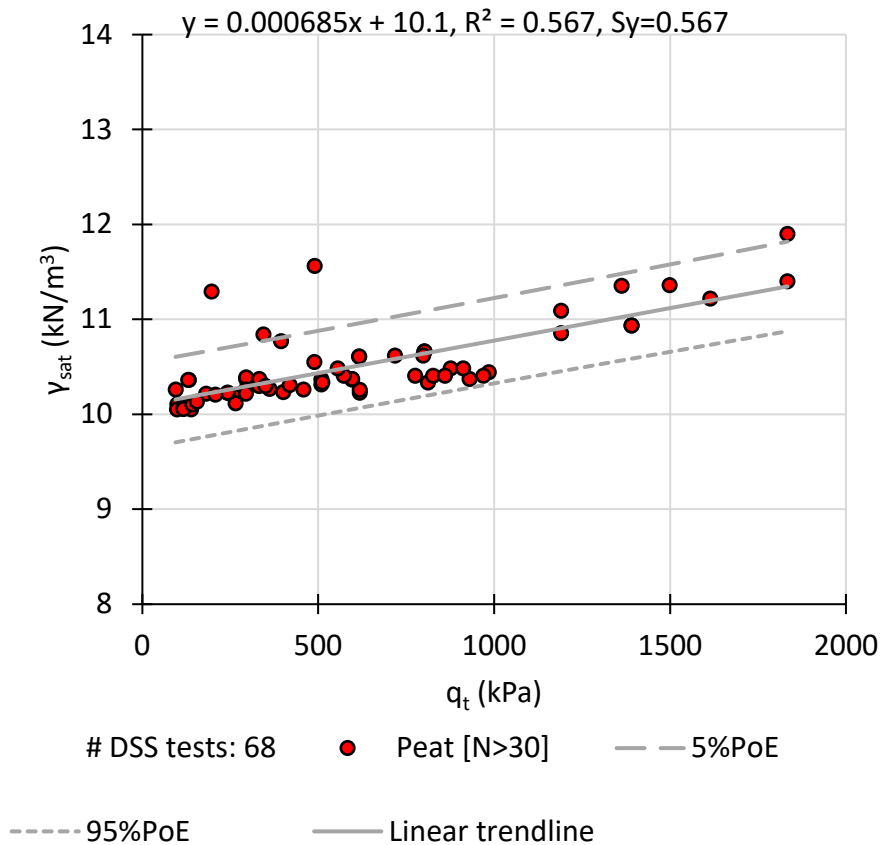
Figure 2.8 Saturated unit weight versus CPT corrected cone resistance, for soils classified as peat. The trendline and the confidence intervals are indicated in the graphs and the statistical parameters are shown in the title.

$$\gamma_{sat,peat} = 0.000685 \cdot q_t + 10.1 \qquad (2\text{-}11)$$

Where $\gamma_{sat,peat}$ is the saturated unit weight of peat in (kN/m³) and q_t is the corrected cone resistance in (kN/m²).

2.7.3   CPT-based correlations for compression parameters

This section presents the correlations between compression parameters and CPT measurements. The compression parameters are derived from Oedometer and CRS tests. The main parameter is the compression ratio CR. The relation to the compression index C_c and other parameters is presented in Table 2-7. In the Netherlands it is more common to use the CR, as this parameter is directly determined from the change in volumetric strains and does not require an accurate determination of the void ratio. The void ratio can only be determined accurately in case the specific gravity is measured, which is not always the case for the exact same sample.

Table 2-7 Compression parameter definitions

Compression parameter	Definition
Compression Ratio (-)	$CR = \dfrac{C_c}{1+e_0} = \dfrac{\Delta\varepsilon_v}{\log\frac{\sigma'_{v2}}{\sigma'_{v1}}}$
Swelling (Recompression) Ratio (-)	$RR = \dfrac{C_r}{1+e_0} = \dfrac{\Delta\varepsilon_v}{\log\frac{\sigma'_{v2}}{\sigma'_{v1}}}$
Secondary Compression (Creep) Ratio (-)	$C_\alpha = \dfrac{C_{\alpha e}}{1+e_0} = \dfrac{\Delta\varepsilon_v}{\log\frac{t_2}{t_1}}$

The pairs of compression parameters and CPT measurements follow from the whole range of soils in the 2021 database. The results are shown in Figure 2.9 and Appendix B, where the subcategories are indicated in the legend, the trendline and the confidence intervals are indicated in the graphs and the statistical parameters are shown in the title. The correlations are shown in Eq.(2-12) to Eq.(2-14).
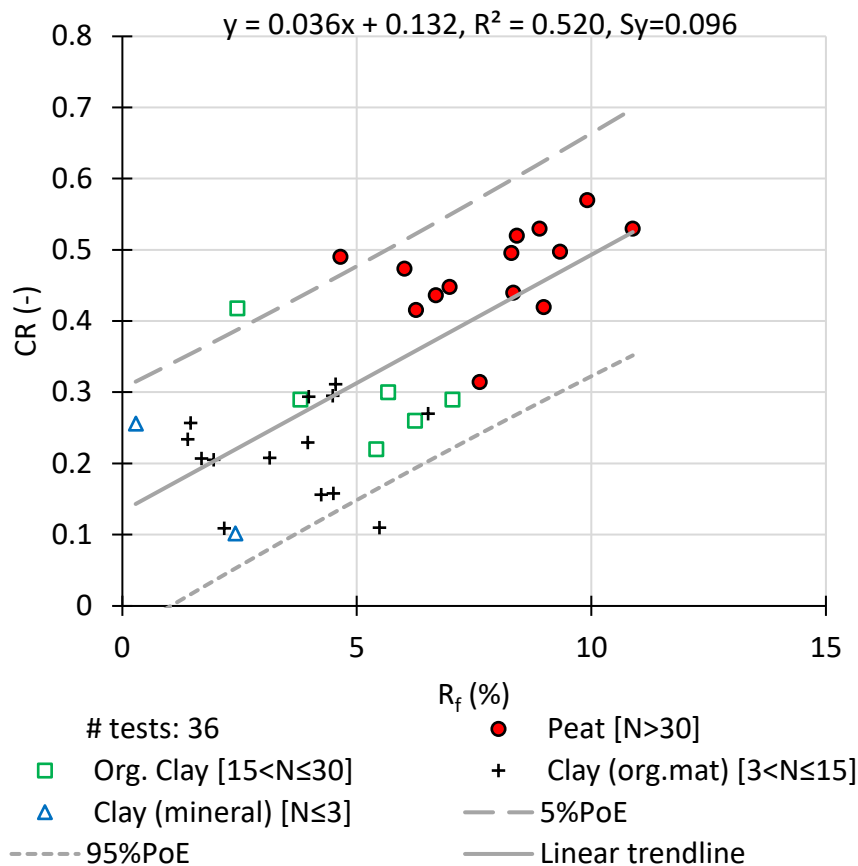
Figure 2.9 Compression ratio versus CPT friction ratio, for organic to mineral soils

Figure 2.9. and Eq.(2-12) show a linear relation between the Compression ratio and the friction ratio, the range is [0.1, 0.6], the R^2 is moderate and the standard deviation on regression S_y=0.096. This correlation is new and useful for automated CPT-based parameter determination.

$$CR = 0.036R_f + 0.132 \tag{2-12}$$

Where CR is the compression ratio (-) and R_f is the friction ratio in (%).

Eq.(2-13) shows the relation between the swelling (recompression) ratio and compression ratio. The results are presented in Appendix B. Although this parameter can also be related to the friction ratio it is preferred to relate it to the main compression parameter CR. The variation is expected to be mainly influenced by non-linearity and variation in unloading ratio. The regression is based on a linear trendline through the origin. The coefficient of determination is adjusted (Ra^2) for the fixed intercept at the origin and the standard deviation (S_a) applies to the variation of the slope of the trendline. The range of swelling ratio is [0.01, 0.15], the Ra^2 is moderate and the standard deviation S_a=0.062 (-). This corresponds to a coefficient of variation CV=0.062/0.160=39%, which is high.

$$RR = 0.160CR \qquad (2-13)$$

Where RR is the recompression ratio (-) and CR is the compression ratio (-).

Eq.(2-14) shows the relation between the secondary compression (creep) ratio and compression ratio. The results are presented in Appendix B. Although this parameter is also related to the friction ratio it is preferred to relate it to the main compression parameter CR. The regression is based on a power trendline. The relation for creep ratio is nonlinear, with relative high values for peats and relative lower values for mineral soils, which is a known trend in geotechnical engineering. The standard deviation (S_a) applies to the variation of the slope of the trendline. The range of creep ratio is [0.02, 0.06], the R^2 is substantial and the standard deviation S_a=0.032 (-). This corresponds to a Coefficient of variation CV=0.032/0.143=22%, which is moderate.

$$C_\alpha = 0.143CR^{1.635} \qquad (2-14)$$

Where C_α is the creep ratio (-) and CR is the compression ratio (-).

2.7.4 CPT-based correlations for preconsolidation parameters

Various correlations are published in literature for the vertical preconsolidation stress (σ'_{vy}), the overconsolidation ratio (OCR) or the preconsolidation net cone factor ($k_p = \frac{\sigma'_{vy}}{q_n}$). The tests have been performed on the whole range of soils. Samples with mixtures or laminations of sand are excluded as their behavior deviates from soils considered here, resulting in inaccurate and unrealistic high preconsolidation stresses.

From these analyses it is concluded that the best relation is found directly between the preconsolidation stress and the net cone resistance. The performance of the overconsolidation ratio (OCR) versus the stress normalized cone resistance (Q_{t1}) performs worse given the same database. In addition, it is shown that a secondary trend is found between cone factor (k_p) and the friction ratio.

Figure 2.10 shows the results of the preconsolidation stress versus net cone resistance, in line with existing published correlations. The correlation is presented in Eq.(2-15). The slope of the trendline is 0.161, which is the average value of cone factor (k_p). This value is almost half the value as published for mineral soils (Mayne 2017). The regression is based on a linear trendline through the origin. The range of preconsolidation stress is [15, 240] kPa, the Ra^2 is moderate, the standard deviation S_a=0.056, the CV=34%, which is high.
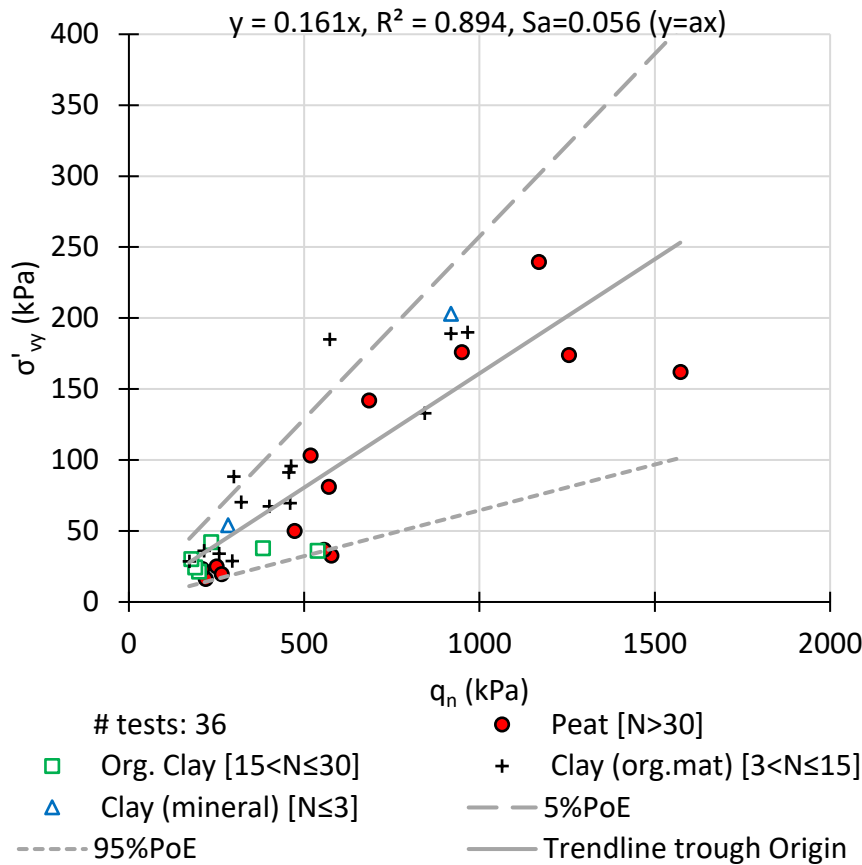
Figure 2.10 Vertical preconsolidation stress versus CPT net cone resistance, for organic to mineral soils, excluding sandy clays.

$$\sigma_{v,y} = 0.161 q_n \tag{2-15}$$

Where $\sigma_{v,y}$ is the vertical preconsolidation stress in (kN/m²) and q_n is the net cone resistance in (kN/m²).

Figure 2.11 presents the secondary trend between the cone factor (k_p) and the friction ratio. The range of k_p is [0.05, 0.32], the R^2 is weak and the standard deviation on regression S_y=0.055. The correlation shown in Eq.(2-16) confirms the expected trend and can be useful to compare site specific data. The use of Eq.(2-15) is preferred over Eq.(2-16).
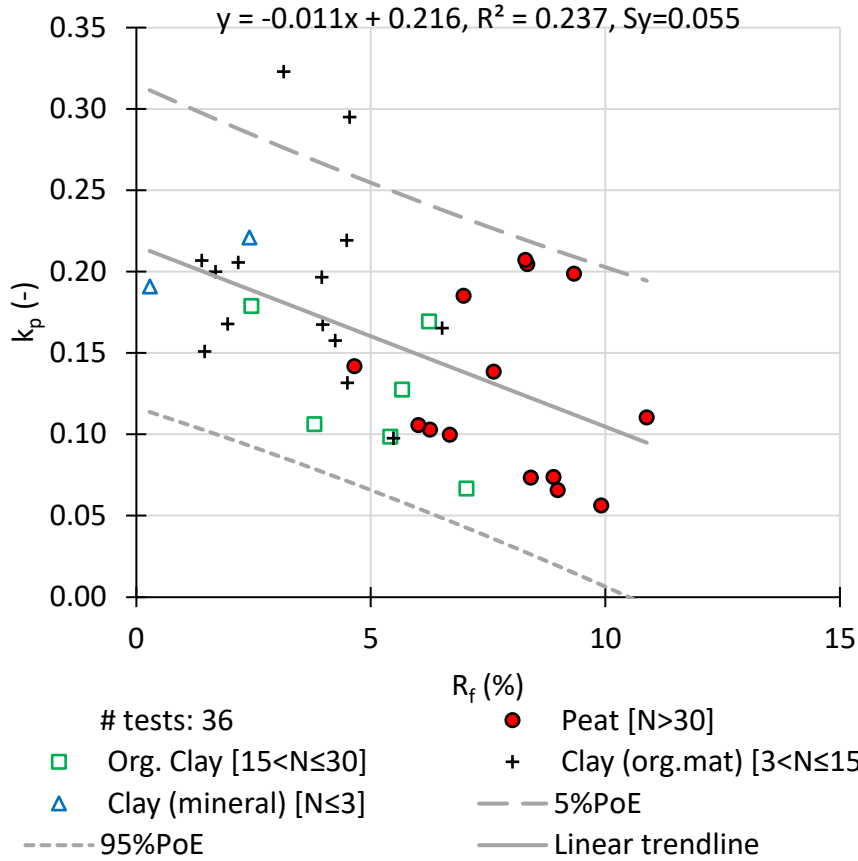
Figure 2.11 Preconsolidation net cone factor versus CPT friction ratio, for organic to mineral soils, excluding sandy clays.

$$k_p = -0.011 R_f + 0.216 \tag{2-16}$$

Where k_p is the preconsolidation net cone factor (-) and R_f is the friction ratio in (%).

2.7.5   CPT-based correlations for DSS strength parameters

This section presents the selected correlations for strength parameters which have proven to be the best for engineering applications and shows the statistical performance. The DSS tests have been performed on peats and organic clays. Samples with sand inclusions are excluded as their dilative behavior deviates from soils considered here, resulting in unrealistic high undrained shear strength. The DSS tests are usually not performed on mineral clays. Triaxial tests are performed instead in line with the protocols for dike engineering projects in the Netherlands.

Various correlations exist in literature, mainly on the in-situ undrained shear strength versus various CPT parameters. Figure 2.12 and Eq.(2-17) present the correlation of the undrained shear strength versus the net cone resistance. The range is [7, 73] kPa. The regression is based on a linear trendline through the origin and the average value for the slope is 0.054. The R_a^2 is strong, the standard deviation S_a=0.009 (-), the CV= 17% which is moderate. Based on the analyses it is concluded that no secondary trend of undrained shear strength net cone factor (N_{kt}) exists with the friction ratio. The range of cone factor N_{kt} is [14, 26] and the average is 18.4 (-). The average cone factor appears to decrease with vertical increasing effective stress, from 20 to 16. Therefore, it is recommended to determine separate N_{kt} values for the same layer below a dike (or embankment) and beside the dike. The results are presented in Appendix B.
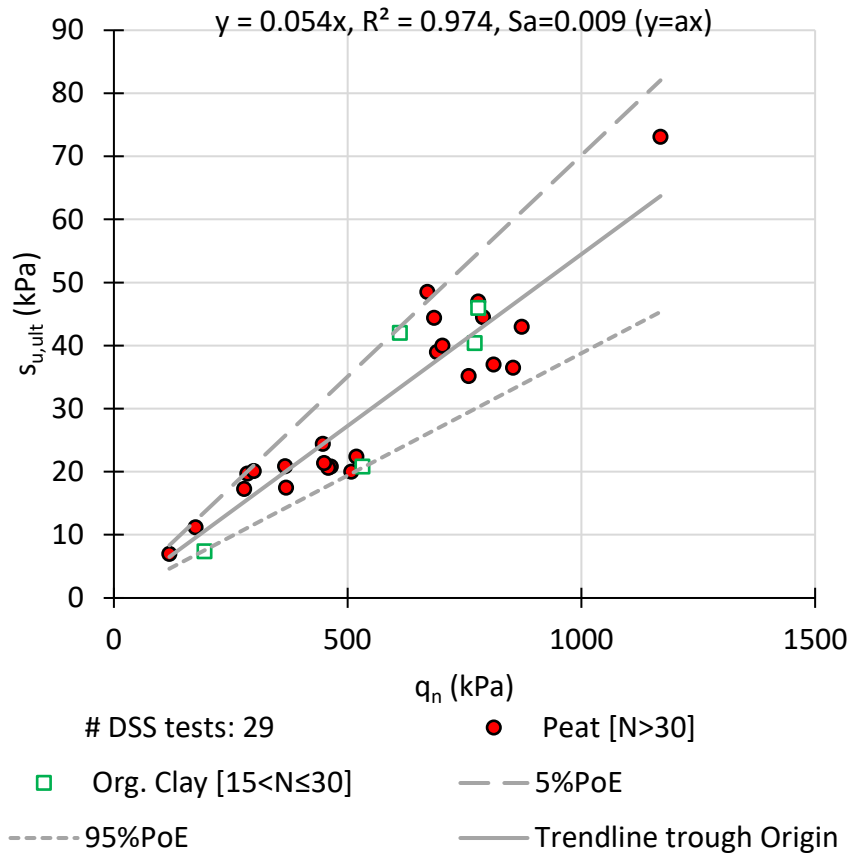
Figure 2.12 Undrained shear strength from at in-situ stress consolidated DSS tests versus CPT net cone resistance, for peats and organic clays, excluding mineral clays and sandy clays.

$$s_{u,ult,DSS} = 0.054 q_n \qquad\qquad (2\text{-}17)$$

Where $s_{u,ult,DSS}$ is the DSS ultimate undrained shear strength in (kN/m^2) and $q_n = q_t - \sigma_{v,0}$ is the net cone resistance in (kN/m^2).

The data analyses revealed a new correlation between the normally consolidated normalized undrained shear strength (S-ratio) and the friction ratio. This parameter can be used in SHANSEP based models, which is relevant for dike engineering. Figure 2.13 shows a linear relation between the S-ratio and the friction ratio, the range is [0.24, 0.54], the R^2 is moderate and the standard deviation on regression S$_y$=0.055. This correlation as shown in Eq.(2-18) is new and useful for automated CPT-based parameter determination. The data analyses further indicate that, in contrast to what might be expected, there is no strong correlation for the sine of the effective friction angle versus the friction ratio. Apparently, the inherent variation is too high for a reliable correlation. The average value of sin(φ'$_{ult}$) is 0.648, which is high as this corresponds to a friction angle of 40 degrees. When the S-ratio is plotted versus sine of the effective friction angle, the regression based on a linear trendline through the origin shows an average value for the slope of 0.633. This positive correlation is in line with literature, although relatively high. The results are presented in Appendix B.
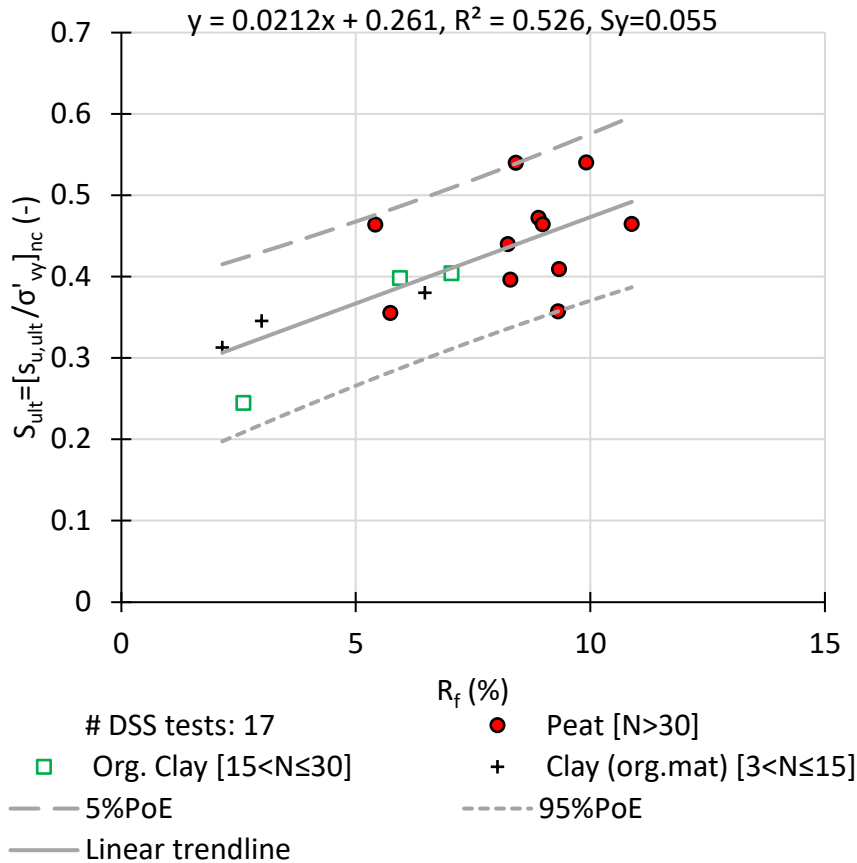
Figure 2.13 S-ratio from normally consolidated DSS tests versus CPT friction ratio, for peats and organic clays, excluding mineral clays and sandy clays.

$$S_{ult,DSS} = 0.021 R_f + 0.261 \tag{2-18}$$

Where $S_{ult,DSS}$ is the DSS ultimate S-ratio (-) and R_f is the friction ratio in (%).

2.7.6 CPT-based correlations for Triaxial CAUC strength parameters

The CAUC tests have been performed on mineral clays and organic clays, excluding samples with sand inclusions, for the same reason as at the DSS tests. CAUC tests are usually not performed on peats, DSS tests are performed instead in line with the protocols for dike engineering projects in the Netherlands.

Various correlations exist in literature, mainly on the in-situ undrained shear strength versus various CPT parameters. Figure 2.14 and Eq.(2-19) present the correlation of the undrained shear strength versus the net cone resistance. The range of s_u is [15, 60] kPa. The regression is based on a linear trendline through the origin and the average value for the slope is 0.069, which is higher than for the DSS tests. The R_a^2 is strong and the standard deviation S_a=0.013. This corresponds to CV=18% which is moderate. A closer look at Figure 2.14 shows that at the dataset consists of two groups, with relative high undrained shear strength values at the higher cone resistances. These points are associated with samples selected below the dike with higher stress levels. The group with relative low undrained shear strength are associated with samples selected in the hinterland with low stress levels.

Based on the analyses it is concluded that no secondary trend of cone factor N_{kt} exists with the friction ratio. The range of cone factor N_{kt} is [10, 23] and the average is 16.0 (-),which is lower

than for DSS tests. The average cone factor decreases with increasing vertical effective stress, from 18 to 12. The same trend is found when plotted against depth. Therefore, it is recommended to determine N_{kt} separately below and beside the dike, even if this is the same layer. The results are presented in Appendix B.
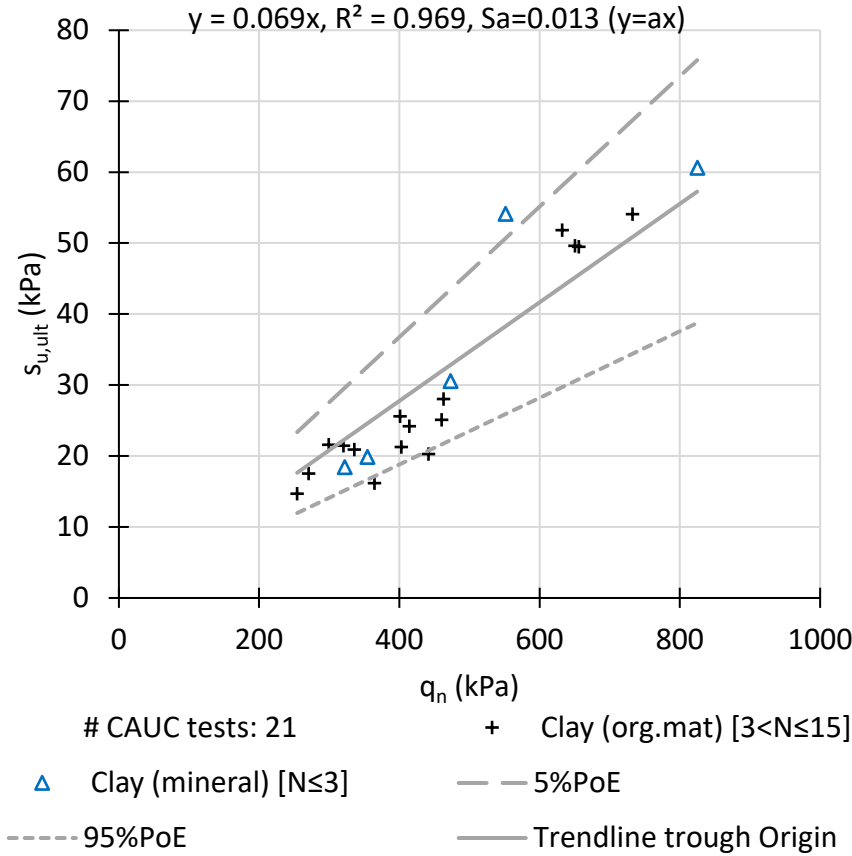
Figure 2.14 Undrained shear strength from at in-situ stress consolidated CAUC Triaxial tests versus CPT net cone resistance, for mineral clays and organic clays, excluding peats and sandy clays

$$s_{u,ult,CAUC} = 0.069q_n \qquad (2-19)$$

Where $s_{u,ult,CAUC}$ is the CAUC ultimate undrained shear strength in (kN/m²) and q_n is the net cone resistance in (kN/m²).

The data analyses confirmed the new correlation between the normally consolidated normalized undrained shear strength ratio and the friction ratio, although less strong than DSS tests which is party caused by the smaller range in friction ratio. Figure 2.15 shows a linear relation between the S-ratio and the friction ratio. The equation is slightly different from Eq.(2-18) based on DSS test. The range of the S-ratio is [0.22, 0.47], the R^2 is weak and the standard deviation on regression is 0.054. The correlation is shown in Eq.(2-20).

The data analyses further indicate that there is no strong correlation for the sine of the effective friction angle versus the friction ratio. Apparently, the inherent variation is too high for a reliable correlation. The average value of sin(ϕ'_{ult}) is 0.605, which is high as this corresponds to a friction angle of 37 degrees. When the S-ratio is plotted versus sine of the effective friction angle, the regression based on a linear trendline through the origin shows an average value for the slope of 0.517. This positive correlation is in line with literature. This average value for the friction

angle and the S-ratio for CAUC tests is lower than for DSS tests. This can be explained by the fact the that the DSS tests are performed on more organic samples such as peat (higher N, higher R_f). The results are presented in Appendix B.

The data analyses indicate that there is no such correlation for the effective friction angle. The range of $\sin(\phi'_{ult})$ is [0.50, 0.77] and the average is 0.606, which is high as this corresponds to a friction angle of 37 degrees. This value is slightly lower than the 40 degrees derived from the DSS tests, which include tests on more organic soils such as peat. The results are presented in Appendix B.

Figure 2.15 S-ratio from normally consolidated CAUC tests versus CPT friction ratio, for mineral clays and organic clays, excluding peats and sandy clays

$$S_{ult,CAUC} = 0.024 R_f + 0.243 \qquad (2\text{-}20)$$

Where $S_{ult,CAUC}$ is the CAUC ultimate S-ratio (-) and R_f is friction ratio in (%).

2.8   Conclusions

Chapter 2 addresses the challenges with CPT-based methods for application in deltaic areas with organic soils. The research question addressed in Chapter 2 is how the stability assessment can be improved by CPT-based classification method and correlations for organic soils. Current CPT-based methods are not well suitable for organic soils. Improvement of the stability assessment can be achieved by the proposed adjustments for CPT-based classification and the new CPT-based correlations.

The research presented is based on a combined database of CPT data and corresponding high quality laboratory data for the whole range of organic soils, from mineral clays to peats. The pairs are selected from predominantly Holocene soils, consisting of peats, organic clays, mineral clays and sands, as encountered in the deltaic area of the Netherlands.

The advantage of combining data from various sites, geological units and depths is that this results in a sufficiently wide range of cone resistance and friction ratio, such that trends are more reliable. Certain correlations would not have been possible if samples were taken from site specific units only. The correlations allow for establishing prior estimates where no laboratory tests are available. The disadvantage of this approach is that it increases inherent variation along the trend and the possibility that site specific units are biased to the trendline. For final estimates of soil parameters, it is recommended to combine these correlations with sampling and testing of site-specific geological units. The required statistical parameters are all presented in the graphs. The statistical approach for combined parameter determination is outside the scope of this thesis. For guidance on this topic reference is made to Lengkeek et al. (2022).

Unit weight correlation

The existing unit weight correlation (Lengkeek et al. 2018) is validated and improved by the extension of the 2018 database with organic soils, resulting in 427 pairs. The statistical parameters of the improved CPT-based unit weight correlation are compared with existing correlations and show better performance. The advantage of this correlation is that is can be applied for organic soils and mineral sedimentary soils. This is useful for SBTn classifications that require stress corrections.

SBT zones for organic soils

The coarse grained and fine-grained soils classified as mineral soils correspond well with existing SBT classifications. The organic soils, classified according to the FHWA method, do not match well with the SBT classification. In the proposed adjustment to Robertson (2010), SBT=2 (Organic soils) is redefined and subdivided into SBT=2a (Peat), SBT=2b (Organic clay) and SBT=2c (Mineral clay with organic matter). The classification is based on data pairs down to 15 m depth and 150 kPa vertical effective stress. The new SBT zones can also be applied in the SBTn classifications by Robertson (2009); (Robertson 2016) in combination with a stress normalization cut-off of C_n=1.7.

CPT-based correlations organic soils

Successful CPT-based correlations are obtained by relating the soil state parameters to the cone resistance, and the unique soil type properties to the friction ratio. As an example for state parameters, reference is made to the correlations for preconsolidation stress and undrained shear strength versus the cone resistance. As an example for unique soil type parameters, reference is made to the correlations for compression ratio and S-ratio versus the friction ratio. The CPT pore pressure measurements appeared to be less reliable for soft organic soils and are not considered suitable for correlations.

The following CPT-based correlations are presented:
- Saturated unit weight for all soils and for soils classified as peat: Eq.(2-9) and Eq.(2-11).
- Compression parameters, for organic to mineral soils: Eq.(2-12), Eq.(2-13) and Eq.(2-14).
- Vertical preconsolidation stress and preconsolidation net cone factor, for organic to mineral soils, excluding sandy clays: Eq.(2-15) and Eq.(2-16).

- Undrained shear strength from at in-situ stress consolidated DSS tests and S-ratio from normally consolidated DSS tests, for peats and organic clays, excluding mineral clays and sandy clays: Eq.(2-17) and Eq.(2-18).
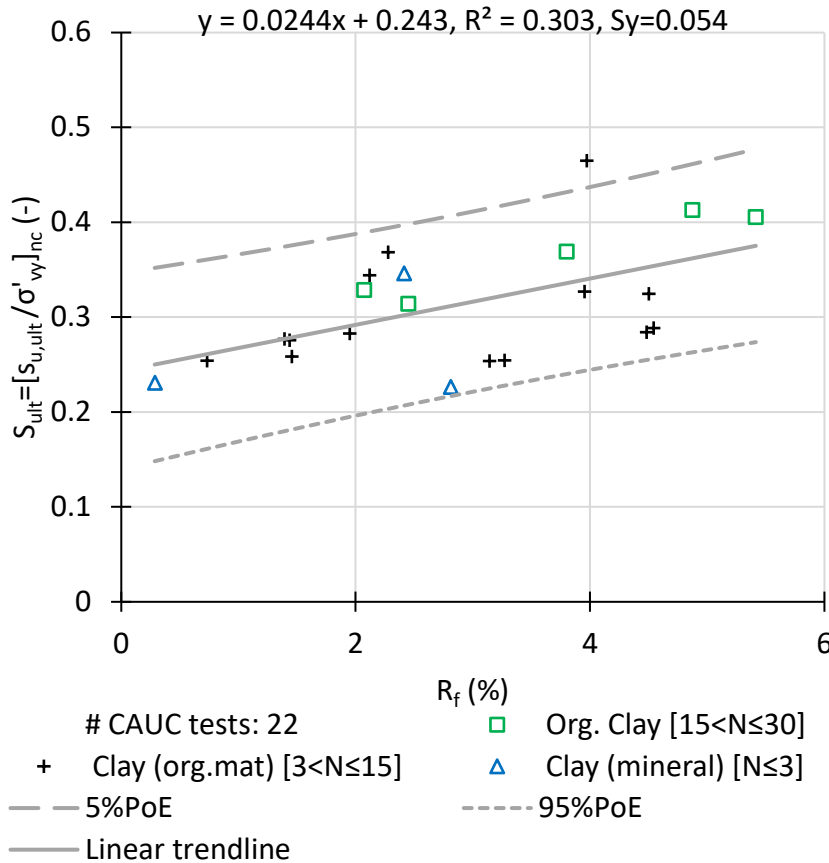- Undrained shear strength from in-situ stress consolidated CAUC Triaxial tests and S-ratio from normally consolidated CAUC tests, for mineral clays and organic clays, excluding peats and sandy clays: Eq. (2-19) and Eq.(2-20).

The statistical performance parameters (R^2, S_y, CV) for DSS tests are more favorable than for the CAUC tests. The correlations confirm a slightly higher undrained shear strength related the net cone resistance (lower N_{kt}) for CAUC tests, which is in line with literature.

From the analyses it can also be concluded that the effective friction angle and the S-ratio for DSS tests is higher than for CAUC tests, which seems surprising. This can be explained by the fact the that the DSS tests are performed on more organic samples, such as peat.

The S-ratio is positively correlated to the sine of the friction angle, both for the DSS and CAUC tests. This is in line with literature. However, this is not reflected in a correlation between the sine of the friction angle and CPT friction ratio. This might be caused by the inherent variation and limited data.

It is recommended to perform CPTs adjacent to boreholes, select pairs of high-quality CPT measurements and laboratory tests according to a standardized protocol (STOWA). This will allow for further substantiation of these correlations, which will improve prior estimates. For projects that require more advanced design methods and site-specific investigations, these insights can be used to identify critical layers and comparison with the laboratory test results.

3

A new Critical Stress Ratio (CSR) model to determine the undrained shear strength from initial oedometric stress states

3.1   Introduction

The previous chapter focused on CPT-based parameter determination. Furthermore, it was shown how two main parameters for stability analysis, the undrained shear strength and the preconsolidation stress, can be derived from CPT. In this chapter the new CSR model is presented which classifies as 'Simplified Critical State Soil Mechanics'. The CSR model is a theoretical version of the SHANSEP equation, it enables a link between effective strength parameters and undrained shear strength parameters.

The assessment of the global stability of earthen dikes is traditionally performed with limit equilibrium methods (LEM). The CSR model can be implemented in LEM and is not a full constitutive model to be implemented in FEM, although it takes various concepts into account. The current implementation of the CSR does not include a stress-path dependent (Active, Direct shear and Passive) undrained shear strength.

The advantage of the CSR model is that it requires a few conventional normally and over-consolidated CAUC tests as input, preferably combined with a few conventional one-dimensional compression tests, similar to the 'SHANSEP model'. The CSR model provides the state dependent undrained shear strength for each stress point, based on oedometric preloading conditions. The CSR model does not require to determine the exact yield contour as in a FEM model, this is taken into account by a variable spacing ratio, called the 'Critical Stress Ratio'. This parameter of the CSR model can be regarded as the over-consolidation ratio at which no net excess pore pressures occur, a parameter which can be fitted based on a few CAUC tests.

The same laboratory tests as used for the CSR model can be used to determine the drained strength parameters as well as compression parameters for other type of LEM analyses. Furthermore, the CSR model contains methods to obtain other model parameters for other existing constitutive models used in the finite element method, such as the Poisson's ratio which determines the horizontal and isotropic stress in unloading. This improves the consistency of the parameters within a model and between models in sequential stages.

The theoretical basis for the new CSR model is presented in the steps throughout the following sections. For the practical application one is referred to Chapter 3.4, where some basic model parameters are derived, and to Chapter 3.6, where two examples are presented.

3.1.1　CSSM and SHANSEP

The theoretical framework of Critical State Soil Mechanics (CSSM) developed by Roscoe and co-researchers (Roscoe et al. 1963; Schofield and Wroth 1968) is a well-known and sound theoretical basis that can be used for the elastoplastic formulation of ultimate limit states in soils. Although the framework is based upon effective stress principles, it can be used in drained as well as undrained conditions.

The CSSM framework, and in particular the Modified Cam-Clay (MCC) formulation (Roscoe and Burland 1968; Muir Wood 1990), are used to formulate the undrained shear strength in Triaxial stress conditions based on the initial stress state and using effective stress parameters. Although such a formulation is not new (Wroth 1984), an attempt is made here to extend the formulation to stress conditions that are more relevant in practical applications, which means: based on vertical effective stress and K0-stress conditions rather than isotropic stress. This results in the formulation of a 'model' called the Critical Stress Ratio (CSR) model that can be used to determine the undrained shear strength for normally consolidated and overconsolidated in-situ stress states.

As a next step, the theoretical formulation of the undrained shear strength from the CSR model is compared to the SHANSEP concept (Ladd and Foott 1974; Ladd and DeGroot 2003), which is an *empirical* concept for the determination of undrained shear strength. It is shown how the SHANSEP parameters (S-ratio and exponent m) can be theoretically obtained from CSSM and where differences with the empirical formulation occur. It is demonstrated how in the new CSR model the S-ratio can be expressed as function of the critical state friction angle (ϕ') and the oedometric compression ratios (CR and RR).

To account for the differences between the theoretical formulation and the empirical formulation of the CSR model, a conversion factor is proposed in line with Gens (1982) for the difference in isotropic swelling ratio (κ) and oedometric swelling ratio (RR) as a function of the elastic Poisson's ratio (ν) and overconsolidation range. The resulting formulation is validated by means of three sets of laboratory test results. One set of data is based on published isotropic and anisotropic Triaxial test results by Gens (1982). The other sets are based on reconstituted samples of 'Oostvaardersplassen' (OVP) clay, presented in Appendix D and in in-situ samples of organic Eemdijk clay, presented in Appendix H.

3.1.2　Need for a new formulation

In the geotechnical engineering practice, both the Limit Equilibrium Method (LEM) and the Finite Element Method (FEM) are used to analyze ultimate limit states. For stability analyses often LEM programs are used with simple models using effective stress (drained: ϕ', c') or total stress (undrained: s_u) strength parameters. The SHANSEP formulation can be used to relate the undrained shear strength to the state variables σ'_v and OCR in a LEM-model. The application of the SHANSEP formulation in stability analysis is shown by Ladd and Foott (1974). The advantage over direct assignment of the undrained shear strength is that the SHANSEP formulation allows for state related strength at all locations in a LEM model, which is ideal for slopes and embankments.

The Finite element method is primary intended for deformation analyses (serviceability limit states, SLS) but also capable of performing strength analyses (ultimate limit states, ULS), using the Shear Strength Reduction (SSR) method. FEM programs allow for total stress analysis in which the undrained shear strength is used as input or determined by the SHANSEP formulation (Grimstad et al. 2012; Panagoulias and Brinkgreve 2017) and for undrained effective stress analysis with effective stress parameters in which (excess) pore pressures are explicitly calculated. In such effective stress calculations, the pore pressure development depends highly on the constitutive model and the undrained (shear) strength is a result of the calculation rather than an input parameter. The more recent critical state models have formulations to account for anisotropic yield surfaces for one-dimensionally consolidated soils such as first developed by Dafalias (1986). Examples of such models are CASM (Yu 1998), MIT-S1 (Pestana et al. 2002), S-Clay1 (Wheeler et al. 2003) and SANICLAY (Dafalias et al. 2006).

In the engineering practice, the above-mentioned methods lead to different results for the undrained shear strength, although the same laboratory tests data are used as a basis. This is undesirable and often not understood. The goal of this chapter is to relate the CSSM and SHANSEP concepts and define a new analytical model, the CSR model, to determine the undrained shear strength, such as to overcome the aforementioned differences. The main advantages of this new CSR model are:

1) The effective friction angle and undrained shear strength are linked and can both be determined from the same set of laboratory tests.

Since the undrained shear strength (as directly determined from in-situ or lab tests) is generally obtained with a lower accuracy than the effective friction angle, linking the undrained shear strength theoretically to the more accurate friction angle will improve the accuracy of any undrained ultimate limit state analysis.

2) The new method is formulated based on the vertical effective stress for oedometric initial stress conditions.

In the geotechnical engineering practice, the vertical stress and anisotropic (K0) stress conditions play a dominant role; both in the field and in the laboratory. Theoretical models based on isotropic stress have less relevance for the engineering practice, as the in-situ state and compression tests are almost always based on vertical stresses. The new method strikes a balance between well accepted theoretical formulations and practical applications.

3) The new CSR model is formulated based on effective strength parameters which can be implemented in a LEM program.

The CSR model is similar to the SHANSEP formulation and uses the vertical effective stress to derive the undrained shear strength. This will allow for a direct comparison of strength and stability results between these two models. The CSR model overcomes the empiricism of SHANSEP. The strength and stability results from the CSR model, as used in LEM, can be compared with Critical State models as used in a FEM program, as basically the same input parameters are used. This comparison remains however outside the scope of this thesis.

3.1.3   Approach
To introduce the CSR model, the following steps will be taken:

1. Analytical formulation of the critical state undrained shear strength based on the Modified Cam Clay model, starting from normally consolidated and overconsolidated <u>isotropic</u> stress states, followed by undrained deviatoric loading.
2. Analytical formulation of the critical state undrained shear strength based on the Modified Cam Clay model, starting from normally consolidated and overconsolidated <u>oedometric</u> stress states, followed by undrained deviatoric loading.
3. Consistent selection of Poisson's ratio, earth pressure ratio, compression ratio and plastic volumetric strain ratio for the relevant range of overconsolidation.
4. Analytical formulation of new CSR model for normally consolidated and overconsolidated <u>oedometric</u> stress states, followed by undrained deviatoric loading.
5. Validation of the new CSR model based on three sets of laboratory tests results.

3.1.4   Basic assumptions

The new CSR model is an analytical model using some basic concepts and assumptions listed below:

- The stress history in the model is based on drained oedometric loading. The soil can be normally consolidated or overconsolidated, described by the overconsolidation ratio (OCR), defined as the ratio of vertical preconsolidation stress and vertical effective stress. The compression parameters are based on effective vertical stresses and can be derived directly from Oedometer tests (OED) or Constant rate of strain tests (CRS), which are common tests in the engineering practice. Alternatively, they can be related to CPT test data, based on the new correlations shown in Section 2.7.
- The undrained shear strength is based on undrained deviatoric loading in K0-consolidated Triaxial tests rather than isotropic consolidated Triaxial tests. The (effective) strength parameter can be derived from Consolidated Anisotropic Undrained Compression test (CAUC), which are common tests in the Dutch dike engineering practice.
- The theory of elastoplasticity is used, whereby strains are divided into elastic strains and plastic strains. Elastic strains are based on Hooke's law of isotropic elasticity. Plastic strains are based on critical state soil mechanics theory and in particular the Modified Cam-Clay formulation of plastic yielding. The purpose of the CSR model is not to determine the strains and deformations as in a full constitutive model, but to determine the correct undrained shear strength.
- The normally consolidated earth pressure coefficient K_{nc} is based on the assumption that Jaky's empirical relation ($K_{nc} \cong 1 - \sin \phi'$) applies under normally consolidated oedometric conditions. The overconsolidated earth pressure coefficient K_0 is based on the assumption that the soil is elastically unloaded from the aforementioned normally consolidated state under oedometric conditions, using Hooke's law of isotropic elasticity.

3.2   Analytical formulation of the critical state undrained shear strength using the MCC model for isotropic consolidation and undrained Triaxial compression

This section presents an analytical expression of the undrained shear strength for isotropic preloading conditions, within the CSSM framework and MCC formulation. Wroth (1984) presents

an extensive elaboration of this and some of that work (figures and equations) will be repeated here as a basis for further elaboration.
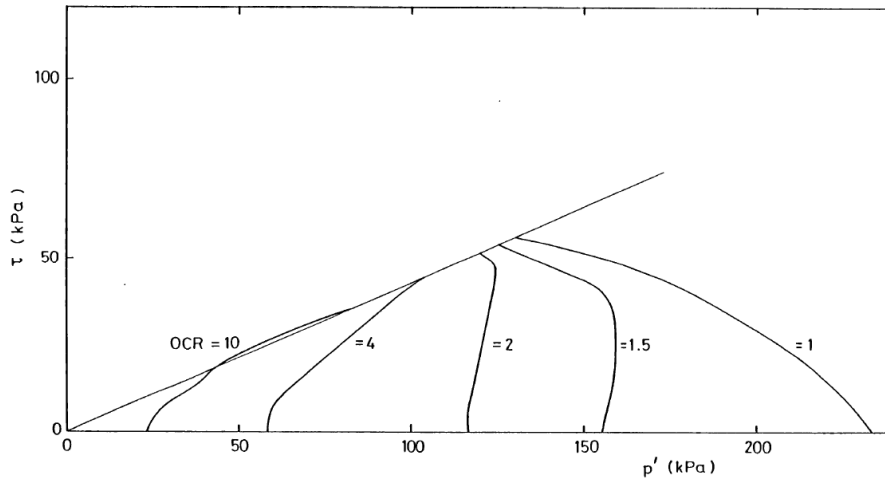
Figure 3.1 Series of CIUC Triaxial tests performed at different overconsolidation ratios and the same preconsolidation stress with τ = deviatoric stress and p' = mean effective stress [Figure courtesy Gens (1982), fig 6.40]

A theoretical understanding of the undrained Triaxial test is desirable to derive the parameters for the engineering practice. Figure 3.1 shows the results of a series of Consolidated Isotropic Undrained Compression (CIUC) triaxial tests by Gens (1982) which can be regarded as representative for a reconstituted mineral silty clay. Figure 3.2 presents the idealized MCC behavior, in terms of stresses p' and q and void ratio e. The isotropic compression and swelling lines are presented in blue and the critical state line (CSL) is presented in red. The initial yield surface at the isotropic consolidation stress is presented in grey. Various undrained Triaxial compression stress paths are indicatively shown by the dashed lines starting at stress point O and X (overconsolidated) and stress point C and E (normally consolidated).
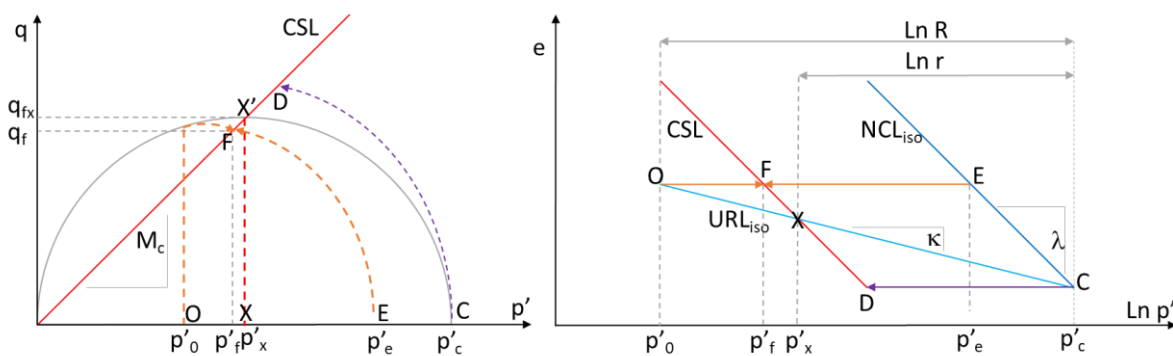
Figure 3.2 MCC model: idealized CIUC behavior, in terms of stresses p' and q and void ratio e, with spacing ratio r=2 in the MCC model

Two basic parameters are introduced first: The state parameter R and the spacing ratio r (Wroth 1984). The state parameter R (isotropic overconsolidation ratio) is defined by the maximum isotropic stress p'_c and the current isotropic stress p'_0; in this example R at stress point O is:

$$R = \frac{p'_c}{p'_0}$$

(3-1)

Stress point X in the left-hand (p', q)-diagram is located on a 'vertical' line (p' = constant) through the top of the ellipse representing the MCC yield contour at Critical State (failure). In the right-hand (p'-e)-diagram, stress point X is located at the 'intersection' of the isotropic unloading/reloading line (URL$_{iso}$) with the CSL (same void ratio and same mean effective stress). It should be noted that it is not a real intersection in the 3-dimensional p'-q-e space, since the corresponding deviatoric stress q is different. The CSL and the isotropic normal consolidation line (NCL$_{iso}$) are parallel in p-e plane. For any consolidation stress, the distance between p'$_c$ and p'$_x$ is constant. For any initial stress p'$_0$ = p'$_x$, the state parameter R has a unique value. This can be regarded as a soil constant (Wroth 1984), called the spacing ratio and is defined as:

$$r = \frac{p'_c}{p'_x} \tag{3-2}$$

In the MCC the spacing ratio r is a property of the shape of the yield surface and equal to r = 2. In some advanced models, e.g. Pestana et al. (2002), the spacing ratio r can directly be used as input parameter or indirectly be modified such that it matches the laboratory tests. This reflects that the yield surface is not necessarily an ellipse.

In the next step the equivalent stress is calculated. The equivalent stress represents the stress on the NCL$_{iso}$ with the same void ratio as the current overconsolidated stress state. The stress points E and C are located on the NCL$_{iso}$ and the stress points C and O on the URL$_{iso}$. The slopes of these lines correspond to the isotropic compression index, λ, and the isotropic swelling index, κ, respectively. In this example, stress point E is the equivalent stress of point O, so the void ratio in stress point E is the same as in stress point O ($\Delta e = 0$). When going from stress point E via C to O, the change of void ratio can be formulated as:

$$\Delta e = \lambda \ln\left(\frac{p'_e}{p'_c}\right) + \kappa \ln\left(\frac{p'_c}{p'_0}\right) = 0 \tag{3-3}$$

Hence:

$$\ln\left(\frac{p'_e}{p'_c}\right) = -\frac{\kappa}{\lambda} \ln\left(\frac{p'_c}{p'_0}\right) \tag{3-4}$$

This can be mathematically elaborated to:

$$\frac{p'_e}{p'_c} = \left(\frac{p'_c}{p'_o}\right)^{-\frac{\kappa}{\lambda}} \tag{3-5}$$

Or:

$$p'_e = p'_0 R(R)^{-\frac{\kappa}{\lambda}} = p'_0 R^{\Lambda} \tag{3-6}$$

Where:

$$\Lambda = \frac{\lambda - \kappa}{\lambda} \tag{3-7}$$

This auxiliary model parameter Λ is the plastic volumetric strain ratio. The equivalent stress of point O can be determined by the state parameter R and the model parameter Λ. At the equivalent stress (in this example stress point E) the void ratio is the same, hence the undrained

shear strength of stress point E and O is also the same, since undrained Triaxial loading from stress point E and O will both end at the same stress point F on the CSL.

The undrained shear strength can be expressed as a function of the void ratio in the MCC model, but as shown by Wroth (1984) one can eliminate the void ratio and directly determine the undrained shear strength based on the initial stress state. This will be elaborated in the next steps.

Stress points F and X lie on the CSL, and by similar triangles (E-C-O versus F-X-O) it can be seen that:

$$\lambda \ln\left(\frac{p'_x}{p'_f}\right) = \kappa \ln\left(\frac{p'_x}{p'_0}\right) \tag{3-8}$$

By subtracting both sides from $\lambda \ln\left(\frac{p'_x}{p'_0}\right)$ this results in:

Left side:

$$\lambda \ln\left(\frac{p'_x}{p'_0}\right) - \lambda \ln\left(\frac{p'_x}{p'_f}\right) = \lambda \ln\left(\frac{p'_x}{p'_0}\right) + \lambda \ln\left(\frac{p'_f}{p'_x}\right) = \lambda \ln\left(\frac{p'_f}{p'_0}\right) \tag{3-9}$$

Right side:

$$\lambda \ln\left(\frac{p'_x}{p'_o}\right) - \kappa \ln\left(\frac{p'_x}{p'_o}\right) = (\lambda - \kappa) \ln\left(\frac{p'_x}{p'_o}\right) = (\lambda - \kappa) \ln\left(\frac{R}{r}\right) \tag{3-10}$$

This is mathematically elaborated to:

$$\frac{p'_f}{p'_0} = \left(\frac{R}{r}\right)^\Lambda \tag{3-11}$$

Note that stress point O should not necessarily be located left of X, it may be any stress point on the URL$_{iso}$. With this expression the initial (isotropic) consolidation stress with a known overconsolidation ratio can be related to the failure stress on the CSL for undrained Triaxial compression. The elaboration above results in the following relation between equivalent stress and isotropic stress at failure:

$$p'_f = p'_0 \left(\frac{R}{r}\right)^\Lambda = p'_e \left(\frac{1}{r}\right)^\Lambda \tag{3-12}$$

The final step is to relate the undrained shear strength to the inclination of the critical state failure line, M_c, and the effective friction angle ϕ'. This friction angle corresponds to the critical state value determined in Triaxial compression. Synonyms for the critical state ($_{cs}$) value are the constant volume ($_{cv}$), ultimate ($_{ult}$) and large strain ($_{>15\%}$) value. This is the value determined at large strains where the excess pore pressure in an undrained test becomes constant or the volume change in a drained test becomes zero. This value does not depend on whether the consolidation is isotropic or anisotropic, but test type and stress path do have an effect as reported in Kulhawy and Mayne (1990). Within the CSSM framework it is required to use the critical state friction angle and not the peak friction angle.

For any initial stress state p'$_0$ on the URL$_{iso}$, the undrained shear strength is defined as:

$$s_u = \frac{q_f}{2} = p'_f \frac{M_c}{2} \tag{3-13}$$

Where M_c is the inclination of the Critical State Line in Triaxial compression conditions defined as:

$$M_c = \frac{6 \sin \phi'}{3 - \sin \phi'} \tag{3-14}$$

Combining the above equations results in the general equation (3-15) of the undrained shear strength for isotropic consolidation and undrained Triaxial compression, for any value of the initial (overconsolidated) isotropic state stress p'$_0$ and corresponding R = p'$_c$/p'$_0$ where p'$_c$ is the isotropic preconsolidation stress:

$$s_{u,CIUC,MCC} = p'_0 \frac{M_c}{2} \left(\frac{R}{r}\right)^{\Lambda} \tag{3-15}$$

At stress point X the overconsolidation ratio R=r=2, and the equation reduces to $s_u = p'_f \frac{M_c}{2}$ as should be expected. The undrained shear strength ratio for isotropic normally consolidated conditions (R=1) can be defined as:

$$S_{p,CIUC,MCC} = \left[\frac{s_{u,CIUC}}{p'_0}\right]_{nc} = \frac{M_c}{2} \left(\frac{1}{r}\right)^{\Lambda} \tag{3-16}$$

The subscript 'p' is added to identify the normalization by the maximum isotropic stress.

3.2.1 Resume

With these analytical equations one can determine the critical state undrained shear strength as function of the effective strength and compression parameters of the MCC model. Although the model involves a unique relation between p'-q-e, it is not required to determine the void ratio. This is an advantage for engineering practice as the uncertainty in void ratio determination as well as the natural variation between samples is larger than the changes in void ratio upon unloading.

3.3 Analytical formulation of the critical state undrained shear strength using the MCC model for oedometric consolidation and undrained Triaxial compression

This section presents the analytical solutions for oedometric consolidation which is regarded as closer to reality for most natural soils and engineering problems. The overconsolidation and vertical preconsolidation stress can be determined from one-dimensional Oedometer or CRS tests and related to geological information on past overburden stress and groundwater variations.

Figure 3.3 presents the results of a series of CAUC (Anisotropic) tests by Gens (1982) which can be regarded as representative for a reconstituted mineral silty clay. Figure 3.4 presents the idealized MCC behavior in terms of stresses p' and q and void ratio e considering oedometric conditions. The isotropic compression and swelling lines are presented in blue and oedometric compression and swelling lines in green. The critical state line (CLS) is presented in red. The initial yield surface at the isotropic consolidation stress is presented in grey.

Figure 3.3 Series of CAUC Triaxial tests performed at different overconsolidation ratios and the same preconsolidation stress with t = deviatoric stress and p' = mean effective stress [Figure courtesy Gens (1982), fig 6.62]

The normally consolidated earth pressure coefficient K_{nc} is assumed to be based on Jaky's empirical formula (Jaky 1944) and the critical state friction angle (Mesri and Hayat 1993):

$$K_{nc} \cong 1 - \sin \phi'$$

(3-17)

The intersection of the oedometric normal consolidation line, NCL_{oed}, with the initial MCC yield surface provides the stress point (p'_y, q_y). The slope η of the NCL_{oed} in the p'-q-diagram is:

$$\eta_{nc} = \frac{q_y}{p'_y} = \frac{3(1 - K_{nc})}{1 + 2K_{nc}}$$

(3-18)

For $K_{nc} = 1 - \sin \phi'$ this can be rewritten to:

$$\eta_{nc} = \frac{3 \sin \phi'}{3 - 2 \sin \phi'} = \frac{3M}{6 - M}$$

(3-19)

For the slope η_{ur} of the URL_{oed} in the (p'-q)-diagram, Hooke's law of isotropic elasticity applies which requires an additional parameter, the elastic Poisson's ratio ν_{ur}. The inclination of the URL_{oed} is defined as:

$$\eta_{ur} = \frac{\Delta q}{\Delta p'} = \frac{3(1 - 2\nu_{ur})}{1 + \nu_{ur}}$$

(3-20)

Stress point X in the left-hand (p'-q)-diagram of Figure 3.4 is still on a 'vertical' line through the top of the ellipse, but in this case, it is located on the intersection with the oedometric unloading/reloading line. The corresponding point X in the right-hand diagram is, in principle, located at the 'intersection' of the oedometric unloading/reloading line (URL_{oed}) with the CSL. However, we can still use the previous definition of stress point X for isotropic conditions, considering that the URL_{iso} coincides with the URL_{oed} and that the isotropic preconsolidation stress p_c is the same.
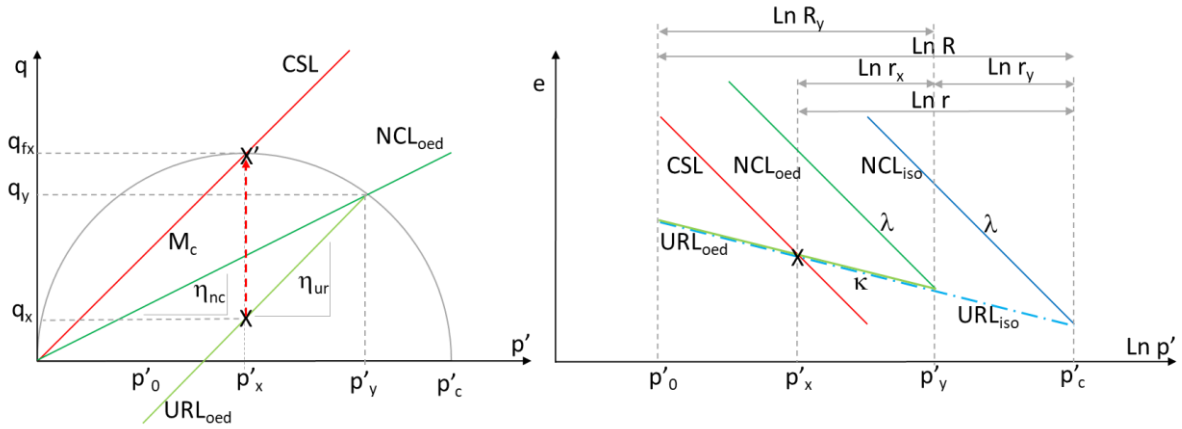
Figure 3.4 MCC model: idealized CAUC behavior, in terms of stresses p' and q and void ratio e

From Figure 3.4 it can be concluded that:

$$r = r_x r_y \qquad (3\text{-}21)$$

Where $r_x = p'_y/p'_x$ and $r_y = p'_c/p'_y$. Since the spacing ratio r is a model constant (r=2 in MCC), r_x is also a model constant, meaning the spacing ratio between the 1-dimensional compression line (NCL$_{oed}$) and the CSL. The model constant r_y can be regarded as the conversion factor for the yield stress at the yield surface in oedometric conditions (p'$_y$) versus the preconsolidation stress on the isotropic axis (p'$_c$). This is elaborated below, with the elliptical yield surface of MCC defined as:

$$q^2 - M_c\left(p'_c p' - p'^2_c\right) = 0 \qquad (3\text{-}22)$$

For $q_y = \eta_{nc} p'_y$ this can be rewritten to:

$$r_y = \frac{p'_c}{p'_y} = \frac{M_c{}^2 + \eta_{nc}{}^2}{M_c{}^2} \qquad (3\text{-}23)$$

And:

$$r_x = \frac{p'_y}{p'_x} = \frac{r M_c{}^2}{M_c{}^2 + \eta_{nc}{}^2} \qquad (3\text{-}24)$$

The overconsolidation ratio expressed for oedometric conditions is defined as:

$$R_y = \frac{R}{r_y} = \frac{p'_y}{p'_0} \qquad (3\text{-}25)$$

Combining these equations and following the same logic as in the previous section, results in the general equation (3-26) of the undrained shear strength for oedometric consolidation and undrained Triaxial compression, for any value of the initial state parameters p'$_0$ and R$_y$. This equation is similar to equation (3-15) with an adjusted overconsolidation ratio definition (R$_y$) and spacing ratio (r$_x$).

$$s_{u,CAUC,MCC} = p'_0 \frac{M_c}{2} \left(\frac{R_y r_y}{r}\right)^\Lambda = p'_0 \frac{M_c}{2} \left(\frac{R_y}{r_x}\right)^\Lambda \qquad (3\text{-}26)$$

The normally consolidated stress point at the intersection with the yield surface (p'_y, q_y) with R_y=1 is on the same yield surface as the stress point (p'_c, q=0). The undrained shear strength for CAUC will however be lower than for CIUC, because the equivalent stress projected on the NCL_{iso} is lower than p'_c. If we consider for CIUC and CAUC the same p'_0 (smaller than p'_y) both equations result in the same undrained shear strength (namely $q_{fx}/2$) as shown below for $p'_0 = p'_x$ and illustrated in Figure 3.4:

$$s_{u,CIUC.MCC} = p'_x \frac{M_c}{2}\left(\frac{2}{2}\right)^{\Lambda} = p'_x \frac{M_c}{2} \tag{3-27}$$

And:

$$s_{u,CAUC.MCC} = p'_x \frac{M_c}{2}\left(\frac{r_x}{r_x}\right)^{\Lambda} = p'_x \frac{M_c}{2} \tag{3-28}$$

These equations allow for comparison of any CIUC and CAUC test with different preconsolidation stresses. In Figure 3.5 below it is illustrated that for oedometric consolidation until $p_{y,1}$ the undrained shear strength is the same, and for oedometric loading until $p_{y,2}$ the undrained shear strength of CAUC is larger than that of CIUC consolidated to p_c.
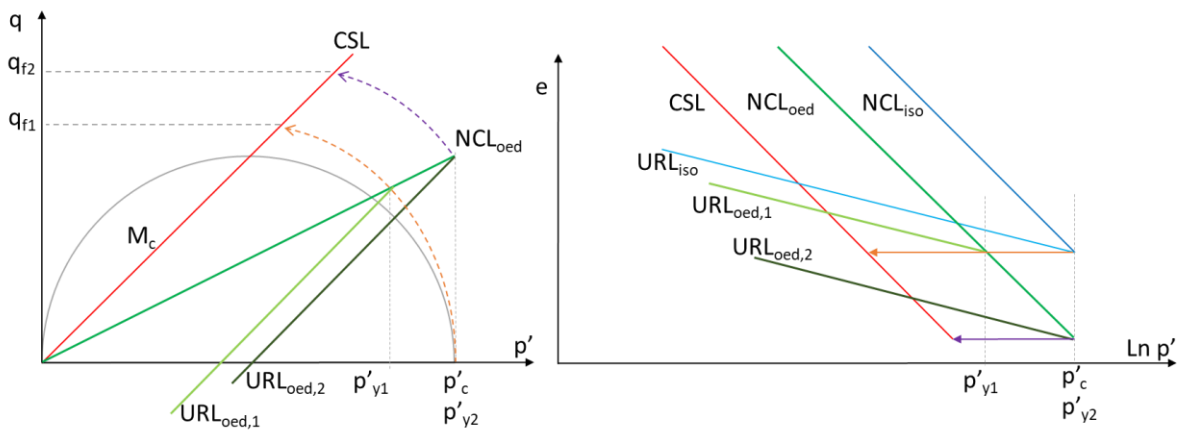
Figure 3.5 MCC model: comparison of CIUC and CAUC tests for different consolidation stresses.

In the next steps Eq.(3-26) will be expressed in terms of vertical stresses to enable a comparison with the SHANSEP formulation. In oedometric stress conditions, the relation between isotropic and vertical stress is:

$$p'_0 = \sigma'_{v0} \frac{(1 + 2K_0)}{3} \tag{3-29}$$

$$p'_y = \sigma'_{vy} \frac{(1 + 2K_{nc})}{3} \tag{3-30}$$

The overconsolidation ratio is defined as:

$$OCR = \frac{\sigma'_{vy}}{\sigma'_{v0}} \tag{3-31}$$

Based on Hooke's law, the change in ratio between horizontal and vertical stress is along URL_{oed} defined as:

$$\Delta K_{ur} = \frac{\nu_{ur}}{1 - \nu_{ur}} \tag{3-32}$$

The ratio of horizontal over vertical stress at the initial overconsolidated stress state is:

$$K_0 = OCR(K_{nc} - \Delta K_{ur}) + \Delta K_{ur} \tag{3-33}$$

The relation between R_y and OCR for oedometric conditions is:

$$R_y = \frac{p'_y}{p'_0} = OCR\left(\frac{1 + 2K_{nc}}{1 + 2K_0}\right) \tag{3-34}$$

And, reversely, OCR can be expressed as a function of R_y:

$$OCR = R_y \frac{1 + 2\Delta K_{ur}}{\left(1 + 2K_{nc} - 2R_y(K_{nc} - \Delta K_{ur})\right)} \tag{3-35}$$

Combining these equations with Eq.(3-26) results in the general Eq.(3-36) of the undrained shear strength for oedometric consolidation and undrained Triaxial compression, based on vertical stress:

$$s_{u,CAUC,MCC} = \sigma'_{v0} \frac{(1 + 2K_0)}{3}\left(\frac{M_c}{2}\right)\left(\frac{OCR}{r_x} \cdot \frac{1 + 2K_{nc}}{1 + 2K_0}\right)^{\Lambda} \tag{3-36}$$

For normally consolidated oedometric conditions $R_y=1$ and $K_0=K_{nc}$. The undrained shear strength ratio, normalized by the vertical effective stress for normally consolidated oedometric conditions, can be defined as:

$$S_{CAUC,MCC} = \left[\frac{s_{u,CAUC}}{\sigma'_{vy}}\right]_{nc} = \frac{(1 + 2K_{nc})}{3}\left(\frac{M_c}{2}\right)\left(\frac{1}{r_x}\right)^{\Lambda} \tag{3-37}$$

Similar expressions for $S_{CAUC,MCC}$ can be found in (Wroth 1984; Ohta et al. 1985; Chang et al. 1999). The equation of (Wroth 1984; Ohta et al. 1985) are only for normally consolidated oedometric conditions whereas Eq.(3-26) and that of (Chang et al. 1999) is also for overconsolidated oedometric conditions.

The analytical MCC results for CIUC and CAUC tests are presented in Figure 3.6. The results are presented for $\Lambda=0.75$, $K_{nc} = 1 - \sin\phi'$ and r=2 (default MCC) over a range of friction angles (15-45 degrees). The analytical solution of Eq.(3-36) coincides with Wroth (1968, 1984) which confirms the correct analytical equations for the MCC model. Furthermore, it appears that the undrained shear strength ratio for CAUC tests based on MCC can be approximated by a linear relation to the sine of the friction angle:

$$S_{CAUC,MCC} \approx 0.59 \sin\phi'$$

(For MCC with $\Lambda=0.75$) $\tag{3-38}$

In Mayne (2008) the results of the 'Wroth-Prevost' and 'Ohta' model are presented for simulations of various tests, including CIUC and CAUC test. The equations for all the tests are summarized in Kulhawy and Mayne (1990). Figure 3.6 shows the linearized approximation and is similar to Figure 9 of Mayne (2008) for normally consolidated CIUC and CAUC (CK$_0$UC) tests.
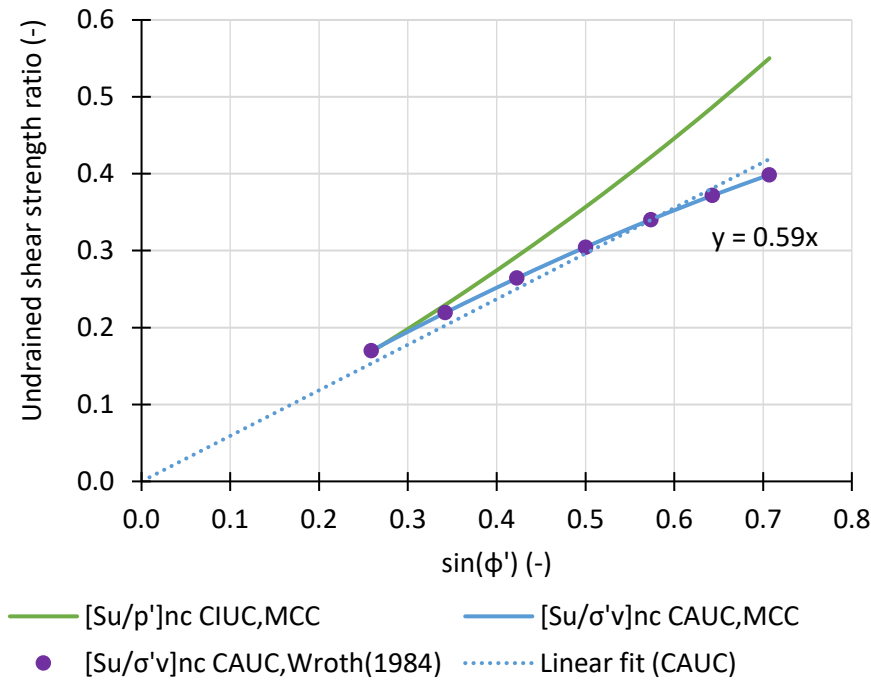
Figure 3.6 MCC model: undrained shear strength ratio versus friction angle for normally consolidated CIUC tests Eq.(3-16) and CAUC tests Eq.(3-37)

Figure 3.7 presents the CIUC and CAUC (CK$_0$UC) results for overconsolidated conditions. In this example ϕ'=30°, Λ=0.75, r=2 (default MCC) and p'$_c$=100 kPa. The p'$_c$ of CIUC and p'$_y$ of CAUC are assumed on the same yield surface, with p'$_y$=p'$_c$/r$_y$=100/1.39=72 kPa.
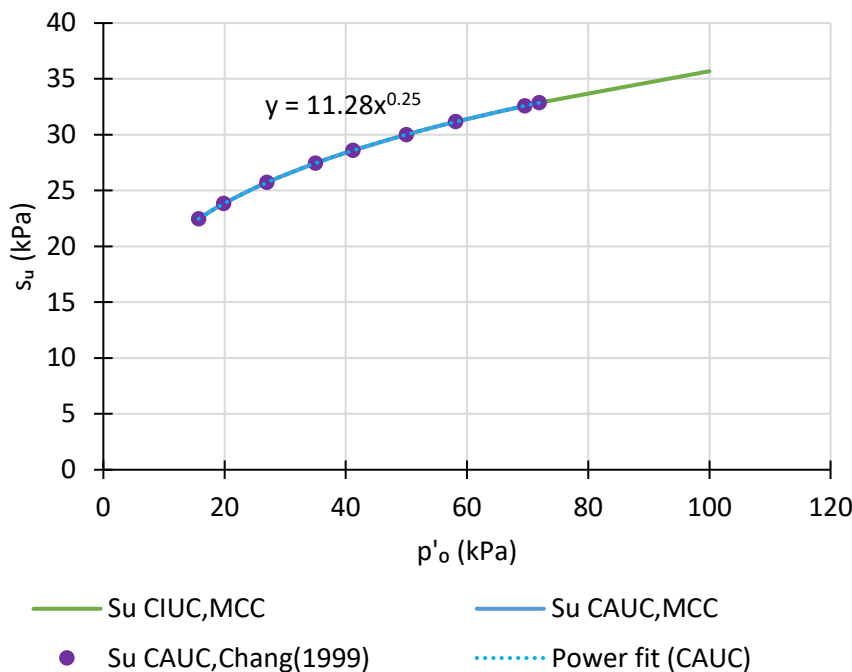
Figure 3.7 MCC model: undrained shear strength versus isotropic stress for overconsolidated CIUC tests Eq.(3-15) and CAUC tests Eq.(3-36)

The undrained shear strength in Figure 3.7 is plotted against the isotropic consolidation stress. The exponent following the power-regression line confirms the theoretically expected value of

(1-Λ)=0.25 for both CIUC and CAUC tests. The results coincide with the analytical solution presented in Chang et al. (1999). The advantage of the followed approach is that it allows for a variable spacing ratio, as will be shown for the CSR model. The approach allows for oedometric initial conditions, in line with empirical relations, for CAUC tests.

The equations above are based on the MCC model with a spacing ratio r=2 and an elliptical yield surface. In Figure 3.8 the analytical MCC solution Eq.(3-37) is compared with published data by Kulhawy and Mayne (1990). The data are added in Appendix C. These data indicate that the theoretical MCC solution (3-38) tends to underpredict the undrained shear strength ratio of in-situ soils, but is still within the 90% prediction interval.
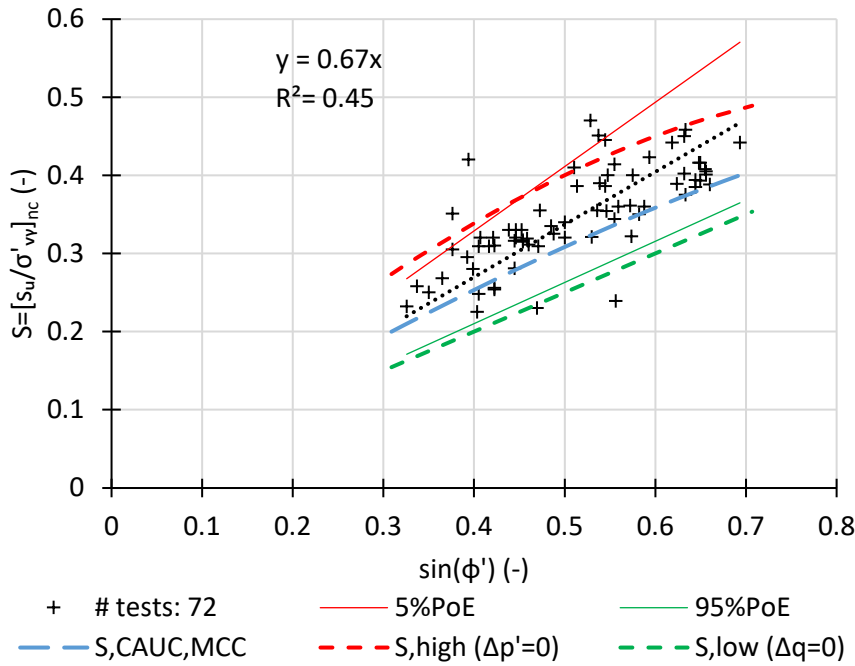
Figure 3.8 Undrained shear strength ratio versus friction angle for normally consolidated CAUC tests, data after Kulhawy and Mayne (1990), provided with permission to use. The data is shown together with the 90% interval, the theoretical S-ratio based on the MCC model and reasonable upper and lower bounds for the S-ratio.

The 90% confidence interval can be linked to the reasonable analytical upper and lower bounds based on the stress paths 1 and 2 shown in Figure 3.9. Stress path 1 is based on idealized undrained elastic behavior, where p' remains constant until CAUC failure and the equivalent Skempton factor A=1/3 (Skempton 1954; Law and Holtz 1978). This results in the following equation for a high undrained shear strength ratio:

$$S_{CAUC,high} = \frac{s_{u,EPP}}{\sigma'_{v0}} = \frac{p'_0 \frac{M}{2}}{p'_0 \frac{3}{(1+2K_{nc})}} = \frac{(1+2K_{nc})M_c}{6} \tag{3-39}$$

In stress path 2 the deviatoric stress (q) remains constant until CAUC failure (Skempton factor A to infinity). This path corresponds to a very sensitive soil with significant pore pressure generation. This results in the following equation for a low undrained shear strength ratio:

$$S_{CAUC,low} = \frac{\frac{q_0}{2}}{\sigma'_{v0}} = \frac{\sigma'_{v0}(1-K_{nc})}{2\sigma'_{v0}} = \frac{\sin\phi'}{2} \tag{3-40}$$

These upper and lower bounds are no true upper and lower bounds, but can be used in engineering practice to interpret the derived parameters in conjunction with the effective friction angle.
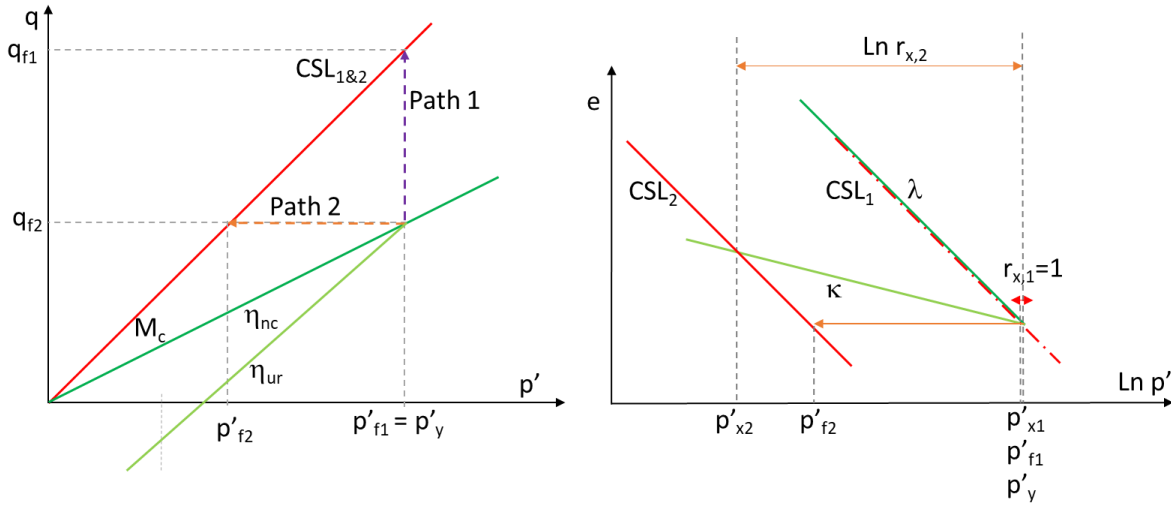
Figure 3.9 Schematic plot of critical state strength for CAUC tests with net constant isotropic stress (path 1) and net constant deviator stress (path 2)

3.3.1 Resume

With these analytical equations one can determine the critical state undrained shear strength based on effective strength for oedometric preloading conditions and CAUC test. The results of CIUC and CAUC are both consistently related to the exponent Λ as shown in Figure 3.7.

The normally consolidated undrained shear strength ratio complies with literature and can be approximated by a linear relation to the friction angle (3-38). However, it is also shown that the MCC formulation generally underpredicts the results from tests on in-situ clays. Table 3-1 presents a summarizing comparison of the equations for CIUC and CAUC tests

Table 3-1 Comparison of MCC formulations for CIUC and CAUC test

CIUC (with R and p') Eq.(3-1), Eq.(3-15), Eq.(3-16):	CAUC (with OCR and σ'ᵥ) Eq.(3-31), Eq.(3-36), Eq.(3-37):
$R = \dfrac{p'_c}{p'_0}$	$OCR = \dfrac{\sigma'_{vy}}{\sigma'_{v0}}$
$s_u = p'_0 \dfrac{M_c}{2} \left(\dfrac{R}{r}\right)^{\Lambda}$	$s_u = \sigma'_{v0} \dfrac{(1+2K_0)}{3} \left(\dfrac{M_c}{2}\right) \left(\dfrac{OCR}{r_x} \cdot \dfrac{1+2K_{nc}}{1+2K_0}\right)^{\Lambda}$
$S_{p,nc} = \left[\dfrac{s_{u,CIUC}}{p'_c}\right]_{nc} = \dfrac{M_c}{2} \left(\dfrac{1}{r}\right)^{\Lambda}$	$S_{nc} = \left[\dfrac{s_{u,CAUC}}{\sigma'_{vy}}\right]_{nc} = \dfrac{(1+2K_{nc})}{3} \left(\dfrac{M_c}{2}\right) \left(\dfrac{1}{r_x}\right)^{\Lambda}$

3.4 Consistent selection of Poisson's ratio, earth pressure ratio and plastic volumetric strain ratio

Before elaborating the CSR model, two relevant aspects related to the effect of the Poisson's ratio on differences for oedometric and isotropic conditions will be discussed in this section.

3.4.1   Poisson's ratio and earth pressure ratio

In the previous section Hooke's law is applied using a constant Poisson's ratio, resulting in a straight (linear) unloading stress path. However, various empirical relations indicate non-linear stress path. In this section a linearized Poisson's ratio will be proposed to approximate the empirical relation.

The elastic equation for K_0 based on Hooke's law is presented in Eq.(3-33). The empirical equation by Mayne and Kulhawy (1982) is as:

$$K_0 \cong K_{nc} \cdot OCR^b \tag{3-41}$$

Setting the elastic and empirical K_0-relation equal results in:

$$\frac{\Delta K_{ur}}{K_{nc}} = \frac{OCR - OCR^b}{OCR - 1} \tag{3-42}$$

The exponent 'b' equals typically $\sin \phi'$ for sands and clays (Ku and Mayne 2015) as well as for peats (Hayashi et al. 2012). With help of Eq.(3-32) the following equation can be deduced for the secant value for the Poisson's ratio (v_{ur}) as function of OCR:

$$v_{ur} = \frac{K_{nc}\left(\frac{OCR - OCR^{\sin \phi'}}{OCR - 1}\right)}{1 + K_{nc}\left(\frac{OCR - OCR^{\sin \phi'}}{OCR - 1}\right)} \tag{3-43}$$

This equations allows for a linearization of the Poisson's ratio based on an unloading range. For OCR=1 this results in an analytical expression for the initial elastic Poisson's ratio at the onset of unloading:

$$v_e = \lim_{OCR \downarrow 1} v_{ur} = \frac{K_{nc}(1 - \sin \phi')}{1 + K_{nc}(1 - \sin \phi')}$$
$$= \frac{K_{nc}^2}{1 + K_{nc}^2} \tag{3-44}$$

In unloading, K_0 is bound by the passive earth pressure ratio, K_p, when considering a stress path based on elastic perfectly-plastic (EPP) behavior. The OCR validity range for the empirical relation is typically [1-30] as shown in Figure 3.12. The corresponding stress ratio K_p and overconsolidation ratio OCR_p are defined as follows:

$$K_p = \frac{1 + \sin \phi'}{1 - \sin \phi'} \tag{3-45}$$

$$OCR_p = \left(\frac{K_p}{K_{nc}}\right)^{\left(\frac{1}{\sin \phi'}\right)} \tag{3-46}$$

In the Dutch engineering practice with predominantly Holocene sedimentary soils, one is interested in OCR up to 10. To comply with elastic behavior in models it requires a proper linearization of the Poisson's ratio as shown in Figure 3.10. The proposed secant value ($v_{K:1}$) is selected such that the elastic and empirical URL lines intersect at the isotropic axis (K_0=1). The corresponding OCR is derived from the equation below. For ϕ'=30° the corresponding

overconsolidation ratio is $OCR_{K:1}=4$. The secant value of the Poisson's ratio can be calculated by substitution of the equation for $OCR_{K:1}$ into (3-43).

$$OCR_{K:1} = \left(\frac{1}{K_{nc}}\right)^{\left(\frac{1}{\sin \phi\prime}\right)} \tag{3-47}$$

By further substitution into Eq.(3-42) this results in the equivalent earth pressure ratio change in oedometric unloading.

$$\Delta K_{ur,K:1} = K_{nc}\frac{OCR_{K:1} - OCR_{K:1}{}^{\sin \phi\prime}}{OCR_{K:1} - 1} \tag{3-48}$$

The results of the initial, maximum and secant value for the Poisson's ratio in an EPP-model are shown in Figure 3.11. It appears that the proposed secant value of Poisson's ratio ($\nu_{K:1}$) can be closely approximated by a linear relation to the sine of the friction angle. It should be noted that certain constitutive models use an upper bound of 0.30 for the Poisson's ratio, which can be conflicting for soils with a very low effective friction angle.

$$\nu_{K:1} = \frac{\Delta K_{ur,K:1}}{1 + \Delta K_{ur,K:1}} \approx 0.54 - 0.58 \sin \phi' \tag{3-49}$$

The linearization of the Poisson's ratio also affects the OCR validity range. The maximum value for OCR_p before reaching the passive stress ratio can be calculated with the equation below. The OCR validity range assuming a constant Poisson's ratio is typically half of that when using a variable Poisson's ratio based on Eq.(3-43) as shown in Figure 3.12. For $\phi'=30°$ the corresponding overconsolidation ratio is $OCR_{p,K:1}=16$.

$$OCR_{p,K:1} = \frac{K_p - \dfrac{\nu_{K:1}}{1 - \nu_{K:1}}}{K_{nc} - \dfrac{\nu_{K:1}}{1 - \nu_{K:1}}} \tag{3-50}$$
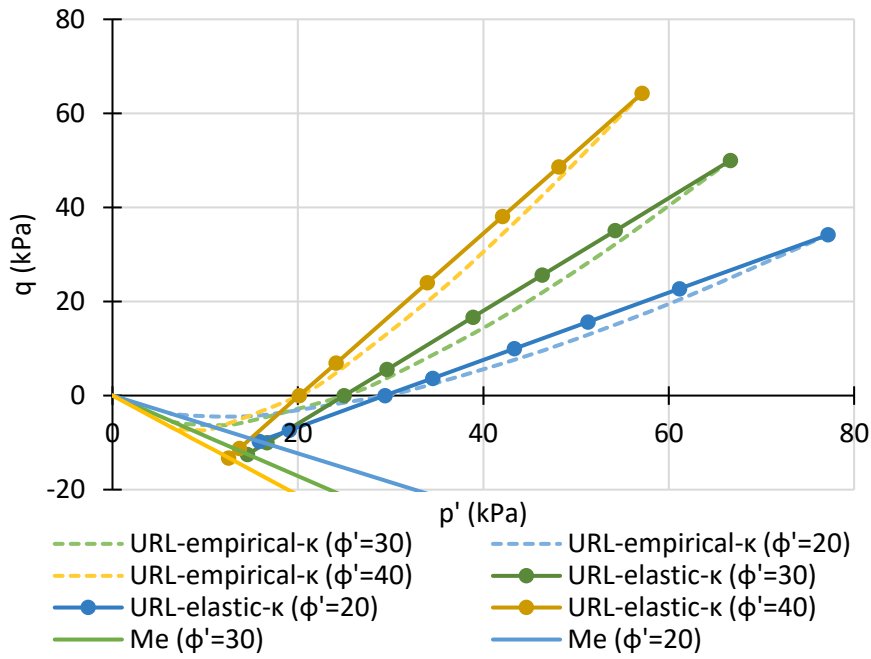
Figure 3.10 Oedometric unloading path in p'-q-diagram shown for three friction angles and vertical consolidation stress of 100 kPa, indicating the empirical relation by **Mayne and Kulhawy (1982)** *and linearized relation*
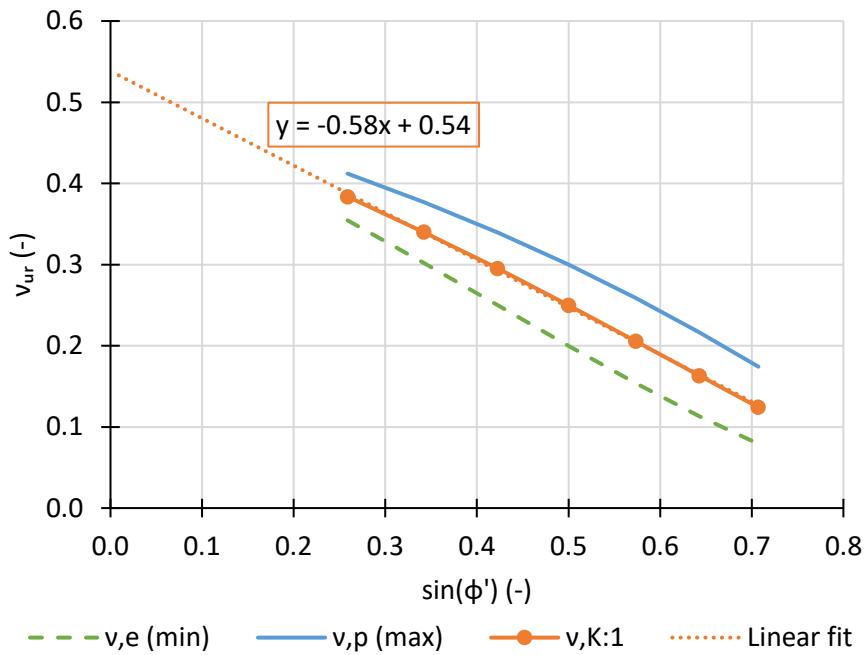
Figure 3.11 Poisson's ratio versus friction angle
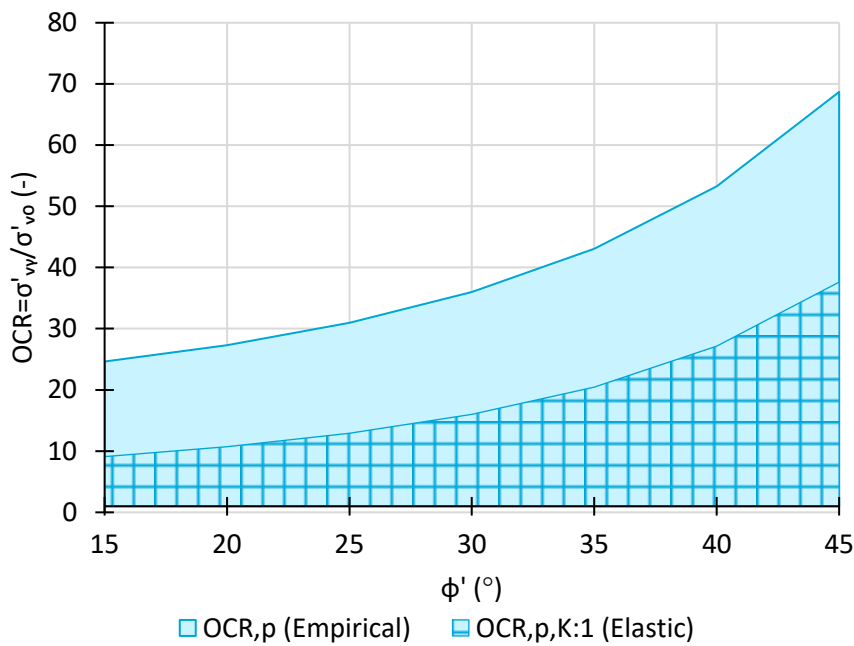
Figure 3.12 OCR validity range for the empirical (3-46) and linearized (3-50) OCR-relation versus friction angle.

3.4.2 Poisson's ratio and plastic volumetric strain ratio

The empirical SHANSEP (Ladd and Foott 1974; Ladd and DeGroot 2003) formulation is shown below where the undrained shear strength and overconsolidation ratio are expressed in terms of vertical stresses:

$$s_{u,SHANSEP} = \sigma'_{v0} \, S \, OCR^{m} \tag{3-51}$$

The exponent m can be derived from CAUC tests. This can be done by following the SHANSEP procedure on identical samples which is often only the case for reconstituted samples. For in-situ material the exponent m can be derived from a regression analysis on a series of overconsolidated CAUC tests. Alternatively, the exponent m can be estimated from Oedometer tests as shown below:

$$m \cong 1 - \frac{RR}{CR} \tag{3-52}$$

In the SHANSEP model the exponent m is used. In this section a comparison will be made of the exponent m derived from the CAUC tests (SHANSEP procedure) and Oedometer tests.

The exponent Λ is based on isotropic stresses and isotropic tests, whereas the oedometric exponent m in the SHANSEP equation is based on vertical stresses and oedometric tests. In this section the relation between these exponents and the Poisson's ratio will be discussed.

Isotropic stress-based models, such as MCC, relate $ln(R)$ to the void ratio e_0 with parameter κ for isotropic compression. Vertical stress-based models (Bjerrum 1967) relate $log(OCR)$ to the vertical (and volumetric) strain ε with parameter RR for one-dimensional compression. The equations are shown in Table 3-2.

The difference in definition of overconsolidation results in different outcome for the strains in oedometric unloading. The strain can be aligned by introducing a conversion factor 'c'. The basic

assumption is that both models (CR, RR and λ, κ based) should yield the same change in volumetric strain (or change in void ratio) upon oedometric unloading, starting from the NCL$_{oed}$ line to the initial stress state σ'_{v0}. To obtain a κ in the MCC model that gives the same ε_v as in a one-dimensional calculation based on CR and RR parameters, κ shall be determined as elaborated below.

Table 3-2 Comparison oedometric and isotropic compression

	Oedometric parameters	Isotropic parameters
Test	**Parameters CR, RR determined from Oedometer test (vertical stress based)**	**Parameters λ, κ determined from Triaxial test (isotropic stress based)**
Primary loading (NCL)	$CR = \dfrac{Cc}{1+e_0} = \dfrac{\Delta\varepsilon_v}{\log\frac{\sigma'_v + \Delta\sigma'_v}{\sigma'_v}}$	$\lambda^* = \dfrac{\lambda}{1+e_0} = \dfrac{\Delta\varepsilon_v}{\ln\frac{p' + \Delta p'}{p'}}$
Unloading (URL)	$RR = \dfrac{Cr}{1+e_0} = \dfrac{\Delta\varepsilon_v}{\log\frac{\sigma'_v + \Delta\sigma'_v}{\sigma'_v}}$	$\kappa^* = \dfrac{\kappa}{1+e_0} = \dfrac{\Delta\varepsilon_v}{\ln\frac{p' + \Delta p'}{p'}}$
Volume strain in oedometric unloading (URL$_{oed}$)	$\Delta\varepsilon_v = RR\log(OCR)$	$\Delta\varepsilon_v = \dfrac{c\cdot\kappa\ln(R_y)}{1+e_0} = \dfrac{\kappa_{oed}\ln(R_y)}{1+e_0}$

Parameters λ^* and κ^* are the modified isotropic compression index and modified isotropic swelling index, respectively (as used in some constitutive models). In oedometric loading K$_{nc}$ is constant which produces a constant ratio between OCR and Ry and a unique relation between CR (or Cc) and λ^* (or λ). In oedometric unloading K$_0$ is not constant, which results in a changing ratio between OCR and Ry. Hence, the relation between RR (or Cr) and κ^* (or κ) requires a conversion factor (c), to yield to the same change of strain in oedometric unloading. The swelling index for oedometric unloading is defined as $\kappa_{oed} = \kappa \cdot c$, where conversion factor (c) over an unloading range (OCR) is:

$$c = \frac{\log(OCR)}{\log(R_y)} \tag{3-53}$$

With:

$$R_y = \frac{p'_y}{p'_0} = OCR\left(\frac{1 + 2K_{nc}}{1 + 2K_0}\right) \tag{3-54}$$

The conversion factor depends on K$_0$ which, as shown previously, depends on the selected secant Poisson's ratio. By assuming a constant Poisson's ratio and further elaboration this produces the following equation:

$$c = \frac{\log(OCR)}{\log\left(\dfrac{OCR \cdot (1 + 2K_{nc})}{1 + 2(OCR \cdot (K_{nc} - \Delta K_{ur}) + \Delta K_{ur})}\right)} \tag{3-55}$$

The conversion factor is applied as multiplication factor to the isotropic swelling index ($\kappa_{oed} = \kappa \cdot c$), as in practice the oedometric compression parameters (CR, RR) are obtained from laboratory tests. Reversely, in case the isotropic compression parameters are given, the equivalent RR-parameter should be divided by the conversion factor to yield to the same change of strain or void ratio in isotropic unloading.

For OCR=1 this leads to an analytical expression for the conversion factor at the onset of unloading. This initial conversion factor value c_e should be regarded in conjunction with the initial value for the Poisson's ratio ν_e Eq.(3-44).

$$c_e = \lim_{OCR\downarrow 1} c = \frac{1 + 2K_{nc}}{1 + 2\Delta K_{ur}} = \frac{1 + 2K_{nc}}{1 + 2K_{nc}^2} \tag{3-56}$$

Higher values of OCR yield to larger conversion factors. Practically it is preferred to apply one conversion factor depending on the OCR range of interest. Therefore, it is proposed to select the conversion factor just as the Poisson's ratio at $OCR_{K:1}$, this factor will be indicated as $c_{K:1}$.

$$c_{K:1} = \frac{\log(OCR_{K;1})}{\log\left(\frac{OCR_{K:1}(1 + 2K_{nc})}{3}\right)} \tag{3-57}$$

$$\approx 1 + 0.82 \sin\phi'$$

In Figure 3.13 three lines are presented, one for the initial value at OCR=1, one for the maximum value at OCR_p and one for the proposed value at $OCR_{K:1}$ It appears that the proposed conversion factor ($c_{K:1}$) can be closely approximated by a linear relation to the sine of the friction angle. The range of the conversion factor in figure [5.26] by Gens (1982) is 1.3 to 1.6, which matches well with Figure 3.13.

Figure 3.14 and Figure 3.15 present the results for an oedometric unloading with vertical and isotropic stress-based models. In this example σ'_{vv}=100 kPa, ϕ'=30°, $c_{K:1} = 1.41$, RR=0.046 and $\kappa_{oed} = \kappa \cdot c_{K:1} = 0.028$. It is concluded that the effect of the conversion factor clearly shows that the results are better aligned with the RR-model in the range of interest, OCR [1-10].
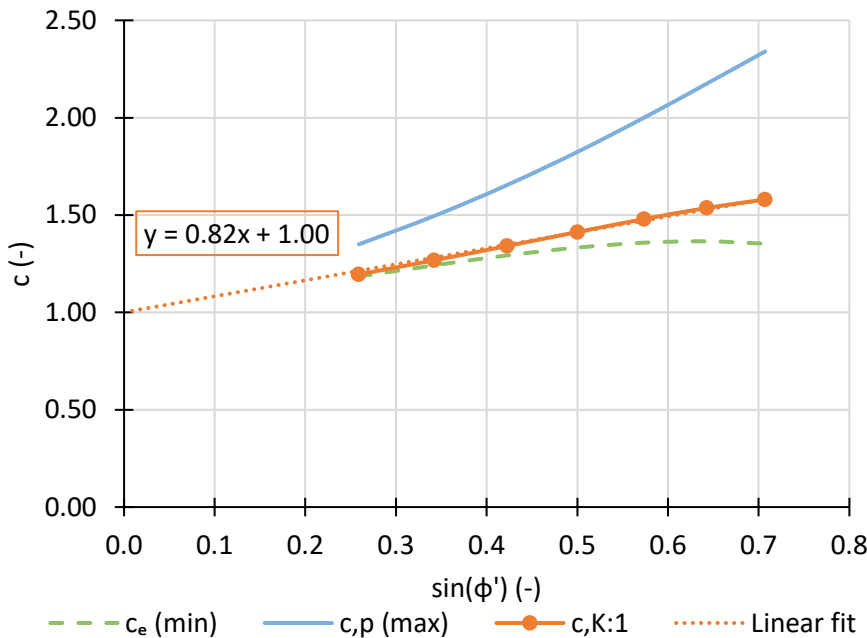
Figure 3.13 Conversion factor versus friction angle

59
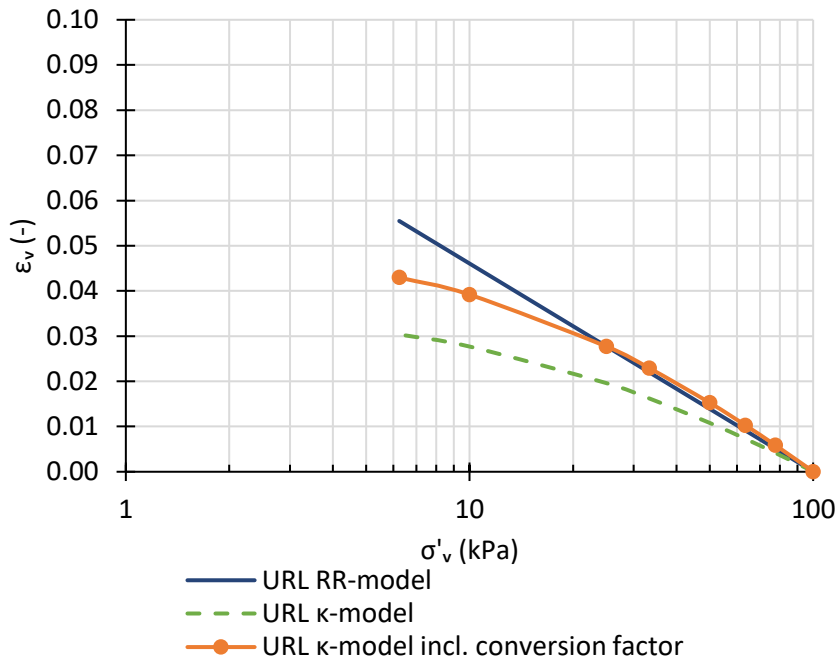
Figure 3.14 Strains in oedometric unloading vs vertical stress. A constant conversion factor is applied to match the strains at a vertical stress of 25 kPa (OCR=4, K_0=1).
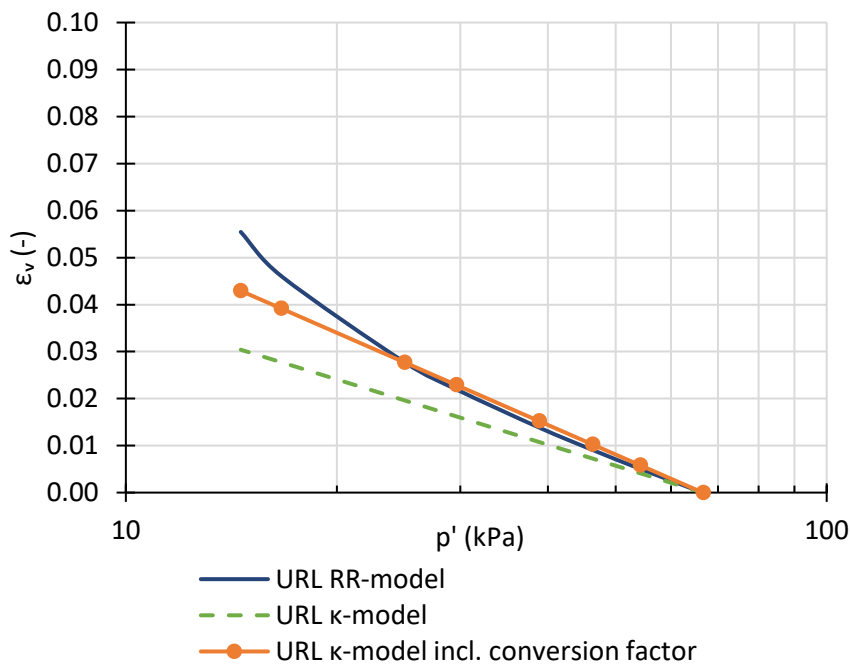
Figure 3.15 Strains in oedometric unloading vs isotropic stress. A constant conversion factor is applied to match the strains at an isotropic stress of 25 kPa (R_y=2.67, K_0=1).

The relation between m and Λ is a function of the same conversion factor as elaborated below:

$$\Lambda = 1 - \frac{\kappa \cdot c_{K:1}}{\lambda} = 1 - \frac{\kappa_{oed}}{\lambda} \tag{3-58}$$

$$m \cong 1 - \frac{RR}{CR} \tag{3-52}$$

$$\Lambda = 1 - (1 - m) \cdot c_{K:1} \tag{3-59}$$

For example, with SHANSEP exponent m=0.8 and a conversion factor $c_{K:1} = 1.41$ the exponent Λ=0.72. This is line with the average value Λ=0.73 based on the published data in Appendix C. The isotropic exponent Λ is thus lower than the oedometric exponent m which is in line with expectations (Ladd and Foott 1974). The conversion factor can be used in practice to either use the exponent m or exponent Λ, depending on whether vertical or isotropic stresses are the basis of the analysis.

3.4.3   Resume

This section shows that, to arrive at the earlier defined equation for the undrained shear strength, starting from oedometric stress conditions, Poisson's ratio should be chosen in conjunction with the overconsolidation ratio. A proposal is made for the selection of a linearized Poisson ratios which accounts for elastic (unloading) behavior. Furthermore, it is shown how the Poisson ratio can be related to the friction angle.

The K_0 is not constant in oedometric unloading. It is shown that in order to develop the same strains, and same void ratio, which is relevant for the CSSM framework, a conversion factor is needed for κ if the parameters are derived from 1-dimensional compression tests. The same principles apply to the conversion factor as it depends on the overconsolidation range and friction angle. An interesting finding is the approximation of the conversion factor based on a linear relation to the friction angle (3-57).

The conversion factor increases κ with approximately a factor 1.41 (for ϕ'=30°) to come to the same volumetric strains in oedometric unloading. Consequently, also the exponent $\Lambda < m$ as shown in Eq.(3-59). The exponent Λ is used together with isotropic stresses, whereas the exponent m is used together with vertical stresses, this results in a difference between these parameters. This is also confirmed by the data presented Appendix C where the isotropic exponent Λ is typically 0.7, whereas the oedometric exponent m typically 0.8 is.

3.5   Analytical formulation of new CSR model for oedometric stress states, followed by undrained deviatoric loading

3.5.1   Introduction

In this section the new CSR model will be introduced. The CSR model is a theoretical version of the SHANSEP equation, to arrive at a realistic undrained shear strength based on the initial stress state defined in vertical effective stress and based on effective strength parameters. The SHANSEP parameters S-ratio and m as well as the elastic Poisson's ratio to be used in conjunction with the CSR model are theoretically substantiated. Furthermore, the CSR model assumes compression and swelling index parameters that are directly based on the results of one-dimensional compression tests.

The model is meant to be implemented in LEM programs, or it can be implemented as an elastic perfectly-plastic (EPP) undrained shear strength model in FEM programs with the only purpose of performing stability calculations. Thereby, the model's shear strength (derived from the stress state, effective friction angle and compression parameters) can be directly compared with more

advanced effective stress based constitutive models without the need to correctly calculate the pore pressures or follow the right effective stress path.

The CSR model classifies as 'Simplified critical state soil mechanics' (Mayne 2006) and is illustrated in Figure 3.16. The formulation of the undrained shear strength strikes a balance between the empirical SHANSEP equation, and the theoretical elaboration of undrained shear strength based on critical state soil mechanics. The CSR model allows for a variable spacing ratio which can be fitted to laboratory test data. This only requires one new model parameter (CSR) without further requirements for specifying a yield function.

The undrained shear strength in the CSR model is based on the assumption that, in line with the elaboration in Section 3.3, in (p', q) stress space a stress point X exists from where, under CAUC test conditions, failure is reached (in point X', Figure 3.16) by following a 'vertical' effective stress path (Δp' = 0), equivalent to the use of an elastic perfectly-plastic model in which the response is neither contractive nor dilative. The key element in the CSR model is finding this point X, or, more generally, the stress point X normalized by the vertical preconsolidation stress, which is called the Critical Stress Ratio (CSR).
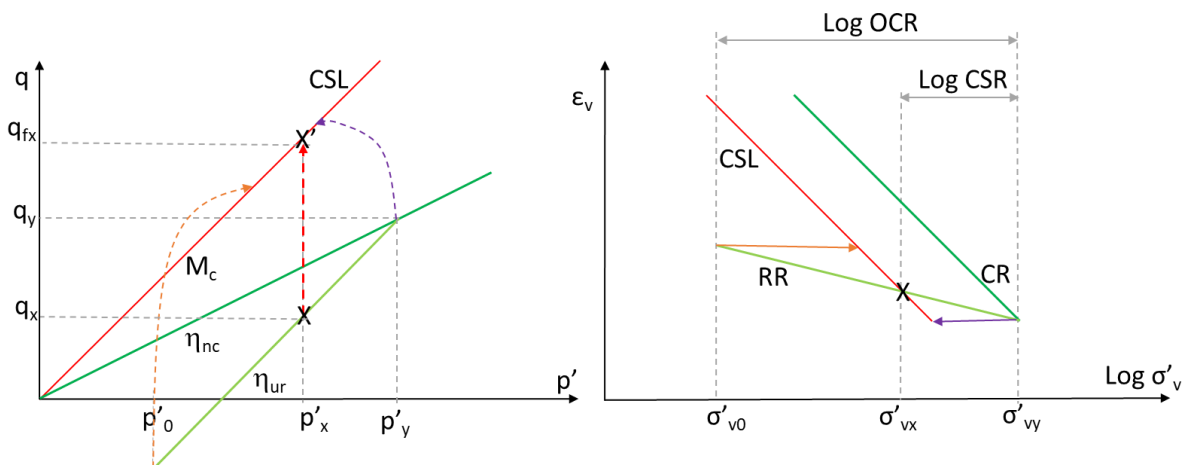
Figure 3.16 CSR model: idealized CAUC behavior in q-p-diagram and vertical stress-strain-diagram

In the empirical SHANSEP (Ladd and Foott 1974; Ladd and DeGroot 2003) formulation the undrained shear strength and overconsolidation ratio are expressed in terms of vertical stresses. In the SHANSEP and CSR model the same exponent m is used on the OCR to calculate the undrained shear strength. In this section a comparison will be made of the exponent m derived from the CAUC tests (SHANSEP procedure) and Oedometer tests.

The SHANSEP parameter S (further called S-ratio) is derived from a normally consolidated CAUC test but can also be derived from regression analysis on a series of overconsolidated CAUC tests. The S-ratio is the undrained shear strength normalized by the vertical effective stress:

$$S_{SHANSEP} = \left[\frac{s_{u,CAUC}}{\sigma'_{vy}} \right]_{nc} \tag{3-60}$$

One can recognize the basic elements below in the MCC formulation for oedometric conditions as derived before:

$$s_{u,CAUC,MCC} = \sigma'_{v0} \frac{(1 + 2K_0)}{3} \left(\frac{M_c}{2}\right) \left(\frac{OCR}{r_x} \cdot \frac{1 + 2K_{nc}}{1 + 2K_0}\right)^\Lambda \tag{3-36}$$

At stress point X where $R_y = r_x$ this leads to:

$$s_{u,x,CAUC,MCC} = \sigma'_{vx} \frac{(1 + 2K_x)}{3} \left(\frac{M_c}{2}\right) \tag{3-61}$$

This can also be formulated with the new CSR model. We first need to define CSR and K_x. CSR is the equivalent OCR at stress point X where $R_y = r_x$, and K_x is the corresponding earth pressure ratio:

$$CSR = \frac{\sigma'_{vy}}{\sigma'_{vx}} = r_x \frac{1 + 2K_x}{1 + 2K_{nc}} \tag{3-62}$$

The corresponding earth pressure ratio is defined as:

$$K_x = CSR(K_{nc} - \Delta K_{ur}) + \Delta K_{ur} \tag{3-63}$$

Substituting the equation for K_x into that of CSR results in:

$$CSR = r_x \frac{1 + 2\Delta K_{ur}}{\left(1 + 2K_{nc} - 2r_x(K_{nc} - \Delta K_{ur})\right)} \tag{3-64}$$

In the CSR model the undrained shear strength for oedometric conditions is formulated as shown in (3-65):

$$s_{u,CAUC,CSR} = \sigma'_{v0} \left(\frac{1 + 2K_x}{3}\right) \left(\frac{M_c}{2}\right) \left(\frac{OCR}{CSR}\right)^m \tag{3-65}$$

At stress point X where $R_y = r_x$ (and OCR = CSR) this produces the same equation as the MCC model:

$$s_{u,x,CAUC,CSR} = \sigma'_{vx} \left(\frac{1 + 2K_x}{3}\right) \left(\frac{M_c}{2}\right) \tag{3-66}$$

Figure 3.17 presents the analytical results of the undrained shear strength for the MCC and CSR model, for overconsolidated CAUC (CK$_0$UC) tests, both based on the same vertical preconsolidation stress σ'_{vy}=100 kPa (p'_y=67 kPa) and oedometric unloading. The isotropic preconsolidation stress is based on the MCC yield surface.

Following a stress path based on elastic perfectly-plastic behavior, as assumed in the CSR model, the undrained shear strength is defined as:

$$s_{u,EPP} = p'_0 \left(\frac{M_c}{2}\right) \tag{3-67}$$

The intersection with the elastic perfectly plastic undrained shear strength EPP-line shows the location of p'_x and ($\sigma'_{vx.}/\sigma'_{vy}$).
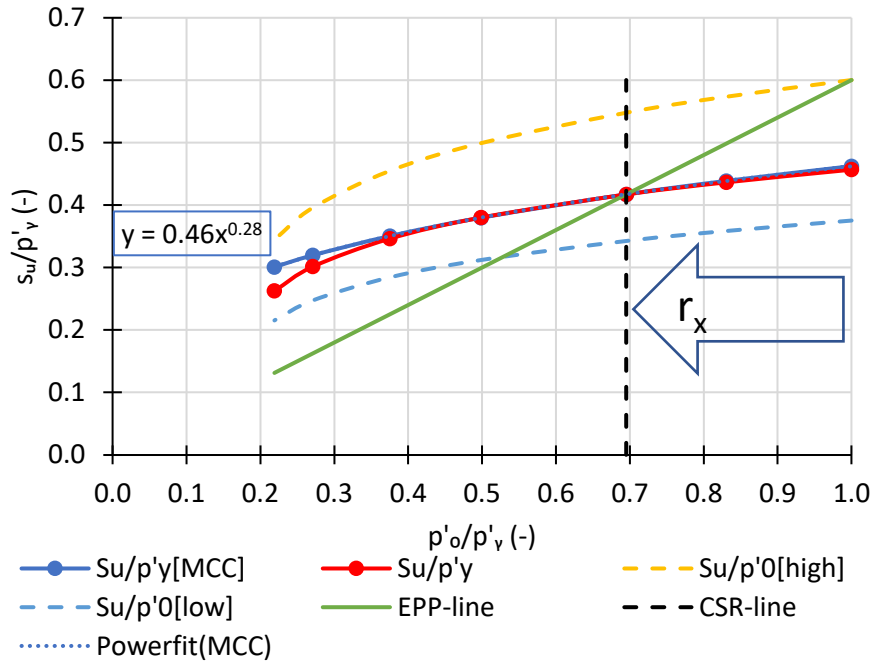
Figure 3.17 MCC and CSR model: undrained shear strength versus isotropic stress. The figure shows that the CSR model is well aligned with the MCC model, although based on vertical stresses and vertical compression parameters. Furthermore is shows a more realistic reduction of the undrained shear strength at an high overconsolidation ratio.

There are two practical simplifications to align with the SHANSEP formulation.

- In the middle term $\left(\frac{1+2K_x}{3}\right)$ the earth pressure is set equal to K_x, which is the K_0 at $R_y=r_x$. This starting point is selected because the S-ratio is a soil constant in the SHANSEP formulation.
- The exponent Λ is in the CSR model replaced by oedometric exponent m because the model is formulated based on vertical stresses.

As shown in the equations above, at OCR=CSR (and $R_y=r_x$), the formulation of the MCC and CSR model yield exactly to the same undrained shear strength. The undrained shear strength ratio equivalent to the SHANSEP S-ratio is defined in the CSR model as:

$$S_{CAUC,CSR} = \left[\frac{s_{u,CAUC}}{\sigma'_{vy}}\right]_{nc} = \left(\frac{1 + 2K_x}{3}\right)\left(\frac{M_c}{2}\right)\left(\frac{1}{CSR}\right)^m \tag{3-68}$$

3.5.2   Parameters

The CSR model is based on oedometric preconsolidation conditions and CAUC loading conditions. It requires the following input parameters. Even if no laboratory data are available as in the theoretical experiment, CSR can be derived from the MCC model. The model constants are:

- Effective critical state friction angle: ϕ' (or M_c)
- Oedometric plastic volumetric strain ratio: m
- Critical Stress Ratio: CSR

The state parameters are:

- Initial vertical stress: σ'_{v0}
- Vertical preconsolidation stress: σ'_{vy}

Alternatively, the OCR can be used with one of the state parameters. The S-ratio is not an input parameter, but an output parameter as defined in Eq.(3-65). The Poisson's ratio ($\nu_{K:1}$) and the earth pressure ratios (K_{nc}, K_0, K_x, ΔK_{ur}) are automatically calculated as shown in the previous section. The K_x Eq.(3-63) is the earth pressure at OCR=CSR.

The exponent m can be derived from:
- A series of CAUC tests based on curve fitting (together with CSR) or,
- Compression ratio CR (or Cc, λ, λ*) and swelling ratio RR (or Cr, κ, κ*) or,
- Plastic volumetric strain ratio Λ (and conversion factor $c_{K:1}$)

Parameter determination procedure, method A

The CSR model requires three model parameters and two state parameters, which is only one model parameter more than in the SHANSEP formulation. All other parameters are automatically calculated following the steps described in the procedure below. Basically, there are two methods (A, B) to derive the parameters as shown in Table 3-3. In the theoretical method A, the CSR is based on the MCC model (same spacing ratio and yield surface) and the exponent m is based on Oedometer tests. In practical method B, the CSR and exponent m are derived from a series of CAUC tests.

Table 3-3 CSR parameter determination procedure

Step	Procedure	
1 - 4	Determination of effective strength parameters and oedometric elastic unloading parameters	
	↙ ↘	
5 - 9	Method A: Determination of CSR based on MCC model (spacing ratio and yield surface). Determination of m based on CRS/OED test.	Method B: Determination of CSR and m based on CAUC tests
	↘ ↙	
10 - 11	Determination of undrained shear strength and S-ratio	
	↓	
12 - 17	Determination of equivalent MCC parameters	

The procedure with steps is described below followed by an example. Step 5 - 9 and 17 in method A (based on MCC) deviate from method B (based on tests), the rest of the steps are the same. Step 12 - 17 are not required for the CSR model and are added to derive the equivalent MCC parameters for verification and to enable a comparison with FEM calculations.

- Step 1: Determine the Critical state friction angle and M-line from a p'-q-diagram or provide friction angle, Eq.(3-14).
- Step 2: Determine the oedometric normally consolidated earth pressure (Jaky), Eq.(3-17).
- Step 3: Determine the overconsolidation ratio at K_0=1, Eq(3-47).
- Step 4: Determine the earth pressure ratio change in oedometric unloading, Eq.(3-48).
- Step 5a: Determine the oedometric normally consolidated p/q-ratio, Eq.(3-18).
- Step 6a: Determine the oedometric spacing ratio r_x, Eq.(3-24).
- Step 7a: Determine the MCC equivalent CSR, Eq.(3-64).

- Step 8a: Determine the earth pressure ratio at OCR=CSR (point X), Eq.(3-63).
- Step 9a: Determine m based on the compression parameters, Eq.(3-52).
- Step 10: Determine the undrained shear strength, Eq.(3-65).
- Step 11: Determine the undrained shear strength ratio, Eq.(3-68).
- Step 12: Determine the Poisson's ratio based on step 4, Eq.(3-49).
- Step 13: Determine the conversion factor, Eq.(3-57).
- Step 14: Determine the plastic volumetric strain ratio, Eq.(3-59).
- Step 15: Determine the compression index from the Oedometer test, Table 3-2.
- Step 16: Determine the swelling index from the Oedometer test, corrected by the conversion factor this leads to the isotropic swelling index, Table 3-2.
- Step 17a: Determine the undrained shear strength based on the MCC model, Eq.(3-36).

3.5.3   Example with method A based on MCC model

In the example below a CAUC test is simulated based on the MCC model; this allows for a comparison of the MCC and CSR results. In this example $\phi'=30^{\circ}$, m=0.80, r=2 (default MCC). Furthermore CR=0.25 and e_0=2, these parameters are required to define MCC parameters in step 15-17. The state dependent parameters are presented in Table 3-4. Test #1 represents the normally consolidated results, test #3 presents the results for OCR=CSR, test #5 presents the results for OCR at K_0=1 and test #7 presents the results for OCR at passive stress ratio.

Table 3-4 State dependent parameters CAUC simulation CSR model

Test	1	2	3	4	5	6	7
OCR (-)	1.00	1.26	1.58	2.51	4.00	8.00	16.00
σ'_{vo} (kPa)	100	80	63	40	25	13	6
K_0 (-)	0.50	0.54	0.60	0.75	1.00	1.67	3.00
p'_0 (kPa)	67	55	46	33	25	18	15
R_y (kPa)	1.00	1.20	1.44	2.01	2.67	3.69	4.57

The model constants and steps required to determine the undrained shear strength for both models are presented in Table 3-5.

Table 3-5 Model constants and calculation steps CSR model method A

Step	Equation	Output
	CSR model	
1	$M_c = \dfrac{6\sin\phi'}{3-\sin\phi'}$	1.20
2	$K_{nc} = 1 - \sin\phi'$	0.50
3	$OCR_{K:1} = \left(\dfrac{1}{K_{nc}}\right)^{\left(\frac{1}{\sin\phi'}\right)}$	4.00
4	$\Delta K_{ur,K:1} = K_{nc}\dfrac{OCR_{K:1}-OCR_{K:1}{}^{\sin\phi'}}{OCR_{K:1}-1}$	0.33
5a	$\eta_{nc} = \dfrac{3(1-K_{nc})}{1+2K_{nc}}$	0.75
6a	$r_x = \dfrac{rM_c{}^2}{M_c{}^2+\eta_{nc}{}^2}$	1.44
7a	$CSR = r_x\dfrac{1+2\Delta K_{ur,K:1}}{\left(1+2K_{nc}-2r_x\left(K_{nc}-\Delta K_{ur,K:1}\right)\right)}$	1.58
8a	$K_x = CSR\left(K_{nc} - \Delta K_{ur,K:1}\right) + \Delta K_{ur,K:1}$	0.60
9a	$m = 1 - \dfrac{RR}{CR}$	0.80
10	$s_{u,CAUC,CSR} = \sigma'_{v0}\left(\dfrac{1+2K_x}{3}\right)\left(\dfrac{M_c}{2}\right)\left(\dfrac{OCR}{CSR}\right)^m$	var
11	$S_{CAUC,CSR} = \left(\dfrac{1+2K_x}{3}\right)\left(\dfrac{M_c}{2}\right)\left(\dfrac{1}{CSR}\right)^m$	0.30
	MCC model	
12	$\nu_{K:1} = \dfrac{\Delta K_{ur,K:1}}{1+\Delta K_{ur,K:1}}$	0.25
13	$c_{K:1} = \dfrac{\log(OCR_{K:1})}{\log\left(\frac{OCR_{K:1}(1+2K_{nc})}{3}\right)}$	1.41
14	$\Lambda = 1 - c_{K:1}(1-m)$	0.72
15	$\lambda = \dfrac{(1+e_0)CR}{\ln(10)}$	0.326
16	$\kappa_{oed} = \kappa \cdot c_{K:1} = \dfrac{c_{K:1}(1+e_0)RR}{\ln(10)}$	0.092
17a	$s_{u,CAUC,MCC} = \sigma'_{v0}\dfrac{(1+2K_0)}{3}\left(\dfrac{M_c}{2}\right)\left(\dfrac{OCR}{r_x}\cdot\dfrac{1+2K_{nc}}{1+2K_0}\right)^\Lambda$	var

The resulting undrained shear strengths are presented in Table 3-6. In the range of OCR=1 to $OCR_{K:1}$ the results are similar and at OCR=CSR equal. For OCR close to the passive stress ratio the MCC model predicts higher values than the CSR model.

Table 3-6 Analytical results CSR model compared with MCC model

Test	1	2	3	4	5	6	7
$s_{u,MCC}$ (kPa)	31	29	28	25	23	21	20
$s_{u,CSR}$ (kPa)	30	29	28	25	23	20	17
$s_{u,EPP}$ (kPa)	40	33	28	20	15	11	9
s_u/σ'_{vy}[CSR] (-)	0.30	0.29	0.28	0.25	0.23	0.20	0.17

Figure 3.18. present the analytical results of the undrained shear strength for the MCC and CSR model (red line), for overconsolidated CAUC (CK$_0$UC) tests, both for the same vertical preconsolidation stress σ'$_{vy}$=100 kPa (p'$_y$=67 kPa) and oedometric unloading. The isotropic preconsolidation stress can be determined from the MCC yield surface, but is not required for the MCC model.

The undrained shear strength is plotted against the vertical consolidation stress; both are normalized by the vertical preconsolidation stress. The exponent following the power-regression line for the CSR line corresponds to $(1 - m) = 0.20$, with $m = 0.80$. The intersection with the elastic perfectly plastic undrained shear strength (EPP-line) shows the location of p'$_x$ and (σ'$_{vx.}$/σ'$_{vy}$). Figure 3.18 illustrates how CSR can be determined graphically, as $\frac{\sigma'_{vx}}{\sigma'_{vy}} = \frac{1}{CSR}$.
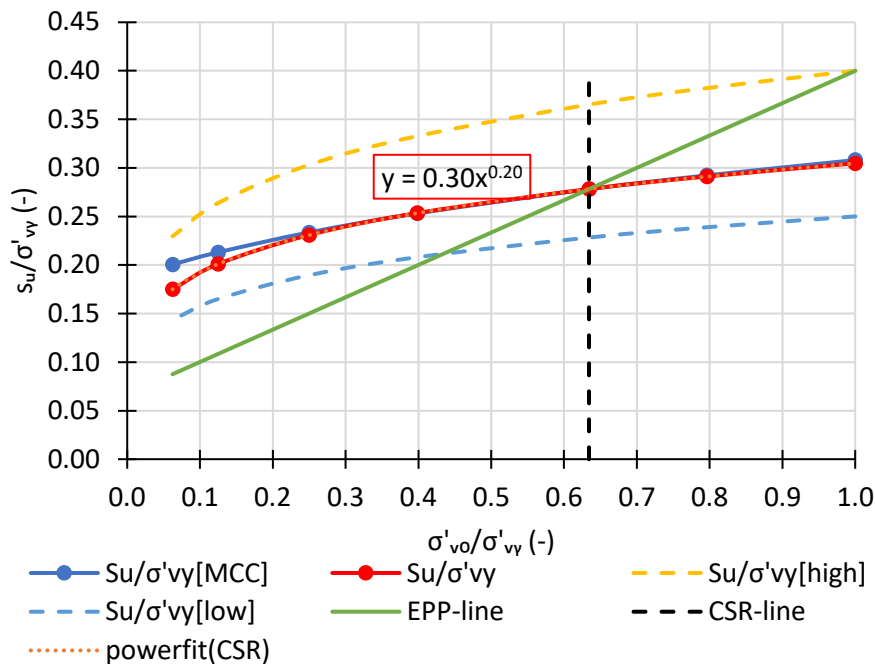
Figure 3.18 MCC and CSR model: undrained shear strength versus vertical stress

3.5.4 Resume

This section shows that the formulation of the CSR model is similar to the SHANSEP formulation and the analytical solution for CAUC tests based on the MCC model. It is shown that the CSR model and the MCC model match well over a wide range of OCR.

Table 3-7 presents a summarizing comparison of the equations of the MCC- and CSR model for a CAUC tests.

Table 3-7 Comparison of MCC and CSR model for CAUC test

MCC model (with OCR and σ'ᵥ) Eq.(3-36), Eq.(3-37):	CSR model (with OCR and σ'ᵥ) Eq.(3-65), Eq.(3-68):
$s_u = \sigma'_{v0} \dfrac{(1+2K_0)}{3} \left(\dfrac{M_c}{2}\right) \left(\dfrac{OCR}{r_x} \cdot \dfrac{1+2K_{nc}}{1+2K_0}\right)^{\Lambda}$	$s_u = \sigma'_{v0} \left(\dfrac{1+2K_x}{3}\right) \left(\dfrac{M_c}{2}\right) \left(\dfrac{OCR}{CSR}\right)^{m}$
$S = \left[\dfrac{s_{u,CAUC}}{\sigma'_{vy}}\right]_{nc} = \dfrac{(1+2K_{nc})}{3} \left(\dfrac{M_c}{2}\right) \left(\dfrac{1}{r_x}\right)^{\Lambda}$	$S = \left[\dfrac{s_{u,CAUC}}{\sigma'_{vy}}\right]_{nc} = \left(\dfrac{1+2K_x}{3}\right) \left(\dfrac{M_c}{2}\right) \left(\dfrac{1}{CSR}\right)^{m}$

3.6 Validation of the new CSR model based on two sets of laboratory tests

In this chapter it will be shown how to derive the CSR model parameters for a series of CAUC tests on a particular soil type.

3.6.1 CAUC requirements

The requirements for the CAUC tests are presented below:
- All samples should be taken from one soil type.
- A series of at least 3 tests; 1 normally consolidated, and 2 overconsolidated at different OCRs.
- Consolidation based on SHANSEP procedure prior to CAUC testing. This will provide an accurate preconsolidation stress. Alternatively, it is possible to use a set of normally consolidated and overconsolidated tests. The preconsolidation stress should then be derived from oedometer tests of adjacent samples (The third example in Appendix D uses this alternative approach).
- K₀ prior to CAUC shearing based on the linearized empirical formulation. Alternatively, it can be based on K0-CRS measurements on adjacent samples or following K₀ controlled consolidation procedures in a Triaxial cell.
- The first step is the determination of the friction angle by plotting the effective stress paths in a p'-q-diagram and define the critical state failure line, as the line through the origin of the stress space and the critical state failure points of the effective stress paths. The stress paths tend to converge to the Mc-line with increasing strain. It is advised to determine the critical state undrained shear strength based on a combined assessment of the p'-q-diagram, q-εₐ-diagram and Δu-εₐ-diagram instead of applying a fixed strain criterium (i.e., 25%).

3.6.2 Parameter determination procedure, method B

The procedure with steps is described below followed by an example. Step 5 - 9 and 17 in method B are based on tests and deviate from method A. Step 12-17 are not required for the CSR model and are added to derive the equivalent MCC parameters for verification.

- Step 1 to step 4 are the same as in Method A, see Section 3.5.2.
- Step 5b: Determine the K₀ in oedometric unloading based on Hooke's law, Eq.(3-33).
- Step 6b: Determine the elastic perfect plastic undrained shear strength, Eq.(3-67), and define the EPP-line in Figure 3.18.
- Step 7b: Determine the CSR. The CSR is defined as the overconsolidation ratio at stress point X. This is indicated by the CSR-line ($CSR^{-1} = \sigma'_{vx}/\sigma'_{vy}$). Stress point X can be found at the intersection of the measured critical state undrained shear strength curve with the EPP-line in Figure 3.18.

- Step 8b: Determine the exponent m. The oedometric exponent-m can be determined by curve fitting the data by a power-function in Figure 3.18.
- Step 9b: Determine the earth pressure ratio at OCR=CSR (point X), Eq.(3-63).
- Step 10 to 16 are the same as in Method A.
- Step 17b: Determine the approximated MCC equivalent Critical State M-parameter, Table 3-9.

3.6.3   Example reconstituted Lower Cromer Till

The first example is based on published CAUC test results by Gens (1982), shown in Figure 3.3. The silty clay called 'Lower Cromer Till' is reconstituted with liquid limit of 25% and plasticity index of 12%. The reported soil properties following the Triaxial tests are: ϕ'=30.0, Λ=0.88 and e_0=0.66. The back-calculated compression parameters from the Oedometer tests are: CR=0.096, RR=0.008 with m=0.92.

The reported test conditions are: K_{nc}=0.5, σ'_{vy}=350 kPa. The K_0 of the overconsolidated tests approaches the empirical relation and is simulated with a constant Poisson's ratio according to the procedure as visualized in Figure 3.10. The state dependent parameters are reported in Table 3-8. The model constants and steps are presented in Table 3-9.

Table 3-8 State dependent parameters CSR model Lower Cromer Till

Test	1	2	3	4	5	6
OCR (-)	1.00	1.50	2.00	4.00	7.00	10.00
σ'_{vy} (kPa)	350	350	350	350	350	350
σ'_{v0} (kPa)	350	233	175	88	50	35
K_0 (-)	0.50	0.58	0.67	1.00	1.50	2.00
p'_0 (kPa)	233	169	136	88	67	58
$s_{u,test}$ (kPa)	79	78	77	73	68	64
$s_{u,EPP}$ (kPa)	140	101	82	53	40	35
$s_{u,CSR}$ (kPa)	80	78	76	71	68	66
s_u/σ'_{vy} (-)	0.23	0.22	0.22	0.20	0.19	0.19
s_u/σ'_{v0} (-)	0.23	0.33	0.43	0.82	1.36	1.88

Table 3-9 Model constants and calculation steps CSR model method B, Lower Cromer Till

Step	Equation	Output
	CSR model:	
1	$M_c = \dfrac{6 \sin \phi'}{3 - \sin \phi'}$	1.20
2	$K_{nc} = 1 - \sin \phi'$	0.50
3	$OCR_{K:1} = \left(\dfrac{1}{K_{nc}}\right)^{\left(\frac{1}{\sin \phi'}\right)}$	4.00
4	$\Delta K_{ur,K:1} = K_{nc} \dfrac{OCR_{K:1} - OCR_{K:1}{}^{\sin \phi'}}{OCR_{K:1} - 1}$	0.33
5b	$K_0 = OCR_{K:1}\left(K_{nc} - \Delta K_{ur,K:1}\right) + \Delta K_{ur,K:1}$	var
6b	$s_{u,EPP} = \left(\dfrac{M_c}{2}\right) p'_0 = M_c \dfrac{1 + 2K_0}{6}$	var
7b	CSR: fit based on graph	2.26
8b	m: fit based on graph $\left(m \cong 1 - \dfrac{RR}{CR}\right)$	0.91
9b	$K_x = CSR\left(K_{nc} - \Delta K_{ur,K:1}\right) + \Delta K_{ur,K:1}$	0.71
10	$s_{u,CAUC,CSR} = \sigma'_{v0} \left(\dfrac{1 + 2K_x}{3}\right)\left(\dfrac{M_c}{2}\right)\left(\dfrac{OCR}{CSR}\right)^m$	var
11	$S_{CAUC,CSR} = \left(\dfrac{1 + 2K_x}{3}\right)\left(\dfrac{M_c}{2}\right)\left(\dfrac{1}{CSR}\right)^m$	0.23
	MCC model:	
12	$v_{K:1} = \dfrac{\Delta K_{ur,K:1}}{1 + \Delta K_{ur,K:1}}$	0.25
13	$c_{K:1} = \dfrac{\log(OCR_{K:1})}{\log\left(\frac{OCR_{K:1}(1 + 2K_{nc})}{3}\right)}$	1.41
14	$\Lambda = 1 - c_{K:1}(1 - m)$	0.88
15	$\lambda = \dfrac{(1 + e_0)CR}{\ln(10)}$	0.069
16	$\kappa_{oed} = \kappa \cdot c_{K:1} = \dfrac{c_{K:1}(1 + e_0)RR}{\ln(10)}$	0.008
17b	$M_{c,MCC,eq} \approx M_c \dfrac{s_{u,test}}{s_{u,CAUC,CSR}}$ and CSR based on method A	0.95

It can be concluded that the CSR model fits the measured undrained shear strength well. The exponent m is 0.91, almost equal to the indicative value m=(1-RR/CR)=0.92. The exponent Λ is 0.88, equal to the reported value. The CSR value corresponds to a spacing ratio r>2, which results in a relative low S-ratio. This is shown in Figure 3.19 and Figure 3.20 where the strength is lower than the equivalent MCC value, even lower than the lower bound S-ratio. The CSR model is able to capture these low S-ratios despite a friction angle of 30 degrees. To fit the data with a MCC model the equivalent friction angle needs to be manually lowered to about 24 degrees ($M_{c,MCC} = 0.95$), which is unrealistically low compared to the M-line from the p'-q-diagram. The value for M_c can also be approximated by the undrained shear strength based on the MCC model, Eq.(3-36).
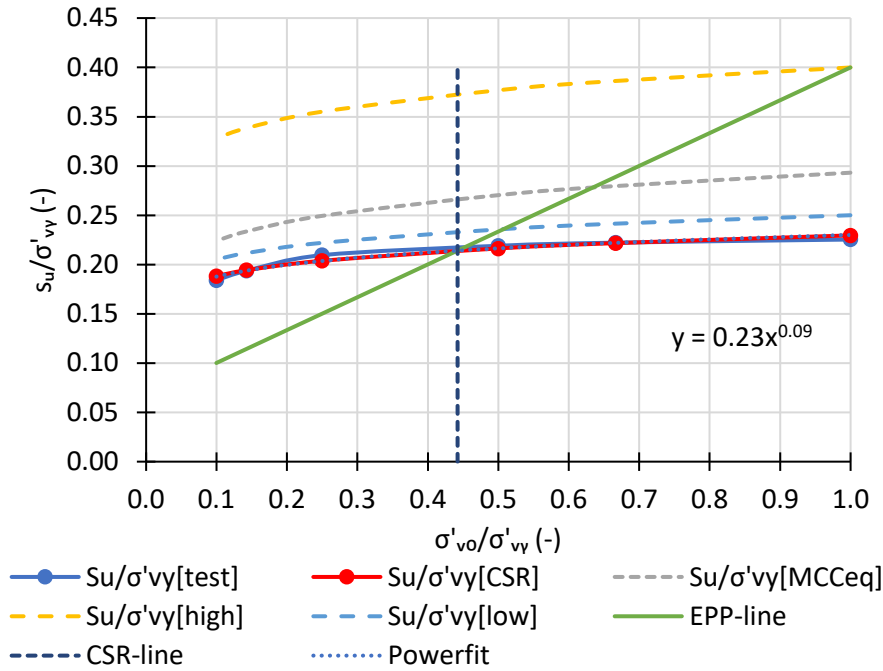
Figure 3.19 LCT clay: Undrained shear strength versus vertical consolidation stress, both normalized by the vertical preconsolidation stress
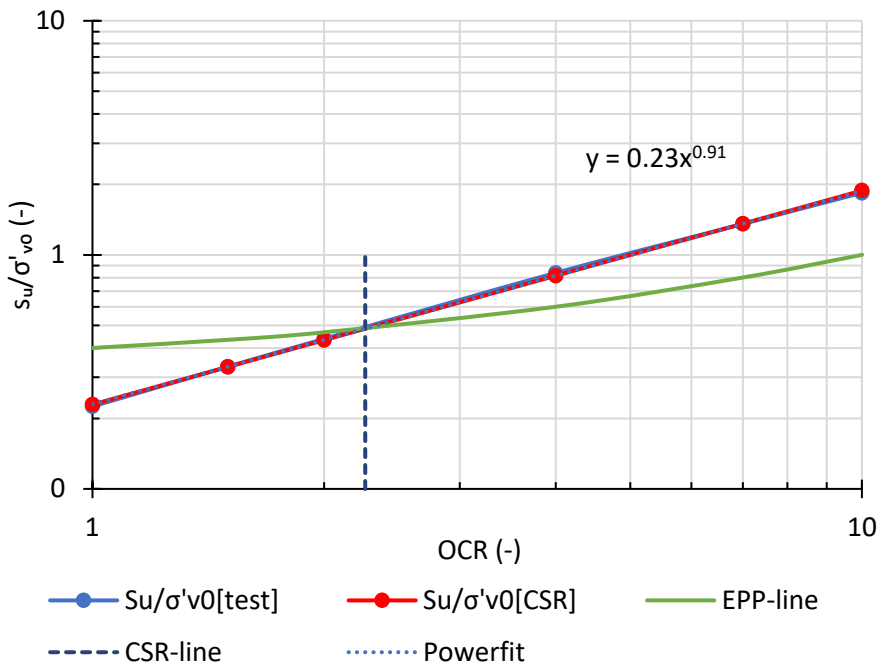
Figure 3.20 LCT clay: Undrained shear strength ratio versus overconsolidation ratio

3.7 Conclusions

Chapter 3 presents the new CSR model. The research question addressed in Chapter 3 is how the stability assessment can be improved by linking effective strength parameters to undrained shear strength parameters using Critical State Soil Mechanics theory. Improvement of the stability assessment can be achieved by the CSR model as it provides a reliable determination of the undrained shear strength, based on effective stress parameters and common laboratory tests.

The formulation of the undrained shear strength strikes a balance between the empirical SHANSEP equation, and the theoretical elaboration of undrained shear strength based on critical state soil mechanics. The CSR model requires one new model parameter called the Critical Stress Ratio (CSR), comparable to a spacing ratio. The spacing ratio r is a model constant in the MCC model and is equal to 2. The CSR model allows for a variable spacing ratio, CSR is a model parameter, which can be fitted to laboratory test data.

There are two procedures to determine the parameters. In Method A the model provides the MCC undrained shear strength based on vertical stresses. In Method B the model is fitted to actual CAUC test results. The examples in the previous section and Appendix D illustrate that both the theoretical MCC undrained shear strength as the actual undrained shear strength of three different soil types can well be approximated. The CSR model is validated for soft organic clay (OVP and Eemdijk clay) and stiff silty clay (LCT), hence it can be applied to a wide range of clays.

The model only requires five input parameters. Other (intermediate) parameters are automatically calculated by the procedure. This is made possible by the proposed linearization and alignment of the Poison's ratio with other model parameter ratios.

The model can be implemented in LEM where it can be used for ULS analysis. The model can also be used to determine the undrained shear strength parameters as input for SHANSEP based undrained shear strength models in LEM or FEM. The procedure also determines the equivalent MCC model parameters.

4

Eemdijk full-scale failure tests

When an earthen dike needs to be heightened it also requires the width at the base to be increased. In many urban areas the land has been developed right up to the base of the dike. To raise and widen the dike would require private property to be purchased or even buildings to be removed. Hence, new structural reinforcement methods with sheet pile stability walls as shown in Figure 1.1 have become more popular. The increased frequency of dike reinforcements by sheet piles is primarily related to constraints from adjacent properties and other functions than flood protection.

The previous chapters discuss empirical relations for organic soils as well as the theoretical relations to determine the undrained shear strength, required for the stability verification. This chapter presents the results and evaluation of the Eemdijk full-scale failure test (In Dutch: 'Eemdijk damwandproef'). The Eemdijk full-scale failure tests involves separate tests on sheet pile panels, on a ground dike, as well as a combined test on a ground dike with sheet pile reinforcement. In addition to a description of the test conditions and results, this chapter includes the results of back-analyses and conclusions on the applicability of the proposed methods of the previous chapters.

The assessment of the global stability of earthen dikes is traditionally performed with limit equilibrium methods (LEM), while the use of numerical methods (e.g., FEM) in dike design is increasing. LEM models cannot be applied to dikes with sheet pile walls because the soil-structure interaction (SSI) is not included. SSI requires the use of more advanced numerical methods, such as the finite element method, which includes structural properties and stiffness and strength parameters for soil.

The evaluation aims to address the question how a dike with sheet pile reinforcement performs towards and beyond failure in a full-scale failure experiment and how this compares to an earthen dike. Furthermore, it will be investigated to what extent the full-scale test can be modelled with FEM using existing constitutive models. The goal of this evaluation is to improve the dike engineering where sheet pile reinforcement is involved.

4.1 Introduction

Over the last 30 years various full-scale tests have been performed, related to large scale geotechnical projects in the Netherlands. Amongst these are four full-scale dike and embankment failure tests (Lindenberg et al. 2002; Van et al. 2005; Zwanenburg et al. 2012; Zwanenburg and Jardine 2015; De Gast et al. 2021). Furthermore one full-scale test on sheet pile retaining walls in a building pit is reported by Kort (2002). Internationally most performed full-scale tests on embankment focus on the deformations, with a few full-scale embankments test

with focus on stability (Rowe et al. 2001; Lehtonen et al. 2015; Tashiro et al. 2015). The combination of a full-scale failure test on an embankment (dike) with sheet pile reinforcement is new and unique.

This chapter presents the main findings of the Eemdijk full-scale failure test on a dike reinforced by a sheet pile wall. The tests have been performed in 2018 near the river Eem in the center of the Netherlands, initiated by the Dutch Flood Protection Programme organization as part of the POVM programme[5]. For the full report[6] (in Dutch) reference is made too Breedeveld et al. (2018a), summarized in Breedeveld et al. (2018b). The databases are available in the Delft University of Technology repository[7] (Lengkeek and Breedeveld 2022).

The stability of flood defenses needs to comply with the Dutch Water Act[8] and requirements defined in 'OI2014' (Rijkswaterstaat 2017, 2021). Global instability of a dike (In Dutch: 'Macrostabiliteit STBI') is defined as a geotechnical failure initiated by high water conditions, resulting in flooding. Slope failure without flooding can be compared to a Ultimate Limit State (ULS) in the Eurocode standards (EN1990 2002). Failure of the flood defense resulting in flooding is comparable to a 'Damage Limitation State' such as defined in Eurocode 8 on seismic design or in general to 'Accidental design situation' in the Eurocode. Instability of the flood defense requires that situation beyond initial local instability is considered. Global stability should be verified with the Critical State strength properties of soil. Practically, the large strain value or so-called ultimate value are used for this. The criteria for the ultimate value determination are discussed in Section 4.3.

Sheet piles along a dike affect the deformations and failure mechanism. Validation is however lacking for sheet pile reinforced dikes, in particular the behavior beyond failure, often referred to as the residual strength and residual profile. The partial factors for semi-probabilistic (level 2) analysis are calibrated for earthen dikes, as well as for retaining walls. Code calibration for dikes with sheet pile reinforcement is lacking. The Eemdijk full-scale failure test is the first step in order to understand physics of the combined system towards and beyond failure. Furthermore, it is the first step to validate the possibility to back-analysis performance of FEM models.

This research is focused on the soil-structure interaction towards and beyond failure of a structural reinforced dike on soft soil conditions. Reduction of unnecessary conservatism in the design approach can be reached through both physical and numerical experiments. Numerical models such as the finite element method can be used to model the deformations until failure and soil-structure interaction (SSI). The combination of these is becoming increasingly relevant for dike engineering projects in the Netherlands. Therefore, it is important to gain insight in the performance of sheet pile reinforced dikes in practice and appropriate ways to model these systems.

Even though global stability is verified with ultimate strength properties, deformations cannot be ignored for the following reasons:

---

[5] https://www.hwbp.nl/kennisbank/pov-macrostabiliteit
[6] https://publicwiki.deltares.nl/display/HWBPDIV
[7] https://data.4tu.nl/portal
[8] https://www.helpdeskwater.nl

- The current Dutch dike design guidelines (Rijkswaterstaat 2017; POVM 2020a, 2020b; Rijkswaterstaat 2021) specify verification of deformations, sheet pile structural forces and geotechnical stability. This should be performed by FEM calculations, using appropriate constitutive models and characteristic soil properties with partial factors. The allowable deformation is defined as a horizontal displacement of 10 cm at the crest. This is in particular critical for dikes reinforced by sheet piles without anchorage, as these tend to allow for larger deformations prior to global failure. Limiting the deformations will have a significant cost impact, as the sheet piles need to be stiffer to meet the performance criteria. A stiffer wall results in higher forces and requires higher strength.
- Dikes can be reinforced by different types of sheet piles, placed at different locations, with or without anchorage. The forces in the sheet pile wall depend largely on the SSI, therefore correct modeling of the soil behavior is important for the verification of the structural safety. The Eemdijk test considers only one configuration, an unanchored sheet pile located on the inboard crest side. The implication for other configurations is discussed in Section 4.9.
- Under certain conditions larger deformations are allowed, eventually resulting in a lower crest and possibly cracks in the dike cover or at transitions. Combined with water overtopping this might result in critical erosion conditions. Furthermore, the geotechnical stability can be adversely affected by increased infiltration and phreatic water level in the dike, due to cracks in the active zone. Accurate prediction of the deformations is thus relevant.
- Large deformations of the dike might result in structural damage of nearby buildings. These buildings need to comply with the Dutch Building Degree[9] (In Dutch: 'Bouwbesluit') and design requirements defined in the Eurocodes. These design conditions differ from flooding conditions following the Dutch Water Act.

The research sub-questions, as formulated in Chapter 1, for Eemdijk full-scale failure test are repeated below and are dealt with in this chapter:
- How does a dike with sheet pile reinforcement perform towards and beyond failure in a full-scale failure experiment and how does this compare to an earthen dike (Research question 4, section 4.6 and 4.7)?
- What is the performance of the sheet piles towards and beyond failure (Research question 5, section 4.4)?
- How can the complex soil-structure interaction and failure mechanism of a sheet pile reinforced dike be analyzed and explained by means of the finite element method (Research question 6, section 4.8) ?
- How can the results of this research be used to improve the (Dutch) dike engineering practice (Research question 7, section 4.9) ?

This chapter can be divided in three parts as shown in Figure 4.1, first a general part with conditions, second a part with the factual results of the field tests and third the interpretative part. The relation of between the sections is presented in Figure 1.2. The validation of proposed methods of the previous chapters is presented in Section 4.3.

---

[9] https://rijksoverheid.bouwbesluit.com/

General	Factual	Evaluation
• 4.1 Introduction • 4.2 Test set-up • 4.3 Geotechnical conditions	• 4.4 PO-test results • 4.5 GD-test results • 4.6 SPD-test results	• 4.7 Comparison GD & SPD • 4.8 FEM back-analysis • 4.9 Evaluation Eemdijk test

Figure 4.1 Outline chapter on Eemdijk full-scale field test

4.2 Eemdijk test set-up

4.2.1 Full-scale tests

The Eemdijk full-scale failure test consists of three tests:

1. sheet pile pull-over test (PO-test)
2. ground dike test (GD-test)
3. sheet pile reinforced dike test (SPD-test)

The focus of the Eemdijk full-scale failure test is on the SPD-test. The GD-test is used as reference case and to optimize the SPD-test conditions. The PO-test is used to investigate the sheet pile properties and the soil structure interaction until and beyond failure.

The GD-test and SPD-test are performed on a newly constructed embankment. The embankment consists of two parallel sections of 60 m length with a maximum height of 5.5 m, see Figure 4.3 to Figure 4.7. The core material consists of sand and the cover layer consists of firm clay with a slope of 1V:1.7H. The center area between the two dikes is about 2 m lower and contains a clay cut-off wall to create two compartments with controllable water levels.

The Eemdijk full-scale failure test enables to investigate failure conditions in a controlled manner, that are representative for a sheet pile reinforced dike as schematically shown in Figure 4.2. The primary loading and reduction of strength follow from the increased water pressures (A). The secondary loading follows from surcharge (C). The sheet pile wall (B) is unanchored and embedded in the deeper sand layers. The corresponding failure mechanism as shown on the right side is a combination of active/passive wedges and a slip circle. In practice also shorter sheet piles supported by inclined anchors are used.
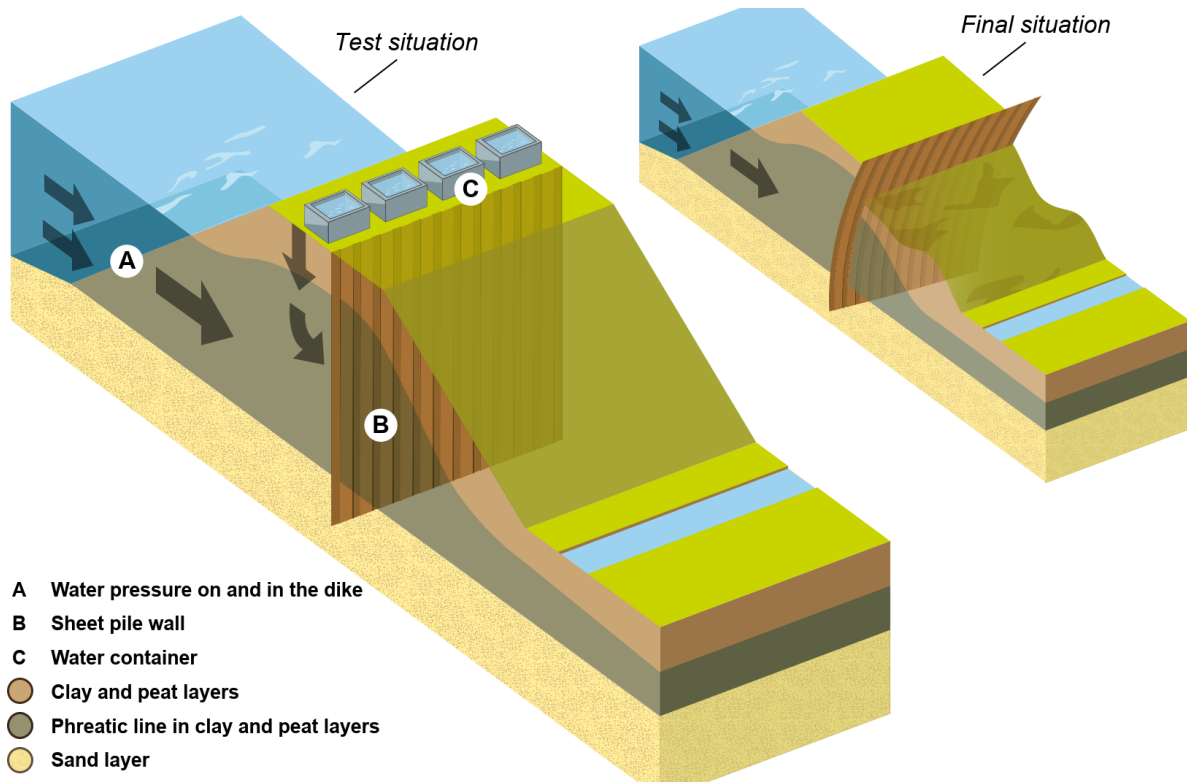
Figure 4.2 Schematic loading conditions of a sheet pile reinforced dike [Figure courtesy Breedeveld et al. (2019)]

The Eemdijk location is suitable for the full-scale tests as the subsoil is relatively homogeneous, consisting of soft soils on top of an aquifer sand layer, which is representative for dikes in the Netherlands. A detailed geotechnical profile is presented in Table 4-3. No existing dike could be used for the failure test, hence a new test embankment is constructed. Realistic loading conditions are created by water infiltration of the sand core and raising the water level inside and behind the dike. At the same time uplift conditions are simulated by excavation of a ditch in front of the dike, combined with lowering of the water level in the ditch.

The construction of a new embankment will cause excess pore pressure. The pore pressures are measured and considered in the back-analysis. This increases the complexity and uncertainty for the back-analysis. More importantly, the fact that the soil is not fully consolidated limits the strength of the soil which enables the possibility to initiate failure of the sheet pile reinforced dike by realistic water pressure loading conditions, without the need for an unrealistic high surcharge.

The project schedule is presented in Table 4-1. Project day 0 is the first day of embankment construction. The project days are used throughout this thesis to present the results in time.

Table 4-1 Eemdijk full-scale failure test project schedule and project days

Phase	Start date	Start project day	Duration (days)
construction GD	6/12/2017	0	226
construction SPD	6/12/2017	0	273
GD-test	1/24/2018	226	6
SP-installation & PO-test	2/23/2018	256	16
SPD-test	3/12/2018	273	6

4.2.2   Monitoring instrumentation

The characterization of the test site has been carried out based on CPTs and boreholes. The initial groundwater regime at the test site is determined by piezometers installed prior to construction. Both during the construction of the embankment and the failure tests an extensive monitoring campaign aiming at geotechnical and structural aspects has taken place in multiple cross sections, to record a complete case for quantitative comparison by back-analysis.
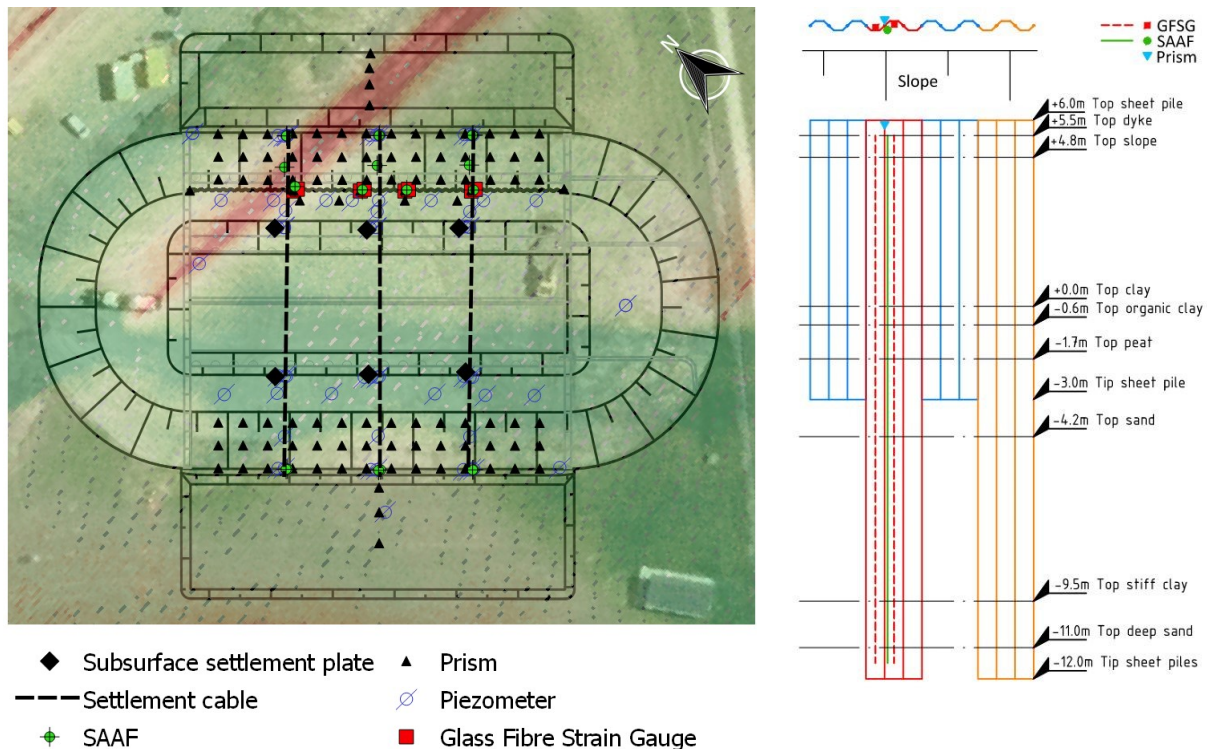
Figure 4.3 Topographic map with contours of embankment and monitoring instrumentation

Figure 4.4 Staggered GU8N sheet piles of SPD-test with monitoring instrumentation and typical soil profile

Figure 4.3 shows a top view of the contours of the test embankment, with the GD-test at the bottom and the SPD-test at the top, including the monitoring instrumentation. The shadings indicate the topography, the red area is slightly lower and associated with an agricultural ditch. The dark green area is slightly higher and associated with the location of on old dike. Figure 4.5 presents the instrumentation in the cross section of the GD and SPD. The construction monitoring comprised: (sub)surface settlement plates, settlement cable, inclinometers (SAAFs) at the toe and piezometers. The failure test monitoring comprised: (sub)surface settlement plates, SAAFs at the toe, slope and sheet pile, piezometers and monitoring wells, prisms on both

slopes. The monitoring instrumentation on the sheet piles of the SPD-test are presented in Figure 4.4.
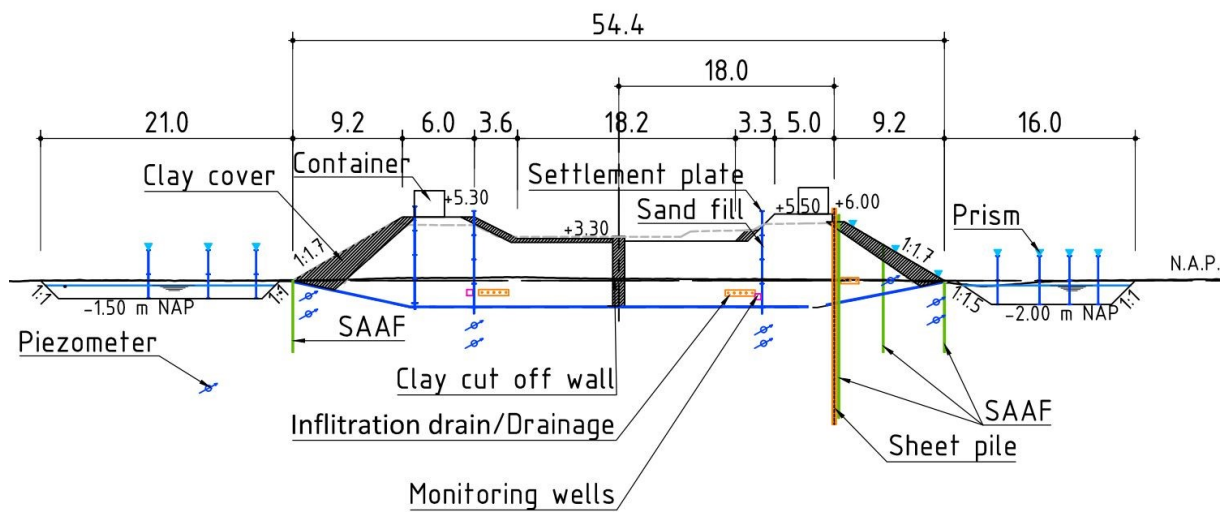
Figure 4.5 Cross section of ground dike (left) and sheet pile dike (right) with monitoring instrumentation [Figure after Lengkeek et al. (2019a)]
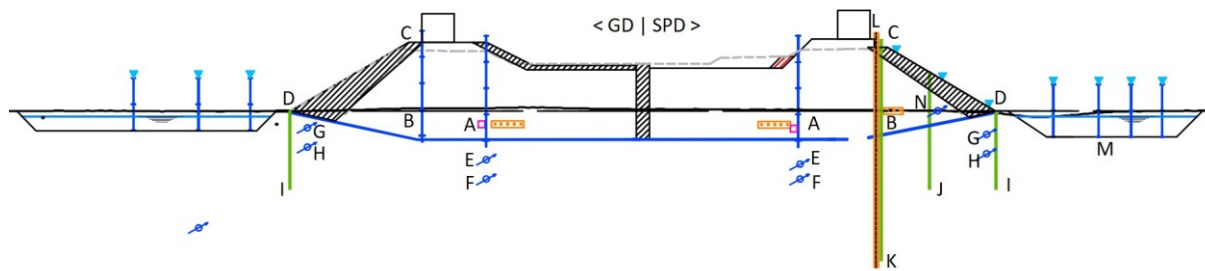
Figure 4.6 Cross section of GD and SPD with locations of monitoring instrumentation (A to I). The coordinates and depths are presented in Appendix K

The overview of monitoring instrumentation locations in the middle cross section of the GD and SPD is shown in Figure 4.6. The locations are identified by [A, …, I]. The coordinates and depths are presented in Appendix K.

Table 4-2 Overview of type and number of monitoring devices

Location / test:	GD		SPD		PO	Total
Instrumentation	Construction phase	Test phase	Construction phase	Test phase	Test phase	
Settlement cables	3	3	3	3		3
Settlement plates	3	3	3	3		6
Inclinometers (SAAF)	3	3	3	10	17	30
Prisms		45		56	55	156
Piezometers	17	17	21	21	4	42
GFSG strings on sheet pile			8		18	18
Load cells					4	4
Optical sensors					4	4

Monitoring is applied to the construction phase and test phase. The embankment is constructed in layers up to 1.2 m thick. The Observational Method approach (EN1997-1 2005), i.e. continuous comparison of the measured and predicted settlements and consolidation, is applied to enhance a quick construction without loss of stability. The monitoring comprises the settlements and pore pressures below the embankment as well as the horizontal deformations at the toe of the slopes. The development of strength is monitored by the additional CPTs during and after the construction of the embankment. The Observational Method also provided an improved insight into the actual properties of the subsoil during construction. The overview of monitoring instrumentation is shown in Table 4-2.

4.2.3   Construction phasing

Figure 4.7 shows a cross section of the first eight stages of the embankment, with the ground dike at the left and the dike with sheet pile reinforcement at the right. Each stage is indicated by a number, where the blue lines represent the sand fill and the purple lines the clay cover. The construction phasing in time for the embankment is presented in Appendix I, including the construction stage height, estimated settlement and construction level. The levels for the GD and the center are similar, except that the maximum level of the GD is 5.3 m NAP (reference datum in The Netherlands) compared to 5.5 m NAP at the SPD. Furthermore, the soil profile based on CPT LMKP34 is presented up to 20 m depth which is representative for the whole site, except at the toe of the GD where an additional sublayer 3a is indicated. In addition, at the GD the preloaded area by an old dike is indicated.

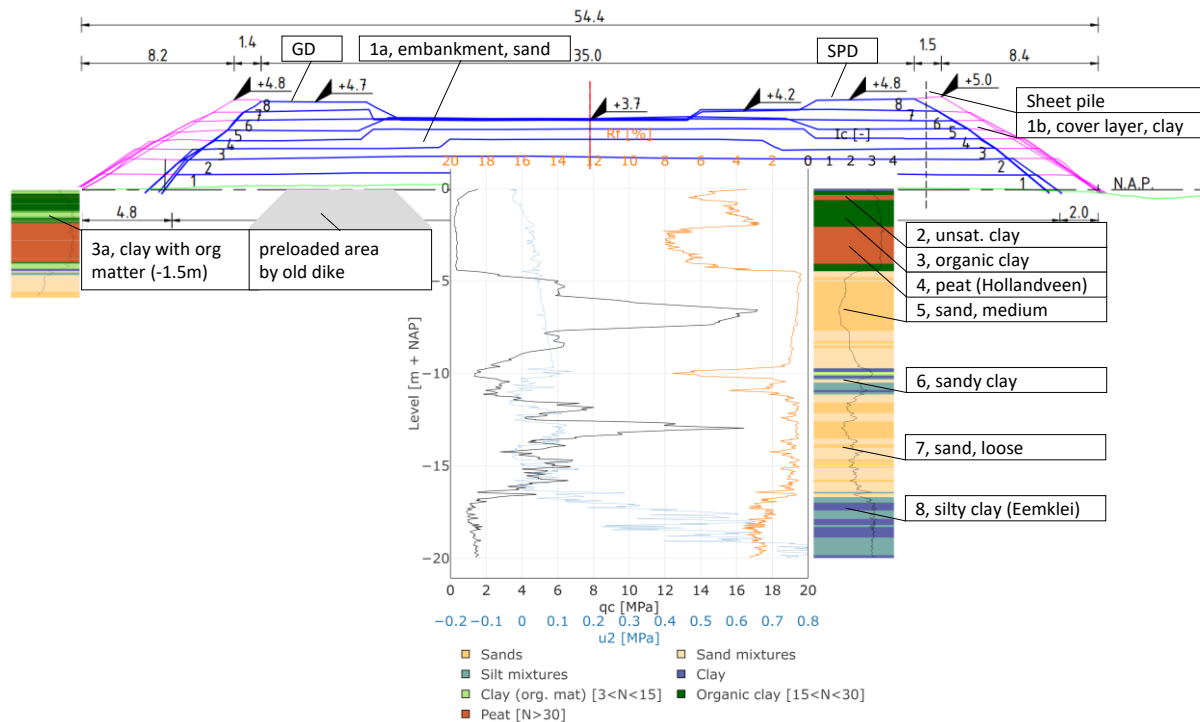*Figure 4.7 Cross section of first eight construction phases, ground dike on left side, sheet pile reinforce dike on right side*

4.2.4   Construction monitoring results

This section presents the main monitoring deformations which are relevant to validate the numerical models as well as defining the starting conditions for the GD-test and SPD-test. The

monitoring and observational method made it possible to construct the dike within the planned period (half a year). Furthermore, the design was based on a low stability factor (<1.1) under normal conditions, because a very stable dike would be very hard to bring to failure, in particular when it is reinforced with a sheet pile. Functional dikes generally have a higher stability under daily conditions, but under design conditions the stability needs to comply with the resistance factor (In Dutch: 'schadefactor') in the range of 1 to 1.5, depending on the target reliability.

Figure 4.8 presents the cross section of the GD and SPD with average initial settlement directly after fill stage #1 and after stage #8. The initial settlements are caused by shear deformations , unsaturated behavior and installation / seating effects of the instruments. The corrected settlements on day 213 are typically 0.6 m to 0.8 m for the GD and 0.8 m to 1.0 m for the SPD. The difference between the settlement plates and cable is up to 0.2 m. Both dikes show increased settlements at the slopes due to shear deformations.

The horizontal displacements over the soft soil layer at the toe are measured by SAAF inclinometers. The results are presented in Figure 4.9. The direction of the deformations is outwards. The horizontal displacements start to develop directly above the sand layer 5, in the peat layer 4. The maximum deformation occurs at 2 m depth and is up to 0.4 m, which is similar for both dikes.

The vertical and horizontal displacements over time of both dikes are presented in Appendix I. The embankment and subsoil showed significant construction induced, vertical displacements up to 1.0 m and horizontal displacements up to 0.4 m without failure. These deformations occurred gradually over time and determine the initial geometry prior to the failure test. These construction induced deformations are considered representative for many existing dikes in the Netherlands which are often constructed on soft soils. The main difference however with existing dikes is the excess pore pressures. Dikes are present for many years such that most of the excess pore pressures have dissipated.
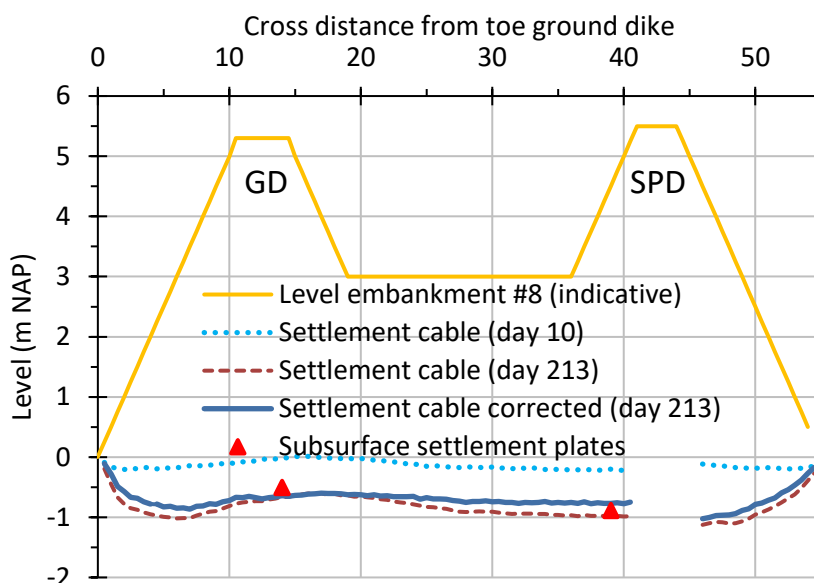
Figure 4.8 Settlements presented the cross section of the dikes after the 1st and 8th fill stage
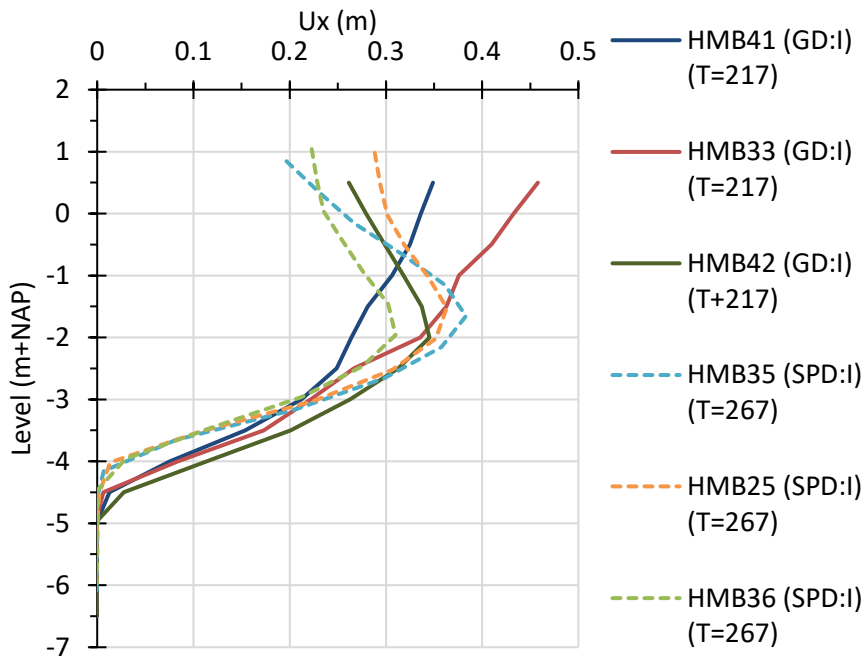
Figure 4.9 Ground dike and sheet pile dike, inclinometer measurements (HM..) of horizontal displacements over depth, at the toe (SAAF location I). The measured horizontal deformations start to develop directly above the sand layer in the peat layer. The deformations are similar for both dikes. The two larger displacements near surface at the GD are related to the presence of soft clay layer 3a.

The measurements of pore pressure at the toe and crest is presented in Appendix I, Figure 4.48 and Figure 4.49. The measured pore pressures are similar at the toe, but different below the crests of the dikes. The difference below the crest for both dikes is caused by the pre-loading of a historic dike at the GD crest. The measurement of the pore pressures below the embankment are of importance for two reasons: Firstly, as primary information for the observational method to prevent premature failure during construction. Secondly, the pore pressures determine the effective stress, soil state and undrained shear strength prior to the failure test.

4.3 Geotechnical conditions

4.3.1 Introduction

This section presents the geotechnical investigations and the parameter determination for the numerical models used to back-calculate the experiment. All tests are carefully examined as well as the procedures to determine the parameters. This is an essential step for the back analysis of the Eemdijk tests. The challenges encountered with the interpretation of the Eemdijk tests, in particular the complex and deviating soil behavior, are also recognized at other sites in the Netherlands.

The aim is to derive best estimate and upper bound parameters for the back-analysis, but also to improve the criteria to derive the ultimate strength parameters and to improve the procedures to determine constitutive model parameters. The proposed methods can be applied in general to dike engineering projects. Furthermore, the Eemdijk site is be used to validate the CPT-based classification and correlations and to validate the CSR-model.

4.3.2 Stratification

This section summarizes the geotechnical investigations at the Eemdijk test site. Figure 4.10 shows a plan view of the site investigation, comprising of 48 CPTs and 18 boreholes with sampling. The embankment consists of two long sections, the SW side is the ground dike (GD). The NE side is the sheet pile reinforced dike (SPD). The performed Deltares Large Diameter Samples (DLDS) are outside the scope of this research.

Most CPTs and boreholes are performed as pairs and most of the CPTs are ISO class 1 (ISO22476-1 2012), except the deeper CPTs. In addition, 6 CPTs are performed during and after the construction of the test embankment. The stratification is based on the CPT interpretation and borehole log description. Table 4-3 presents the generalized stratification for each side, with the GD at left side and the SPD the right side. The variation in level of the layer boundaries is typically +/-20 cm for each investigation point.
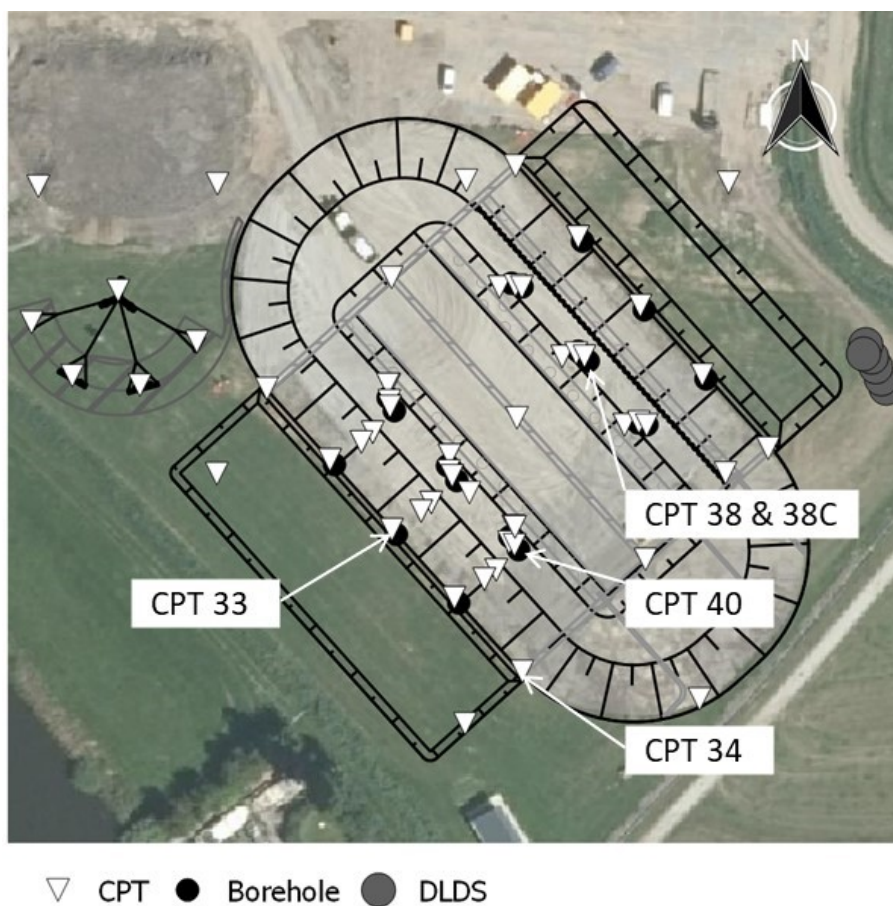
Figure 4.10 Plan view site investigations with indication of five illustrative CPTs

Table 4-3 Stratification at Eemdijk site, levels refer to top of layer

Layer	Level GD (m NAP)	Level SPD (m NAP)	Lithology	Geology
1a	5.3	5.5	Sand fill	Anthropogenic
1b	5.3	5.5	Clay cover	
2	0.0	0.0	Clay, unsaturated	Holocene, Naaldwijk Formation, Walcheren Member
3	-0.8	-0.6	Organic Clay	
3a	-1.5		Soft Clay with organic matter	
4	-2.0	-1.7	Peat (Basisveen)	Holocene, Nieuwkoop Formation, Hollandveen Bed.
5	-4.3	-4.1	Sand, medium dense	Middle Pleistocene-Holocene, Boxtel Formation, Wierden Member
6	-9.5	-9.5	Sandy Clay	
7	-11.0	-11.0	Silty Sand, medium dense	Pleistocene, Eem Member
8	-17.0	-17.0	Silty Clay (Eemklei)	

Although the site is homogeneous, there are two important deviations identified at the ground dike:

- The presence of a soft clay layer over the length of about 30 m at the toe of the ground dike.
- The area below the crest of the GD is preloaded by an older dike along the river Eem. This is still visible in the topographic map of Figure 4.3.

These deviations are confirmed by various measurements. In the back-analysis this has been considered by an additional layer (3a) at the toe of the ground dike and a preloading at the crest of the ground dike.

Figure 4.11 presents four CPTs to illustrate these aspects. CPT LKMP38 is located at below the crest of the SPD and can be considered as representative for the site. In CPT LKMP33, located at the toe of the ground dike, it is shown that a soft layer is present between -1.5 and -2.0 m NAP depth, identified in the CPTs by a lower cone resistance (0.1 MPa) and lower friction ratio (2%). In CPT LKMP40, located at the crest of the ground dike, the preloading by the old dike can be identified by a higher cone resistance (0.5 MPa). In addition, the CPT LKMP38C is presented, which is performed after construction of the test embankment prior to failure. This CPT shows that the layers are compressed by the embankment, starting 1 m deeper at -1 m NAP. Furthermore, the cone resistance is increased to 0.5 MPa and higher from -1 m to -4 m NAP (CPT LKMP38C).
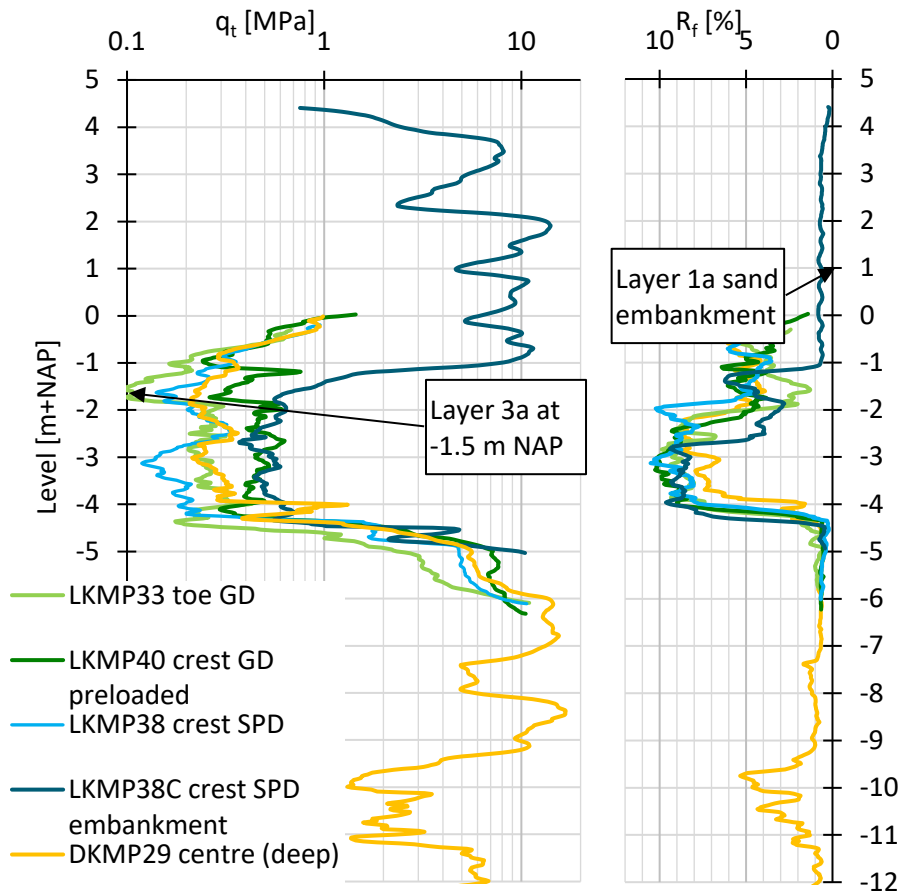
Figure 4.11 Four representative CPTs at the Eemdijk test embankment

4.3.3 Laboratory tests results

4.3.3.1 Classification tests

An extensive laboratory test programme was undertaken comprising classification tests, compression tests (K0CRS), anisotropic consolidated undrained Triaxial tests (CAUC) and Direct simple shear tests (DSS). The tests were initially performed for the most relevant layers 3 and 4. After completing the investigations, soft clay layer 3a has been identified and where possible parameters are also determined for this layer. Limited tests have been performed on the other layers as these are less relevant.

The results of the classification tests on layer 3, 3a and 4 are shown in Table 4-4. Layer 4 is a peat layer. Layer 3 is an organic clay layer, identified by the high organic content (N=20). Layer 3a is a soft clay layer with organic content (N=12). The comparison with the newly developed CPT-based classification and correlations of Chapter 2 is presented in Appendix G.

Table 4-4 Classification properties cohesive layers

Layer	γ_{unsat} (kN/m³)	γ_{sat} (kN/m³)	γ_{dry} (kN/m³)	w (%)	e_o (-)	G_s (-)	N (%)
3	13.0	13.1	5.9	122	2.7	2.23	20
3a	12.6	12.7	5.0	154	4.0	2.45	12
4	9.4	10.3	1.4	663	10.2	1.50	86

4.3.3.2 Oedometer tests

This section presents the results and parameter determination of the K_0CRS compression tests. The test results, average values and in some cases the coefficient of variation (VC), of layers 3 and 4 are shown in Table 4-5 and Table 4-6. Unfortunately, no tests are available for layer 3a.

Table 4-5 K_0CRS compression parameters

Layer	# Tests	CR (-)	RR_1 (-)	RR_2 (-)	RR/CR (-)	Cα (-)	Cα/CR (-)
3	7.0	0.272	0.028	0.048	0.14	0.018	0.07
4	5.0	0.514	0.076	0.081	0.15	0.054	0.11

The RR_1 is based on an unloading ratio of 2 and RR_2 on an unloading ratio of about 10. Starting point for the parameter determination is the average of these two. The compression to recompression ratio is within the expected range [5, 15], the compression to creep ratio for the peat layer is relatively low compared to the expected range [10, 30].

Table 4-6 K_0CRS permeability and earth pressure parameters

Layer	k_v at e_0 (m/d)	C_k (-)	K_{nc} (-)	v_{ur} (-)
3	8.06E-04	0.61	0.32	0.19
4	1.59E-03	3.04	0.15	0.10

Where C_k is the strain dependent permeability coefficient normalized by the void ratio.

The Peat layer is more permeable than the clay layer at in-situ conditions (e_0 taken from Table 4-4), however the decrease of permeability with compression is higher for the peat layer. The K_0 measurements indicate for both layers a low normally consolidated earth pressure ratio (K_{nc}) and low unloading Poisson's ratio (v_{ur}), in particular for the Peat layer. These values measured in the K_0CRS test are regarded as indicative. The preconsolidation stresses for layer 3, 3a and 4 are presented in Table 4-10 and Table 4-11.

4.3.3.3 DSS tests

This section presents the results of the DSS tests and parameter determination for layer 3, 3a and 4. The stress paths for layer 3 is presented in Figure 4.12. A complete overview for all layers with tables and figures of test results is presented in Appendix F, including a comparison with the numerical simulations for various constitutive soil models.

Global stability should be verified with the critical state strength properties of soil according to Dutch guidelines. In practice the 40% shear strain ultimate value is used. From the DSS Figure 4.12 it can be concluded that the NC samples show contractive behavior, and the OC samples show a slightly dilative response. The peak strength is reached between 25% and 40% shear strain and the amount of softening is marginal.

The normally consolidated S-ratio and effective friction angle are determined from the NC samples by Ordinary Least Squares (OLS) regression through the origin, in line with the model application (no cohesion). The S-ratio follows from the ultimate shear stress and vertical

consolidation stress. The effective friction angle follows from the ultimate shear stress and ultimate normal stress. These strength parameters are used in critical state based models.

The definition of the friction angle is presented in Eq.(2-5) and Eq.(2-6). Multiple definitions exist, as the boundary conditions for DSS tests are not exactly known. However, the selected definition provides consistent results with numerical simulations (Lengkeek and Bouw 2011).

The exact preconsolidation stress is not known for each sample, as the samples are not preloaded by the SHANSEP procedure. As an alternative, the preconsolidation stress is back calculated for each sample using the average S-ratio and the exponent-m. The strength hardening exponent m can be estimated from the CR and RR parameters, see Eq.(3-52), and is in the range of 0.72 to 0.93, on average 0.86. It should be noted that RR and exponent-m depend on the extent of unloading. The SHANSEP failure envelope of the organic clay layer 3 is presented in Figure 4.19.

The alternative Mohr-Coulomb effective strength parameters (ϕ'_{mc} and c'_{mc}) are determined from NC and OC samples, by OLS regression with free intercept. These strength parameters are also based on the ultimate strength at 40% strain and can used for the back-analysis with non-critical state models.

The DSS tests show almost no softening, both the NC and OC samples, and the strain at peak strength is sometimes not even reached at 40% shear strain. The strain at peak strength is typically 25% for soft clay layer 3a, 30% for organic clay layer 3 and 35% for peat layer 4.
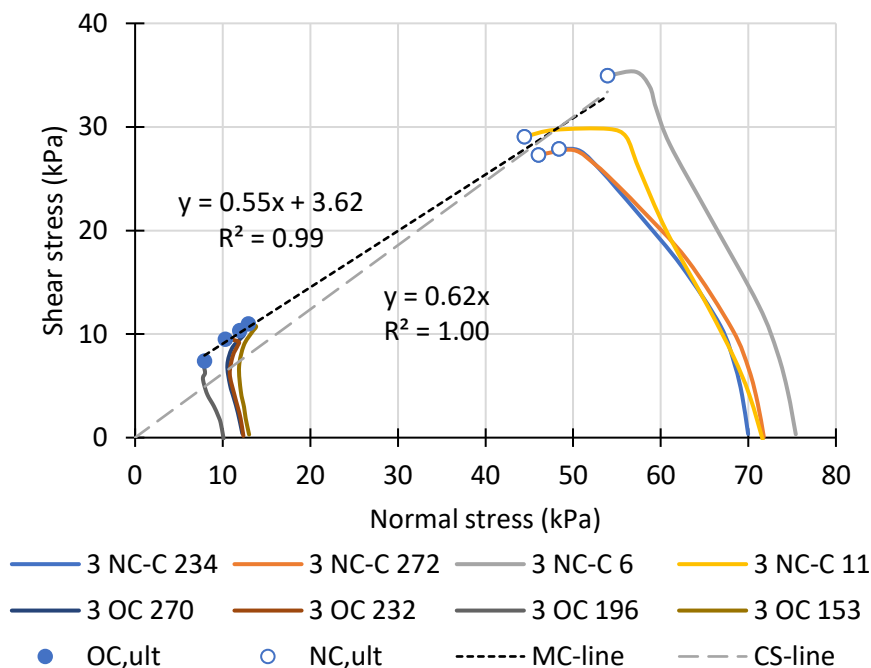
Figure 4.12 DSS results organic clay layer 3: shear stress versus normal stress

The resulting parameters for layer 3, 3a and 4 are presented in Table 4-7. The friction angle at the peak undrained shear strength is slightly lower than at 40% strain and generally shows more variation. The ultimate friction angle for organic clay layer 3 is typically 38°, and 43° for peat layer 4. This is significantly higher than for mineral clays. The S-ratio for organic clay layer 3 is typically 0.42, and 0.49 for peat layer 4. This is also significantly higher than for mineral clays.

The S-ratio for the soft clay layer (3a) is 0.33, which is more in line with mineral soils and relatively low compared to the other layers present at the site. The coefficient of variation for the friction angle is 6%, for the S-ratio 9% and for the cohesion 39%. The maximum of the peak and ultimate value is used as upper bound value for the back-analysis.

The alternative Mohr-Coulomb effective strength parameters, also based on 40% shear strain, still show an effective cohesion intercept of about 4 kPa for the clay layers. The cohesion for the peat layer is significantly higher. Such high values should be verified by numerical simulations before applying in non-critical state constitutive models.

Table 4-7 DSS results layer 3, 3a and 4: summary of strength parameters

Layer	Strength criterion	$\sin(\phi')$ (-)	ϕ' (°)	$S=[s_u/\sigma'_{vy}]$ (-)	$\sin(\phi'_{mc})$ (-)	ϕ'_{mc} (°)	c'_{mc} (kPa)
3	peak	0.58	35.6	0.42	0.51	30.4	4.6
3	ultimate	0.62	38.3	0.41	0.55	34.4	4.1
3a	peak	0.61	37.6	0.33	0.55	33.4	2.5
3a	ultimate	0.62	38.3	0.33	0.55	33.5	3.1
4	peak	0.68	42.7	0.50	0.49	29.1	11.4
4	ultimate	0.68	43.2	0.49	0.52	31.1	9.9

4.3.3.4 CAUC tests

This section presents the results of the CAUC tests and parameter determination for layer 3 and 3a. There are no CAUC test performed on the peat layer 4. In total 3 NC tests and 6 OC (at in-situ stress) CAUC tests haven been performed. The test conditions are presented in the tables of Appendix F. Two of these tests are performed on the sublayer 3a. There are too little tests on this layer, hence the parameter set will be partly based on layer 3. The stress paths for layer 3 and 3a are presented in Figure 4.13. A complete overview for all layers with tables and figures of test results is presented in Appendix F, including a comparison with the numerical simulations for various constitutive models.

The strength parameters (M_c and ϕ') follow from the p'-q-chart, using all tests. The S-ratio follows from the shear stress versus consolidation stress, based on NC samples only. The determination is based on OLS regression through the origin without intercept, in line with the model application (no cohesion). The strain at peak strength depends to a large extent on the stress path. Normally consolidated samples with contractive behavior typically reach the peak strength at 5% strain whereas overconsolidated samples reach the peak strength at much higher strain levels, sometimes beyond 25% strain.

Global stability should be verified with the critical state strength properties of soil according to Dutch guidelines. In practice the 25% axial strain ultimate value is used. Internationally the 15% axial strain value seems more common. The consequences of the strain level are discussed in this section.

The advantage of CAUC tests is that all stress components are measured, whereas in the DSS this is not the case. The selection of the ultimate strength for CAUC tests however is more complicated than for DSS tests. This is related to the applied corrections and large variation in

stress paths. CAUC tests require membrane and filter corrections. For these tests this implies that the deviator stress is reduced by approximately 2 kPa, which is still relevant for low strengths of typically 10 kPa at in-situ stress levels.
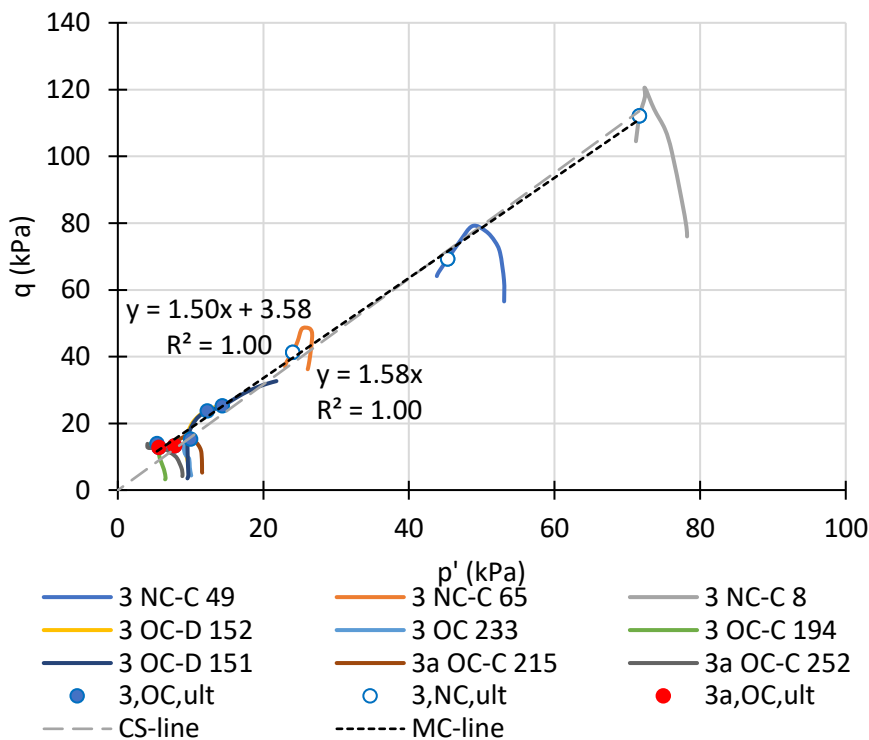

Figure 4.13 CAUC results organic clay layer 3: deviator stress verses isotropic stress

Furthermore, a geometrical correction is normally applied, related to the average cross section area as a function of the vertical strain. There are two methods defined in Head (1998) to calculate the geometrical correction (area correction). The first method is called the 'barreling' correction. In an undrained test it is assumed that the volume remains unaltered. This method accounts for the increasing area with increasing axial strain. It is assumed that the increase in area results in a decrease of stress compared to the original area and diameter. This method has been applied to the samples of Eemdijk by the laboratory to all samples, apparently as default method. The second method is called the 'slip plane' correction. When failure occurs along an inclined plane, the effective overlapping area of the elliptical surfaces decreases with increasing strain. It is assumed that the decrease in area results in a increase of stress. The correction is in fact opposite of the 'barreling' correction and correction is more significant, up to a factor 2.5 for 25% strain, although in Head (1998) a lower value is recommended, up to a factor 1.5.

The photo's of the Eemdijk CAUC test samples show in most cases a combination of both failure mechanisms, sometimes more 'barreling' and sometime more 'slip plane'. The difficulty with applying these corrections is that the 'barreling' correction should start from the initial strain, whereas the 'slip plane' correction should start from the point the slip begins. In practice, this point is difficult to observe and mostly not reported. When both corrections are applied, the 'slip plane' correction will largely compensate for the 'barreling' correction.

Moreover, it is questionable whether the CAUC test should be interpreted based on large strains and updated geometry and stresses, whereas the numerical simulations are not performed with

a large strain analysis. Besides, the vertical stress correction is based on the change in area, but does not account for eccentricity, stress rotation and accompanying radial and tangential stresses. Therefore, it is decided to perform two CAUC interpretations for this research, one with the default geometrical correction by the laboratory ('barreling'), and one without any geometrical correction.

Figure 4.14 shows a comparison for three samples with and without geometrical correction. The effect of the geometrical correction on the undrained shear strength and S-ratio is significant, whereas the friction angle is affected to a lesser extent.

The best estimate strength parameters for the back-analysis of the Eemdijk test are based on the average ultimate value including geometrical correction. The upper bound strength parameters for the back-analysis of the Eemdijk test are based on the peak strength without geometrical correction, while maintaining the default membrane and filter corrections.

The definition of the peak undrained shear strength depend on the stress path. For NC contractive behavior the peak strength is selected at $[q_{peak}]$, whereas for OC dilative behavior the peak strength is selected at the maximum obliquity stress ratio $[\sigma'_1/\sigma'_3]_{max}$.
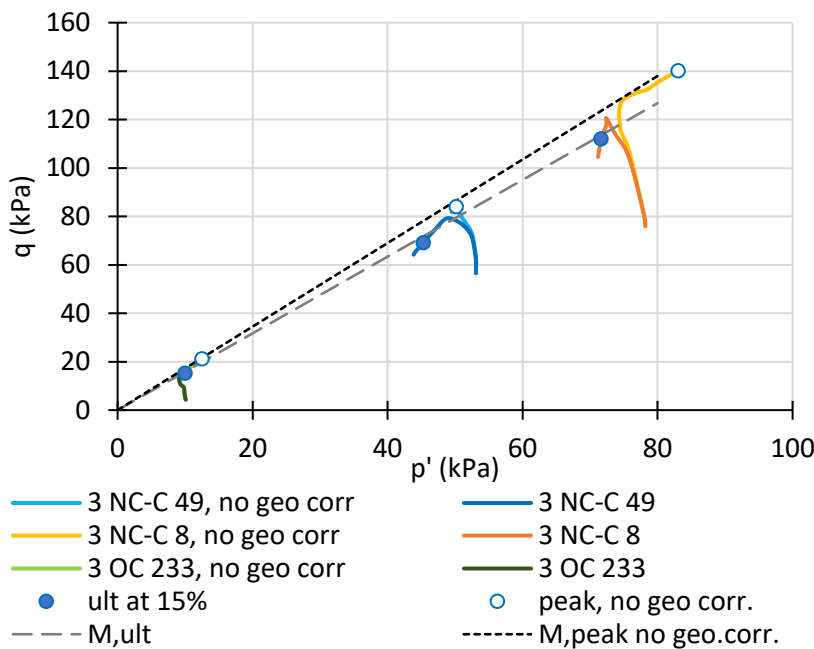
Figure 4.14 CAUC results organic clay layer 3: comparison of stress paths for three samples with and without geometrical correction

The resulting parameters for layer 3 are presented in Table 4-8. Both the ultimate critical state parameters without cohesion, as the Mohr-Coulomb ultimate strength parameters with cohesion are presented. The upper bound friction angle, defined at the peak undrained shear strength without geometrical correction, is 42°. The ultimate friction angle for the organic clay is typically 39°, similar as the DSS value. The S-ratio for organic clay is typically 0.42, similar as the DSS value. The coefficient of variation for the critical state friction angle is 23%, for the S-ratio 6% and for the cohesion 63%.

The Mohr-Coulomb effective strength parameters are also based on 15% strain and still show an effective cohesion intercept of about 2 kPa. The upper bound effective strength parameters are

about 5 to 10% higher, mainly caused by applying the peak strength criterion. The upper bound undrained shear strength parameters are 20 to 25% higher, mainly caused by ignoring the geometrical correction.

Table 4-8 CAUC results organic clay layer 3: strength parameters

Strength criterion	M_c (-)	$\sin(\phi')$ (-)	ϕ' (°)	$S=[s_u/\sigma'_{vy}]$ (-)	$\sin(\phi'_{mc})$ (-)	ϕ'_{mc} (°)	c'_{mc} (kPa)
peak & without geometrical correction	1.72	0.67	42.0	0.52	0.63	39.2	2.9
ultimate	1.58	0.63	38.8	0.42	0.60	36.9	1.7

The strength parameters could not be determined for soft clay layer 3a due to the limited number of tests.

4.3.3.5 Criteria ultimate strength CAUC test

The ultimate value is determined beyond the peak strength. Defining the ultimate strength at 25% axial strain has two disadvantages. Some NC samples show significant softening during, even when the pore pressures are stabilized, resulting in a low undrained shear strength and S-ratio. On the other hand, some OC samples show significant hardening, even with negative excess pore pressures, resulting in a high undrained shear strength and S-ratio . Both extremes are frequently observed in the 2021 database of dike projects the Netherlands.

Examination of the CAUC test of clay layer 3 indicates that 3 out of 9 tests show significant deviating stress paths. These 3 tests have a significant effect on the parameter determination, resulting in unrealistic outcome and large variation. After careful evaluation of the tests, it is proposed to define the default ultimate strength for a CAUC test at 15% axial strain value, more in line with international practice, with additional requirements. The proposed primary and secondary criteria for the ultimate strength selection are presented in Table 4-9. The additional criteria are elaborated with help of Figure 4.15.

Sample 194 and 252 (Figure 4.15) are consolidated at in-situ stress and show contractive behavior ending up in zero horizontal effective stresses. For such contractive stress paths it is proposed to select the strength before the tension cut-off line is reached [$\sigma'_3 > 0$] and the minor effective stress becomes zero.

Sample 151 (Figure 4.15) is also consolidated at in-situ stress level and shows significant dilative behavior with continuous hardening along the M-line resulting in negative excess pore pressures. For such dilative stress paths it is proposed to select the strength before the zero excess pore pressure line is reached [$\Delta u > 0$] and the excess pore pressures become negative.

Normally in engineering these will be regarded as outliers. For this research it was decided to include them. Applying the criteria of Table 4-9 to sample 151, 194 and 225 results in a selected ultimate strain level of 5%, lower than the recommend strain level of 15%.

Sample 65 (Figure 4.15) is normally consolidated and shows contractive behavior. The stress path is added for comparison with OC samples. The ultimate value is selected at 15% axial strain, in line with the proposed first criterion.

Table 4-9 Recommended criteria for ultimate strength parameter selection

Criteria	Primary (default)	Secondary
Stress path	**Axial strain level**	**Maximum strain level**
Contractive behavior at failure (NC samples)	15%	$\sigma'_3 > 0$ before the TCO-line is reached
Dilative behavior at failure (OC samples)	15%	$\Delta u > 0$ before the zero excess pore pressure line is reached
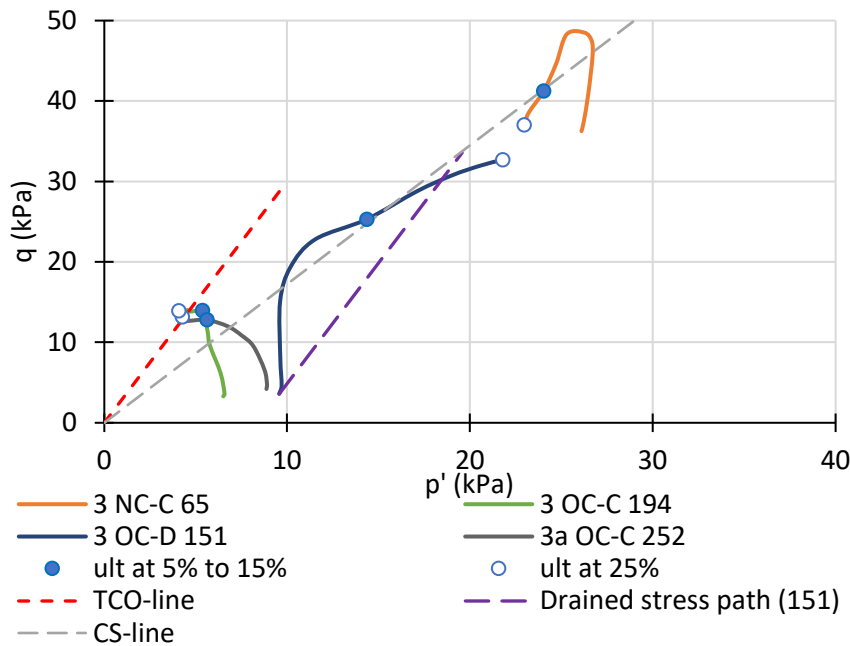
Figure 4.15 CAUC results organic clay layer 3: examples of strongly deviating stress paths of three samples, sample 194 and 252 contract till the tension cut-off line is reached and sample 151 dilates until negative pore pressures occur one passing the drained stress path.

The new proposed criteria result for the Eemdijk layers in more realistic strength parameters, both drained and undrained, with less variation. It is recommended to use the criteria Table 4-9 in dike engineering practice in the Netherlands.

4.3.4   Parameter selection

4.3.4.1   *Preconsolidation stress K_0CRS with DSS and CAUC test*

The preconsolidation stresses for layer 3, 3a and 4 are presented in Table 4-10, with an indication of the borehole number and the location within the embankment. The locations are added to identify the preloaded area at the crest of the ground dike by an older dike. The OED test results are directly determined from the K_0CRS tests. The DSS and CAUC test results are indirectly determined based on the strength parameters and the SHANSEP formulation. The variation in preconsolidation stress obtained from samples of different boreholes is 5 to 10 kPa. The same variation is found between the OED, DSS and CAUC tests. The preconsolidation stress of sublayer 3a is clearly lower than the other two layers. It is concluded that the SHANSEP determination of the preconsolidation stress matches reasonably well with the direct determination from the CRS

tests. It should be noted that a difference of 10 kPa in preconsolidation stress gives a significant difference in OCR for low effective stresses.

Table 4-10 Comparison preconsolidation stress in kPa per test, borehole and layer

Location	Section	North West			Middle			South East		
	Layer	OED	DSS	CAUC	OED	DSS	CAUC	OED	DSS	CAUC
toe SPD			BH35			BH25			BH36	
	3		25	19	31				28	
	4					31				
crest SPD			BH37			BH27			BH38	
	3	26			23				30	
	4	25			18			21		
crest GD			BH39			BH31			BH40	
	3	32			39			30		34
	4		47		36	49		41	40	
toe GD			BH41			BH33			BH42	
	3			19						
	3a		20			20	16		20	16
	4									

The preconsolidation stress below the crest of the ground dike is clearly higher than at the other locations. This is relevant for the back-analysis of the settlements. For the stability it is not relevant as the stresses below the new embankment will exceed the preconsolidation stresses. The resulting preconsolidation for the Eemdijk failure test back-analysis is presented in Table 4-11. The coefficient of variation for the preconsolidation stress and OCR of layer 3 is about 18% and 35% for the POP.

Table 4-11 Resume preconsolidation parameters

Layer	Location	Mean/max	σ'_v (kPa)	σ'_{vv} (kPa)	POP (kPa)	OCR (-)
3	GD+SPD	mean	12	25	13	2.1
3	GD+SPD	max	12	31	19	2.6
3a	GD+SPD	mean	12	19	7	1.5
4	GD+SPD	mean	12	24	12	2.0
3	crest GD	mean	12	34	22	2.8
4	crest GD	mean	12	43	31	3.6

4.3.4.2   Strength parameters

The DSS strength parameters, as presented in Table 4-7, are determined for all relevant layers (3, 3a and 4). These will be used as basis for the Eemdijk validation. On the organic clay layer 3a complete series of DSS and CAUC tests are performed. This is unique, as Dutch guidelines prescribe DSS tests for peat and CAUC tests for clay. From the comparison it can be concluded that the ultimate strength parameters of the DSS and CAUC tests are very similar. The upper

bound CAUC effective strength parameters are about 5 to 10% higher, mainly caused by applying the peak strength criteria. The upper bound CAUC undrained shear strength parameters are 20 to 25% higher, mainly caused by ignoring the geometrical correction. This is relevant for the back-analysis of the Eemdijk test and these ratio's can be used in anisotropic constitutive soil models that include a stress path dependent shear strength. Table 4-12 summarizes the average strength parameters and ratios for the organic clay layer (3).

Table 4-12 Organic clay layer 3: resume strength parameters based on DSS and CAUC tests

	Criterion	$\sin(\phi')$ (-)	ϕ' (°)	$S=[s_u/\sigma'_{vy}]$ (-)	$\sin(\phi'_{mc})$ (-)	ϕ'_{mc} (°)	c'_{mc} (kPa)
average DSS & CAUC	ultimate	0.62	38.5	0.42	0.58	35.7	2.9
ratio DSS/CAUC (-)	*ultimate*	*0.98*	*0.99*	*0.99*	*0.92*	*0.93*	*2.41*
ratio DSS/CAUC (-)	*peak & without geometrical correction*	*0.87*	*0.85*	*0.81*	*0.81*	*0.78*	*1.59*

4.3.4.3   Equivalent MC strength parameters

The Mohr-Coulomb strength parameters are presented in the previous sections. Applying these effective strength parameters in an advanced non-critical state constitutive model (such as the Hardening Soil model, see next section) will not automatically provide the same undrained shear strength as from the laboratory tests. An advanced model accounts for elastoplastic behavior in undrained deviatoric loading prior to failure, which affects the effective stress path and the resulting undrained shear strength. In the NC range the actual strength depends also on various model parameters. Finally, at low stresses it may depends on the application of the tension-cut-off criterion. Applying this criterion will prevent tension stresses and at the same time increases the undrained shear strength as the stress path follows the tension-cut-off line until the Mohr-Coulomb failure line. The procedure to determine the equivalent MC strength parameters is shown in Appendix E.

This procedure results in the equivalent MC strength parameters as presented in Table 4-13. The values for the cohesion are slightly higher than directly determined, except for peat which is significantly lower. The equation for the maximum cohesion corresponding to the in-situ undrained shear strength is shown in Eq.(4-1). The values for the friction angle can change significantly. For soft clay layer 3a, which develops more excess pore pressures upon shearing, the equivalent friction angle is lower, while for organic clay 3 and peat layer 4 it is higher. The selected friction angle is limited to 45 degrees as upper limit.

$$c'_{max} = \frac{s_u(1 - \sin\phi')}{\cos\phi'} \qquad\qquad (4\text{-}1)$$

Table 4-13 Resume equivalent ultimate MC-strength parameters for all layers to approximate the SHANSEP undrained shear strength (based on HS-model, see Figure 4.19)

layer	criterion	test	sin(ϕ') (-)	ϕ'_{mc} (°)	c'_{mc} (kPa)
3	ultimate	DSS & CAUC	0.62	38.5	4.0
3	peak & without geometrical correction	CAUC	0.71	45.0	6.0
3a	ultimate	DSS	0.50	30.0	2.0
4	ultimate	DSS	0.71	45.0	5.0

4.3.4.4 Plaxis constitutive soil model parameters

This section presents the model parameter determination for various constitutive soil models available in Plaxis[10]. Plaxis is a finite element program, developed for the analysis of deformation, stability and groundwater flow in geotechnical engineering. This software package is frequently used in geotechnical engineering and is used in this research for the back-analysis of the Eemdijk full-scale tests. Parameters are determined for the following constitutive soil models:

Table 4-14 Overview considered constitutive soil models Plaxis.

Abbreviation	Constitutive soil model
MC	Linear Elastic Perfectly Plastic model (Mohr-Coulomb model)
SS	Soft Soil model
SSC	Soft Soil Creep model
HS	Hardening Soil model
HSS	Hardening Soil model with small-strain stiffness
MCC	Modified Cam-Clay model
SHANSEP	SHANSEP NGI-ADP model
CSC1S	Creep-SCLAY1S model

The ultimate strength parameters without cohesion are used in critical state based models, such as the MCC model, the CSC1S model (Sivasithamparam et al. 2015; Laera et al. 2018) and both the NGI-ADP and SHANSEP NGI-ADP model (Grimstad et al. 2012; Panagoulias and Brinkgreve 2017). The SHANSEP NGI-ADP model is a stress-path dependent undrained shear strength model with shear hardening in which shear strength is determined by the SHANSEP formulation. This model is currently used in dike engineering projects in the Netherlands. The Creep-SCLAY1S model is an anisotropic creep model with rotational hardening and de-structuration.

The MC-model, SS(C)-model and HS(S)-model are based on the equivalent Mohr-Coulomb strength which includes cohesion to approximate the undrained shear strength.

The procedure for the determination of the constitutive soil model parameters is schematically presented in Appendix E. The procedure is such that a minimum of input parameters is needed. The strength parameters are primarily based on the DSS or CAUC test. The stiffness parameters

---

[10] https://www.bentley.com/en/products/brands/plaxis

are primarily based on the K_0CRS test. The K_{nc} and Poisson's ratio are calculated automatically based on the equations in Chapter 3, developed for the CSR model.

Each constitutive model furthermore requires specific stress related corrections depending on the formulation of each constitutive model. For example, the stress-dependent stiffness can either be based on the minor, major or isotropic effective stress. In addition, the stress dependency differs for each model (e.g., power law or logarithmic stress-strain relation, see Plaxis Material Manual).

The advantage of the procedures in Appendix E is that only a few parameters are used to determine all required parameters for a constitutive model. This will result in a consistent parameter set. Another advantage of these procedures is that it allows for switching of constitutive model in staged construction, as the material model approximately result to the same stiffness and strength. This is relevant as in Dutch dike engineering protocols the initial stages are performed drained with SS(C) and HS(S) models, whereas the design verification with high water is performed undrained with the SHANSEP model.

Probabilistic analyses require many calculations, which includes extremes for all random variables. It is crucial that the parameter sets are consistent in the first place to prevent erroneous calculations. More important, it is better to select the correct random variables. The correct random variable are the underlain unique soil properties and state parameters, basically the same input parameters as used for the CSR-model. For example, the S-ratio (α) in the CSR-model and CSC1S model is related to the friction angle as well as the compression parameters. Model constants which are not related to these input parameters can be added as stochastic parameter, as well as parameters such as unit weight and permeability. The constitutive model parameters follow from consistent procedures and relations such as presented in Appendix E. In order to perform a probabilistic FEM analysis this would require preprocessing of the parameter set for every calculation. The additional advantage is that fewer well defined input parameters are used as random variables (stochastic parameters).

Certain parameters determined from laboratory tests cannot directly be used as input parameter. For example, the undrained elasticity modulus, here determined at 0.1% and 1% strain. Values at lower and higher strain levels show significant variation. These values can be seen as representative for the $E_{ur,undr}$ and $E_{50,undr}$, although a direct transformation is not possible. In Figure 4.16 the log value of the E-moduli is plotted versus the horizontal consolidation stress. The slope of the regression lines is typically 0.8. This value is used for the power of stress dependent stiffness (m) in the HS(S)-model for these Holocene layers.

Figure 4.17 presents an example of the K_0CRS stress strain curves for organic clay layer 3 compared with the analytical solution, for simulations by the SS (based on critical state strength), SSC and HS-model (based on MC strength parameters). This figure shows an excellent fit for all constitutive models considered. The numerical simulations have been performed with the Plaxis Soiltest facility. This is a single stress point constitutive driver in which stress and strain conditions can be stepwise applied on available constitutive models.
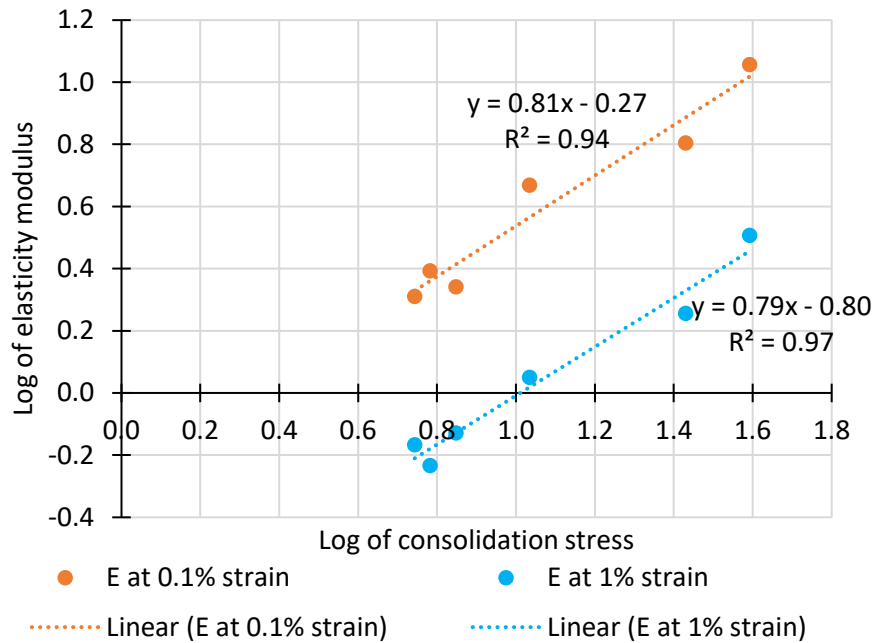
Figure 4.16 CAUC results organic clay layer 3: log of stiffness modulus (in MPa) versus log of horizontal consolidation stress. The slope of the line is an indication of the stress dependency
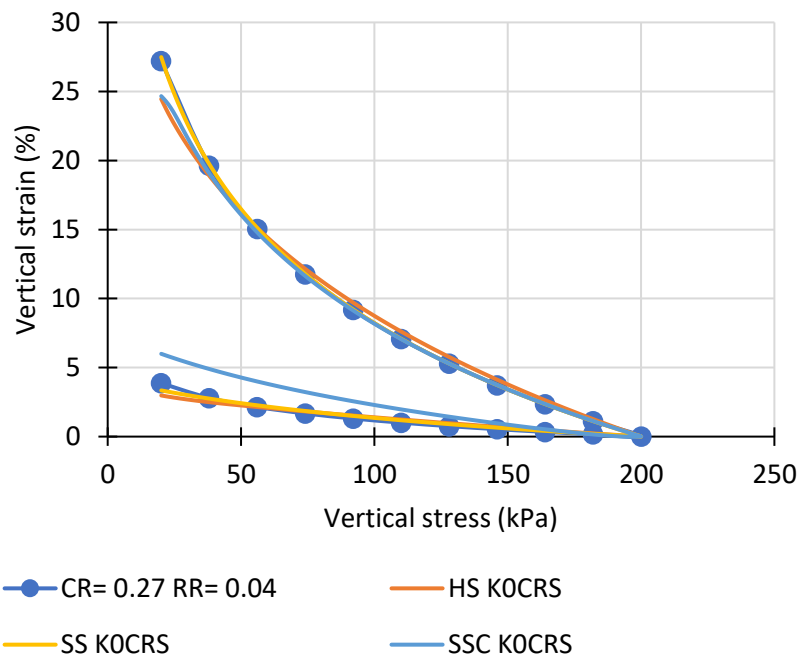

Figure 4.17 Organic clay layer 3: K0-CRS simulation, stress-strain curve

Figure 4.18 presents the results of numerical simulations for various constitutive soil models and the stress strain curve of a representative OC DSS test on organic clay layer 3. This figure shows an excellent fit for the SHANSEP model and good fit for the other models. The MCC model and SS(C)-model overestimate the stiffness upon shearing and reach failure at about 5% shear strain instead of 30%. The implemented version of the MCC model is based on a Drucker-Prager type (p', q) formulation of the critical state line in the deviatoric plane, where the deviatoric stress q is independent of the Lode's angle. This model shows an overprediction of the DSS strength as

99

the strength is defined for triaxial compression. Therefore, the simulation results of the MCC are not shown in Figure 4.18, but shown in Appendix F.

Figure 4.19 presents an example HS-model simulation versus the SHANSEP undrained shear strength 'envelope' for DSS tests on organic clay layer 3. This figure shows a good fit of the HS-model with the equivalent MC strength parameters. Similar fits can be obtained by the other non-critical state based models.

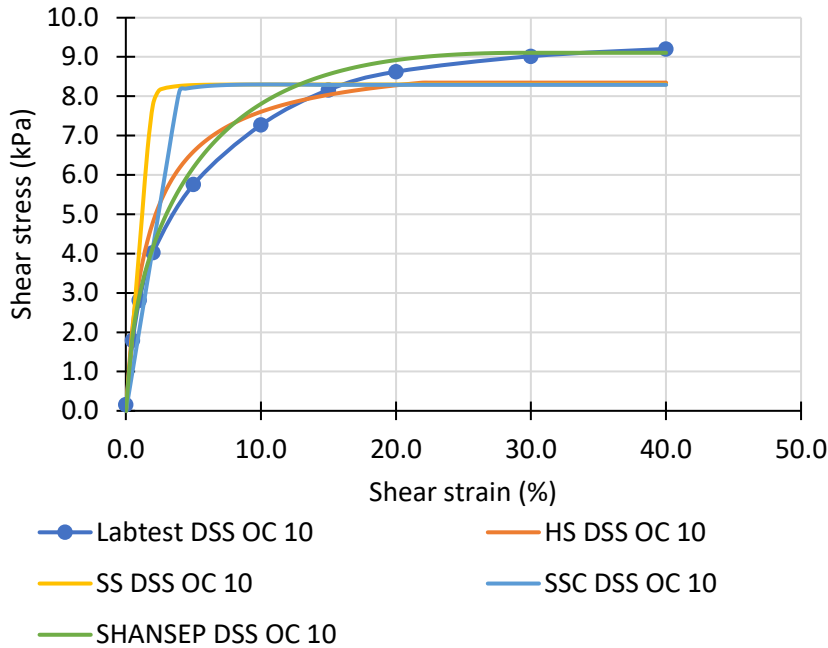*Figure 4.18 Organic clay layer 3: OC DSS test simulation (ultimate strength), stress-strain curve*
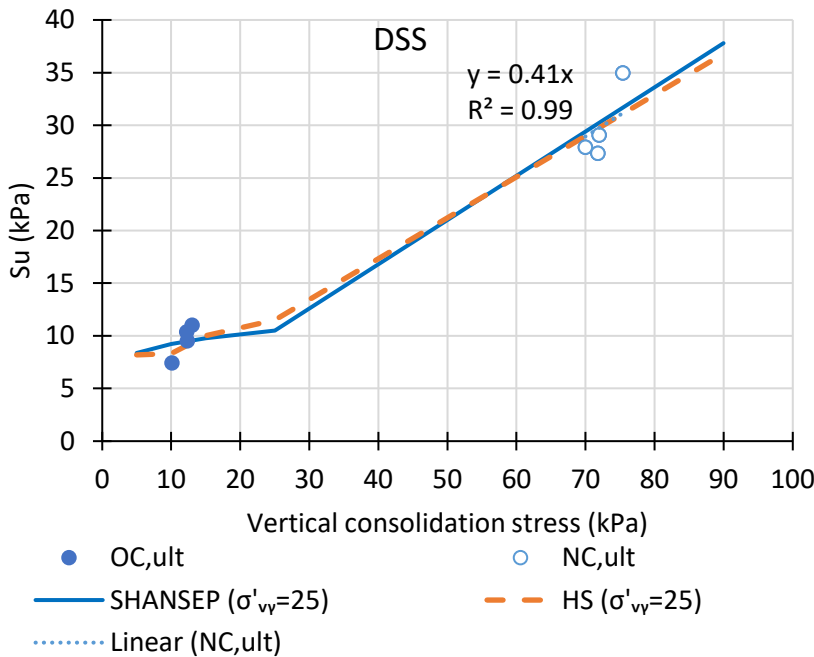

Figure 4.19 Organic clay layer 3: DSS simulation (ultimate strength), SHANSEP failure envelope

Figure 4.20 presents the results of the numerical simulations for various constitutive soil models and the stress strain curve of a representative NC CAUC test on organic clay layer 3. This figure

shows a good match of the ultimate strength at 15% strain. The peak strength and softening cannot be accounted for, although it appears that the SSC-model shows apparent softening due to creep relaxation. The duration is set to 1 day in all simulations, comparable with the laboratory tests. The fit for OC simulations is shown in Appendix F. All models underestimate the stiffness for NC CAUC simulations, they slightly overestimate the stiffness for OC CAUC simulations, and they match best for DSS simulations. These discrepancies are due to inherent model limitations and cannot be solved with any further parameter set optimizations.

A complete overview for all layers with tables and figures of test results is presented in Appendix F, including a comparison with the numerical simulations of various constitutive models. The main conclusion is that with one set of strength parameters the ultimate strength of DSS and CAUC can be matched, both in OC as NC state. The SHANSEP model performs best of all the considered models. The HS(S)-model and SS(C)-model all perform satisfactorily and are also suitable for the back-analysis. The strength results of the SSC-model are affected by the creep which generally results in 20% softening in the NC range and less than 10% in de OC range. The MCC model is less suitable for the back-analysis.

Furthermore, the response of the SSC model in a DSS and CAUC numerical simulation appears to be stiffer than by the SS-model and HS-model. To the author's experience, more realistic deformations can be obtained with the SSC model by multiplying the modified recompression index (κ^*), obtained from a K0CRS test, by approximately a factor 2 and dividing the modified creep index (μ^*), obtained from a K0CRS test, by approximately a factor 2. The exact factor depends on the situation, there is no theoretical basis for this correction.

To match both the CAUC and DSS strength with one parameter set, anisotropic strength models are required. For that reason, two additional simulations are performed, one with the CSC1S-model and one with the SHANSEP-model, the model version in which the undrained shear strength is based on the SHANSEP procedure. Figure 4.21 presents the numerical simulations and the stress strain curves of a representative NC and OC CAUC test on organic clay layer 3, with and without geometrical correction. The main determining parameter of the CSC1S-model to match the test results appears to be the α_0. A higher undrained shear strength for a NC CAUC test compared to a DSS test is achieved by a low value for α_0. The strength differentiation in the SHANSEP-model can simply be defined by strength ratios for Active (compression) loading, Direct simple shear and Passive (extension) loading (ADP). The ratio based on the CAUC and DSS tests is set to 1 : 0.8: 0.67.
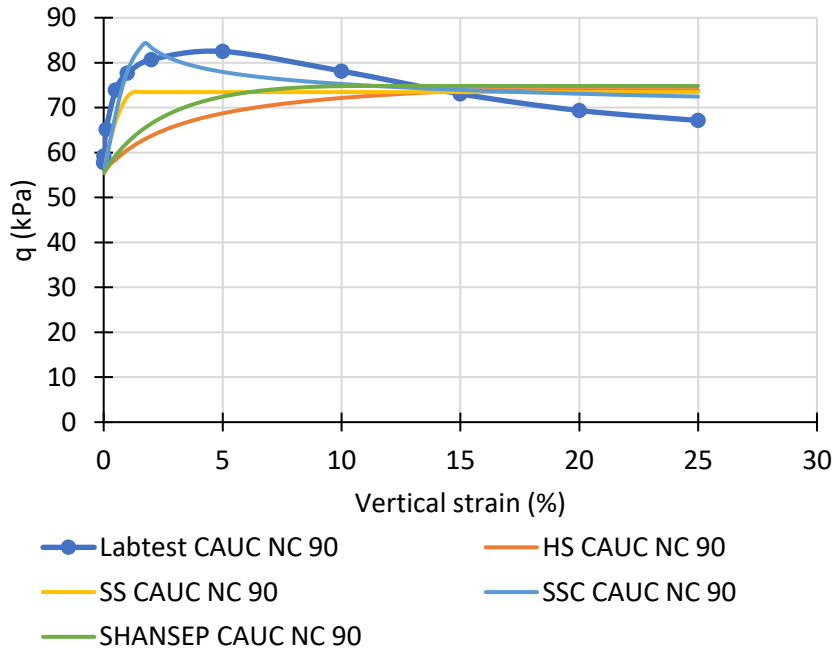
Figure 4.20 Organic clay layer 3: NC CAUC test simulation (ultimate strength), stress strain curve
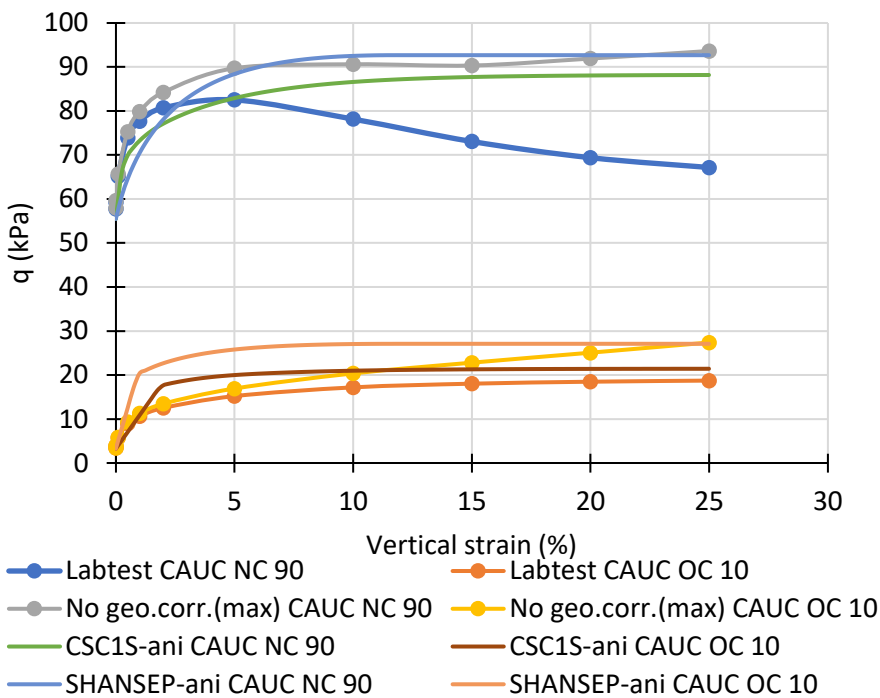
Figure 4.21 Organic clay layer 3: OC and NC CAUC with simulation anisotropic strength models, stress strain curve

4.3.4.5 Parameters other layers

For the parameters of the remaining layers reference is made to Breedeveld (2018). The strength parameters of the embankment sand layer 1a are based on the Triaxial test, shown in Table 4-15. The HS-model stiffness parameter $E_{50,ref}$ is selected as 40 MPa based on the CIDC tests and relative density obtained from CPT correlations. The overview with tables and figures of test results is presented in Appendix F, including an excellent fit for the HS-model. The same basis

will be used for sand layer 5, silty sand layer 7. The parameters of the other fine-grained layers are estimated in comparison with layer 3 and 4 combined with CPT correlations.

Table 4-15 Embankment sand layer 1: resume strength parameters based on CIDC tests

	Criterion	$\sin(\phi')$ (-)	ϕ' (°)	Criterion	$\sin(\phi'_{mc})$ (°)	ϕ'_{mc} (°)	c'_{mc} (kPa)	ψ (°)
Sand layer 1	ultimate	0.52	31.5	peak	0.58	35.5	2.9	9.4

4.3.5 Validation of CPT-based classification and correlations at Eemdijk

The new proposed changes to the SBT classification (Chapter 2) are validated for the Eemdijk site. The new classification is shown for CPT LMKP34 in Figure 4.7. Two comparisons are presented in Appendix G, with the figures shown side by side. From the comparisons it can be concluded that the new classification performs better, as it identifies the thin organic soft layer at the toe of the GD, whereas in the original classification it is classified as peat layer due to the low cone resistance, despite the low friction ratio. Overall, it can be concluded that new SBT classification, as introduced in Chapter 2, has proven to be successful for the Eemdijk test site in that the organic clay layers and peat layer are properly identified. This can be regarded as a validation of the new SBT classification. Additional validations at other locations have been performed but not reported here.

The Eemdijk laboratory tests results of layer 3, 3a and 4 as presented in this chapter are compared with the CPT results. The site-specific correlations, as shown by the regression line in the figures, are compared with regional correlations for the Netherlands. From the comparison it can be concluded that all correlations follow the same trend, and all results are within the 90% confidence interval as defined in Chapter 2. The Compression ratio and S-ratio comply well, the preconsolidation stress and in-situ undrained shear strength are lower by 30 to 50 %, but still within the 90% confidence interval as defined in Chapter 2.

Based on the comparison for Eemdijk it is concluded that certain site-specific correlations can be biased in trend for the correlations with intercept at the origin, or biased in offset for the correlations with free intercept. It is important to acknowledge these biases for each site and each correlation. Without prior knowledge of the site-specific conditions, it is recommended to select a value in between the 5% fractile value and the 5% probability of (no)-exceedance of the average from a regional correlation. The statistical approach for the selection of characteristic parameter is outside the scope of this thesis. For guidance on this topic reference is made to (Hicks et al. 2019; Calle et al. 2021; Lengkeek et al. 2021).

4.3.6 Validation of CSR model for Eemdijk organic clay

The CSR model parameters require the preconsolidation stress and CAUC tests results, assuming that the test conditions correspond to oedometric consolidation, which is often but not necessarily the case for embankments. The parameter determination following method B (Section 3.6) is described in Chapter 3. The results are presented in Appendix H.

The parameters of the CSR model have been determined based on effective strength parameters from the CAUC tests and result in similar values for the S-ratio (0.42) and exp-m (0.86) as the SHANSEP model parameters, directly determined from the undrained test results (Table 4-8). The value for CSR is 1.18, which means that at an OCR as low as 1.18 the undrained response is

neither contractive (NC) nor dilative (OC) and results in the same undrained shear strength as in an elastic perfectly plastic model.

With the MCC model this would occur at OCR ≈1.5, hence the undrained shear strength of the MCC model is significantly lower. To derive similar strength with MCC, the strength needs to be increased by about 15 % to Mc=1.82, corresponding to an equivalent friction angle of 44 degrees. This is shown by the numerical simulations for the MCC model presented in Appendix F.

The CSR model can reproduce the undrained shear strength of both the Eemdijk organic clay (Appendix H) as the 'Oostvaardersplassen' clay (Appendix D). The properties (CR, RR, φ') of these clays are similar. The Eemdijk organic clay tests are performed on undisturbed samples, resulting in a low CSR value (1.18), a relative high S-ratio (0.42) and higher undrained shear strength than simulated by the MCC model. The 'Oostvaardersplassen' clay tests are performed on reconstituted samples, resulting in a high CSR value (1.75), a relative low S-ratio (0.33) and lower undrained shear strength than expected from the MCC model. Although these are just two examples, on different organic clays with similar properties, there might be a tendency that the normalized undrained shear strength (S-ratio) from samples on intact natural soils is higher than from reconstituted remolded soils with the same critical state strength (Mc). The CSR model with the variable spacing is able to reproduce the behavior for both conditions.

In Leroueil et al. (1985) a comparison is shown of swelling consolidated samples and intact consolidated samples for various clays. Although all samples are overconsolidated and undisturbed, loss of structure due to swelling is demonstrated by a reduced peak strength. The effect on the Critical State strength is less pronounced. The properties of reconstituted 'Murro' clay are reported In Karstunen and Koskinen (2008) and of intact 'Murro' clay in Karstunen and Yin (2010). Unfortunately, the S-ratio is not reported. Further research is recommended as this would improve the application of Critical State models for intact soils as present in dike engineering projects.

4.3.7 Concluding remarks on geotechnical conditions and parameters
This section presents the concluding remarks on the geotechnical conditions relevant for the Eemdijk full-scale tests and on parameter determination, including constitutive model parameters.

Geotechnical conditions
The focus in this section is on organic clay layer 3, soft clay layer 3a and peat layer 4, as these are decisive and most important for the stability of the Eemdijk embankment. The parameters are based on a comprehensive series of high-quality CPT tests and laboratory tests.

The intensive geotechnical investigations reveal a local soft clay layer (3a) at the toe of the ground dike. This layer is important for the validation as it is encountered within the potential failure zone. The new proposed R2010-ORG-NL CPT classification (Chapter 2) enables to identify this soft layer, as shown in Appendix G.

The layer is only present in two CPTs, hence the extent is about 30 m. This layer is detected by a dense grid, CPT spaced 15 m, ISO class 1 CPTs and sufficient laboratory tests. It is recognized that in many dike engineering projects in the Netherlands the CPTs are generally spaced more than 30 m, and such local layers may be overlooked.

The new proposed R2010-ORG-NL CPT classification enables a more successful identification of peat and organic clay layers. This improved CPT-based classification not only allows a better identification of local soft layers, but it also improves the assignment of laboratory tests to the correct layer, which improves the reliability of the parameter set, both in terms of average value and coefficient of variation. It is recommended to apply this updated CPT-based classification for organic soils, in particular for dike engineering projects in the Netherlands.

The CPT-based correlations as presented in Chapter 2 are compared with the site-specific test results. All results plot within the 90% confidence interval of the regional correlations. It is concluded that certain Eemdijk specific correlations with intercept at the origin are biased in trend, and correlations with free intercept are biased on offset. It is important to acknowledge these biases for each site and each correlation. Without prior knowledge of the site-specific conditions, it is recommended to use the 5% fractile value of a regional correlation instead of the 5% probability of (no)-exceedance of the average.

Geotechnical parameters
The back-analysis of the Eemdijk full-scale test requires ultimate strength parameters as well as constitutive model parameters for the finite element analysis (FEA). Both best estimate as upper bound parameters are determined. The lower bound parameters are not relevant for the back-analysis as it is shown in Section 4.8 that the actual stability is higher than determined in the back-analysis based on best estimate parameters.

The friction angle and S-ratio of the encountered layers are high compared to mineral clays, i.e., $\sin(\phi')=0.62$ and S-ratio=0.42 as best estimate values for organic clay layer 3. From the analyses it is concluded that both parameters are consistent and in line with the correlations presented in Chapter 2. It is also concluded that the parameter determination procedure as proposed for the new CSR model is well able to determine the S-ratio for organic soils, whereas the MCC model would underestimate the S-ratio.

The strength parameters of Peat layer 4 are higher than organic clay layer 3. This is often encountered in other dike projects too. For soft clay layer 3a it appears that the preconsolidation stress and S-ratio are significantly lower despite similar effective strength parameters. Both parameters result in a lower in-situ undrained shear strength.

After careful evaluation of the CAUC tests it is concluded that there are two challenges. The first challenge is the definition of the ultimate strength. The Dutch guidelines specify selection at 25% axial strain. This often results in significant softening for NC samples, even after the pore pressures are stabilized. This will result in a lower undrained shear strength and S-ratio. On the other hand, for OC samples it often results in significant hardening associated with negative pore pressures. This will result in a high estimate of the in-situ undrained shear strength and the equivalent preconsolidation stress. It is concluded that the 25% strain value is not always appropriate and not necessarily conservative for design of dikes. Therefore, it is recommended to determine the ultimate strength at 15% axial strain, more in line with international practice, with additional requirements as presented in Table 4-9.

The second challenge related to CAUC interpretation is the geometrical correction. The applied geometrical correction is called the 'barreling' method. This correction was by default applied to all samples, although in most cases a combination of 'barreling' and 'slip plane' occurred.

Geometrical corrections are normally included in the presented results by the laboratory and it requires the 'raw' data to verify this and to alter it. The effect of the geometrical correction on the undrained shear strength is significant, up to 20% on the undrained shear strength, and consequently also on the S-ratio for NC samples. The larger the strain the larger the geometrical correction. The effect on the effective strength parameters is negligible.

Both DSS and CAUC tests are performed on organic clay layer 3. From the comparison it can be concluded that the CAUC undrained shear strength, determined including geometrical correction, is similar to the DSS undrained shear strength. The laboratory tests are back-analyzed by numerical simulations. It appears that the isotropic constitutive models fit reasonably well, although the CAUC strength is underestimated.

The CAUC undrained shear strength determined without geometrical correction results in a higher undrained shear strength, typically 20% higher, which is line with the well accepted ADP concept where the CAUC strength is larger than the DSS strength, and the DSS strength is lager than the CAUE strength. From the numerical simulation it is concluded that the anisotropic constitutive models (SHANSEP, CSC1S) are capable to fit both the DSS and CAUC test well with one set of parameters.

The procedures to determine the constitutive parameters is presented in Appendix E. The advantage of these procedures is that only a few well defined (input) parameter are used to determine all required (output) parameters for a constitutive model. The strength parameters are primarily based on the DSS or CAUC test. The stiffness parameters are primarily based on the K_0CRS test. This will result in a consistent parameter set. Another advantage of these procedures is that it allows for switching of constitutive model in staged construction, as the constitutive models approximately yield to the same stiffness and strength.

Probabilistic analyses require many calculations, which include extreme values for all random variables. It is crucial that the parameter sets are consistent in the first place to prevent erroneous calculations. More important, it is better to select the correct random variables. The correct random variables are the underlying unique soil properties and state parameters, basically the same input parameters as used for the CSR-model. For example, the S-ratio is related to the friction angle as well as the compression parameters. The constitutive model parameters follow from consistent procedures and relations such as presented in Appendix E. In order to perform a probabilistic FEM analysis, this would require preprocessing of the parameter set for every calculation of the probabilistic analysis. This approach is different from current practice, where the model parameters are considered as stochastic parameters. The preprocessing and parameter set generation can also be combined with a probabilistic analysis, such as FORM, in order to determine the PDF of the model parameters, for example the S-ratio, as well as the correlation with the power-m.

The best estimate parameter set is used as basis for the back-analysis as presented in section 4.8. The upper bound parameter set is used as upper bound value for the back-analysis (Class C prediction), both in the isotropic and anisotropic constitutive model parameter sets.

4.4 Results of sheet pile pull-over test

4.4.1 Introduction

One of the research goals of the Eemdijk full-scale field test is to gain more insight in the performance of the sheet piles towards and beyond failure (research question 5). This resulted in the sheet pile pull-over tests (PO-test) programme, involving four different sheet pile configurations. The PO-test provides the actual properties of the sheet piles that are used as reinforcement in the full-scale dike failure test (SPD).

4.4.2 Test programme

The sheet piles and test programme are presented in Table 4-16 and Figure 4.22 and elaborated below:

- AZ26 profile is tested to validate the plastic bending capacity since this profile is a Class 2 profile according to the Eurocode and therefore is expected to reach the full plastic bending capacity with additional plastic rotation capacity. The elastic section modulus of the AZ26 is 2600 cm^3/m, which can be regarded as representative for sheet piles reinforcement in the Netherlands, although also lighter and heavier profiles are used in applied in dike engineering practice.
- AZ13-700 is a Class 3 profile according to the Eurocode and is tested for comparison with the AZ26 profile. It is expected to reach the full elastic bending capacity (plastic resistance in term of Eurocode (EN1993-5 2007)) but not the full plastic bending capacity.
- GU8N triple is a Class 3 profile according to the Eurocode (EN1993-5 2007) and the same type as used in the SPD-test. To assess the influence of the loading direction, this profile is also tested in the reversed direction (GU8N-rev). The GU8N sheet pile is selected as it is also applied in the full-scale dike failure test.
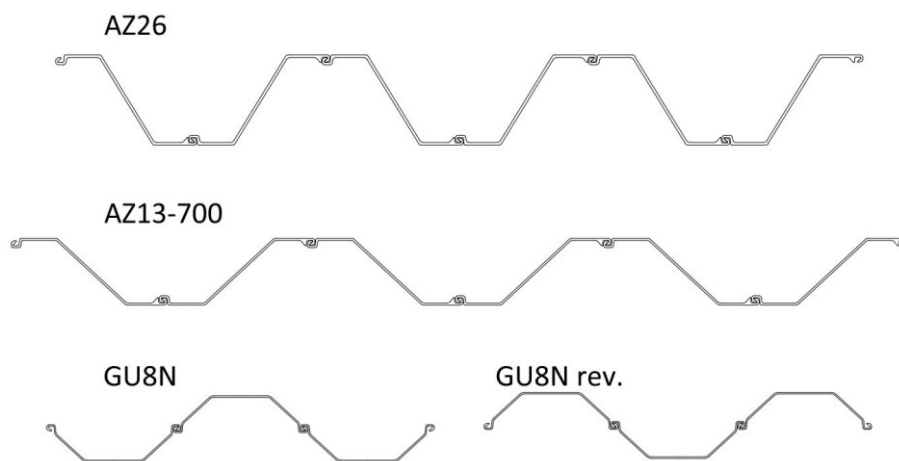

Figure 4.22 Four sheet pile configurations of the PO-test

Table 4-17 shows an overview of the structural properties of the PO-test sheet piles based on the manufacturer's brochure[11]. The actual thickness and dimensions deviate within the tolerances prescribed in EN10248-1 (2006). Based on the measurements and back calculations it is concluded that the average properties match very well, i.e., moment of inertia is 11097

---

[11] https://sheetpiling.arcelormittal.com/products-services/production-range/

cm^4/m for the triple GU8N, with a coefficient of variation (CV) of 2%. This variation also applies to the section moduli.

Table 4-16 PO-test sheet pile configuration and schedule

PO-test sheet pile configuration	Start time	Project day	Duration (hour)
AZ13-700, 3 double profiles	2/23/18 11:38	256	5:53
GU8N, 1 triple profile	2/27/18 11:16	260	4:49
GU8Nrev, 1 triple profile reversed	3/2/18 12:15	263	3:42
AZ26, 3 double profiles	3/10/18 10:45	271	5:39

In case of the GU8N triple, the center line is not exactly in the middle of the profile and therefore this profile has a reduced section modulus and reduced moment of inertia, compared to a continuous wall. The values of the full plastic section modulus are theoretical values as local buckling is expected to reduce the ultimate capacity for the Class 3 profiles. The actual PO-test measurements will be used to determine the maximum capacity for the sheet piles of the SPD-test.

Table 4-17 PO-test structural sheet pile properties

Panel / profile: Property	Unit	3 Double AZ26	3 Double AZ13-700	1 Triple GU8N	Continuous GU8N
Length	L (m)	16.5	14	14	
Width panel	B (m)	3.78	4.2	1.8	
Elastic section modulus	W_e (cm^3/m)	2600	1305	600	770
Plastic section modulus	W_{pl} (cm^3/m)	3059	1540	729	935
Moment of inertia	I (cm^4/m)	55510	20540	11128	12010
Flange width	b_f (mm)	376	370	246	
Flange thickness	t_f (mm)	13.1	9.5	7.5	

The measured strength properties, steel name and cross-section class are presented in Table 4-18. The CV is presented to indicate the variation in strength. For the back-analysis of the Eemdijk full-scale tests the average properties will be used. For application in projects, EN10248-1 (2006) requires that the minimum properties are used, presented in Table 4-19. The Eurocode (EN 1993-5, 2007) allows for plastic calculation, but this depends on the cross-section class. The reasoning for this is that local plate buckling may occur before the plastic capacity is reached. The classes are related to the slenderness of the compression flange and the steel grade of the sheet pile. The following cross-section classes are distinguished:
- Class 1 cross-sections for which a plastic analysis involving moment redistribution may be carried out, provided that they have sufficient rotation capacity.
- Class 2 cross-sections for which elastic global analysis is necessary, but advantage can be taken of the plastic resistance of the cross-section.
- Class 3 cross-sections which should be designed using an elastic global analysis and an elastic distribution of stresses over the cross-section, allowing yielding at the extreme fibers.
- Class 4 cross-sections for which local buckling affects the cross-sectional resistance.

Table 4-18 PO-test measured and interpreted sheet piles strength

Measured strength properties	Unit	AZ26	AZ13-700	GU8N
Yield strength at peak strength (ReH): Average Minimum coefficient of variation (CV)	f_y (N/mm^2)	327 314 3.2%	406 367 6.1%	388 368 3.2%
Tensile strength at fracture (Rm): Average Minimum CV	f_u (N/mm^2)	422 417 0.8%	464 453 1.9%	440 431 1.5%
Elongation at fracture (A): Average Minimum CV	ε_u (%)			28.4 25.0 5.2%
Cross-section number $\left(\dfrac{b_f}{t_f}\sqrt{\dfrac{f_y}{235}}\right)$ **[range for cross-section class 3]**	(-)	33.9 [45-66]	51.2 [45-66]	42.2 [37-49]
EN1993-5 (2007) cross-section class	(-)	2	3	3
Ultimate bending moment capacity (Mu) for a continuous wall	(kNm/m)	M_p=1000	M_e=529	M_e=299

Table 4-19 Steel properties for sheet piling (EN10248-1 2006; EN1993-5 2007)

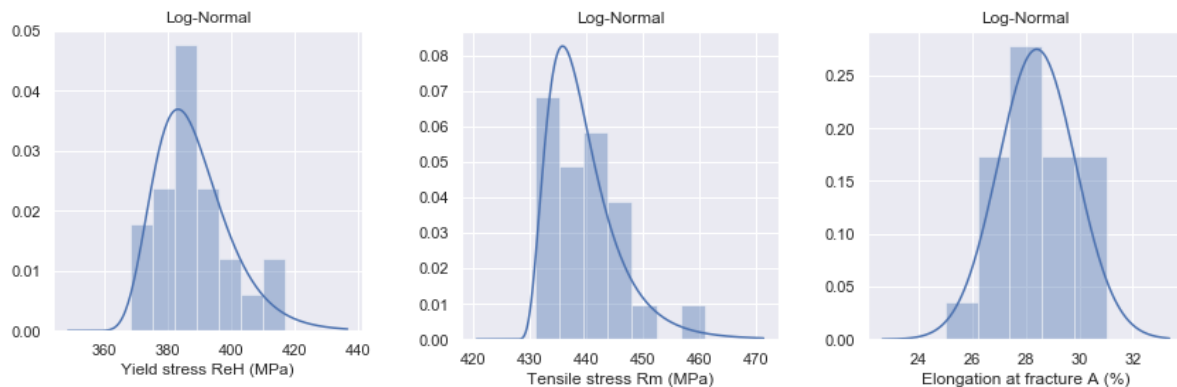| Steel designation	Minimum yield stress ReH (MPa)	Minimum tensile stress Rm (MPa)	Minimum elongation at fracture A (%)
S240GP	240	340	26
S270GP	270	410	24
S320GP	320	440	23
S355GP	355	480	22
S390GP	390	490	20
S430GP	430	510	19
S460GP	460	530	17

Figure 4.23 Histogram and PDF of GU8N steel properties based on 24 measurements. The left figure presents the yield strength, the middle figure the tensile strength and the right figure the elongation at failure. The Log-Normal PDF is presented.

The steel designation is based on the minimum measured, or inferior characteristic value (95% PoE), for the three categories presented. Based on this table the GU8N classifies as S270GP due to the relatively low tensile strength. The classification based on the other criteria is S355GP. In case the sheet piles are designated as S270GP, the nominal yield stress is defined as 270 MPa, which results in an underestimation compared to the measurements. In case the sheet piles are designated as S355GP, the nominal tensile stress is defined as 480 MPa, which results in a significant overestimation compared to the measurements. The number of measurements for the AZ26 and AZ13-700 is limited to 6. The steel designation is respectively S270GP and S355GP.

The cross-section class results are presented in the table below. The AZ26 sheet piles are cross-section class 2. This implies that the ultimate bending moment capacity equals the plastic bending moment capacity. The ultimate bending moment capacity of the AZ13-700 and GU8N is in between the elastic and plastic bending moment capacity. The rotation capacity is however limited, hence the full elastic bending moment capacity is used for the back-analysis of the PO-test.

The GU8N is installed as triple panel in the PO-test and in the SPD-test over the lower part (staggered wall). The capacity of the triple profile deviates from the theoretical value of a continuous wall. The actual ultimate bending moment capacity can be determined by a 4-point bending test. An example of a reported 4-point bending test on a sheet pile can be found in Kort (2002). This physical test could not be performed.

The actual strength of the GU8N is therefore estimated by numerical simulations of 4-point bending tests. The results of these simulations are reported in Breedeveld et al. (2018a); (Meijer 2019). The ultimate bending moment capacity of 1 triple GU8N panel, with 2 flanges in compression, is 274 kNm/m (493 kNm per panel). In case the triple profile is placed as a staggered wall the ultimate bending moment capacity is 137 kNm/m. This value is applied in the back-analysis of the PO-test and SPD-test for the staggered part. For the continuous part the elastic section modulus (Me=299 kNm/m) is used in the back-analysis of the SPD-test.

The test setup is presented in Figure 4.24. The four sheet pile configurations are placed in a circular formation around a reaction frame. This reaction frame consists of 3 tubular piles interconnected with a steel Y-frame. To prevent any soil interaction between the sheet piles and the reaction frame the sheet piles are installed at a 15 m distance of the tubular piles.

A hydraulic jack is placed between the reaction frame and the sheet piles, 2 m above surface level. This jack can generate a pull-force of 1200kN and has a stroke of 2 m. The pulling force is imposed by constant rate of displacement. The total displacement imposed on the sheet pile is sufficient to reach the maximum (peak) capacity of the sheet piles. The jack is placed on a sliding table to support the jack and prevent the self-weight of the system to influence the behavior of the sheet pile. The jack is connected to a steel cable to both sides of a waling (girder) on the sheet pile. This connection is such that the pull force is evenly distributed over both sides of the waling and the pull force remains centric on the waling even for large rotations of the sheet pile wall.

To monitor the horizontal displacements of the sheet pile, prisms are placed at three levels on the sheet pile and are monitored with total stations. Two SAAFs (Shape Accel Array Field) are installed on the sheet pile wall and two SAAFs in the ground in front of the wall to monitor the

deflection and horizontal displacements in depth. The total pulling force applied by the hydraulic jack is measured by a force gauge and the stroke of the hydraulic jack is measured by an optical sensor. On the sheet pile wall Glass Fiber Strain Gauges (GFSG) are installed. The GFSG suffered damage from the installation and are excluded from this research (Meijer 2019). Figure 4.25 shows the location of the monitoring instrumentation for the AZ26 sheet pile configuration.
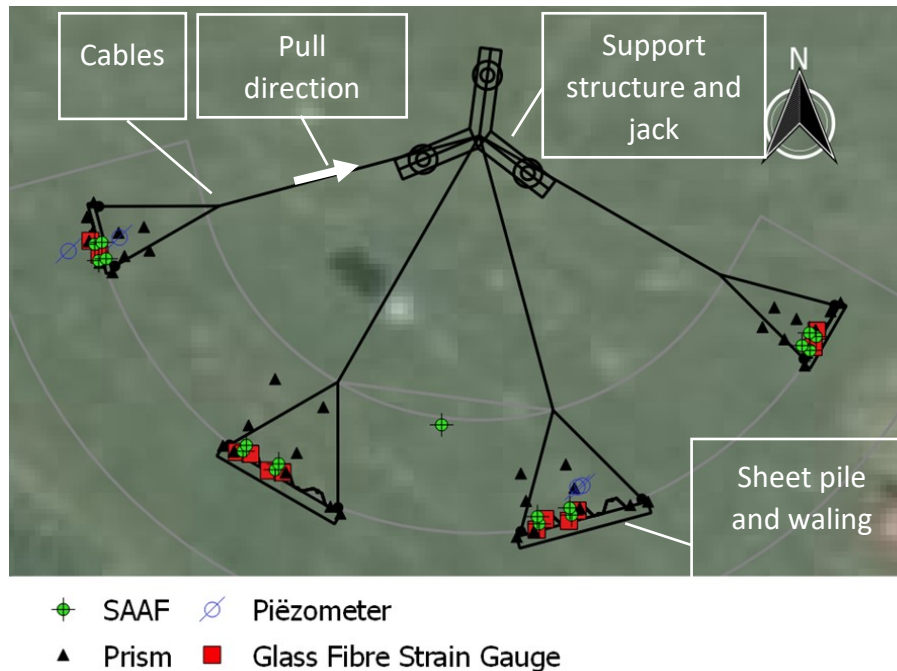

Figure 4.24 Top view PO-test site with monitoring instrumentation. Sheet piles from left to right: GU8N, AZ13, AZ26, GU8N-reversed
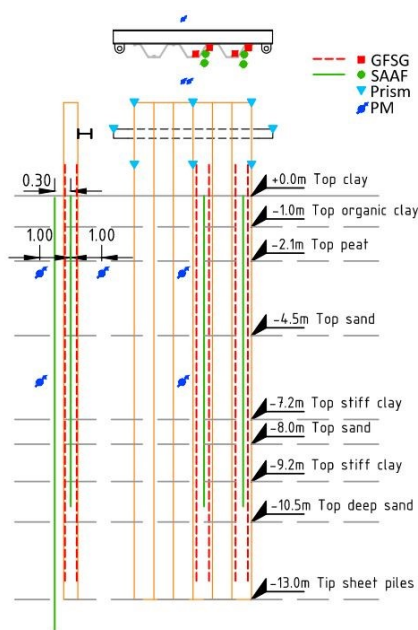

Figure 4.25 top, front and side view of PO-test AZ26 sheet pile panel with monitoring instrumentation and typical soil profile

Figure 4.26 PO-test on triple AZ26 panel, with pushed up soil on front (passive) side and gaping on back (active) side.

4.4.3 Test results

The PO-tests are reported in Breedeveld et al. (2018a); (Lengkeek et al. 2019a; Meijer 2019). This section summarizes the main results. The forces and displacements of the PO-test are presented in the table below. The cross-section class 3 profiles all failed due to local plate buckling of the compression flanges and adjacent webs. The AZ26 cross-section class 2 profile showed a zone with plastic deformation without local buckling.

All tests were continued after the maximum pulling force was reached. The load-displacement diagrams all showed significant softening which stabilizes at large displacements (>1m). The stabilizing effect is caused by the increase in passive resistance once the sheet piles are pushed forward and downward due to the plastic hinges at depth.

The sheet pile walls in the PO-test extended 3 m above surface with the load imposed 2 m above surface. On the active (back) side of the sheet pile wall, gaps occurred over the full length of the sheet pile panel, see

Figure 4.26. The width of the gap was almost equal to the horizontal deformation at surface level and the depth was up to a few meters, till the level of structural failure.

Furthermore, all PO-tests exceeded the rotation capacity as defined by the Eurocode (EN1993-5 2007). Despite the local failure, the ductility of sheet piles allowed for the occurrence of a hinge with reduced bending moment capacity where the sheet piles and interlocks remained intact as one piece.

Table 4-20 PO-test measured forces and displacements

Panel / profile: Measurement	Unit	3 Double AZ26	3 Double AZ13-700	1 Triple GU8N	1 Triple GU8N-reversed
F_{max}	kN	982	634	180	179
U_x at F_{max}	m	0.53	0.54	0.33	0.32
Rotation at F_{max}	rad	0.10	0.10	0.09	0.09
Level of maximum curvature	m NAP	-4.0	-3.0	-1.5	-1.0
Level of sheet pile buckling	m NAP	N.A.	-2.5 to -3.0	-1.5 to -2.0	-1.5
F_{end} (Compared to Fmax)	kN	800 (-18%)	400 (-32%)	140 (-23%)	120 (-31%)

4.4.4 Back-analysis and validation

The FEM back-analysis of the PO-tests is reported in Breedeveld et al. (2018a) and not repeated here. The back-analysis has been performed with the best estimate set using the HS model and the SHANSEP NGI-ADP model. The results of both models are similar. From this analysis it is concluded that for the AZ26 PO-test the maximum force complies with a cross-section class 2 profile with the full plastic bending moment resistance. The maximum force for the AZ13 and GU8N PO-tests comply with a cross-section class 3 profile with the full elastic bending moment capacity. These findings are in line with the Eurocode (EN1993-5 2007). However, in Dutch guidelines for sheet piles in dikes (POVM 2020a, 2020b) it is not allowed to apply the full plastic bending moment resistance for cross-section class 2 sheet piles. This is regarded as unnecessary

conservative, as the SSI of a cross-section class 2 sheet pile is well captured by the FEM analysis and is not different for sheet piles applied in dikes.

4.4.5 Edge effects sheet pile panels

The PO-tests are performed on panels of sheet piles. The middle and outer piles are instrumented with inclinometers. This allows for an estimate of the edge effect of the outer piles of each panel. This interpretation and evaluation of the inclinometers is reported in Meijer (2019) and summarized below.

For sheet piles installed as panels or as a staggered wall, a distinction has to be made between mid and side piles. Compared to mid piles, side piles experience two additional effects, namely:
- Mobilization of more soil as a result of 3D effects.
- Less restriction against cross-sectional deformation due to one of the sides being unconstrained.

The comparison between the middle and side sheet pile displayed a clear presence of these effects, which resulted in larger curvature at the side pile. The curvature near failure is 10 to 15% larger for the side sheet piles compared to the middle sheet piles.

Figure 4.27 indicates that at the depth of local buckling of the 3 double AZ26 sheet pile, the side sheet pile has a lower stiffness than the mid sheet pile. From this it can be concluded that the neutral axis shifts at the edge of the panel, resulting in a lower moment of inertia and also lower stresses in the flange.

For the triple GU8N panel, the neutral axis is slightly eccentric due to asymmetry. The influence of the edge effect on displacement and curvature is shown in Figure 4.28. Deformation of the outer piles will result in a reduction of the stiffness since the outer flanges displace towards the neutral axis. Similar as for the Z-section, the side pile has a lower stiffness than the mid pile at the location of local buckling. Accordingly, the side has a lower moment of inertia and thus lower stresses in the flange.

In Figure 4.29 and Figure 4.30 the permanent plastic deformations of the panels at two levels are shown, based on a 3D laser scan after partial excavation of the panels. At the higher level, -1.0 m NAP, plastic deformations mainly occur in the outer flange or web of the side sheet piles. The lower level is selected at the maximum curvature. In particular the GU8N shows significant deformation of the compression sheet piles.
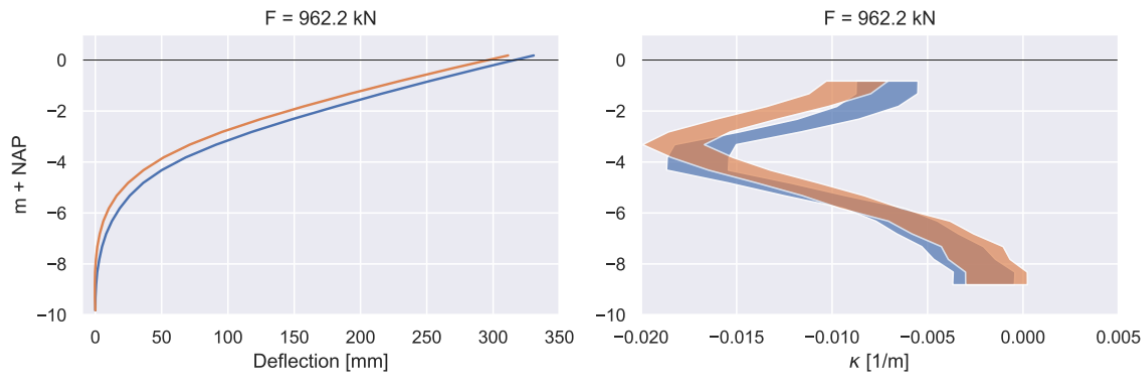
Figure 4.27 AZ26 panel: Deflection (left) and curvature (right) of middle (blue) and side (orange) sheet pile
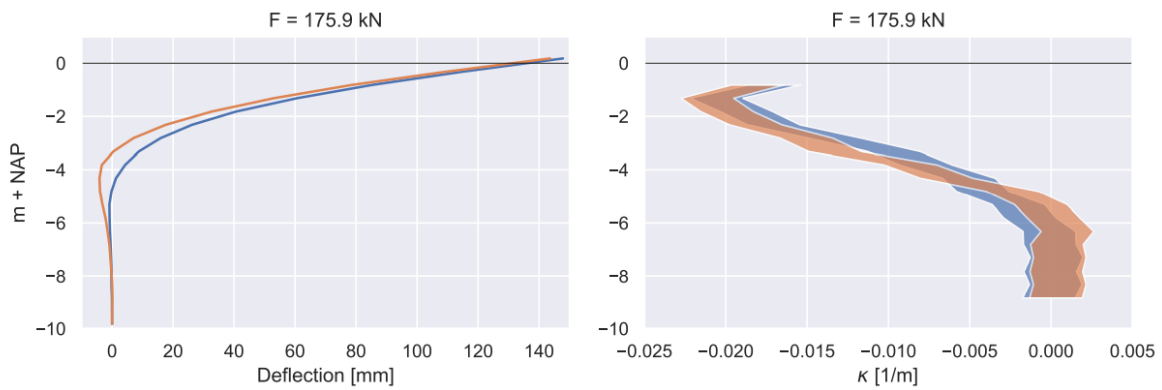

Figure 4.28 GU8N: Deflections and curvature of middle (blue) and side (orange) sheet pile

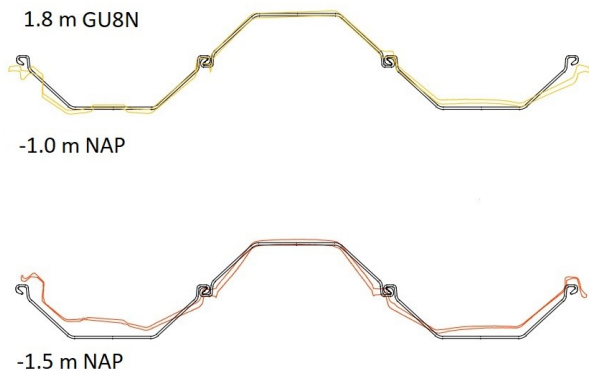Figure 4.29 AZ26: 3D laser scan of excavated panel at two depths

Figure 4.30 GU8N: 3D laser scan of excavated panel at two depths

4.4.6   Concluding remarks on PO-test

The Eemdijk pull-over test is analyzed to address the research question what the performance is of sheet piles towards and beyond failure.

Validation of sheet pile properties for SPD-test

The centerline of the GU8N triple is not exactly in the middle of the profile and therefore this profile has a reduced section modulus and reduced moment of inertia, compared to a continuous wall. The values of the full plastic section modulus are theoretical values as local buckling is expected to reduce the ultimate capacity for the cross-section class 3 profiles. The actual strength of the GU8N is therefore estimated by numerical simulations of 4-point bending tests. The results of these simulations are reported in Breedeveld et al. (2018a); (Meijer 2019). The ultimate bending moment capacity of 1 triple GU8N panel, with 2 flanges in compression, is 274 kNm/m (493 kNm per panel). These properties are confirmed by the PO-test measurements and back-analysis.

In case the triple profile is placed as a staggered profile the ultimate bending moment capacity is 137 kNm/m. This value is applied in the back-analysis of the PO-test and SPD-test for the staggered part. For the continuous part the elastic section modulus (Me=299 kNm/m) is used in the back-analysis of the SPD-test.

The actual geometrical properties and moduli match well with the expected values provided by the sheet pile manufacturer, with small variations (i.e., CV=2%). The CV of the yield strength is larger, typically 3 to 6%. Furthermore, there is a margin between the average yield strength and the nominal value following the steel designation, as this is based on the minimum or 5% superior characteristic value. For the PO-test it is concluded that the average yield strength properties are about 10% larger compared to the steel designation. The steel designation based on the tensile strength is not always similar, and appears to be 1 or 2 grades lower, i.e., S270GP instead of S355GP.

Validation of sheet pile cross-section class

The back-analysis of the PO-tests did not show a reduced bending moment capacity. The cross-section class 2 AZ26 reached the full plastic bending moment capacity and the cross-section class 3 AZ13-700 and GU8N reached at least the elastic bending moment capacity, where the capacity is based on the average yield stress.

Edge effects

The back-analysis confirms the depth of the local (buckling) failure for the cross-section class 3 profiles, as derived from the SAAF measurements and 3D-laser scans. Furthermore, from the analysis of the SAAF measurements it is concluded that the stiffness (moment of inertia) of the side sheet piles of panels should be reduced by about 10% due to edge effects.

Consequently, it is recommended to reduce the bending moment capacity (section modulus) by 10% for each side sheet pile, in combination with the elastic or plastic section modulus, depending on the cross-section class. For the AZ26 panel this would result in a reduction of 10%*2/6=3.3%.

4.5   Results of ground dike test

4.5.1   Introduction

This section presents the main findings of the Eemdijk full-scale failure tests. The tests are performed in 2018 near the river Eem in the center of the Netherlands. The first results of the Eemdijk full-scale failure test are presented in Lengkeek et al. (2019b). As part of this test program, two parallel 60 m long full-scale test dikes are built of which one is reinforced with a sheet pile wall. The purpose of the GD-test is firstly to gain prior knowledge to improve the execution of the sheet pile reinforced dike which is performed after the GD-test. Secondly, it is a unique opportunity to be able to compare the performance and behavior of both dikes, as well as the performance of back-analysis models (Research question 4 and 6).

The total duration of the failure test is one week. This time was required for all the sequential loading steps. One week is also a representative period for most river dikes in the Netherlands subjected to a high-water event.

The subsoil consists of 4 m soft Holocene soils underlain by sand. The core of the two dikes is constructed with sand and vertical clay cut-off walls in between, allowing for independent infiltrating and drainage. The slope cover consists of clay of sufficient thickness to prevent a cover sliding failure. The ground dike is on the left side of Figure 4.5 and the dike with sheet pile reinforcement is on the right side. The maximum height of the GD prior to the failure test is 5.3 m NAP.

Additional loading on both dikes was applied by an excavation of the ditch and by means of containers with water. The aim is to create a realistic load scenario and failure mechanism. The infiltration of the core of the dike simulates a high-water flood. The ditch excavation in front of the dike and lowering of water level simulates the near uplift situation due to high water pressures in the aquifer.

4.5.2   GD-test programme and conditions

The phreatic water level in the summer prior to the embankment construction is -0.8 m NAP. During construction and the failure test it increased to -0.5 m NAP. The ground water head in the first aquifer is -0.3 m NAP. The water level in the ditch in front of the dike is kept at -0.5 m NAP, with a temporary increase to -0.2 m during excavation of the ditch and ultimately decrease to -1.1 m NAP after failure. The water level in the sand core of the dike is +0.5 m NAP during construction. During the failure test this water level is stepwise increased by infiltration from +0.5 m to ultimately +2.9 m. The liquid-tight containers on top of the dike, in case extra load was required, were not used in the end.

The ground dike failure test phases were mainly performed during daytime. The test programme is presented in table 3.

Table 4-21 GD-test schedule

GD-test phase	Start time	Project day	Duration (hour)
Excavation ditch -1.5 m NAP, 7 m width	1/24/18 8:00	226	24:00
Excavation ditch -1.5 m NAP, 13 m width	1/25/18 8:00	227	24:00
Excavation ditch -2.0 m NAP, 20 m width	1/26/18 8:00	228	8:00
Water level ditch -0.5 m NAP	1/26/18 16:00	228	16:00
Water level fill +1.0 m NAP	1/27/18 8:00	229	12:00
Water level fill +1.5 m NAP	1/27/18 20:00	229	17:00
Water level fill +2.0 m NAP	1/28/18 13:00	230	14:00
Water level fill +2.5 m NAP	1/29/18 3:00	231	17:00
Water level fill +2.9 m NAP	1/29/18 20:00	231	12:30
Failure GD	1/30/18 8:30	232	7:30
End GD-test	1/31/18 16:00	232	

4.5.3   GD failure mode

The total duration of the failure test was seven days. The deformations in the first six days are small, generally less than 5 cm displacement and only start to increase significantly in the last day. Failure started to be visible with tension cracks at the crest and top of the slope in the morning of January the 30th . The rate of deformation increased rapidly after 10 cm displacement, see Figure 4.40. The total duration of the failure was about 7 hours. At the end of the day a new equilibrium was reached. The dimensions of the slip circle in the GD are:

- Height 7.3 m, from crest to bottom.
- Width 15 m (in cross-section), about twice the height.
- Length 30 m (along the dike), half to total length of the GD and about 4 times the height.
- The maximum horizontal displacement in the middle section of the ditch is about 7 m.
- The insert of the failure surface at the crest is 1 m.
- The level of the failed wedge of the crest is 1.8 m NAP, 1.1 m below the infiltration water level in the sand core of the GD.
- The vertical crest displacement of the failed wedge is 3.5 m. The horizontal displacement of the crest is typically the same.

The monitoring results are presented in Appendix J, together with a 7-hour time lapse on January the 30th. Figure 4.31 presents the inclinometer measurements at the toe in the middle of the GD over the last two days prior to failure. It clearly shows the rapid increase close to failure and the level of the sliding surface at -2.0 m NAP in the middle of the soft Holocene layers. The failure of the GD did not result in a breach and flooding, as the water level also dropped due to free drainage at the slip circle and the infiltration was stopped after failure.
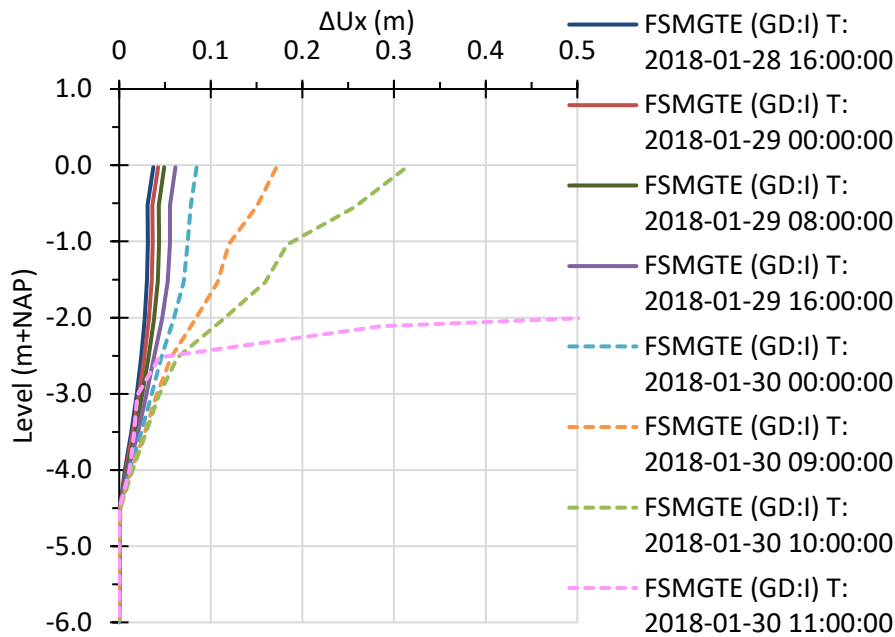
Figure 4.31 GD: inclinometer measurements (HM..) at the toe (SAAF location I). The final eight measurements are presented starting 1 day prior to failure. The last measurements are after failure and less reliable due to excessive deformations. These deformations are additionally to the construction deformations. The failure surface is located at approximately 2.0 m depth.

The failure occurred over approximately the middle 30 m of the 60 m long ground dike, see areal view in Figure 4.32. Both ends of the dike remained stable under the same loading. The deformations at the sides of the 30 m are less, which clearly indicates a 3D mechanism. From the monitoring it is concluded that the failure mechanism can be described as a typical rotational failure, although the lower part is horizontal due to the presence of a weak layer 3a. This is confirmed by the excavation after the failure test and shown in Figure 4.33. The deepest point of the sliding plane is in layer 3a, just above the peat layer at -2 m NAP. Layer 3a is only present in the middle part of the GD, which initiated the local failure over 30 m length.

Figure 4.32 Areal view of the Eemdijk test embankment with the failed slope of the GD on the left side (February 2018). The total length of the sliding wedge is about 30 m. The sheet piles and the ditch of the SPD at the right side are not yet present. [Photo courtesy https://www.hwbp.nl/kennisbank/pov-macrostabiliteit].

Figure 4.33 Left: Failure surface at the embankment in the sand layer 1a indicated by the dashed lines. Right: failure surface at the toe in soft clay layer 3a just above peat layer 4.

The GD failure test illustrates the importance of a high density of soil investigations at the toe. The spacing of the soil investigations should be related to the size of the failure body. For GD-test a spacing of 30 m was sufficient. For typical river dikes spacings of 50 m would be appropriate as the local failures would not directly result in a breach. The typical spacing in many dike projects is 100 m, hence it depends on the variability and knowledge of local geology whether this is sufficient for the assessment of the global stability.

Secondly, it also illustrates the importance of high quality CPTs (ISO class 1) and a proper classification as a thin layer of 0.5 m thickness with lower cone resistance can easily be overlooked. Thirdly, it illustrates the importance of proper laboratory testing in particular on deviating layers with low cone resistances. Finally, it illustrates that peats, although having a very low stiffness can still have a high strength and in this case definitely not the lowest strength of the present layers.

4.6   Results of sheet pile reinforced dike test

4.6.1   Introduction

The first results of the Eemdijk full-scale failure test are presented in Lengkeek et al. (2019b). The main research goal of the Eemdijk full-scale failure tests is to gain more insight in the actual behavior of a structural reinforced dike such that a reliable or more economical design is possible (research question 4 to 7). This section presents the results of the dike with a sheet pile wall reinforcement (SPD-test).

The intention for the full-scale failure test is to create a realistic load scenario and failure mechanism. The infiltration of the core of the dike simulates a high-water flood on the active side of the sheet pile. The ditch excavation in front of the dike and lowering of water level simulates the near uplift situation due to high water pressures in the aquifer. In case the loading is insufficient to initiate failure additional loading could be applied by increasing the water level below the slope at the passive side of the sheet pile and by filling containers with water on the crest of the SPD.

The subsoil consists of 4 m soft Holocene soils underlain by sand. The core of the dike is constructed with sand and the slope cover with clay. The geometry of the SPD is presented in Figure 4.5. The maximum height prior to the failure test is 5.5 m NAP with the top of the sheet pile at +6.0 m NAP. The cut-off wall in the middle together with the clay covers allowed for a maximum water level of +5.0 m NAP.

4.6.2   SPD-test programme and conditions

The phreatic water level in the summer prior to the embankment construction is -0.8 m NAP. During construction and the failure test it increased to -0.5 m NAP. The water level in the first aquifer is -0.3 m NAP during construction and -0.4 m NAP during the failure test. The ground water head in the ditch is -0.5 m NAP during the test and ultimately lowered to -0.9 m NAP at failure. The water level in the sand core of the dike is +0.4 m NAP during construction. This water level is stepwise increased by infiltration from +0.5 m to ultimately +5.0 m NAP during the failure test. The water level in the sand core at the passive side of the sheet pile is ultimately increased to +1.5 m NAP. The liquid-tight containers on the crest of the SPD are ultimately filled with 2 m of water.

It was intended to initially construct a continuous wall of the lightest double Z-profile. After more information was gathered on the strength of the soil at the GD and actual yield strength of the sheet piles, the configuration was changed. The yield strength of the sheet piles was much higher than expected and the soft clay layer 3a is not present at the SPD side. Based in the prediction it was expected that the dike would not fail. The chosen configuration exists of a staggered wall with alternating panels of 18 m and 9 m length. The panels consist of triple U-profiles (GU8N), see Figure 4.4. The properties of the sheet piles are presented in (Lengkeek, 2019a) and Chapter 4.4. The monitoring instrumentation on the sheet piles are presented in the same figure. The GFSGs are placed on both flanges to measure the strains in compression and extension due to the deflection. The SAAF is placed on the web in the centerline to measure the inclination over the full height. Prisms are placed at the top to measure the horizontal deformation.

The sheet pile dike failure test was performed 24/7. The test programme is presented in Table 4-22. The phasing followed practically the intended protocol, with slight adjustments during the test and based on the experience of the GD.

Table 4-22 SPD-test schedule

SPD-test phase	Start time	Project day	Duration (hours)
Excavation ditch -2 m NAP, 7 m width	3/12/18 8:00	273	24:00
Excavation ditch -2 m NAP, 15 m width	3/13/18 8:00	274	9:00
Water level fill to +2 m NAP	3/13/18 17:00	274	24:00
Water level fill to +3 m NAP	3/14/18 17:00	275	17:00
Water level fill/basin to +4.2 m NAP	3/15/18 10:00	276	22:00
Water level container 1 m	3/16/18 8:00	277	8:00
Water level container 2 m & slope +1.0 m NAP	3/16/18 16:00	277	18:00
Water level fill/basin to +5.0 m NAP	3/17/18 10:00	278	3:00
Water level ditch -0.9 m NAP & slope +1.5 m NAP, start slope failure	3/17/18 13:00	278	3:00
Failure sheet pile, collapse, end SPD-test	3/17/18 16:00	278	

4.6.3 SPD failure mode

The total duration of the failure test was seven days. The deformations in the first six days are small, generally less than 5 cm and only start to increase significantly in the last day. The maximum water level prior to failure was +5.0 m NAP, see Figure 4.36. Failure started to be visible with active wedge cracks on the crest behind the sheet pile the day before failure (March 16th).

The rate of deformation increased rapidly after 10 cm displacement, up to a horizontal displacement at the crest of about 60 cm and at the toe of about 35 cm. At this deformation the sheet pile failed which caused a collapse of the SPD and ultimately a flooding. The total duration of the collapse was about 7 minutes. The deformations stopped after the top of the sheet pile was deflected to almost 45 degrees. The dimensions of the failure surface are:
- Height 9 m, from crest to bottom.
- Width 20 m, from active wedge to exit point slip circle, about twice the height.
- Length 60 m, almost the full length of the SDP and about 6 times the height.
- The horizontal displacement of the top of the sheet pile was 6.3 m.
- The vertical displacement of the top of the sheet pile was 1.9 m.
- The vertical displacement of the slope in front of the sheet pile is 2.4 m.
- The maximum horizontal displacement at the crest is about 5 m.
- The insert of the active failure surface at the crest is 5 m.

The vertical displacement of the crest prior of flooding is also about 2 m and the highest point after failure is still the top of the sheet pile (+4.1 m NAP versus 3.5 m NAP). The top of the sheet pile wall acted as a weir during flooding as the maximum water level was about 0.9 m higher (+5.0 m NAP).

The monitoring results are presented in Appendix K, together with a 7-minute time lapse on March the 17th. Figure 4.34 presents the inclinometer measurements at the toe in the middle of the SPD over the last day prior to failure. It clearly shows the rapid increase close to failure and the deepest level of the sliding plane at -4.0 m NAP. Figure 4.35 presents the inclinometer measurements at the sheet pile in the middle of the SPD over the last day prior to failure. It clearly shows the rapid increase close to failure and the sheet pile failure at about -3.5 m NAP. At his level the maximum bending moment capacity of the sheet pile is exceeded which resulted in a local failure, similar as observed for the PO-test.
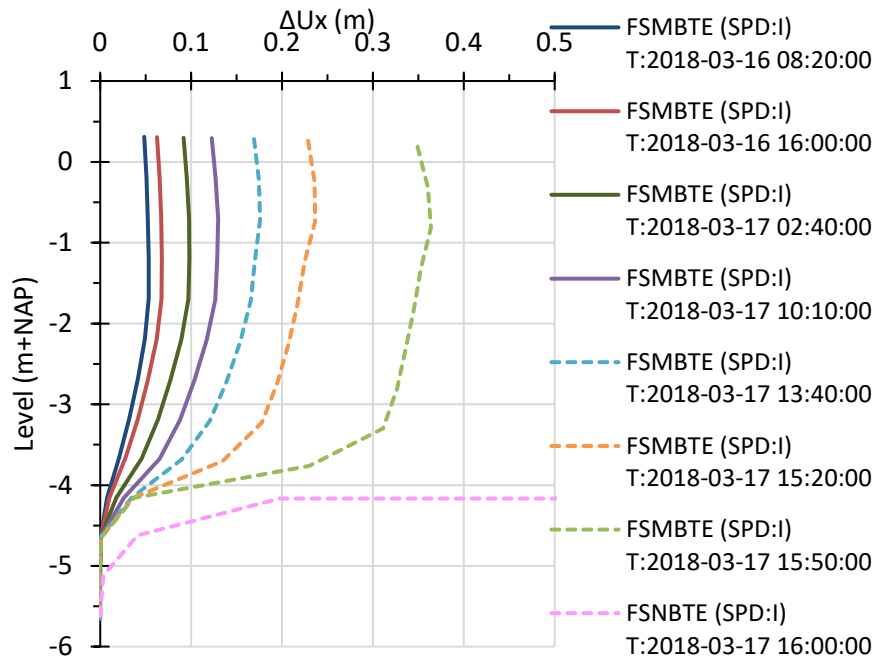
Figure 4.34 Sheet pile dike, inclinometer measurements (HM..) of horizontal displacements over depth, at the toe (SAAF location I). The final eight measurements are presented starting 1 day prior to failure. The last measurement is as after failure and not reliable due to excessive deformations. These deformations are additionally to the construction deformations. The failure surface is located at approximately 4.0 m depth.
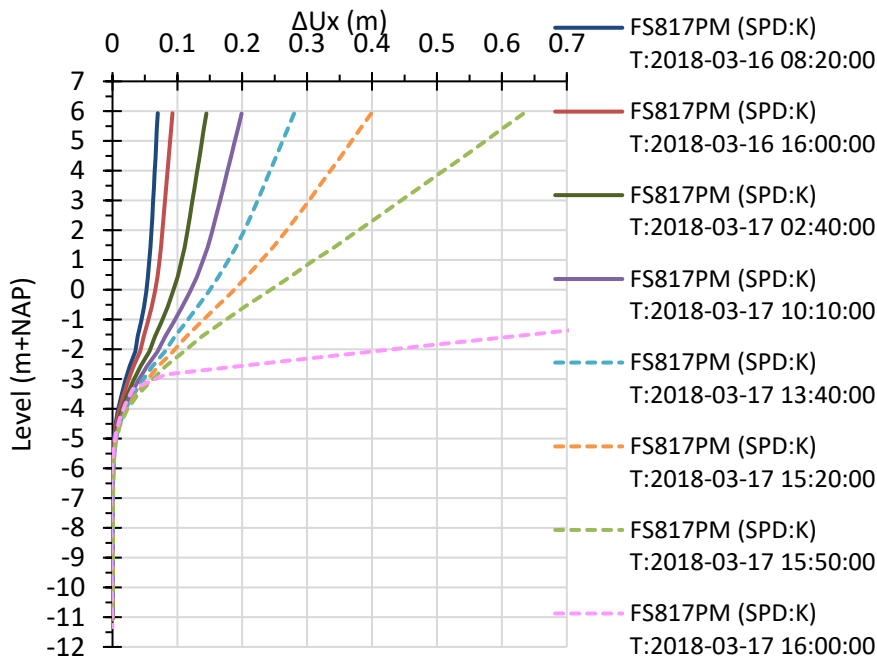
Figure 4.35 Sheet pile dike, inclinometer measurements (HM..) of horizontal displacements over depth, at the slope (SAAF location K). The final eight measurements are presented starting 1 day prior to failure. The last measurement is as after failure and not reliable due to excessive deformations. These deformations are additionally to the construction deformations. There is no sliding plane in a sheet pile, but the plastic hinge based on field observations is located at approximately -3.5 m NAP.

Progressive failure started after the sheet piles failed. This pushed the slope downward and created a circular failure mechanism with the exit point of the circle in the ditch. The bottom of the ditch was pushed up by about 2 m. With the ongoing deformation of the sheet pile the failed soil mass in the ditch was pushed up further partly on top of the bottom.

All sheet piles are removed after the test. From this inspection it is concluded than only the outer panels on each side did not fail, all other sheet pile panels failed as shown in Figure 4.38. The failure is caused by local buckling of the compression flanges.

All interlocks of all sheet piles remained intact. The total elongation at the top determined from the 3D scan is 1.8 m on a total length of 61 m, which is 3%. This elongation is caused by plastic yielding in the corners between flange and web. The required force to create yielding is typically 20 kN/m based on sheet pile properties. The membrane action induced longitudinal tension force is thus limited by this strength. This capacity of the Larssen interlocks is typically 100 kN/m, which is much larger. This explains the observation that all sheet piles remained connected by the interlocks. This is an important finding which is not considered in any guideline for the application of sheet piles along dikes.

The maximum deformation of the failed sheet pile is thus stopped by the resistance of the failed soil mass in front of the sheet pile, which is pushed upward, combined by the membrane action in the sheet pile. In addition, 3D side friction effects are expected too, although less prone than for the GD as the total length is about 60 m instead of 30 m.

Figure 4.36 Left: Side view of failure deformations at the moment of flooding. Right: Top/side view of the SPD prior to failure.

Figure 4.37 Left Side view of the SPD failure mode after draining the ditch, with clear indication of the exit point of the slip circle. Right Top/back view of the sheet piles after failure and local excavation, the dashed line indicates the inclination of the sheet pile. All interlocks of sheet piles are still intact.

Figure 4.38 Left: Removal of the long sheet piles after the test and after excavation of embankment. Right: Failed sheet pile, with visible buckling of the compression flanges.
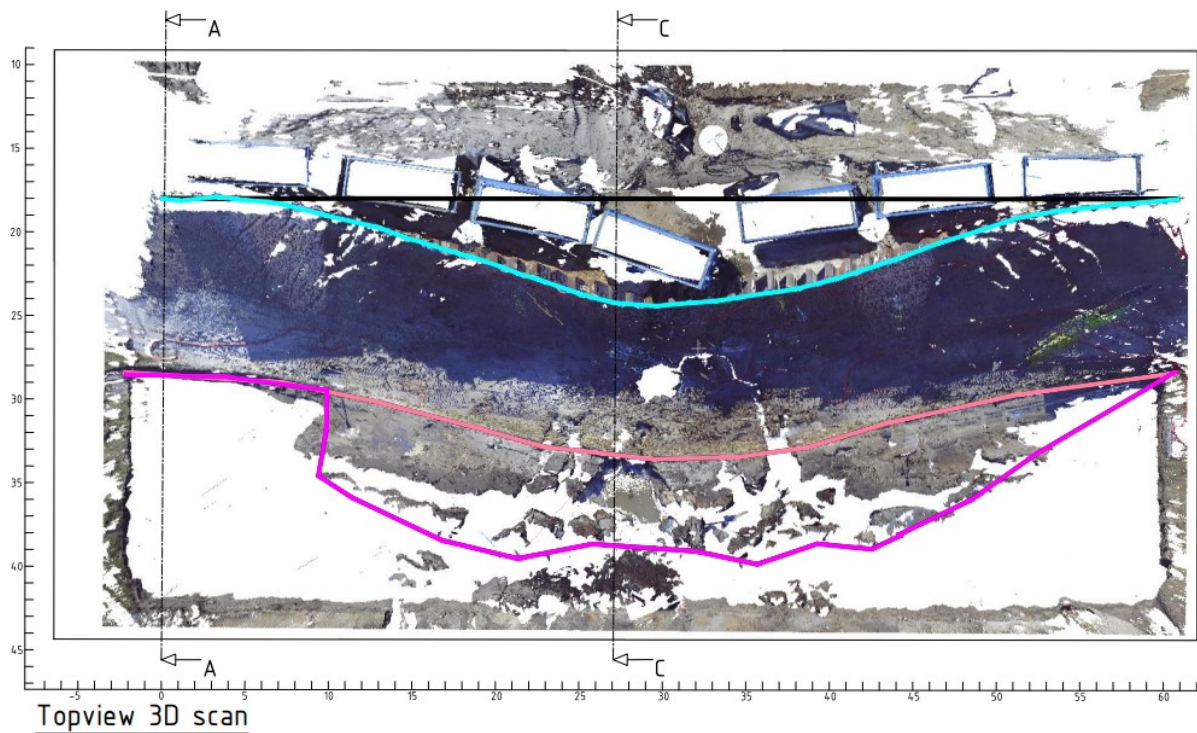
Figure 4.39 Top view generated from 3D laser scan of the failed SPD. The black line is the original sheet pile location with 61 m length. The blue line is the top of the sheet pile after failure, which is elongated by 1.75 m. The orange line is the toe of the slope after failure. The purple line is the extend of the failure surface that is pushed up above the water level of the ditch.

4.7 Evaluation of failure and deformations

The Eemdijk full-scale failure tests provides a unique opportunity to compare the deformations of a ground dike with a sheet pile reinforced dike (Research question 4). The measured

125

deformations of both dikes are presented and evaluated in this section, as well as the performance in terms of safety. The purpose of this evaluation is:

- To determine and compare the 'moment of failure' for both dikes.
- To determine the deformations prior to failure, as this is relevant for (1) other failure mechanisms, such as erosion due to overtopping, and for (2) specifications for monitoring, remote sensing and the observational method.
- To determine the final displacements of the residual profile, as this is relevant for the sequential failure path analysis and ultimately the failure of the flood defense.
- To determine the basis for monitoring instrumentation specifications and to evaluate performance criteria as a basis for sheet pile reinforced dikes, such as allowable deformations.

4.7.1 Definition of failure

In order to determine the deformations prior to slope failure, the 'moment of failure' needs to be defined. This is defined as the moment in time when progressive failure under constant loading is permanent (irreversible). This moment is based on the evaluation of the measurements presented in Figure 4.40 to Figure 4.47. From this evaluation, the moment of failure is set to a horizontal displacement rate of 1 cm per hour at the toe of the dike, see vertical line in Figure 4.60 and Figure 4.61. This moment coincides with a sharp increase in displacement rate, and with the occurrence of visual cracks in the slope. The corresponding horizontal displacement is in the order of 10 to 20 cm.

Prior to slope failure, the displacement rate is typically one order of magnitude lower, while loads increase. After slope failure, the displacement rate is more than one order of magnitude larger, with constant loads. The progressive failure is stopped after reaching a new equilibrium between loads and strength, resulting in a residual geometrical profile.

Based on the evaluation of the SPD measurements it is concluded that failure of the slope occurs prior to the buckling failure of the sheet pile. The latter is considered the point where the integrated system of the sheet pile reinforced dike fails. The failure results in a partial flooding (i.e., overflow of the sheet pile wall middle section), without breach.

Figure 4.40 and Figure 4.41 present the slope displacements in time for both dikes. Figure 4.42 and Figure 4.43 present a comparison of the horizontal versus vertical displacement, and the crest versus toe displacement. Figure 4.44 and Figure 4.45 present the horizontal displacements versus the absolute and relative water level for both dikes. Figure 4.46 and Figure 4.47 present the horizontal displacement rate at the crest and toe for both dikes. The figures are evaluated in the next sections.

It should be noted that the construction induced deformations prior to the test are excluded from these figures, as these occurred over a long period (6 to 9 months) with partial consolidation and were not related to the failure test. The horizontal displacements during construction are about 30 cm at the toe. This is larger than the additional undrained displacement at the moment of failure.
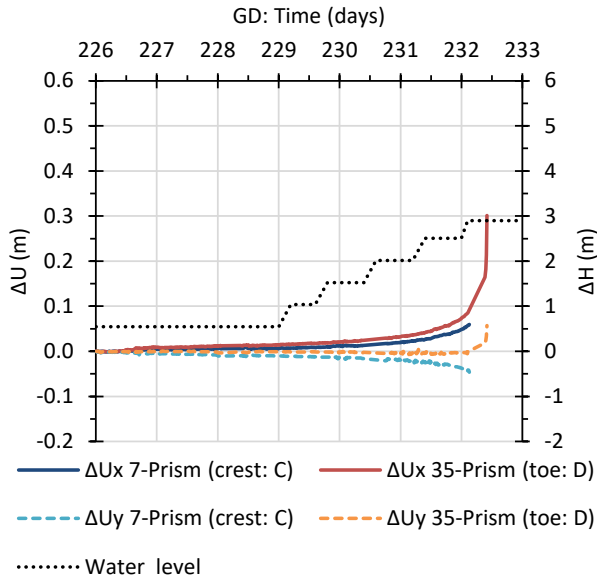
Figure 4.40 Horizontal and vertical displacements of the GD during the failure test. The approximate water level is indicated on the secondary y-axis. The displacements at the crest are identified by point (C) and at the toe by (D). Not all prisms could be monitored at larger displacements than 5 cm.
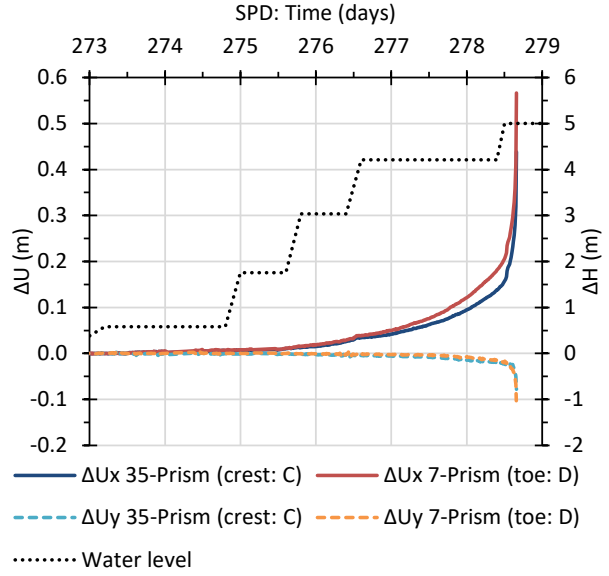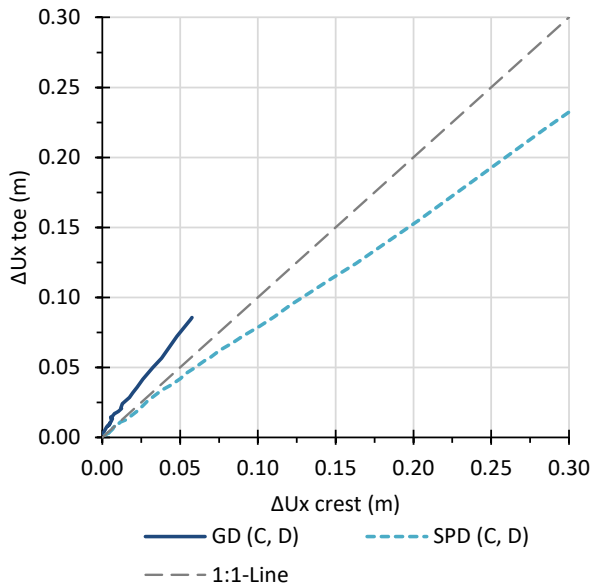
Figure 4.41 Horizontal and vertical displacements of the SPD during the failure test. The approximate water level is indicated on the secondary y-axis. The displacements at the crest are identified by point (C) and at the toe by (D). Not all prisms could be monitored at larger.

Figure 4.42 Horizontal displacements at the crest (C) versus horizontal displacement at the toe (D) for the GD and SPD.
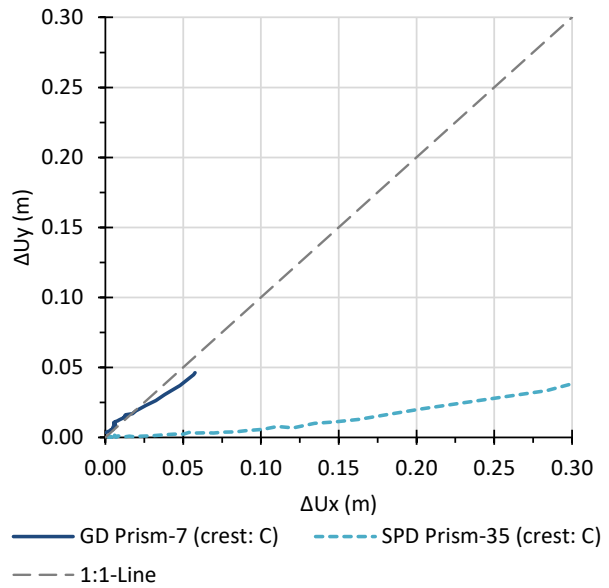
Figure 4.43 Horizontal displacements versus vertical displacement, at the crest (C), for the GD and SPD.
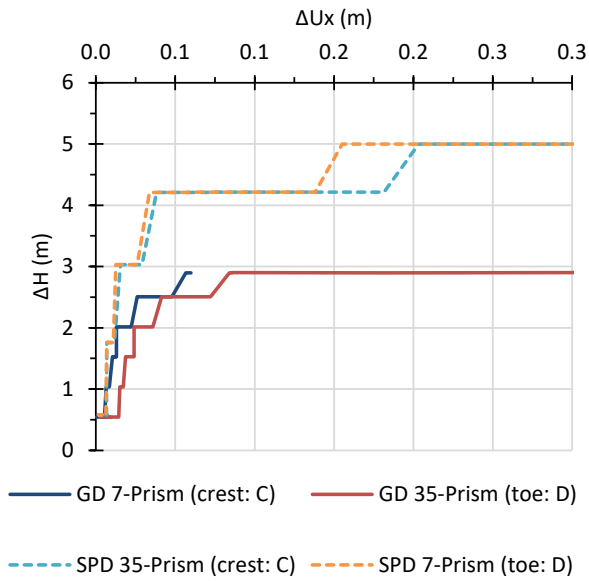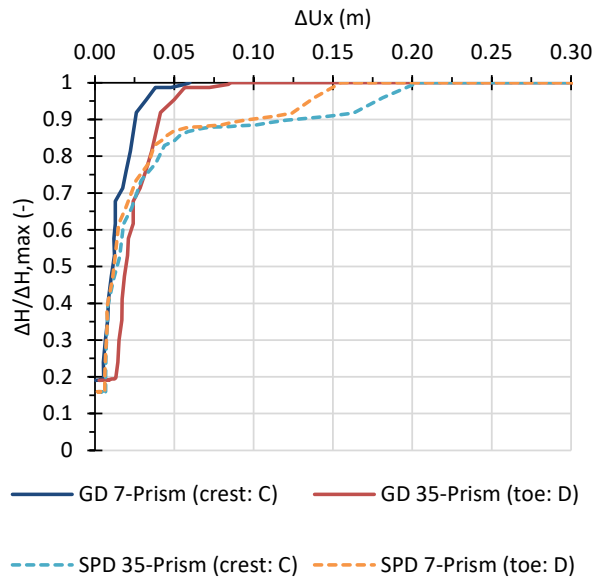
Figure 4.44 Horizontal displacement s of the GD and SPD versus the maximum water level in the embankment. The displacements at the crest are identified by point (C) and at the toe by (D). Not all prisms could be monitored at larger displacements than 5 cm.

Figure 4.45 Horizontal displacement s of the GD and SPD versus the relative water level in the embankment. The relative water level is defined as the water level normalized by the maximum water level at failure.
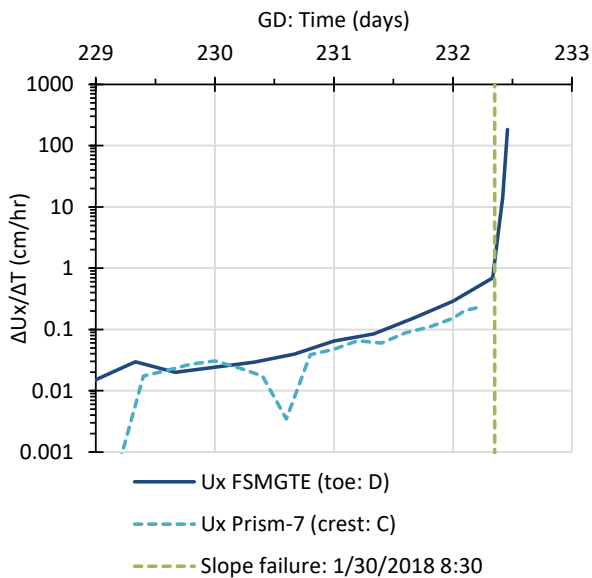

Figure 4.46 Horizontal displacement rate of the GD during the last days of failure test. The displacement rate at the crest followed from the prism and at the toe from the inclinometer measurements. The inclinometer could be measure beyond slope failure. The slope failure, defined at a rate of 1 cm/hr, is indicated in the graph at 8:30 hr.
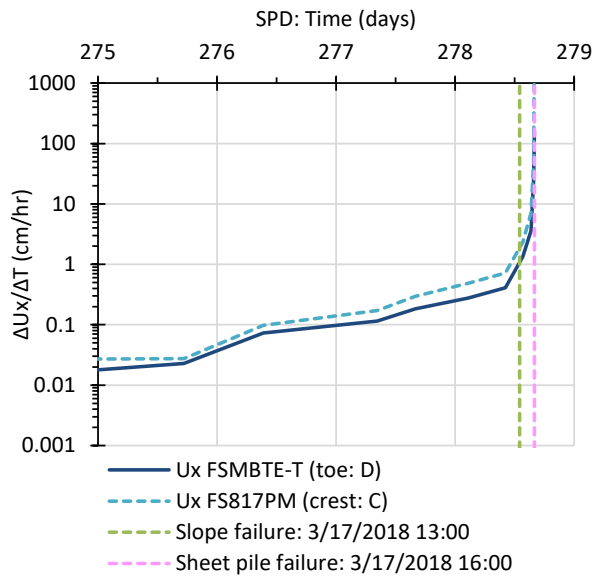
Figure 4.47 Horizontal displacement rate of the SPD during the last days of failure test. The displacement rate at the crest and toe followed from the inclinometer measurements. The slope failure, defined at a rate of 1 cm/hr, is indicated in the graph at 13:00 hr. The sheet pile failure is indicated in the graph at 16:00hr.

4.7.2   Resume of failure deformations at the GD

This section summarizes the deformations at the GD, based on the measurements at the crest and toe of the slope. The failure can be characterized by two stages, (1) prior to slope failure and (2) after slope failure. For the deformations at the GD prior to slope failure it is concluded that:

- The horizontal displacements at the crest are smaller than at the toe, see Figure 4.42. Apparently, the slope failure starts at the toe.
- At the moment of slope failure, the horizontal displacements at the toe are about 10 to 20 cm, with some first small visual cracks at the crest and top of the slope (Breedeveld et al. 2018a).
- The vertical displacements at the crest are slightly smaller than the horizontal displacements at the crest, see Figure 4.43.
- The vertical displacements at the toe are negligible and eventually switch direction upwards, see Figure 4.40.

For the deformations at the GD after slope failure it is concluded that:
- From the Triaxial tests it is concluded that softening occurs at large strains. Softening causes the displacements to increase with a large displacement rate, in the order of one meter per hour. Tension cracks appeared at the crest and top of the slope, shear cracks at the sides and circumferential cracks at the toe, see photos Appendix J.
- With the ongoing deformation, the driving forces decrease until a new equilibrium is found based on the residual strength and residual profile.
- The vertical displacement of the failed slope is 3.5 m, which is 66% of the initial height, reducing the height to about 1/3 the initial height, see Figure 4.51.

4.7.3   Resume of failure deformations at the SPD

This section summarizes the deformations at the SPD, based on the measurements at the sheet pile, at the crest and toe of the dike. The SPD-test can be characterized by three stages, stage 1 prior to slope failure, stage 2 after slope failure and prior to sheet pile failure, stage 3 after slope failure and sheet pile failure. For the deformations at the SPD, prior to slope failure, it is concluded that:
- The horizontal displacements at the crest, on the slope side of the sheet pile, are larger than at the toe, see Figure 4.42. Apparently, the deflection of the sheet pile pushes the slope at the crest forwards.
- The vertical displacements at the crest, on the slope side of the sheet pile, are negligible, see Figure 4.43. The same applies to the vertical displacement of the sheet pile top.
- The vertical displacements at the crest on the outboard side (water side) of the sheet pile are not shown here, but are typically half the horizontal displacement at the crest.
- The vertical displacements at the toe are negligible and remained downwards, see Figure 4.41.
- At the moment of slope failure, the horizontal displacements at the toe are in the order of 10 to 20 cm. Cracks occur at the active side (water side) of the sheet pile. On the passive side, cracks are mitigated by the compression of the sheet pile (Breedeveld et al. 2018a).
- The duration of this stage was about 7 days.

For the deformations at the SPD, after slope failure and prior to sheet pile failure, it is concluded that:
- Softening after slope failure causes the displacements rate to increase to about 10 cm/hr until structural failure of the sheet piles, see Figure 4.47. The sheet piles failed due to the large deflection and associated exceedance of the maximum bending moment capacity (local buckling failure), see Figure 4.38.

- At the moment of sheet pile failure, the horizontal displacement at the crest is up to 60 cm, the horizontal displacement at the toe is up to 40 cm, see Figure 4.41.
- The vertical displacement of the sheet pile is still limited to 2 cm, see Appendix K.
- The duration of this stage was about 3 hours.

The failure of the sheet pile occurred at approximately -3.5 m NAP. The corresponding maximum curvature at -3.5 m NAP is approximately 0.015 m^{-1}. Technically the sheet piles lost most of the bending moment capacity, basically creating a plastic hinge. It didn't cause rupture of the sheet piles. The upper part of the sheet piles was pushed forwards and at some point could not move further due to resistance of the soil mass in front. Although this soil mass failed and deformed significantly, a new equilibrium was reached once the sheet pile deflection was almost 1:1. The interlocks of all sheet piles remained intact. The top of the sheet pile ended about 1 m below the maximum water level, which created a weir (overflow barrier) and partial flooding. For the deformations at the SPD, after slope failure and sheet pile failure, it is concluded that:

- The sheet pile deflection increases significantly after sheet pile failure. This is regarded as the moment of system failure, failure of the dike with sheet pile reinforcement, resulting in a partial flooding.
- Softening causes the deformations to increase with a very large displacement rate in the order of one meter per minute, see Figure 4.47.
- With the ongoing deformations the driving forces decrease, until a new equilibrium is found based on the residual strength of soil and sheet pile, residual geometrical profile and the membrane action in the sheet pile wall, as shown Figure 4.39. This membrane action in horizontal direction was possible because a continuous wall was installed over the upper part. This requires that the sheet piles should all be interlocked.
- The vertical displacement of the slope is 2.3 m, which is 47% of the initial height, reducing the height to about 1/2 the initial height, see Figure 4.55.
- The final vertical displacement of the top of the sheet pile was 1.9 m. The associated level was the highest point of the SPD middle cross section, as well as the lowest crest level location for the whole SPD, see Figure 4.37.
- The failure was followed by a flooding due to overflow of the wall. The flood did not damage the clay cover of the slope, but it caused further disintegration of the pushed-up peat layers in the ditch, see Appendix K.

4.7.4   Comparison of failure deformations both dikes

This section presents a comparison between the GD-test and SPD-test. The maximum water level at the SPD is about 2.1 m higher than at the GD (+5.0 m NAP versus+2.9 NAP), which is a considerable increase. This water level in the embankment is considered as the primary parameter of the loading, although also other loading effects are present at both dikes. The main conclusions with respect to the comparison of displacements at lower water levels are:

- The horizontal displacements at the SPD are typically a factor 3 times smaller, given the same water level, up to +2.5 m NAP. The horizontal displacements at the SPD are only 2 cm at a water level of +2.9 m NAP, the water level at which the GD failed. The sheet pile wall clearly increases the strength and stiffness of the dike.

- In relative terms, up to 80% of the maximum water level the horizontal displacements for both dikes are limited to 5 cm. Above 80% of the maximum water level, the horizontal displacement of the SPD exceeds that of the GD, see Figure 4.45.

The comparison of the failure deformations for the GD-test and SPD-test is presented in Table 4-23

Table 4-23 Comparison of failure deformations GD-test and SPD-test

Criteria	GD-test	SPD-test
Water retaining height at failure	2.9 m	5.0 m
Relative water retaining height at failure ($\Delta H_{water}/H_{dike}$)	0.6 H	0.9 H
First failure mode (element level)	slope failure	slope failure
Second failure mode (element level)	N.A.	structural failure of sheet pile
Global failure flood defense (system level)	no, the infiltration of water in the dike was stopped after slope failure.	yes, the sheet pile failure lowered the crest below the water level and caused a flooding without breach.
Visual signs before slope failure:	tension cracks at the top of the slope	active wedge cracks on the crest behind the sheet pile on the outboard side
$U_{hor;toe}$ prior to slope failure	10 to 20 cm	10 to 20 cm
Ratio of $U_{hor;crest}$: $U_{hor;toe}$	1.0 : 1.5	1.0 : 0.7
Ratio of $U_{hor;crest}$: $U_{ver;crest}$	1.0 : 1.0	1.0 : 0.1
Duration of failure:		
Duration prior to slope failure	7 days	7 days
Duration of slope failure	7 hours	3 hours
Duration of sheet pile failure	N.A.	7 minutes
Horizontal deformation rates:		
Deformation rate prior to slope failure	up to 1 cm/hour	up to 1 cm/hour
Deformation rate after slope failure	up to 1 m/hour	up to 10 cm/hour
Deformation rate after sheet pile failure	N.A.	up to 1 m/minute
Residual profile:		
Vertical displacement of failed slope	3.5 m	slope: 2.3 m top sheet pile: 1.9 m
Relative height of failed slope ($H_{failed\ slope}/H_{dike}$)	1/3 H	1/2 H
Horizontal displacement of failed slope	3.7 m	slope: 5 m top sheet pile: 6.3 m
Failure width along dike	30 m, half dike section	60 m, full dike section
Stability after reaching residual profile	meta-stable: the crest height is still sufficient but the crest width is reduced and the dike is vulnerable to retrogressive failure	stable: the upper part of sheet pile rotates around a 'hinge' caused by the structural failure, but the sheet piles remained intact and interlocked.

Criteria	GD-test	SPD-test
Sketches of failure mechanism		

The failure surface at the crest of the GD is located in soft clay layer 3a above the peat layer, despite the uplift conditions. Layer 3a is only present at the mid section of GD and initiated the failure over half the length of the dike. This illustrates the importance of spatial variation and the sensitivity of a ground dike to the presence of local soft layers. The failure wedge dimensions are still significant, L=30 m, H=7.3 m, W=15 m. Dikes reinforced with continuous sheet pile walls are less vulnerable to local weak layers, due to the redistribution in vertical and longitudinal direction.

After failure of the GD the residual profile of the remaining dike has become vulnerable for a breach. The breach did not occur as the test conditions prevented for this. The SPD conditions however allowed for a flooding condition. After structural failure, the upper part of sheet pile rotates around a 'hinge', but the sheet piles remained intact and interlocked. The lowering of the top of the sheet pile caused a flooding due to overflow in the middle section of the wall. The sheet pile wall acted as a weir and partial flooding occurred. The sheet pile wall prevented however a breach and uncontrolled flooding. A further discussion of the robustness of the SPD is included in section 4.9.

4.8   2D FEM back-analysis of full-scale dike failure tests

4.8.1   Introduction

This section presents the results of the back-analysis. The purpose of the back-analysis is to evaluate the performance of the FEM models (Research question 6). The GD and SPD are each back-analyzed with one representative geometrical model, based on the same initial conditions and construction stages but different failure stages. Both failure tests are simulated with the same sets of constitutive models and parameter, which makes these back-analyses unique.

The stresses and deformations in the back-analysis models are compared at the locations of the actual monitoring instrumentation. The overview of monitoring instrumentation locations in the middle cross section is shown in Figure 4.6. The locations are identified by [A, …, M].

All phases of the back-analysis are modelled in a large deformation analysis (Updated Lagrange) with pore pressure update, to account for the large initial deformations prior to failure test phase. The construction calculation phases consist of a mixture of alternating undrained effective stress calculations (in which the loading is instantaneously applied and excess pore pressures are calculated) and consolidation calculations (in which excess pore pressures are dissipated in a certain time interval). The failure test calculation phases are all considered undrained without intermediate consolidation during these seven days.

Various constitutive models have been analyzed in the back-analysis. Four of these back-analysis models will be reported in this research. The basic parameter set for each constitutive model is

based on the best estimate (average) values derived from the laboratory test results and numerical simulations, as presented in Chapter 4.3. An overview of the constitutive parameter sets is presented in Appendix L. The clay cover and top layer at the surface are modelled by the Mohr Coulomb model. The sand layers are modelled by the Hardening Soil model. The clay and peat layers are modelled by the Soft Soil Creep model during construction and switched to the SHANSEP NGI-ADP model during the test phase. The SHANSEP NGI-ADP model is the prescribed model in Dutch guidelines for FEM modeling of dikes (POVM 2020a, 2020b), whereby the prior (effective) stress state is used to derive the undrained shear strength, as used in the NGI-ADP model, according to the SHANSEP equation.

The difference between these back-analyses and a design calculation is the selection of average parameters instead of characteristic or design parameters. Average parameters are used as the aim is to simulate the behavior in the field tests, and to allow for a fair comparison with the monitoring results.

The following sections present an introduction to the FEM back-analysis models, the back-analysis results and comparison with the measurements. The effect of reduced strength and reduced stiffness parameters, as considered in geotechnical design by using partial factors, is investigated in the variation study.

4.8.2 Back-analysis models

For the compressible layers, the Soft Soil Creep model is used during the construction phases. This is applied for all back-analysis models of the GD and SPD. This model was selected as it accounts for primary (consolidation) settlements and secondary (creep) settlements. Furthermore, applying one model is preferred as different models result in different excess pore pressures at the end of the construction stage, which would make the results (of the failure phase) between the different calculations incomparable.

After the construction stage, the constitutive models are switched to another constitutive model to simulate the failure phase. The following FEM back-calculations are performed and compared with the actual measurements of both failure tests:
- FEM back-calculation c02: best estimate parameters and SHANSEP NGI-ADP model with isotropic strength. Ultimate strength parameters are determined in line with dike design calculations, however, the criteria are adjusted as presented in Chapter 4.2. The best estimate parameters are average values in contrast to characteristic values or design values as used in design calculations.
- FEM back-calculation c07: best fit parameters and SHANSEP-NGI-ADP model with isotropic strength. Best fit is based on a strength adjustment such that in 2D the maximum loading conditions can be calculated without premature failure such as in FEM back-calculation c02. The stiffness parameters are not adjusted to fit the measurements. The strength of the Holocene layers (2, 3, 3a and 4) is increased with a fit factor 1.15. The justification of this factor is discussed below.
- FEM back-calculation c03: best estimate parameters and SHANSEP NGI-ADP model with anisotropic strength. The basic parameters and DSS strength are the same as in FEM back-calculation c02, but the Active loading strength is based on the Triaxial strength without

geometric correction and the Passive loading strength is assumed to follow the ratio A : D : P is 1.0 : 0.8 : 0.67.
- FEM back-calculation c09: best estimate parameters and Creep-SClay1S effective stress model with anisotropic strength. The strength parameters are fitted both on the Triaxial strength without geometrical correction and the DSS strength.

4.8.3   Justification of FEM back-calculation c07, c03 and c09

The strength parameters of FEM back-calculation c07 are increased by a factor 1.15. The primary reason to do this is to be able to calculate all loading stages and reach failure at the correct maximum loading condition. A higher stability can be justified by two following two contributions:
- In reality failure of dikes is three dimensional, this is clearly seen in the aerial view of the GD failure. The '3D effect' is not accounted for in a2D analysis, but can be simulated by increased strength properties.
- The strength of the soil is higher, between the average and upper bound parameter set, as a function of anisotropy, peak strength instead of ultimate strength and ignoring the geometrical correction in the CAUC tests.

Conventional design of dikes is based on a 2D analysis. In Baligh and Azzouz (1975); (Vanmarcke 1977; Michalowski 2010) various analytical approaches to three-dimensional slope stability are presented, with a reported '3D factor' of 1.19 for the strength increase. The smaller the length of the cylinder the larger the end effects. A similar approach is presented in for the Eemdijk failure tests in Leclercq (2020) for a cylindrical extension of a circular failure in cohesive material. In this report it is concluded that the 3D effect approximately corresponds to a factor 1.2 for the GD and a factor 1.1 for the SPD.

In the POVM analysis report (Breedeveld et al. 2018a) a comparison is made between a 2D and 3D back-analysis for the GD. In this report it is concluded the 3D effect is significant. Where in the 2D back-analysis the stability was lower than in reality, whereas in the 3D analysis it was higher than in reality. A factor is not mentioned.

The 3D factor as summarized above is in the range of 1.1 to 1.2. The back-analysis of the GD-test shows that a factor of 1.15 is required to achieve the required stability. A factor 1.2 would overestimate the equivalent strength and would not result in failure at the maximum loading stages.

The second reason to perform back-analysis c07 with a higher strength is to verify whether this factor is lower than the ratio between the Triaxial strength without geometrical correction and the DSS strength. This factor is about 1.25 which is higher than the required factor of 1.15 to reach the same stability in the back-analysis. This has led to the other two anisotropic strength FEM back-calculations, c03 and c09, with explicit modeling of DSS and Triaxial compression strength.

4.8.4   Back-analysis of the construction phase

The embankment and subsoil showed significant construction induced displacements, vertical up to 1.0 m and horizontal up to 0.4 m without failure. These deformations are in line with expectations given the embankment height of 5 m on soft subsoil. The construction induced

deformations prior to the test occurred over a long period (6 to 9 months) with partial consolidation.

The construction phases of all FEM back-calculations are performed with the SSC model for the Holocene layers. The hydraulic parameters of the SSC model are adjusted such that during and in particular at the end of construction pore pressures match the measurements, as this determines the actual stress state and strength during the test phase. The applied adjustments are the same for the GD and the SPD. The value for the permeability parameter (k) is increased by a factor 2, except for the preloaded part at the GD. The value for the void ratio dependency parameter (C_k) is decreased by a factor 2. In addition, the horizontal permeability is increased to 10 times the vertical permeability.

Figure 4.48 and Figure 4.49 present the pore pressures during construction phase and failure test phase. The comparison of the construction phase is only shown for FEM back-calculation c07, as the construction phases are the same for all FEM back-calculations. The solid lines are the measurements and the dashed lines the back-analysis results. Based on these figures it is concluded that the excess pore pressures are correctly modelled.

A more extensive overview with comparison of deformations for both dikes is presented in Appendix J and Appendix K. In general, it can be concluded that the back-analysis deformations match very well with the measurements.
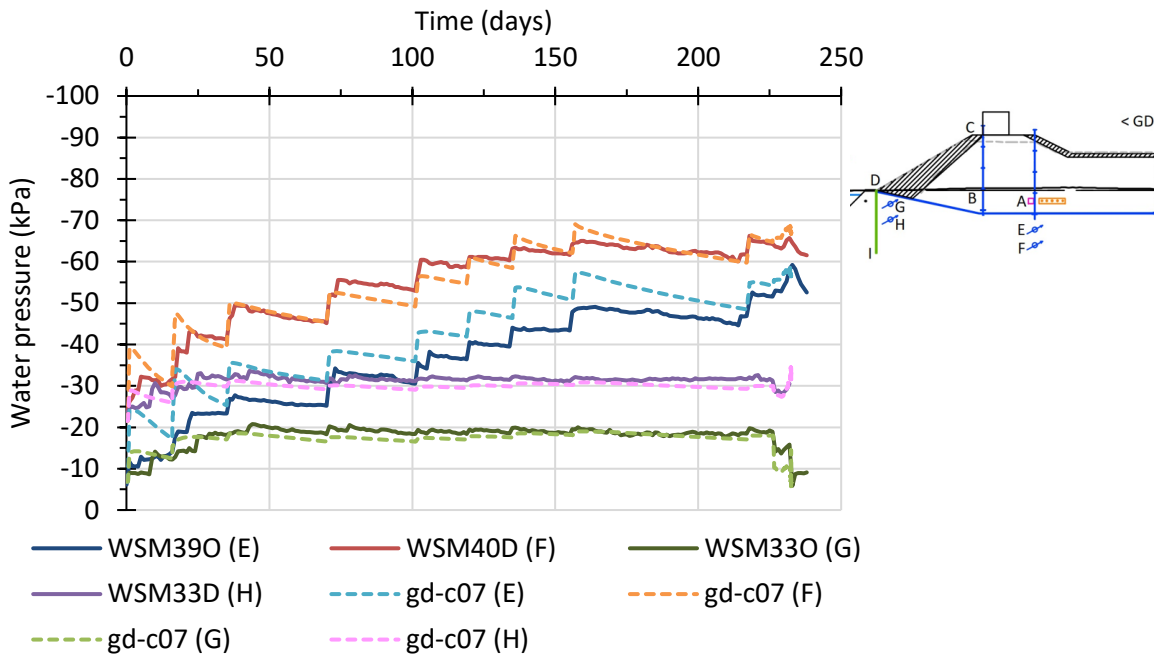
Figure 4.48 Ground dike, measurements (WS..) and back analysis (gd-c07) of pore pressure, at 1.5 m depth in the clay and 3.0 m depth in the peat, at the toe and crest. The initial pore response in the FEM back-calculation was higher than the measurements, but . the final response is well aligned with the measurements. The pore pressure response in the peat layer at the toe is about 10 kPa and below the crest about 40 kPa at the start of the GD-test.
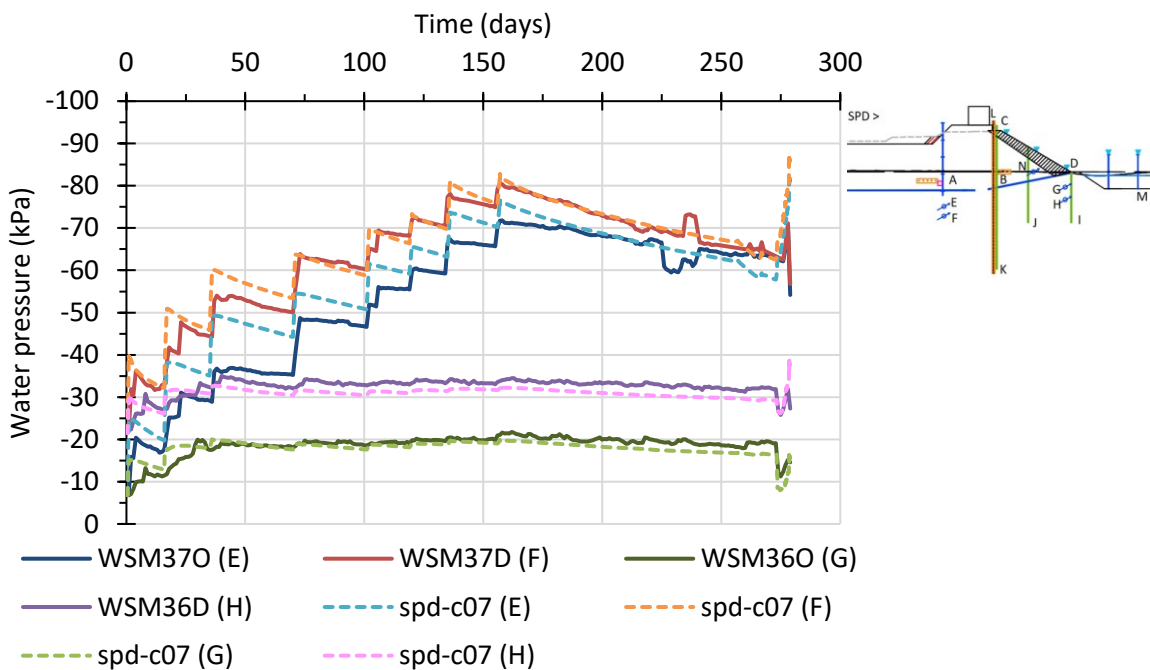

Figure 4.49 Sheet pile dike, measurements (WS..) and back analysis (spd-c07)of pore pressure, at 1.5 m depth in the clay and 3.0 m depth in the peat, at the toe and crest. The measured and back-calculated pore pressure response below the crest (E, F) at the GD is lower than the SPD because of the preloading. At the toe the pore pressure response is equal for both dikes.

4.8.5   Back-analysis of the GD failure test phase

This section presents the results of the back-analysis of the GD-test. The performance of the four FEM back-calculations is compared with the monitoring results and with each other.

Figure 4.50 presents the phase displacements of FEM back-calculation c07. The deformation mode complies well with the reconstructed failure mode based on observations as presented in Figure 4.51. The deformation mode is similar for all four back-analyses with a failure surface in the soft clay layer 3, just above the peat layer 4.
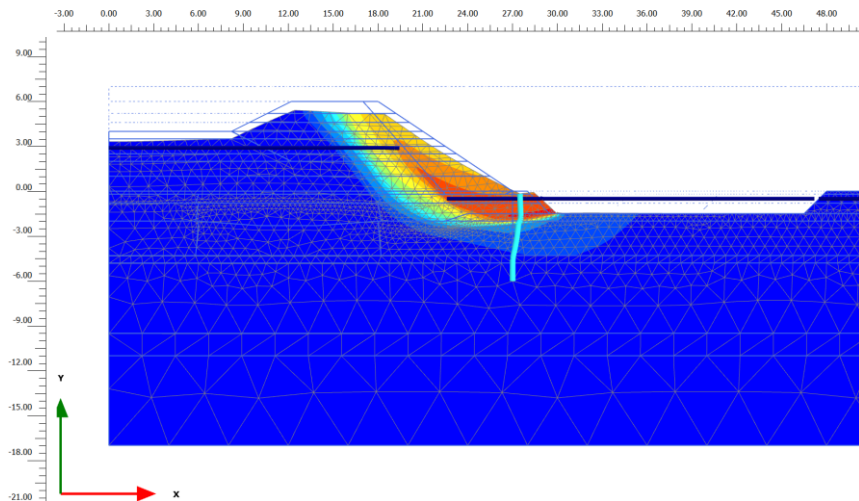
Figure 4.50 Ground dike, phase displacements prior to failure. The shading is an indication of the relative displacement (red is large, blue is small). The failure surface of the back analysis is located in soft clay layer 3a at 2 m depth and extends in the fill just behind the clay cover. The light blue line indicates the modelled inclinometer (SAAF I).
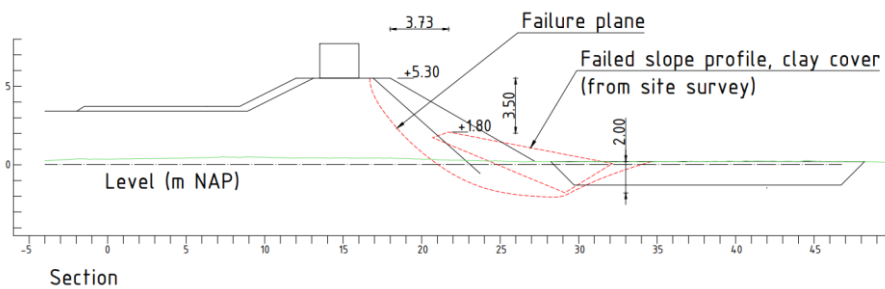
Figure 4.51 Reconstructed failure surface of the GD with deepest point at 2 m depth just above the peat layer 4.

The vertical displacements at the crest are presented in Figure 4.52. This is the first figure of the GD where all four FEM back-calculations are presented and compared. It is concluded that the back-analysis c02, with average properties, overestimates the vertical displacements at any moment in time and results in a premature instability. Also, the horizontal displacement, for the same location (C), in back-analysis c02 overestimates the displacements at any moment in time.

FEM back-calculation c07 with the increased strength is fitted such that the moment of instability matches the measurements. From this analysis it can be concluded that also the displacements match considerably better, albeit still underestimated. The performance of FEM back-calculation c03 and C09 are similar and perform in between FEM back-calculation c02 and c07. This is conformed by the results from the back-analysis of the horizontal displacement measured by the inclinometer at the toe, presented in Figure 4.53.
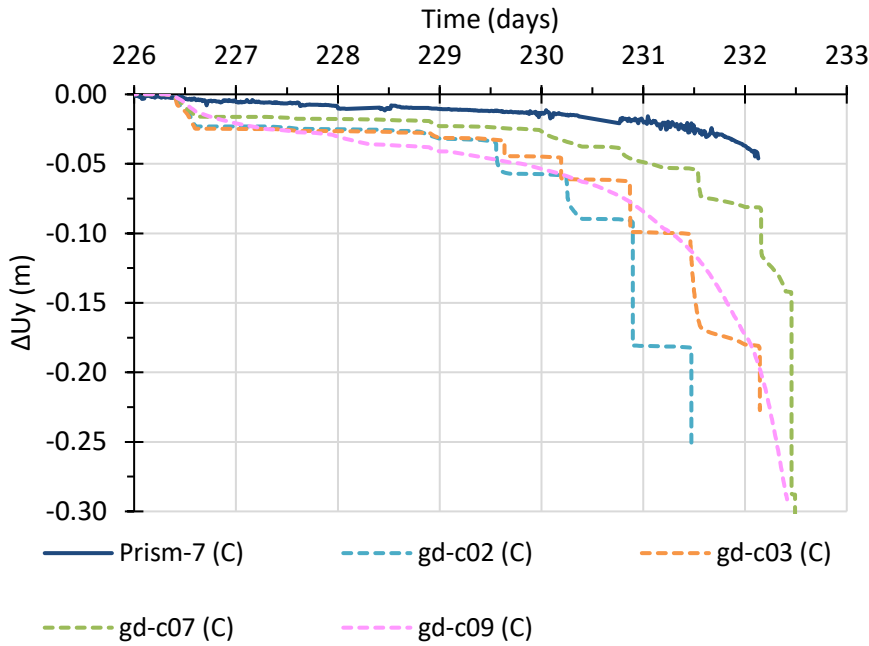
137

Figure 4.52 Ground dike, measurements (Prism..) and back analysis (gd..) of vertical displacements, at the crest (location C). The vertical displacements (settlement) following the FEM back-calculations are all larger than the measurements during the field test. FEM back-calculation gd-c02 deviates the most due to early failure following the relative lower strength. FEM back-calculation gd-c07 performs best with no early failure and slightly larger displacements.
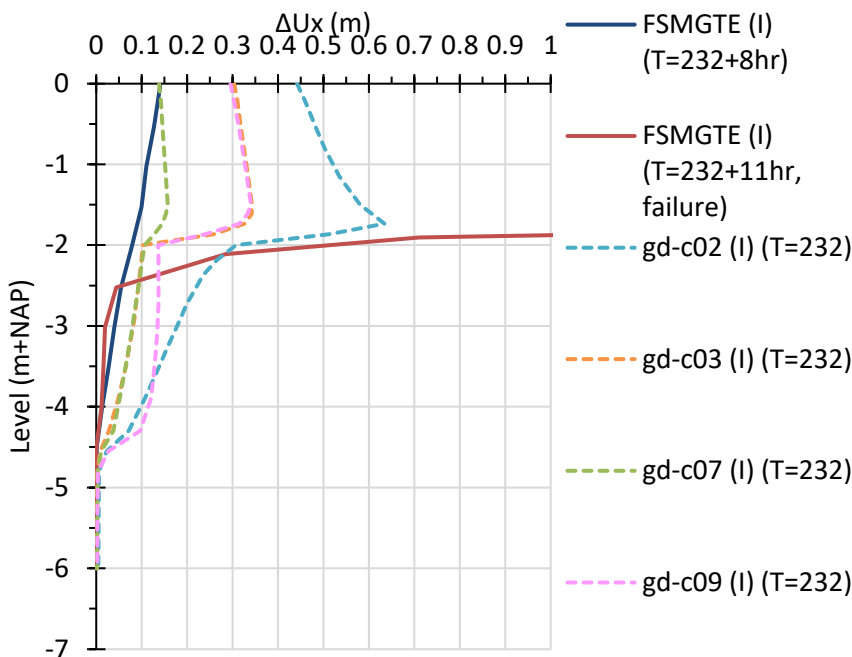

Figure 4.53 Ground dike, inclinometer measurements (FS..) and back analysis (gd..) of horizontal displacements over depth, at the toe (SAAF location I). Last loading stage prior to failure with water level +2.5 m NAP. The location of the sliding surface at -2 m NAP is well captured by the FEM back-calculations. FEM back-calculation gd-c02 deviates the most due to early failure following the relative lower strength. FEM back-calculation gd-c07 performs best with no early failure and slightly larger displacements.

Numerically, FEM back-calculation c03 and c09 with anisotropic strength finished successfully. It is concluded that despite the difference in constitutive model and input parameters the performance of FEM back-calculation c03 and c09 is similar.

A more extensive overview with comparison of the FEM back-calculations is presented in Appendix J. In general, it can be concluded that the direction of the displacement and the relative displacements match very well with the measurements.

4.8.6   Back-analysis of the SPD failure test phase

This section presents the results of the back-analysis of the SPD. The performance of the four FEM back-calculations is compared with the monitoring results and with each other.

Figure 4.54 presents the phase displacements of FEM back-calculation c07. The deformation mode complies well to the reconstructed failure mode as presented in Figure 4.55. The deformation mode is similar for all four FEM back-calculations. The failure of the sheet pile occurred in all FEM back-calculations at the same level (about -3.5 m NAP) followed by a global failure of the dike.

Figure 4.56 presents the horizontal displacements of the four FEM back-calculations. This is the first figure of the SPD where all four FEM back-calculations are presented and compared. As for the GD, it is concluded that the back-analysis c02 overestimates the displacements at any moment in time, with a premature instability. The vertical displacement are far less, hence the differences are also much smaller. With the increased strength properties of FEM back-calculation c07, failure occurs in the correct stage with the correct loading and with a slight overestimation of the displacements. The performance of FEM back-calculation c03 is in between FEM back-calculation c02 and c07. Other than in the GD back-analysis, the performance of FEM back-calculation c09 with the anisotropic CSS1S model is even slightly better than c07.

The horizontal displacements measured by the inclinometer at the sheet pile are presented in Figure 4.57. The failure location is in all four FEM back-calculations located at a level of about -3.5 m. The same conclusions, as for Figure 4.56 , apply to the performance of the back-analysis models based on this figure.

A more extensive overview with comparison of the FEM back-calculations is presented in Appendix K. In general, it can be concluded that the direction of the deformation and the relative deformations match very well with the measurements. The performance of each FEM back-calculation is as described above. The performance of the anisotropic FEM back-calculation c03 in the SPD back-analysis is slightly better than in the GD back-analysis as it closer the actual measurements.
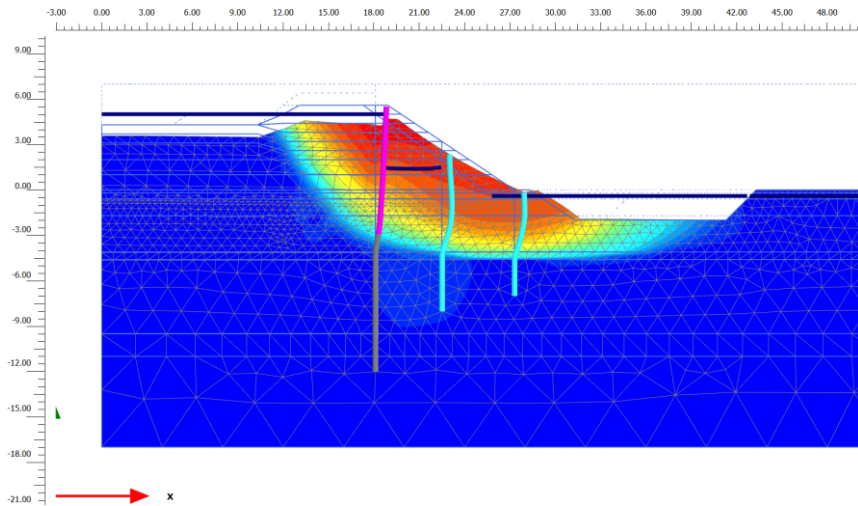
Figure 4.54 Sheet pile dike, shaded plot of phase displacements prior to failure (red is large, blue is small). Near the toe, the failure surface of the back analysis is located at the base of peat layer 4 at 4 m depth. Below the slope in front of the sheet pile, the failure surface changes to a failure zone over the height of the peat layer 4. Behind the sheet pile an active wedge occurs. The magenta line is the continuous sheet pile and the grey line is the staggered part. The turquoise lines are the modelled inclinometers.
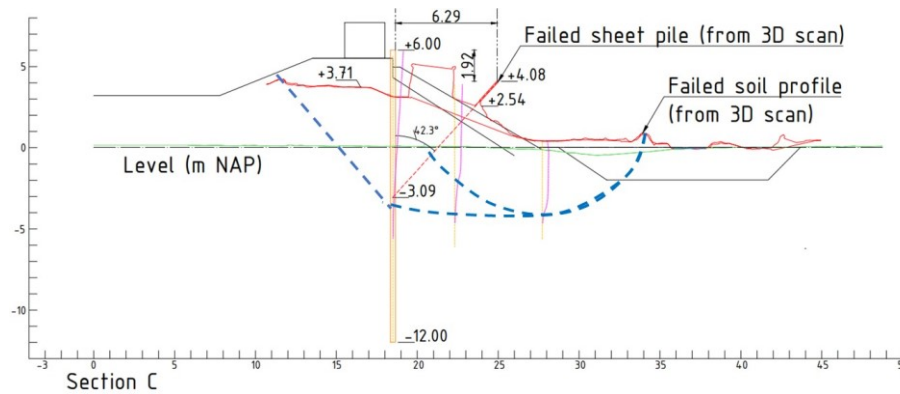
Figure 4.55 Reconstructed failure surfaces from 3D scans and surveys. On the passive side the exit point of the slip circle is at the left side of the ditch, where the soil is pushed up more than 2 m. At the toe, the failure surface is at the boundary between the peat layer and sand layer at -4.2 m NAP. Towards the sheet pile there seems no single failure surface, but a failure zone indicated between the two dashed lines. The maximum inclination of the sheet pile is 42 degrees. The failure point of the sheet pile is approximately at -3.5 m NAP and in all cases between -3.0 m (the stagger level) and -4.1 m NAP (the top level of the sand level). On the active side an area of active wedges developed.
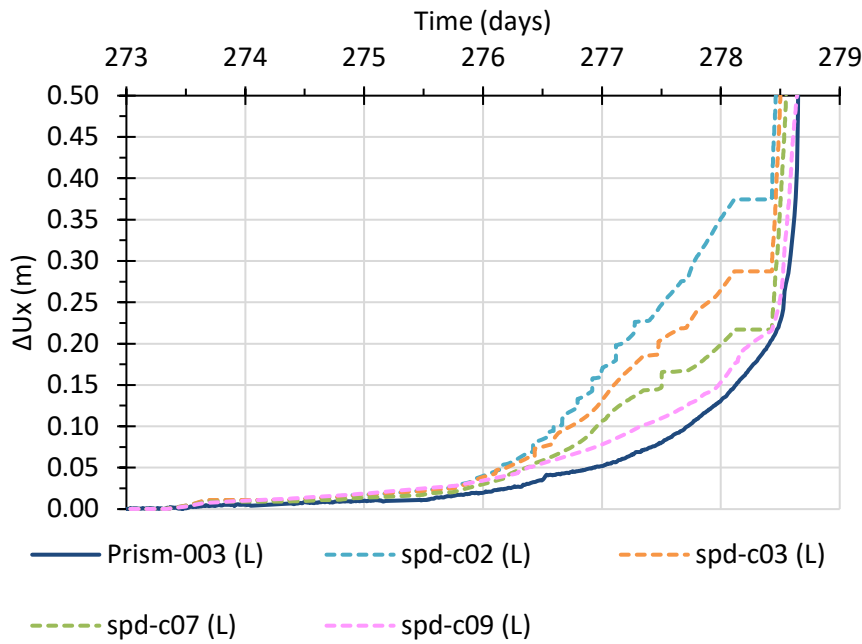
Figure 4.56 Sheet pile dike, measurements (Prism..) and back analysis (spd..) of horizontal displacements, at the top of the sheet pile (location L). The horizontal displacements following the FEM back-calculations are all larger than the measurements during the field test. The performance of FEM back-calculation spd-c07 and spd-c09 is the best. The performance of these models is better than for the ground dike without sheet pile.
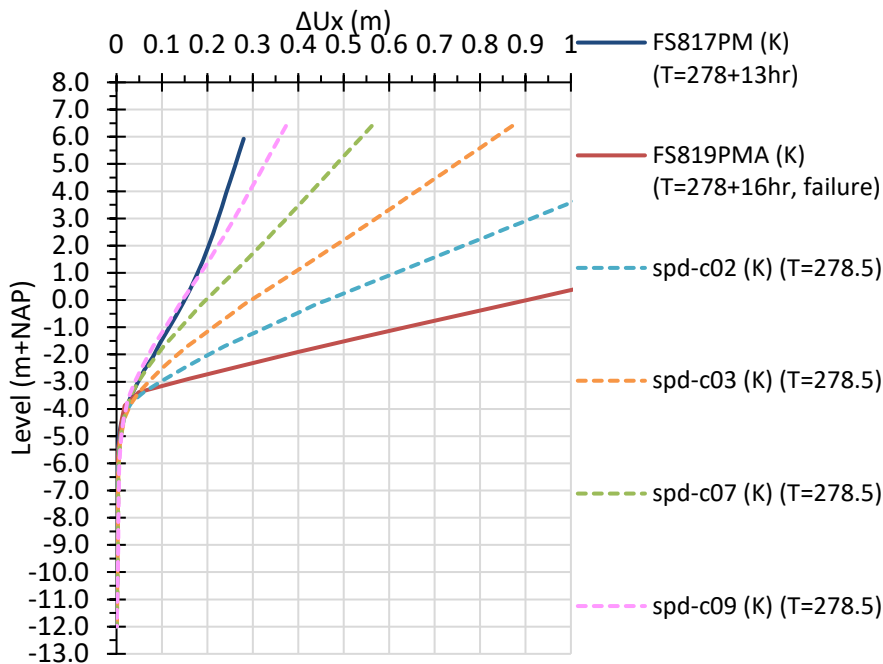

Figure 4.57 Sheet pile dike, measurements (FS..) and back analysis (spd..) of horizontal displacements over depth, at the sheet pile (SAAF location K). Last loading stage prior to failure with water level +5.0 m NAP. The location of the plastic hinge in the sheet pile at about -3.5 m NAP is well captured by the FEM back-calculations. FEM back-calculation spd-c02 deviates the most due to near failure following the relative lower strength. FEM back-calculation spd-c07 and spd-c09 performs best with no early failure and slightly larger displacements.

4.8.7   Variation study

The comparison between FEM back-calculation c02 and c07 clearly indicates the effect of increased (or reduced) strength on the deformations. A lower strength results in a higher

deformation, due to more plastic straining, and a higher strength in a lower deformation, given the same loading condition. This is shown in all back-analysis results. This is typical for advanced non-linear models, in contrast to simple elastoplastic models, such as the linear-elastic perfectly plastic Mohr-Coulomb model. This means that in a serviceability limit state (SLS) analysis with parameters based on characteristic strength the deformations will increase compared to an analysis with parameters based on average strength. In an ultimate limit state (ULS) analysis, where the characteristic strength is reduced by partial factors, the deformations will further increase.

The effect of reduced strength and reduced stiffness parameters is investigated in an additional variation study presented in this section. For the sake of comparison, FEM back-calculation c07 is regarded as a model with characteristic strength parameters and average stiffness parameters. FEM back-calculation c02 is regarded as a model with design strength parameters and average stiffness parameters. Two additional FEM back-calculations (c07k and c02k) are added where for both models the stiffness is further reduced with a factor 1.5 to simulate a characteristic stiffness. Table 4-24 presents an overview of the FEM back-calculations.

Table 4-24 Overview of FEM back-calculation models to investigate effect of strength and stiffness reduction

	Average stiffness	Characteristic stiffness
Characteristic strength	c07	c07k
Design strength	c02	c02k

Figure 4.58 presents the variation-analysis results of the horizontal displacements at the crest of the GD and Figure 4.59 presents the results for the SPD. Both figures confirm that the displacements are mainly affected by a reduction in strength, even though the factor on the strength parameters is 1.15 compared to 1.5 on the stiffness parameters.

The combined effect of reduced strength and stiffness is shown by comparison FEM back-calculation c07 with c02k. The combined effect results in a significant overprediction of the displacements, approximately a factor 2. This is regarded as not representative for SLS conditions, and the suggestion of large deformations without failure can be an unsafe perception. Furthermore, if these reductions are used in SLS calculations for performance-based design criteria (or observational method) this would lead to over-designed stiff structures leading to significant cost increase. Therefore, it is recommended whenever advanced constitutive models are applied, not to apply characteristic stiffness parameters in addition to characteristic strength parameters, but to use average stiffness parameters, as the plastic straining already reduces the stiffness and increases the deformations.
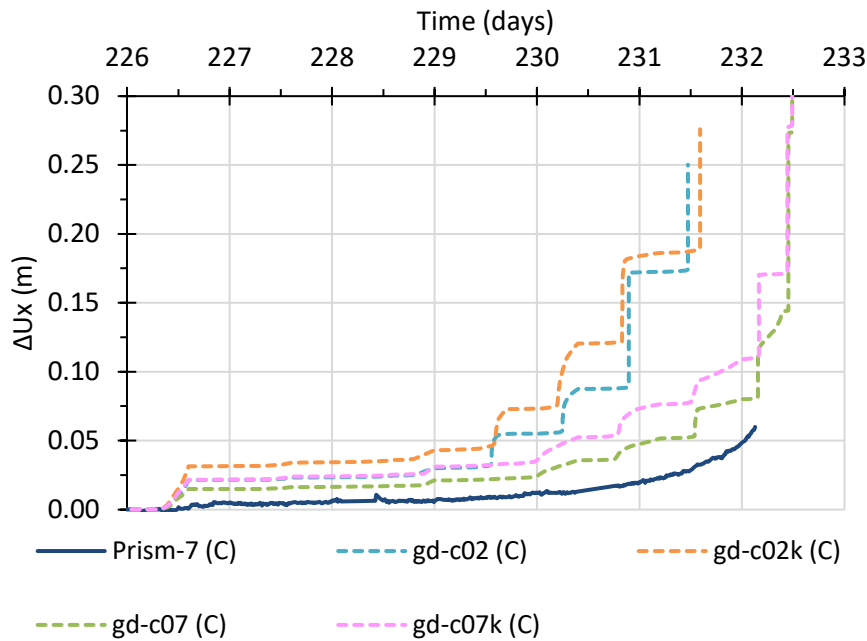
Figure 4.58 Ground dike, analysis of characteristic value on horizontal displacements, at the crest (location C). The horizontal displacements following the FEM back-calculations are all larger than the measurements during the field test. FEM back-calculation gd-c02 and gd-c07 are presented to show the effect of 15% strength reduction on the displacements and stability. Both FEM back-calculations are also calculated with a factor 1.5 reduction of the stiffness to simulate the effect of a characteristic stiffness.
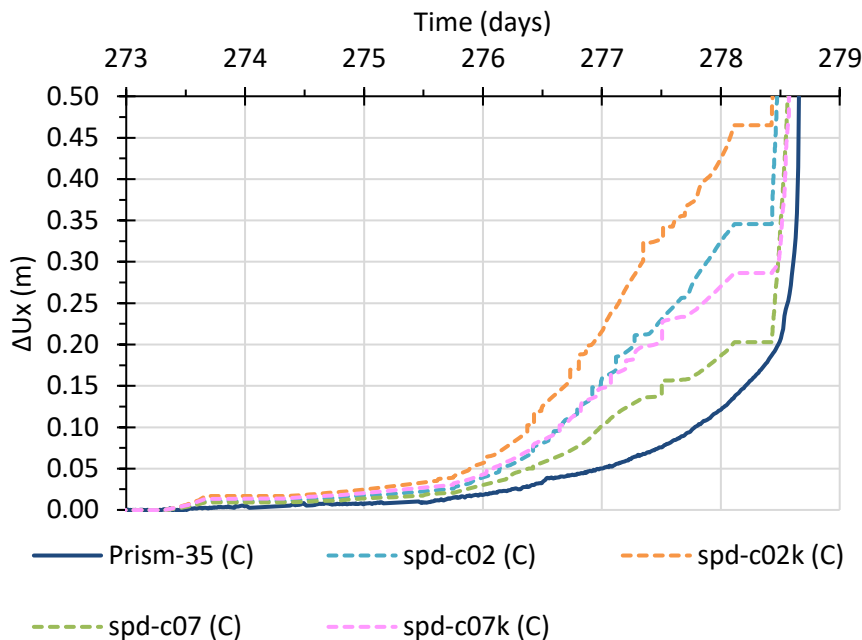

Figure 4.59 Sheet pile dike, analysis of characteristic value on vertical displacements, at top of the sheet pile (location L). The horizontal displacements following the FEM back-calculations are all larger than the measurements during the field test. FEM back-calculation spd-c02 and spd-c07 are presented to show the effect of 15% strength reduction on the displacements and stability. Both FEM back-calculations are also calculated with a factor 1.5 reduction of the stiffness to simulate the effect of a characteristic stiffness.

143

4.8.8   Concluding remarks back-analysis

Both the vertical and horizontal construction induced displacements are well captured by the Soft Soil Creep (SSC) model. Alternatively, the CSC1S model can be used as it also accounts for creep. The HS model can be used but it requires a correction of the compression stiffness to account for creep.

The back-analysis of the pore pressures in the embankment fill and subsoil are well aligned with the measurements, both for the GD-test and SPD-test. This is crucial to obtain correct effective stresses, state and undrained shear strength in the SHANSEP model. The permeability parameters, although primarily based on the K_0CRS test, are iteratively determined as they are constitutive model dependent.

The GD-test back-analysis confirms the location of the failure surface at the toe in soft clay layer 3a at 2 m depth, which extends in the fill just behind the clay cover. This is confirmed in all models and each back-analysis, which means that the strength properties are well selected. It also implies that even a small layer of about 0.5 m thickness over 30 m length can be determining for the safety and design.

The SPD-test back-analysis confirms the location of the failure surface at the toe in peat layer 4 at 4 m depth. Below the slope and in front of the sheet pile, the failure surface changes to a failure zone over the height of the peat layer 4. Behind the sheet pile an active wedge occurs.

The back-analyses show the sheet pile deformations and structural forces are well captured by the FEM analysis where SSI is properly taken into account. Based on the measurements and the FEM back-analysis it is concluded that the complex failure mechanism and the SSI of a dike with sheet pile should not be modelled in a LEM analysis, which considers either a slip circle analysis of a slope, or an active/passive wedge analysis of a sheet pile wall.

The displacements following the back analysis models of the GD-test and SPD-test are all larger than the measurements during the field test. The vertical displacements of the back analysis of the SPD are better aligned as these are very low due to the interaction with the sheet pile. FEM back-calculation c02 deviates the most due to early failure following the lower strength compared to the other models. With the increased strength properties of FEM back-calculation c07, failure occurs in the correct stage with the correct loading and with a slight overestimation of the displacements.

For the GD-test it is concluded that the performance of anisotropic FEM back-calculation c03 (SHANSEP) and c09 (CSC1S) is intermediate of c02 and c07. For the SPD-test it is concluded that FEM back-calculation c09 (CSC1S) even performs better than c07.

The 2D FEM back-analysis of the GD-test and SPD-test indicate a 3D effect. The stability of a real 3D failure is typically 10% higher. It is however not recommended to account for this 3D effect in designs based on regular 2D stability analysis. The GD-test shows that despite the 3D effect the stability can still be lower due to a local weak layer (3a). Therefore, it is recommended not to take the 3D effect into account in 2D analysis of dike design projects.

The anisotropic strength models with the increased Active loading strength and decreased Passive loading strength (ADP), perform better than the isotropic strength model. The effect on

the increased stability is about 10%. This would explain at least half the difference between the back-analysis and the actual measurements. This is an improvement compared with the current approach in the Netherlands. In order to implement this in dike design practice, the interpretation of the CAUC tests with respect to the geometrical correction should be reexamined. Applying a higher CAUC strength makes sense as this agrees with literature and consensus on anisotropic strength. The current applied geometrical correction, in particular when combined with 25% strain level seems too conservative.

The variation study shows that the displacements in advanced models are strongly affected by the strength. For that reason, it is not recommended to use reduced characteristic stiffness parameters in a SLS or ULS dike design analysis with advanced models, as stiffness reduction is already covered by the reduced strength parameters.

4.9 Discussion on Eemdijk full-scale failure test results

The conclusions on each Eemdijk full-scale test were presented in the subsequent previous sections. The evaluation of the Eemdijk results in the light of the research questions is presented in the next chapter. This section presents the discussion on the robustness of sheet pile reinforced dikes based on the SPD-test, how this compares to other configurations and experiences with sheet pile reinforcement and how it can used to improve dike engineering practice.

4.9.1 Robustness

In the context of codes and standards for structural design such as the Eurocode, the term robustness has been used to indicate the ability of a structural system to resist damage under extreme loads. In Stochino et al. (2019), robustness is described as the structure's ability to avoid disproportionate collapse due to an initial damage. Some recommendations they provided to enhance robustness are alternative load paths and redundancy at various levels, i.e., material level, member level, and system level.

The full-scale failure tests are regarded as representative for real river dikes in the Netherlands, given the retaining height of 5 m, the soft subsoil layers followed by a sand layer, the loading by an increase of the groundwater level in the dike over a period of one week and the uplift conditions. The failure mechanisms of the GD and SPD are illustrated in Figure 4.60 and Figure 4.61. The slope instability of the GD causes a significant displacement of the inboard slope and lowering of the inboard crest (Δz_{crest}). This is the first or initiating failure mechanism, and can be regarded as element failure, an exceedance of the ultimate limit state (ULS). It is not the system failure of a flood defense.

System failure requires retrogressive failure which ultimately results in a breach and flooding. The sequential failures can be assessed by a failure path analysis, for example a secondary failure surface near the outboard crest followed breaching due to seepage and erosion. The quantification, however, is associated with large uncertainties, both in terms of physical processes as probability of occurrence. The state of the dike after initial failure is vulnerable to sequential failures and the remaining crest is regarded as 'metastable'. It should be noted that the GD-test was stopped after the first failure, as the test conditions and time would not allow

for an increase of water level and continuation of the groundwater flow. For real earthen dikes with a sand core this is however a realistic scenario.

The failure path analysis is a crucial part of the new flood risk management plan in the Netherlands. The risk assessment of sequential failures and the assessment of the residual dike resistance by Material Point Method (MPM) are part of other research performed within theme D of the All-Risk research programme.

The slope instability of the SPD causes a significant displacement of the inboard slope and deflection of the sheet pile. This is the first and initiating failure mechanism, and can be regarded as element failure, an exceedance of the geotechnical ULS. Before reaching a new equilibrium the second element failure occurred, by exceeding the ULS of the sheet pile strength. The second failure resulted directly in the system failure and lowering of the top of the sheet pile (Δz_{sp}), and basically the complete crest. This resulted in a partial flooding, until the water level was lowered to the top level of the sheet pile.

Sheet pile failure is expected when the maximum bending moment is exceeded, typically at the transition from the embedment sand layer to the soft layers above. The lowering of the sheet pile top, hence the crest level, is a function of the length of the sheet pile above the failure depth ($L_{sp,f}$) and the rotation angle ($\alpha_{sp,f}$) of the failed sheet pile (typically 45 degrees).
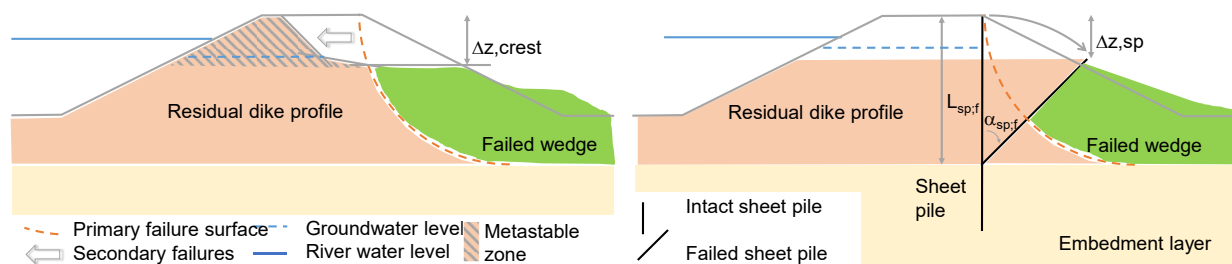

Figure 4.60 Slope failure of an earthen dike. The green shaded part is the approximate residual profile of the failed wedge.

Figure 4.61 Slope failure of a dike reinforced with an unanchored sheet pile at the crest.

There are certain advantages in this failure mechanism associated with a continuous sheet pile at the crest of the dike, with sufficient embedment:
- The failure of the sheet pile compresses the slope on the landside. The compression prevents reduction of the stresses and undrained shear strength in the slope cover. The clay cover remains intact despite the significant flood. This keeps the sheet pile supported and allowed the function of the sheet pile to change from a dike reinforcement to a weir structure with a controlled overflow.
- The advantage of the 'weir' is that it enhances a controlled overflow. This results in a longer evacuation time before flooding in the hinterlands becomes significant. Furthermore, the 'weir' allows for the possibility for local strengthening (for example placing of big bags of sand) as the material on the active side of the sheet pile is not immediately eroded to a deep scour hole.

In the Eemdijk full-scale test it is observed that the SPD maintains to a large extent the ability to act as a flood defense, after initial failure of the slope as well as the sheet pile. Furthermore, in the GD-test it appears that the stability is governed by a local weak layer. A dike with sheet pile reinforcement penetrates such layers and a continuous wall allows for redistribution along the

dike. Therefore, it can be concluded that dikes reinforced by a continuous sheet pile, with sufficient length and embedment, are more robust than earthen dikes.

4.9.2   Other sheet pile wall configurations

The results of the SPD test are representative for sheet piles embedded in the underlying sand layer and located at the inboard crest (land side) of the dike. The behavior of anchored sheet piles or sheet piles located at the toe of the dike is expected to be different, both with respect to deformations prior and post to failure. The SPD-test results are representative for a continuous sheet pile wall placed at the inboard crest, without anchorage and without waling (girder). This section discusses to what extent the results are applicable for other configurations, as well as a high-level evaluation of the advantages and disadvantages.

Panels versus continuous walls

In the current engineering practice in the Netherlands, dikes with sheet pile reinforcement consists mostly of sheet pile panels of 3 double sheet piles with typically 1 m spacing. Such dikes with discontinuous sheet pile panels are more vulnerable to erosion and breaching, just as normal earthen dikes. Furthermore, the membrane action is not present in dikes with discontinuous sheet pile panels. If the panels are connected by a waling (girder), it is still questionable if the waling under such large deformations remains connected and can transform the longitudinal forces. Based on this evaluation of the Eemdijk full-scale tests it can be concluded that dikes with a continuous wall at the crest are more robust than dikes with discontinuous walls. Furthermore, based on the PO-test is it concluded the properties (W, I) of side sheet piles of panels should be reduced.

Other sheet pile configurations

In many projects, sheet piles are placed along the crest. As most dikes have a road on top, this is one or the other side of the road. Placing the sheet piles at the crest is practical from construction point of view. Furthermore, the placement at the crest ensures the crest level, which is important for overtopping related failures. Placement of a sheet pile at the crest increases the water retaining capacity, but it cannot prevent failure of the steep inboard slopes, this is clearly illustrated in the Eemdijk tests.

Occasionally, sheet piles are placed along the toe as well. The advantage of a sheet pile wall placed at the toe is that it stabilizes the inboard slope, which is particularly relevant for steep slopes on soft soils. However, shallow slope instabilities above the sheet pile might still occur. The other advantage of a sheet pile wall along the toe is that the length of the wall can be significantly less. The investment costs are expected to be less for walls placed at the toe, compared to cantilever walls. The disadvantage is that placement is less practical from construction point of view, as the access is limited on private properties in urban areas. Besides, sheet pile installation in close proximity of buildings, such as vibrations and settlement, should be carefully examined. Sheet piles placed at the toe are regarded as less robust, as they cannot maintain the crest level as sheet piles at the crest, in particular after initial failure of the slope or wall.

Sheet pile walls, whether located along the crest or toe, can also be equipped with anchors. The advantage of anchorage is that it requires less embedment of the sheet pile, as well as lower structural capacity. Anchors are unavoidable if the structural capacity of the cantilever sheet pile

wall is insufficient. Anchors generally require a waling, firstly as part of the structural connection and secondly to redistribute the structural forces in case of anchor failure. An anchored wall, and in particular the connections, should allow for settlement induced forces. Asset management and inspections over the lifetime are certainly no advantage. The investment costs are expected to be less for anchored walls, compared to cantilever walls. The advantage of a cantilever wall is that on the long term the wall can be upgraded by adding anchorage, which can extent the lifetime considerably with limited materials, limited costs and limited disturbance to nearby buildings.

FEM modeling

The Eemdijk conclusions on deformations are not directly applicable for other configurations, i.e., sheet piles placed along the toe, berm or slope. The same applies for anchored sheet pile walls. The FEM back-analysis shows that the SSI is well captured, as well as the correct structural forces and most important the correct failure surfaces. Furthermore, it is shown that the full-scale tests (GD-test and SPD-test) can both be modeled with one parameter set for each constitutive model. The Eemdijk full-scale test is the first full-scale test where the SHANSEP NGI-ADP model is validated. The advantage of this model is that it complies to the Dutch guidelines, which specify the verification of dikes based on the undrained shear strength. Based on this research it is concluded that this constitutive model is suitable for design of dikes with sheet pile reinforcement. Furthermore, it is expected that also dikes with other sheet pile configurations can be accurately modeled with the selected constitutive models evaluated in this thesis. This requires of course sufficient geotechnical information, appropriate parameters determination and FEM modeling skills.

4.9.3 Comparison with flood walls in New Orleans

A dike with continuous wall as reinforcement by itself is not a guaranteed stable flood defense system. This is well known from the devastating damages caused by the flooding of New Orleans during Hurricane Katrina. The surge through the channels produced numerous breaches and partial breaches along both of these waterways. A detailed examination of two catastrophic failures that occurred at the west end of the Lower Ninth Ward is presented in Andersen et al. (2007); (Seed et al. 2008). A fully definitive determination could not be made between the multiple potential failure mechanisms, such as under seepage induced piping, overtopping and scouring of erodible soils, under seepage induced strength reduction and resultant lateral stability failure.

Numerous breaches along the channels resulted from several sets of causes. They all had in common that the walls are extended above the crest level (about 1.5 m), and the walls are shallow in depth (about 6 m), with marginal embedment in stable layers and marginable seepage cut-off. Figure 4.62 shows two photos of the flood defenses with significant deformation and severe damage. The situation in New Orleans is different than at the SDP-test, and most dikes in the Netherlands. As reported in Seed et al. (2008), the gap on the outboard side occurred when the water level exceeded the crest level. When the gap opens, water infiltrates into the gap, strength reduction in the soil layers occurs, the embedded support condition of the cantilever sheet pile wall reduces, resulting in an abrupt deterioration in the stability.

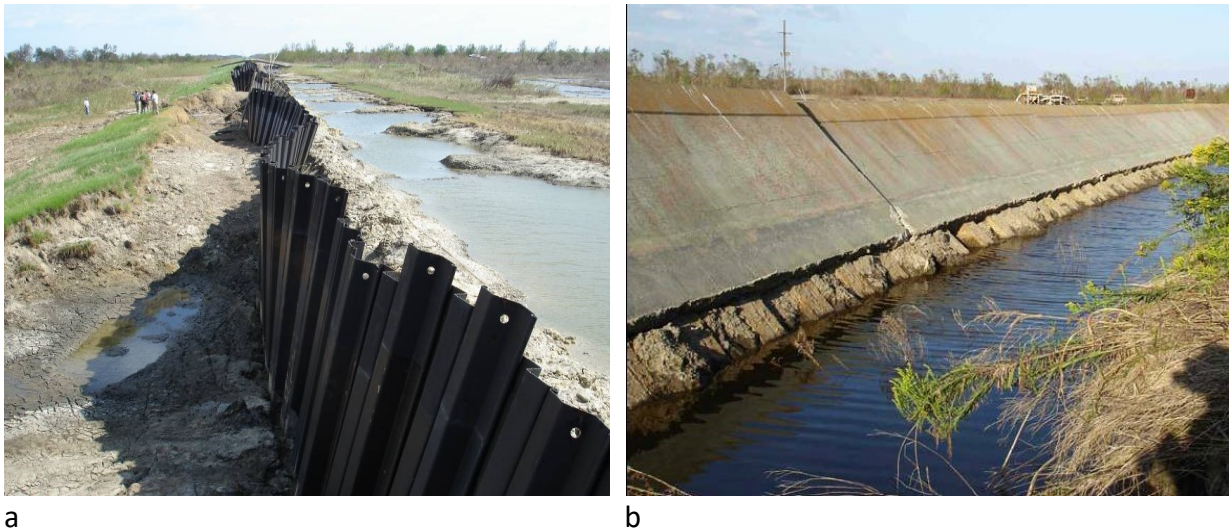a   b

Figure 4.62 Left figure (a) showing deflections of the extended sheet pile wall. Despite the significant deformations, the sheet piles are still interlocked and maintaining the level. The gaps are visible on the left side (outboard) and the effects of erosion are visible at the right side (inboard). Right figure (b) showing significant tilting of the floodwall (concrete I-wall with sheet pile) with large gaps on the outboard side. [Figure courtesy Interagency Performance Evaluation Taskforce (IPET, convened by the Army Corps of Engineers.]

At the SPD-test the water level was 0.5 m below the crest level. Although the sheet pile wall extended above the crest and cracks occurred in the active wedge on the outboard side, there were no observations of gapping. Furthermore, the sheet piles at the SPD-test are long, provide seepage cut-off and are embedded in the deeper sand layer.

The PO-test observations however show that the gapping certainly can occur in the soft organic clays and peats layers. The sheet pile walls in the PO-test extended 3 m above surface with the load imposed 2 m above surface. On the active (back) side of the sheet pile wall gaps occurred over the full length of the sheet pile panel, starting when the deformations exceeded a few centimeters. The width of the gap was almost equal to the horizontal deformation at surface level and the depth was up to a few meters, till the level of structural failure.

The crucial aspect is whether the wall extends above the crest surface, thereby exposed to an elevated water level which can create gapping. The majority of the dikes with sheet pile reinforcement in the Netherlands do not extent above the crest. However, this does occur at certain locations where the river Meuse passes a city. Besides that, in the future this might be the case at more densely populated locations where the crest surface cannot be raised. In case the wall extents above the crest, although this not the preferred solution, the effects related to gapping should be verified and the wall should be sufficiently embedded, as recommended in the New Orleans evaluations.

The post failure surveys at the SPD-test showed no significant erosion of the clay cover of the failed slope. The clay cover consisted of 1.5 m thick well compacted clay of medium to high plasticity (In Dutch: 'Klasse 1, stevige klei'). The total volume of water was about 2000 m³, resulting in an overflow discharge of about 300 liter per second per meter width of the 'weir'. It is concluded that the clay cover, although slope failure already occurred, remained robust. Possibly due to the compression of the sheet piles, which prevented the tension cracks as seen at the GD-test. Furthermore, the thickness of the clay cover and the clay material properties at the SPD-test are considered much more favorable than the erodible soils largely present in New

Orleans. Finally, the duration of the overflow was limited to 7 minutes due to the size of the basin. In New Orleans or in any other real high-water situation this would be hours. Extending these conclusions to situations with longer periods of overflow requires more research, in particular the retrogressive erosion starting at the pushed-up wedge near the toe.

Finally, a crucial recommendation taken from the New Orleans breaches is the importance of designing and constructing compatible transitions between two separate sections of the flood protection system (i.e., ground dike section and sheet pile reinforced dike section). Such locations are more vulnerable for seepage and erosion effects, related to soil-structure interaction and differential displacements.

<div style="text-align: right; font-size: 3em; color: #1a9fd6;">5</div>

Conclusions and recommendations

The thesis addresses the question how a dike on organic soil reinforced by a sheet pile wall performs under high water conditions, and how this can be modelled. Firstly, the parameter determination aspects were addressed and secondly, the full-scale test and back-analysis by the finite element method (FEM) was performed. This chapter summarizes the main findings and the answer to the research questions are subsequently addressed, with the expected implications for dike engineering.

5.1 Conclusions

The main conclusions per chapter are summarized below:

Chapter 2: Organic soils
- The CPT-based correlation to derive the soil unit weight (Lengkeek et al. 2018) has been improved and validated. Furthermore, new CPT-based correlations for organic soils are obtained by relating the soil state parameters to the cone resistance, and the unique soil type properties to the friction ratio.
- Organic soils are not well captured by existing SBT classifications. An adjustment to Robertson (2010) has been developed. In this novel SBT classification organic soils (SBT=2) are redefined and subdivided into peat, organic clay and mineral clay with organic matter.

Chapter 3: Undrained shear strength
- The newly proposed Critical Stress Ratio (CSR) model provides a reliable determination of the undrained shear strength, based on effective stress parameters and common laboratory tests.
- The model can be implemented in LEM where it can be used for ULS analysis. Furthermore, it can be used to derive the undrained shear strength parameters as input for SHANSEP based undrained shear strength models.

Chapter 4: Eemdijk full-scale tests
The Eemdijk test provides a unique insight into the behavior of two similar dikes with and without sheet pile reinforcement and the performance of the FEM modeling.
- Applying sheet piles in dikes considerably increases the stability. In the Eemdijk experiment it was found that reinforcing a ground dike with a cantilever sheet pile in the crest resulted in 2 m extra water retainment.
- The ground dike (GD) and sheet pile reinforced dike (SPD) provided insight in the critical deformations prior to progressive failure. Slope failure starts when the horizontal displacement rate at the toe of the dike exceeds 1 cm/hour.
- A continuous sheet pile, with sufficient length and embedment, makes an important contribution to the robustness of the dike after failure.

- The dike design guidelines for the Netherlands currently prescribes the SHANSEP model for undrained stability analysis. The back-analyses of the Eemdijk full-scale tests confirm that this model is well suitable for the design of dikes, with and without sheet pile reinforcement.
- The combined effect of the stress path dependent strength and 3D failure mode explains the difference between the measured and back-calculated stability factor and displacements using best fit average parameters.
- With the proposed standardized procedures, it is possible to derive consistent sets of parameters for constitutive models based on the underlying main soil parameters, applicable for normal and probabilistic FEM analysis.

The conclusions per research question are subsequently addressed below, with the expected implications for dike engineering. Research question number 7, how the results of this research can be used to improve the dike engineering practice, is addressed in the recommendations.

CPT-based methods
The research question (1) addressed in Chapter 2 is how the stability assessment of dikes can be improved by CPT-based classification methods and correlations for organic soils. The challenges with CPT-based methods for application in deltaic areas with organic soils are presented. Current CPT-based methods are not well suitable for organic soils. This is the case for CPT-based correlations and SBT classifications. Improvements are proposed in this research for CPT-based methods based on a comprehensive database of carefully selected pairs of laboratory tests and CPT measurements.

The newly proposed CPT-based correlations are obtained by relating the soil state parameters to the cone resistance and the unique soil type properties to the friction ratio. Regarding soil state parameters, reference is made to the correlations for preconsolidation stress and undrained shear strength versus the cone resistance. Regarding unique soil type parameters, reference is made to the correlation for compression ratio versus the friction ratio and the correlation for normally consolidated normalized undrained shear strength (S-ratio) versus the friction ratio. The CPT pore pressure measurements appear to be less reliable for organic soils and are not considered suitable in correlations for organic soils.

Combining data from various sites, geological units and depths results in a sufficiently wide range of cone resistance and friction ratio, such that trends for correlations become more reliable. This allowed for the proposal of new correlations, which can be applied for the whole range of organic soils, from peats to mineral clays with minor organic content. The disadvantage of this approach is that it enlarges the inherent variation along the trend and the possibility that site specific units introduce bias to the trendline. The confidence interval and statistical parameters are all presented in the presented graphs. The following CPT-based correlations for the whole range of organic soils, from peats to mineral clays, are presented in Chapter 2:
- Saturated unit weight specifically for peat.
- Compression parameters.
- Vertical preconsolidation stress and preconsolidation net cone factor.
- Undrained shear strength from an in-situ stress consolidated DSS tests and S-ratio from normally consolidated DSS tests.
- Undrained shear strength from an in-situ stress consolidated CAUC Triaxial tests and S-ratio from normally consolidated CAUC tests.

This research also resulted in a updated unit weight correlation (Lengkeek and Brinkgreve 2022b) based on 427 data pairs. The statistical parameters of the updated correlation are compared with existing correlations and show better performance on all parameters. The correlation can be applied to both mineral and organic soils, which is useful for SBT classifications and CPT-methods that require stress correction.

It is concluded that organic soils are not well identified in existing SBT classifications. Therefore an adjustment to Robertson (2010) is proposed, where SBT=2 (Organic soils) is redefined and split into SBT=2a (Peat), SBT=2b (Organic Clay) and SBT=2c (Mineral Clay with organic matter). The adjusted classification is based on data pairs up to 15 m depth and 150 kPa vertical effective stress. The new SBT zones can also be applied in the SBTn classifications by Robertson (2009); (Robertson 2016) in combination with a $C_n=1.7$ as stress normalization cut-off.

CSR model

The new Critical Stress Ratio (CSR) model is presented in Chapter 3. The research question (2) addressed in Chapter 3 is how the stability assessment can be improved by linking effective strength parameters to undrained shear strength parameters using Critical State Soil Mechanics theory. The CSR model can be implemented in LEM and can also be used to determine the SHANSEP parameters which can be used as input in a LEM or FEM calculation.

The formulation of the undrained shear strength in the CSR model integrates the empirical SHANSEP equation, and the theoretical elaboration of undrained shear strength based on critical state soil mechanics. The CSR model requires one new model parameter called the Critical Stress Ratio, which is comparable to a spacing ratio in the MCC model. The advantage of the CSR model is that it allows for a variable spacing ratio, which can be fitted based on conventional laboratory tests.

The CSR model requires three model parameters and two state parameters. This is made possible by the proposed linearization and alignment of the Poisson's ratio with other model parameter ratios. The advantage of this procedure is that effective stresses and K_0 are well aligned with empirical methods. There are two procedures to determine the CSR model parameters. Based on the examples it is concluded that the undrained shear strength matches well with the theoretical MCC undrained shear strength (Method A) as with the undrained shear strength of three real soil types (Method B).

Eemdijk full-scale test: soil parameter determination

The Eemdijk full-scale test evaluation is presented in Chapter 4. The conclusions are summarized below by addressing research question 3 to 7.

Research question 3 addresses how the stability assessment can be improved by re-examination of ultimate strength criteria, standardized procedures and numerical simulations to determine constitutive model parameters. The following was found.

Firstly, after careful examination of CAUC tests performed at the test site, it is concluded that additional criteria are required to prevent unrealistically high or low undrained shear strength values. Furthermore, it is concluded that the 15% axial strain value is more appropriate as a basis for the ultimate value, instead of the 25% axial strain currently used in the Dutch guidelines (Rijkswaterstaat 2017, 2021). It is expected that this will result in more reliable values for the

undrained shear strength with less variation. Ultimately, this is intended to result in a more economic dike design.

The second challenge related to CAUC interpretation is the geometrical correction. It is shown by numerical simulation that the anisotropic constitutive models are capable to fit both the DSS and CAUC test well with one set of parameters, as long as no geometrical correction is applied to the CAUC tests. This is because the geometrical correction reduces the undrained shear strength for CAUC tests by approximately 20% at large strains. It is concluded that the application of anisotropic constitutive models without the geometrical correction applied to the CAUC tests results in a more realistic assessment of the stability and a more economic dike design.

Thirdly, various constitutive models are currently used in dike engineering practice, such as the SHANSEP model. These constitutive models require specific model parameters. With the proposed standardized procedures for each constitutive model, a limited number of input parameters are defined which can be derived from the conventional soil investigations. The procedures are applied to the Eemdijk soil investigation, and it is concluded that this results in a consistent set of parameters that fit in the formulation of the constitutive models. Furthermore, it is shown by the numerical simulations that the constitutive models provide comparable results. This results in an improved performance of the constitutive models and allows for switching of constitutive models in a staged construction analysis.

Eemdijk full-scale test: performance of dikes with sheet pile reinforcement
Research question 4 addresses how a dike with sheet pile reinforcement performs leading up to and beyond failure in a full-scale failure experiment and how this compares to an earthen dike. The Eemdijk test provides a unique insight into the performance of a dike with and without sheet pile reinforcement under realistic loading conditions. During the experiment, the water level behind the sheet pile reinforced dike (SPD) could be increased by 2.1 m (from 2.9 to 5.0 m NAP) compared to the ground dike without sheet pile reinforcement (GD). This is a significant increase of water retainment for a dike with similar dimensions and soil conditions. An equivalent ground dike would require a significant increase in base width to safely retain an additional 2.1 m of water. Widening the base of a dike is often not possible in urban areas and clearly shows the advantage of sheet pile reinforcement. The disadvantage is that dikes with sheet piles are generally more costly than ground dikes.

The Eemdijk full-scale test also provides valuable insights into the deformations prior to and beyond failure. In general, the deformations are considered negligible (<5 cm) up to 80% of the maximum retained water height in all tests. Furthermore, slope failure starts at the toe at a deformation rate of 1 cm/hour in all tests. This corresponds to a situation where 10 to 20 cm of horizontal displacement is reached.

The advantage of a sheet pile reinforced dike is that the crest level is maintained by the top of the sheet pile in contrast to earthen dikes, so that other failure mechanisms related to overflow and erosion are not adversely affected. Another advantage of a dike with sheet pile reinforcement in the crest is the lower vulnerability to erosion associated with the compression of the clay cover of the inboard slope and prevention of cracks, due to the deflection of the sheet pile. The Eemdijk full-scale test shows that this even holds after slope and structural failure. Lastly, the deformations in the SPD-test prior to failure are larger than in the GD-test. The

maximum horizontal displacement at the crest in the SPD-test at the start of slope failure was 0.3 m and at structural failure was 0.6 m. The deformation rate increases in this stage from 1 to 10 cm/hour. The advantage of these large deformations is that they provide for an early warning and allow for mitigating measures before structural failure and timely evacuation before system failure and flooding occurs. The final equilibrium of the failed slope is reached after significant deformation. The lowering of the top level of the sheet pile corresponds to a reduction of about a third in height.

An interesting finding from the Eemdijk full-scale test is that a continuous sheet pile, with sufficient length and embedment, also makes an important contribution to the stability of the dike after failure. Although the sheet pile fails, the tensile and shear force capacity remains sufficient to create a system of two sheet pile parts, which are connected by a hinge. This keeps the lower part of the sheet pile in place, while allowing the top of the sheet pile to deflect and find equilibrium with the failed inboard slope. This creates a local crest lowering which acts as a weir as the deflected sheet pile top level was 1 m below the maximum water level.

During the tests, all sheet piles remained interlocked even after failure. The back-analysis shows that the longitudinal force is significantly less than the interlock capacity. This makes the application of a waling beam unnecessary for continuous walls, which saves on costs, detailed engineering and lifelong inspection of the connections.

The SPD-test also shows that even after failure, a properly designed clay cover can resist an extreme discharge of water for a limited duration. This is a result of compression of the clay cover by the sheet piles, preventing cracking of the clay cover. However, this may only serve as an advantage in the short term because the long-term erosion of the pushed-up toe could cause a retrogressive failure.

The failure surface at the toe of the GD is in the thin, soft clay layer. This layer is only present at the mid-section of the GD and initiated the failure over half the length of the dike. The failure surface at the toe of the SPD is located at the base the peat layer and occurred over almost the full length of the SDP. This illustrates the sensitivity of a ground dike stability to the presence of local soft and the importance of spatial variation of geotechnical properties. Although the soft clay layer 3a was not present at the SPD, it is expected that the sheet pile would allow for more redistribution of the soil properties, both in the vertical and longitudinal direction, and thus will be less vulnerable to instability in variable soils. To conclude, the early warning by sheet pile deflection, the hinged sheet pile after structural failure, the compressed clay cover without cracks, the sheet pile membrane acting as 'weir' all contribute to a high robustness of the SDP.

Eemdijk full-scale test: performance of sheet piles
The performance of the sheet piles is investigated by the pull-over (PO) test reported in Chapter 4.4 and the SPD-test reported in Chapter 4.6. Research question 5 addresses the performance of the sheet piles leading up to and beyond failure.

The PO-test shows that the performance of the sheet piles complies with the Eurocode. The bending moment capacity of class 2 cross-section profiles corresponds to the plastic capacity, and that of class 3 cross-section profiles correspond to at least to the elastic bending moment capacity. Sheet pile designs are normally based on the nominal steel properties in compliance with the steel designation instead of the real properties determined from measurements. The

margin between the nominal and measured properties can be useful in case the yield strength of the sheet piles is slightly insufficient in future safety assessments. It should be noted that the steel designation also includes the tensile strength and elongation at rupture. The PO test indicates that the tensile strength for these sheet piles was relatively low compared to the yield strength. Consequently, this would reduce the steel designation and increases the costs or would result in non-compliance to the Eurocode.

The side piles of sheet pile walls installed as panels or as a staggered wall endure two additional effects, namely:
- Mobilization of more soil as a result of 3D effects.
- Less restriction against cross-sectional deformation due to one of the sides being unconstrained.

The comparison between the middle and side sheet pile shows larger curvatures at the side pile, demonstrating the aforementioned effects . The measurements during the PO-test shows that the neutral axis shifts at the edge of the panel, resulting in a lower moment of inertia. Furthermore, the 3D laser scans after the tests shows that at the level of maximum curvature in the sheet pile wall, the compression flanges of the outer sheet piles are permanently deformed. The PO-test confirm the reduced efficiency of the side sheet piles in panels compared to the mid sheet piles.

Eemdijk full-scale test: performance of FEM back-analysis
The research question (6) presented in Chapter 4.8 addresses to what extent the full-scale test can be modelled with FEM.

A comprehensive set of field and laboratory tests has been performed. This allowed for a validation of the CPT-based methods of Chapter 2 and the CSR model of Chapter 3 and resulted in the following improvements with respect to parameter determination: 1) new criteria for the ultimate limit state undrained shear strength determination. 2) schemes to derive constitutive model parameter from basic soil parameters that are internally consistent and reproduce the numerical simulations of the laboratory tests. 3) a best fit set of average isotropic parameters and average anisotropic parameters.

Both the GD-test and SPD-test are back-calculated with the same set of input parameters and four FEM post-dictions are reported. The back-analyses were able to reproduce the correct deformations and excess pore pressures for each stage by allowing for consolidation. The duration of the construction phase is about 6 to 9 months, and the duration of the test phase is about one week, with the failure occurring on the last day. The test phase is considered undrained based on the pore pressure response during failure and the deformation rate at failure. Therefore, the back-analysis of the test phase is performed with the SHANSEP model based on undrained shear strength, as well as the CSC1S model with effective stress models in an undrained analysis.

The dike design guidelines for the Netherlands currently prescribes the SHANSEP model for undrained analysis during a dike's functional lifetime. The construction phase can be modelled with other models such as SSC-models to account for settlements. The back-analysis of the Eemdijk full-scale tests confirm that these models are also well suitable for the design of dikes

with sheet pile reinforcement. It is concluded that all back-analyses show the correct failure modes for both dikes as well as the failure of the sheet pile.

The best fit isotropic parameters underestimated the stability and overestimated the displacements at all load stages. This corresponds to about 15% underestimation in strength of the soft soil layers. Hence, the deformation of the sheet pile and the bending moment are overestimated too. The anisotropic strength models, with the increased Active loading strength, same Direct simple shear strength and decreased Passive loading strength (ADP), perform better than the isotropic strength model. The effect is an increased stability by 10% relative to the isotropic strength model. This would explain at least half the difference between the back-analysis and the actual measurements. The combined effect of the anisotropic strength and 3D failure mode explains the difference between the actual measured and back-calculated stability and displacements using best fit average parameters. The 3D failure mode includes side friction effects which increases the stability compared to a 2D failure mode.

5.2 Recommendations

The final research question (7) is how the results of this research can be used to improve dike engineering practice. A number of more specific findings have been included in the previous conclusions. This section presents the recommendations for dike engineering practice and further research based on the conclusions of this thesis.

Engineering application of CPT

It is recommended to extend the pairwise established databases introduced in this thesis. It is recommended to perform CPTs adjacent to boreholes, select pairs of high-quality CPT measurements and laboratory tests according to a standardized protocol (STOWA) and extend these pairwise established databases. This will allow for further substantiation of frequently used correlations, as well as site specific correlations. It is important to acknowledge possible bias in the correlations for each site, as appeared from the validation of the correlations for the Eemdijk site (Appendix G). Without prior knowledge of the site-specific conditions, it is recommended to select a value in between the 5% fractile value and the 5% probability of (no)-exceedance of the average from a regional correlation.

Engineering application of CSR model

It is recommended to implement the CSR model in LEM for stability analysis of dikes. The CSR model provides a reliable determination of the undrained shear strength based on effective stress parameters and common laboratory tests. The model can also be used to determine the undrained shear strength parameters as input for SHANSEP based models in LEM or FEM. Furthermore, it is recommended to develop a similar model for DSS-tests such that the determination of undrained shear strength of peat can also be improved.

Parameter determination and CAUC tests

Based on a careful examination of the CAUC test it is recommended to revise the current criteria (Rijkswaterstaat 2017, 2021)for the ultimate undrained shear strength determination, and to reexamine the applied geometrical corrections. It is recommended to use the 15% axial strain value as a basis for the ultimate value and to apply the following criteria to prevent unrealistic high or low undrained shear strength values:

- For overconsolidated samples and contractive stress paths it is proposed to select the strength before the tension cut-off line is reached ($\sigma'3 > 0$) and the minor effective stress becomes zero.
- For overconsolidated samples and significant dilative behavior resulting in negative excess pore pressures it is proposed to select the strength before the zero excess pore pressure line is reached ($\Delta u > 0$) and the excess pore pressures become negative.

It is shown that the CAUC undrained shear strength determined without geometrical correction can results in approximately 20% higher undrained shear strength. This results in a higher undrained shear strength for CAUC tests than for DSS tests, which is in line with the well accepted ADP concept. It is recommended to perform further research on how and whether this correction should be applied.

Anisotropic constitutive models
The anisotropic constitutive models (SHANSEP-ani, CSC1S-ani) are capable to fit both the DSS and uncorrected CAUC test well, with one set of parameters. The back-analysis of the Eemdijk SPD-tests shows that these models perform better than the isotropic models. It is recommended to investigate the possibilities for application of anisotropic constitutive models for dike engineering projects, as this results in a more realistic assessment of the stability and a more economic dike design.

Probabilistic FEM analysis
A limited number of input parameters are defined for the proposed standardized procedures for each constitutive FEM model. For probabilistic FEM analysis is recommended to use these defined input parameters, e.g., CR, ϕ', as random variables, instead of using the various constitutive model parameters as stochastic parameters. The relationship between the parameters is defined in the procedures presented in Appendix E. This prevents physical and numerical inconsistent sets of parameters and does not require the definition of relations between the constitutive parameters. This will improve the robustness of probabilistic analysis with a FEM-model.

Sheet pile properties and performance
From the PO-test it is concluded that the bending moment capacity of class 2 cross-section profiles corresponds to the plastic capacity, and that of class 3 cross-section profiles corresponds to at least to the elastic bending moment capacity. The verification is based on the average yield strength. The PO-test shows that the performance is in line with the Eurocode. The Dutch guidelines for sheet piles in dikes (POVM 2020a, 2020b) do not allow the use of the plastic capacity for class 2 cross-section profiles. It is recommended for these guidelines to align with the Eurocode (EN1993-5 2007) because the unnecessarily stringent deviation cannot be justified and is uneconomic.

Based on the PO-test it is concluded that the unconstrained side sheet piles of the panels deform slightly with respect to the neutral axis and original shape, whereas the middle sheet piles remained unchanged. The Dutch guidelines for sheet piles in dikes specify a 10% reduction of the bending moment capacity for all sheet pile in panels. A reduction is justifiable based on the measurements from the Eemdijk tests; however, a reduction of 10% for the complete panel is

not in line with the back-analysis. This specification can be further optimized by specifying a 10% reduction in strength (W) and stiffness (I) for the outer sheet piles only.

Monitoring of dikes

It is recommended to focus monitoring (remote sensing or the observational method) of deformations on the horizontal displacement at the inboard crest or toe. It appears that the measured vertical displacements are generally less than the horizontal displacements. The insights in deformation from the Eemdijk experiment and this thesis can be used to set critical values of deformations for both the GD and SPD. The recommended accuracy is at least 1 cm at a monitoring frequency of at least once per day. For critical dike sections with sheet pile reinforcement the monitoring can be supplemented with an inclinometer on the sheet pile and in the inboard toe of the dike.

3D effect

The GD-test clearly shows a 3D failure mode. The failure wedge length along the dike is limited to about 30 m. The side friction increases the stability compared to a 2D failure mode with a factor 1.1 to 1.2. The GD also shows that despite the 3D effect, the stability can still be reduced due to a single weak layer (3a in the test). Therefore, it is recommended not to take the 3D effect into account in regular 2D analysis of dike design projects. Moreover, it is recommended to account for the 3D effect during a past performance analysis, in order not to overestimate the real strength of the dike.

Residual profile

Slope instability causes a significant deformation of the inboard slope and lowering of the inboard crest. In the GD-test this was approximately one third of the initial height and in the SPD-test this was approximately half. However, these post failure deformations are considered largely variable and uncertain as smaller deformations often occur in practice. Furthermore, normal FEM analyses are not capable of calculating these large deformations. This requires Material Point Method (MPM) analyses, which are under development and investigated within theme D of All-risk (Remmerswaal et al. 2021). Therefore, for dike engineering it is recommended to assume the level for the residual profile after first failure based on the Eemdijk tests, followed by the reduction of the strength properties within the failure wedge such that it is just in equilibrium.

Characteristic properties

The performed variation study in Section 4.8 shows that the displacements in advanced non-linear models are strongly affected by the strength. For that reason, it is recommended to use average stiffness parameters in a SLS or ULS dike design analysis when performed with advanced constitutive models in FEM. There is no need for the application of reduced characteristic stiffness parameters, as this is already covered by the reduced characteristic strength parameters in a design calculation. On the contrary, the effect of reduction in strength is even larger than the effect of reduction in stiffness. A double reduction would result in unrealistic overprediction of deformations.

Continuous walls

It is recommended to apply continuous sheet piles instead of sheet pile panels, as Eemdijk full scale failure test shows increased robustness. Declutching detectors can be used to verify the

159

interlocking during installation. Furthermore, the waling and connections can be left out from designs of continuous walls.

Transitions

A crucial conclusion taken from the 2005 levee failures in New Orleans is the importance of designing and constructing adequate transitions between two separate sections of a flood protection system. These transitional sections are more vulnerable to seepage and erosion effects because of soil-structure interaction and differential displacements. This is relevant to adjacent dikes with and without sheet pile reinforcement. The full-scale tests confirm that the deformations prior to failure in the SDP-test are larger than in the GD-test. Furthermore, the PO-test confirms that cantilever wall that extend the surface create gapping. Therefore, it is recommended to carefully examine these transitions.

Risk-based approach

Since 2017 the Dutch flood risk legislation builds upon a risk-based approach. In the current state of practice, the reliability of earthen dikes can be verified by semi and full probabilistic LEM analyses, as well as FEM analyses. For dikes with sheet pile reinforcement, the current applied framework is insufficiently substantiated. With the recommended procedures for parameter determination, it is possible to perform probabilistic FEM analyses with multiple stages and different constitutive models, required for the analysis of sheet pile reinforced dikes.

This research of the Eemdijk full-scale tests confirms the applicability of the SHANSEP model and the capability to model a dike with sheet pile reinforcement in FEM. This is, together with the recommendations for parameter determination and probabilistic analysis, a solid basis for the next step to determine the corresponding partial factors for semi-probabilistic analysis in line with the target reliability in the risk-based approach.

Furthermore, the Eemdijk experiment shows that a continuous cantilever sheet pile wall, placed in the crest, significantly improve the stability and enhance the robustness. This is in particular useful for critical dike sections in urban areas, where widening of the base is not possible. It is recommended to investigate to what extend the enhanced robustness can be accounted for in risk-based approach.

For other dike critical sections without constraints by adjacent structures, traditional heightening and widening by soil remains the preferred solution, as this is a more sustainable solution that allows for long term adaptation for changes in environmental conditions such as flood intensities, sea level rise and subsidence.

APPENDIX A   DEFINITION CPT PARAMETERS AND LIST OF SYMBOLS

Table A 1 Definition of CPT parameters

Symbol	Unit	Definition	Name
$\sigma_{v,0}$	kPa		in-situ total vertical stress
$\sigma'_{v,0}$	kPa		in-situ effective vertical stress
σ'_{vy}	kPa		in-situ vertical preconsolidation stress
u_0	kPa		in-situ hydrostatic stress
q_c	kPa		cone tip resistance
f_s	kPa		sleeve friction
u_2	kPa		measured pore pressure just behind the cone
Δu	kPa	$\Delta u = (u_2 - u_0)$	excess pore pressure
a		$[0.5, 0.9]$	cone area ratio
q_t	kPa	$q_t = q_c + (1-a)u_2$	corrected cone resistance
q_e	kPa	$q_e = q_t - u_2$	effective cone resistance
q_n	kPa	$q_n = q_t - \sigma_{v,0}$	net cone resistance
p_a	kPa	$[100]$	atmospheric pressure
$\dfrac{q_t}{p_a}$			dimensionless corrected cone resistance
R_f		$R_f = \dfrac{f_s}{q_t} 100\%$	friction ratio
I_{SBT}		$I_{SBT} = \sqrt{\left(3.47 - \log \dfrac{q_t}{p_a}\right)^2 + \left(1.22 + \log R_f\right)^2}$	soil behavior type index (Robertson 2010), based on $\dfrac{q_t}{p_a}$
Q_{t1}		$Q_{t1} = \dfrac{q_n}{\sigma'_{v,0}}$	linear normalized cone resistance (Robertson 1986)
F_r		$F_r = \dfrac{f_s}{q_n} 100\%$	normalized friction ratio
I_{c1}		$I_{c1} = \sqrt{(3.47 - \log Q_{t1})^2 + (1.22 + \log F_r)^2}$	linear soil behavior type index (Robertson 1998), based on Q_{t1}
B_q		$B_q = \dfrac{\Delta u}{q_n}$	pore pressure ratio
n		$n = \min\left\{1, 0.381(I_{cn}) + 0.05\left(\dfrac{\sigma'_{v,0}}{p_a}\right) - 0.15\right\}$	stress normalization exponent
C_n		$C_n = \min\left\{C_{n,max}, \left(\dfrac{p_a}{\sigma'_{v,0}}\right)^n\right\}$	stress normalization factor and cut-off. $C_{n,max}$=1.7 in this thesis
Q_{tn}		$Q_{tn} = C_n \dfrac{q_n}{p_a}$	nonlinear normalized cone resistance (Robertson 2009)
I_{cn}		$I_{cn} = \sqrt{(3.47 - \log Q_{tn})^2 + (1.22 + \log F_r)^2}$	nonlinear soil behavior type index (Robertson 2009), based on Q_{tn}

I_B		$I_B = \frac{100(Q_{tn}+10)}{(Q_{tn}F_r+70)}$	modified soil behavior type index (Robertson 2016)
CD		$CD = 70 = (Q_{tn}-11)(1+0.06F_r)^{17}$	The contractive–dilative boundary
U_2		$U_2 = \frac{\Delta u}{\sigma'_{v,0}}$	normalized pore pressure
G_0	kPa	$G_0 = \rho V_s{}^2$	small-strain shear modulus
I_G		$I_G = \frac{G_0}{q_n}$	small-strain rigidity index
K_G^*		$K_G^* = I_G Q_{tn}{}^{0.75}$	modified normalized small-strain rigidity index
N_{kt}		$N_{kt} = \frac{q_n}{s_u}$	undrained shear strength net cone factor
N_{ke}		$N_{ke} = \frac{q_e}{s_u}$	undrained shear strength effective cone factor
$N_{\Delta u}$		$N_{\Delta u} = \frac{\Delta u}{s_u}$	undrained shear strength excess pore pressure cone factor
k_p		$k_p = \frac{\sigma'_{vy}}{q_n}$	preconsolidation stress net cone factor

Table A 2 List of symbols Chapter 2

Symbol	Unit	Name
AC	%	Ash Content
CR		Compression Ratio
MC	%	Mineral Content
OC	%	Organic Content
RR		Recompression (Swelling) Ratio
a_o		SBT parameter (Eq.2-10)
b_o		SBT exponent (Eq.2-10)
C_c		compression coefficient
C_k		strain dependent permeability coefficient
C_r		swelling coefficient
c_v	m²/s	coefficient of consolidation
C_α		secondary compression ratio
$C_{\alpha e}$		secondary compression coefficient
e_0		void ratio
G_m		specific gravity mineral content
G_o		specific gravity organic content
G_s		specific gravity soil particles
N	%	organic content
S		normalized undrained shear strength (S-ratio)
S_a		standard deviation of regression parameter a

$S_{cv,tx}$	[32]	normalized undrained shear strength, based on critical state strength, triaxial tests and normally consolidated samples
s_u	kPa	undrained shear strength
$s_{u,ult,DSS}$	kPa	ultimate value of the undrained shear strength, from DSS test
$s_{u,ult,CAUC}$	kPa	ultimate value of the undrained shear strength, from CAUC test
S_y		standard deviation on regression
R^2		coefficient of determination
$R_{f,ref}$	kPa	reference friction ratio (Eq.2-9)
w_{nat}	%	natural water content
$q_{t,ref}$	kPa	reference corrected cone resistance (Eq.2-9)
β		unit weight slope parameter (Eq.2-9)
γ_{dry}	kN/m³	dry unit weight
γ_{nat}	kN/m³	bulk unit weight at natural water content
γ_{sat}	kN/m³	saturated unit weight
$\gamma_{sat,ref}$	kN/m³	reference unit weight (Eq.2-9)
$\sigma'_{v,0}$	kPa	effective vertical in-situ stress
$\sigma'_{v,con}$	kPa	effective vertical consolidation stress
$\sigma'_{v,y}$	kPa	vertical preconsolidation stress
ϕ'	°	effective friction angle
ϕ'_{ult}	°	ultimate value of the effective friction angle

Table A 3 List of symbols Chapter 3

Symbol	Unit	Name
$CAUC$		Consolidated Anisotropic (K_0) Undrained Compression triaxial test
$CIUC$		Consolidated Isotropic Undrained Compression triaxial test
CSR		Critical Stress Ratio (model)
EPP		Elastic Perfectly-Plastic (stress path)
FEM		Finite Element Method
LEM		Limit Equilibrium Method
MCC		Modified Cam-Clay (model)
NC		Normally consolidated state
OC		Over-consolidated state
OCR		Over Consolidation Ratio, based on vertical effective stress
b		OCR exponent (Eq.3-41)
c		conversion factor for the swelling index over an unloading range
c_e		conversion factor for the swelling index at the onset of unloading
$c_{K:1}$		conversion factor for the swelling index for oedometric unloading to earth pressure ratio equals one
K_0		initial earth pressure ratio
K_{nc}		normally consolidated earth pressure ratio

Symbol	Unit	Name
K_p		passive earth pressure ratio
K_x		earth pressure coefficient at stress point X where OCR=CSR
m		OCR exponent (Eq.3-51)
M_c		Critical State failure line
$M_{c,MCC,eq}$		equivalent MCC Critical State failure line based on CSR model method B
OCR_p		empirical overconsolidation ratio at passive earth pressure ratio
$OCR_{K:1}$		overconsolidation ratio after oedometric unloading to isotropic condition
$OCR_{p,K:1}$		overconsolidation ratio at passive earth pressure ratio based on linearized Poisson's ratio
p'_0	kPa	initial effective isotropic stress
p'_c	kPa	isotropic preconsolidation stress
p'_e	kPa	equivalent isotropic stress
p'_f	kPa	isotropic stress at failure
p'_x	kPa	isotropic stress at stress point X where R=r
p'_y	kPa	isotropic yield stress for oedometric conditions
q_0	kPa	initial deviatoric stress
q_f	kPa	deviatoric stress at failure
q_y	kPa	deviatoric yield stress for oedometric conditions
R		overconsolidation ratio, based on isotropic effective stress
r		spacing ratio
r_x		spacing ratio for oedometric conditions
R_y		isotropic overconsolidation ratio for oedometric conditions, based on isotropic effective stress
$S_{CAUC,CSR}$		CSR undrained shear strength ratio, normalized by the vertical effective stress, for oedometric normally consolidation and CAUC loading
$S_{p,CIUC,MCC}$		MCC undrained shear strength normalized by the isotropic effective stress, for isotropic normally consolidation and CIUC loading
$S_{CAUC,high}$		theoretical upper bound of undrained shear strength ratio
$S_{CAUC,low}$		theoretical lower bound of undrained shear strength ratio
$S_{CAUC,MCC}$		MCC undrained shear strength ratio normalized by the vertical effective stress, for oedometric normally consolidation and CAUC loading
$s_{u,CAUC}$	kPa	undrained shear strength from CAUC test
$s_{u,CAUC,CSR}$	kPa	CSR undrained shear strength for oedometric consolidation and CAUC loading
$s_{u,CAUC,MCC}$	kPa	MCC undrained shear strength for oedometric consolidation and CAUC loading
$s_{u,CIUC,MCC}$	kPa	MCC undrained shear strength for isotropic consolidation and CIUC loading
$s_{u,EPP}$	kPa	undrained shear strength based on elastic perfectly-plastic behavior
$s_{u,SHANSEP}$	kPa	undrained shear strength based on empirical SHANSEP formulation
$s_{u,x,CAUC,CSR}$	kPa	CSR undrained shear strength, at stress point X where OCR=CSR
ΔK_{ur}		tangent earth pressure coefficient for unloading/reloading

Symbol	Unit	Name
$\Delta K_{ur,K:1}$		earth pressure ratio change after oedometric unloading to to isotropic condition
η_{nc}		slope of the normal compression line in the p'-q-diagram
η_{ur}		slope of the unload-reload line in the p'-q-diagram
κ		isotropic swelling index
κ^*		modified isotropic swelling index
κ_{oed}		isotropic swelling index for oedometric unloading
Λ		plastic volumetric strain ratio
λ		isotropic compression index
λ^*		modified isotropic compression index
ν_e		initial elastic Poisson's ratio (tangent)
ν_{ur}		elastic Poisson's ratio
$\nu_{K:1}$		linearized elastic Poisson's ratio after oedometric unloading to to isotropic condition
σ'_{vx}	kPa	vertical stress at stress point X where OCR=CSR, based on oedometric conditions
σ'_{vy}	kPa	effective vertical preconsolidation stress

Table A 4 List of symbols Chapter 4

Symbol	Unit	Name
ADS		Accidental Design State
$CSC1S$		Creep-SCLAY1S model
GD		Ground Dike (test)
$DLDS$		Deltares Large Diameter Sample
DLS		Damage Limitation State
$GFSG$		Glass Fiber Strain Gauges
HS		Hardening Soil model
HSS		Hardening Soil model with small-strain stiffness
MC		Linear Elastic Perfectly Plastic model (Mohr-Coulomb model)
MCC		Modified Cam-Clay model
PO		Pull-Over (test)
POP		Pre Overburden Pressure
$SAAF$		Shape Accel Array Field
$SHANSEP$		SHANSEP NGI-ADP model
SLS		Serviceability Limit State
SPD		Sheep Pile Dike (test)
SS		Soft Soil model
SSC		Soft Soil Creep model
SSI		Soil Structure Interaction
ULS		Ultimate Limit State
A	%	(steel) minimum elongation

Symbol	Unit	Name
B	m	width (of panel)
b_f	mm	flange width
C_k		train dependent permeability coefficient normalized by the void ratio
c'_{mc}	kPa	equivalent Mohr-Coulomb effective cohesion intercept
H_{dike}	m	dike height
$H_{failed,slope}$	m	residual height of failed wedge
I	cm^4/m	moment of inertia
L	m	length (of sheet pile panel)
$L_{sp,f}$	m	length of failed sheet pile part
M_u	kNm/m	ultimate bending moment capacity
ReH	N/mm^2	(steel) minimum yield stress
Rm	N/mm^2	(steel) minimum tensile stress
t_f	mm	flange thickness
$U_{hor,crest}$	m	horizontal displacement at crest
$U_{hor,toe}$	m	horizontal displacement at toe
$U_{ver,crest}$	m	vertical displacement at crest
$U_{ver,toe}$	m	vertical displacement at toe
W_e	cm^3/m	elastic section modulus
W_{pl}	cm^3/m	plastic section modulus
$\alpha_{sp,f}$	°	angle of failed sheet pile part
ΔH_{water}	m	water retaining height
Δu	kPa	excess pore pressure
Δz_{crest}	m	vertical displacement of failed wedge at crest
Δz_{sp}	m	vertical displacement of sheet pile top
ε_u	%	(steel) elongation at fracture
f_y	N/mm^2	(steel) yield strength at peak strength
f_u	N/mm^2	(steel) tensile strength at fracture
σ'_1	kPa	major principal stress
σ'_3	kPa	minor principal stress
ϕ'_{mc}	°	equivalent Mohr-Coulomb effective friction angle

APPENDIX B   SUPPLEMENTARY TEST RESULTS ORGANIC SOILS
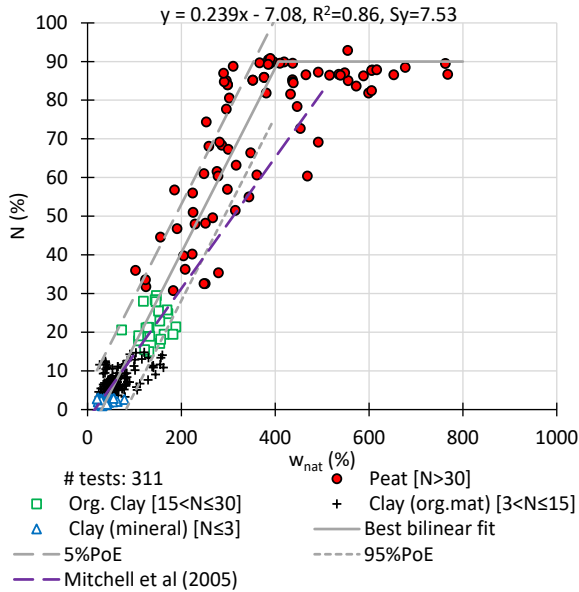
Figure B 1 Organic content versus natural water content, for organic to mineral soils, compared with the correlation by *Mitchell and Soga (2005)*.

$$N = \min[90\%, 0.239 \cdot w_{nat} - 7.08]$$
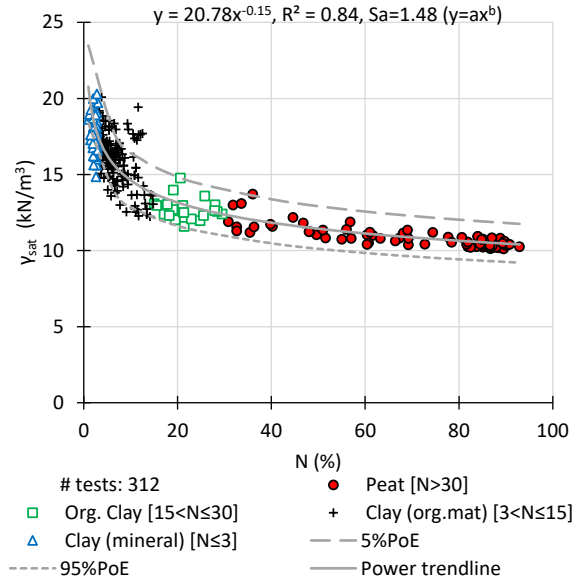
Figure B 2 Saturated unit weight versus organic content, for organic to mineral soils.

$$\gamma_{sat} = 20.8N^{-0.153}$$
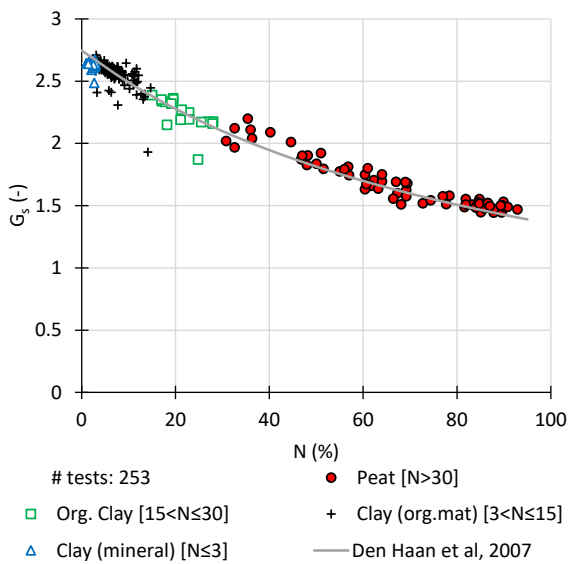
Figure B 3 Specific gravity versus organic content, for organic to mineral soils, compared with the correlation by *Den Haan and Kruse (2007)*.
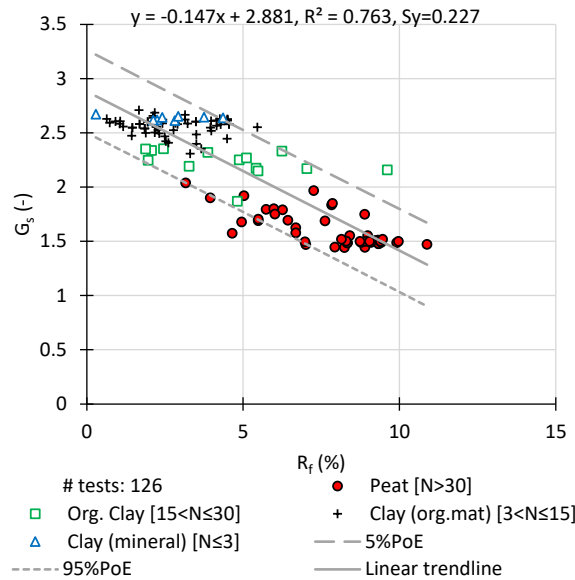
Figure B 4 Specific gravity versus CPT friction ratio, for organic to mineral soils.

$$G_s = 2.88 - 0.147R_f$$

167
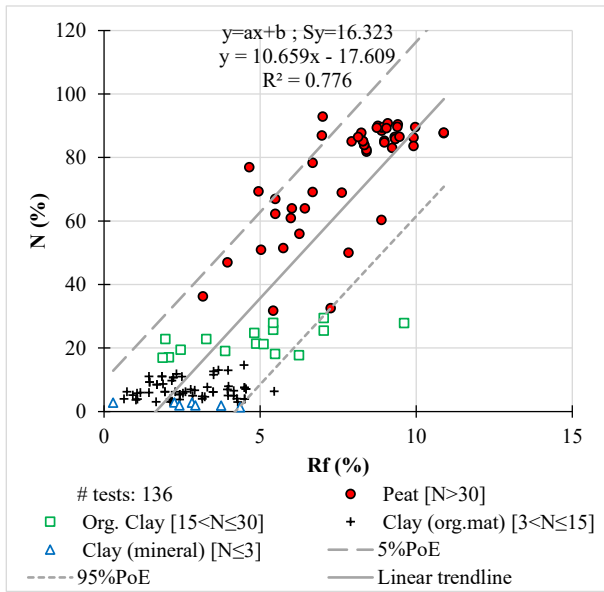
Figure B 5 Organic content versus CPT friction ratio, for organic to mineral soils. The subcategories are indicated in the legend.

$$N = 10.7R_f - 17.6$$
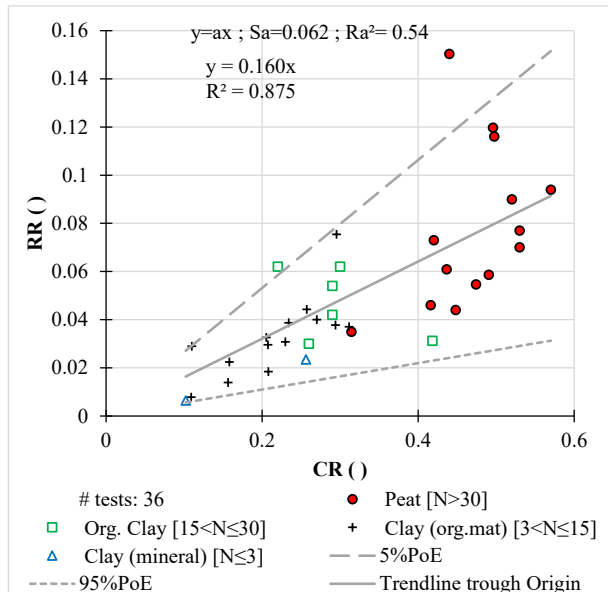
Figure B 6 Swelling (recompression) ratio versus compression ratio, for organic to mineral soils.

$$RR = 0.160CR$$
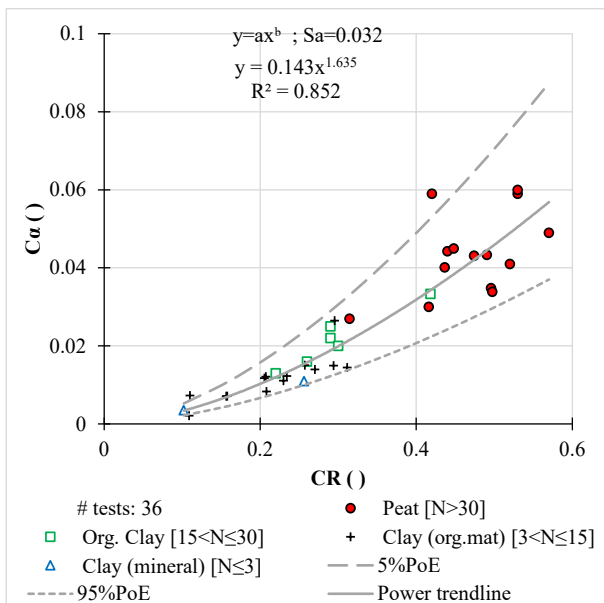
Figure B 7 Secondary compression (creep) ratio versus compression ratio, for organic to mineral soils.

$$C_\alpha = 0.143CR^{1.635}$$
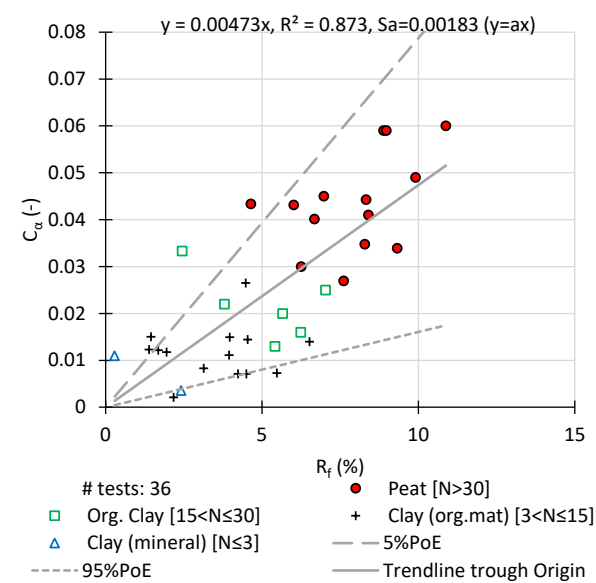
Figure B 8 Secondary compression (creep) ratio versus CPT friction ratio, for organic to mineral soils.

$$C_\alpha = 0.00473R_f$$
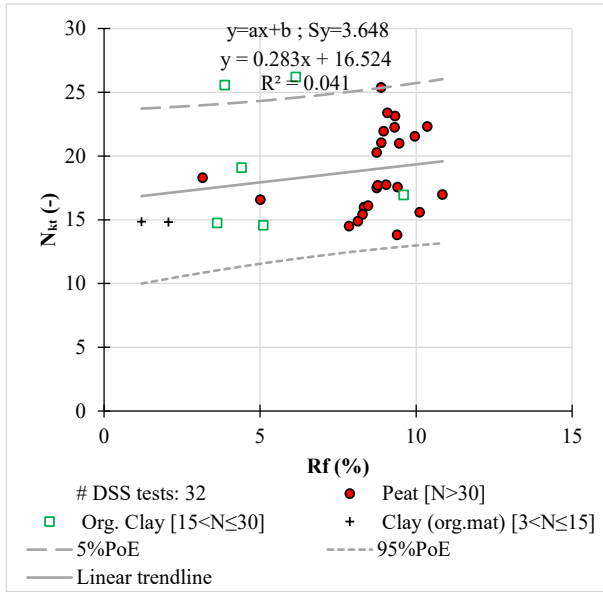
Figure B 9 Cone factor N_{kt} from at in-situ stress consolidated DSS tests versus CPT net cone resistance, for peats and organic clays, excluding mineral clays and sandy clays.
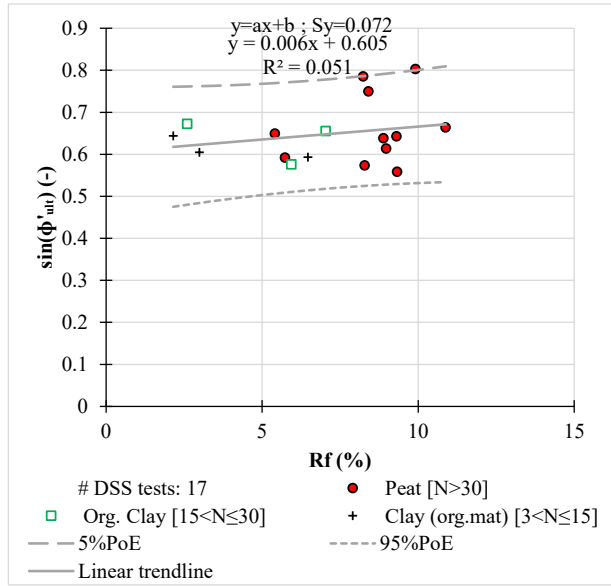
Figure B 10 Sine of friction angle from normally consolidated DSS tests versus CPT friction ratio, for peats and organic clays, excluding mineral clays and sandy clays.
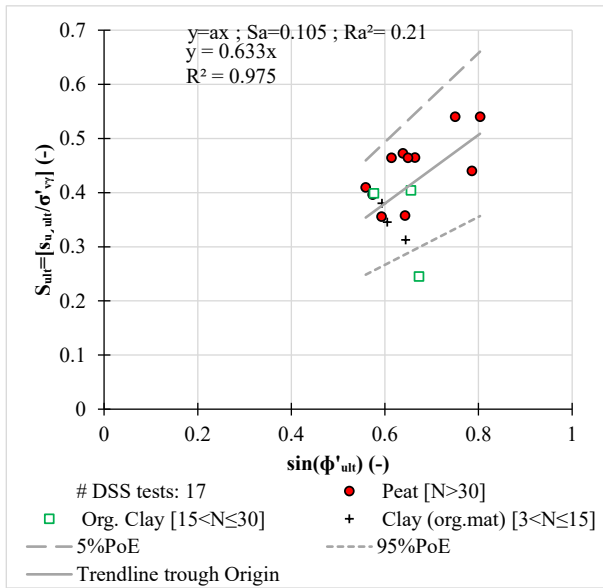
Figure B 11 S-ratio from normally consolidated DSS tests versus sine of friction angle, for peats and organic clays, excluding mineral clays and sandy clays.

$$S_{ult,DSS} = 0.633\sin(\phi'_{ult})$$
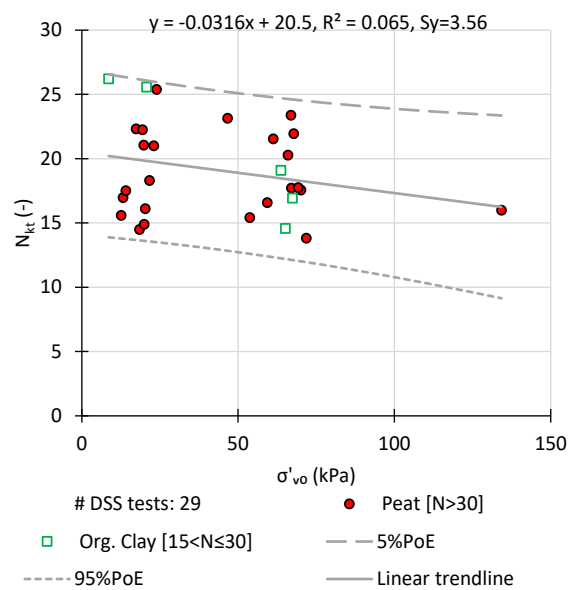
Figure B 12 Cone factor N_{kt} from at in-situ stress consolidated DSS tests versus in-situ vertical effective stress, for peats and organic clays, excluding mineral clays and sandy clays.
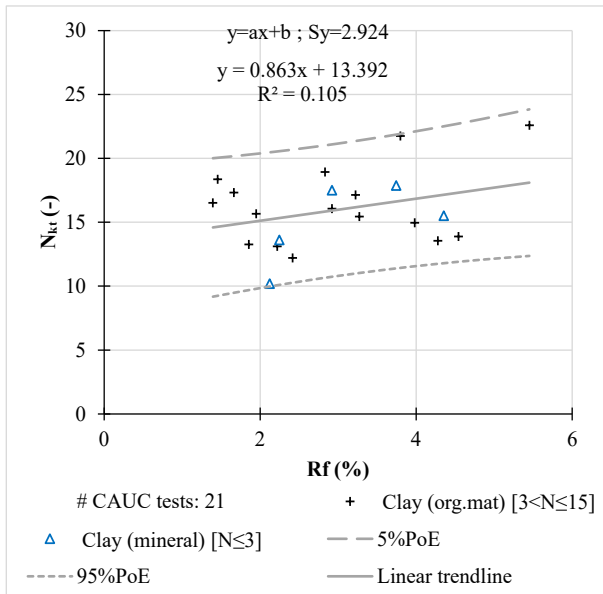
Figure B 13 Cone factor N_{kt} from at in-situ stress consolidated CAUC Triaxial tests versus CPT net cone resistance, for mineral clays and organic clays, excluding peats and sandy clays.
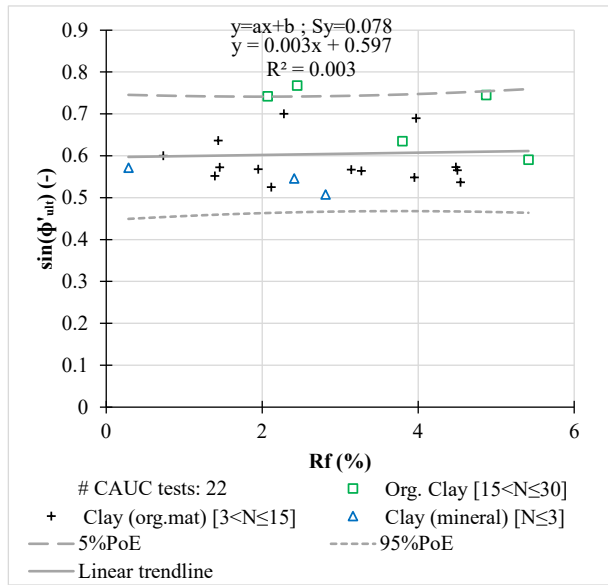
Figure B 14 Sine of friction angle from normally consolidated CAUC tests versus CPT friction ratio , for mineral clays and organic clays, excluding peats and sandy clays.
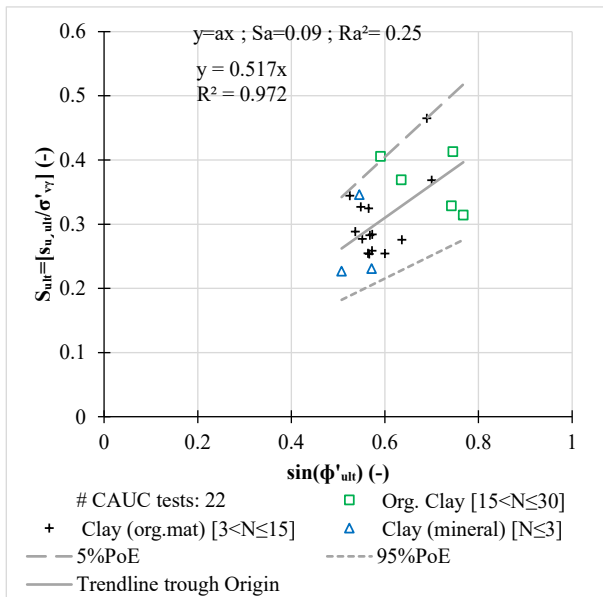
Figure B 15 S-ratio from normally consolidated CAUC tests versus sine of friction angle, for mineral clays and organic clays, excluding peats and sandy clays.

$$S_{ult,CAUC} = 0.517 \sin(\phi'_{ult})$$
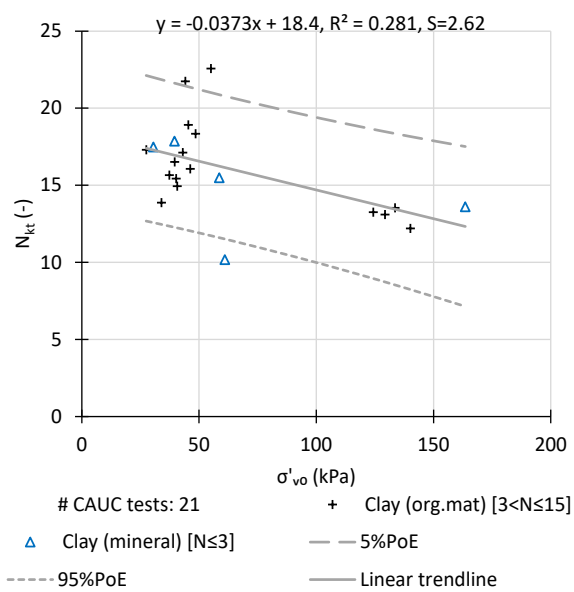
Figure B 16 Cone factor N_{kt} from at in-situ stress consolidated CAUC Triaxial tests versus in-situ vertical effective stress, for mineral clays and organic clays, excluding peats and sandy clays.
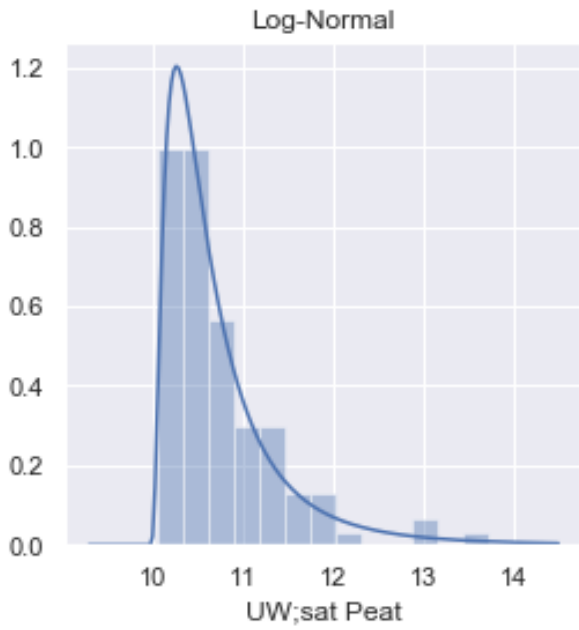
Figure B 17 Histogram and PDF database unit weight Peat
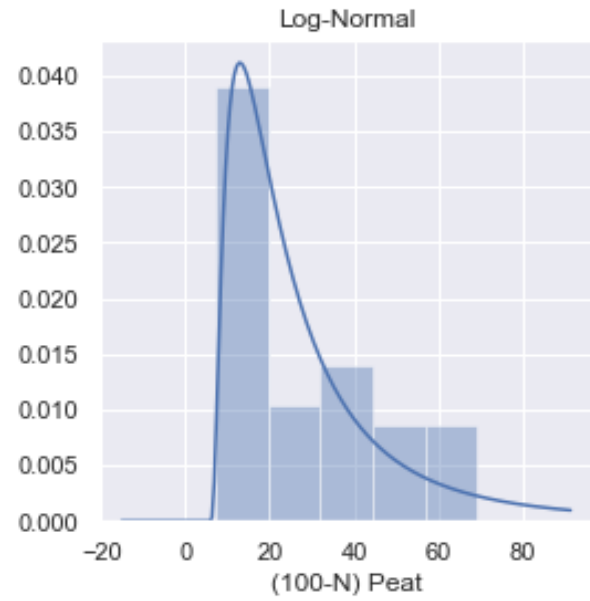
Figure B 18 Histogram and PDF database organic content Peat; note 100-N is presented instead of N (%).
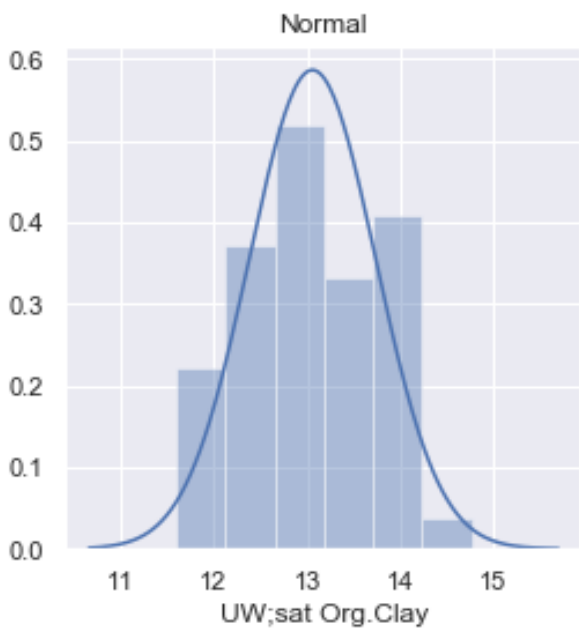
Figure B 19 Histogram and PDF database unit weight Organic Clay
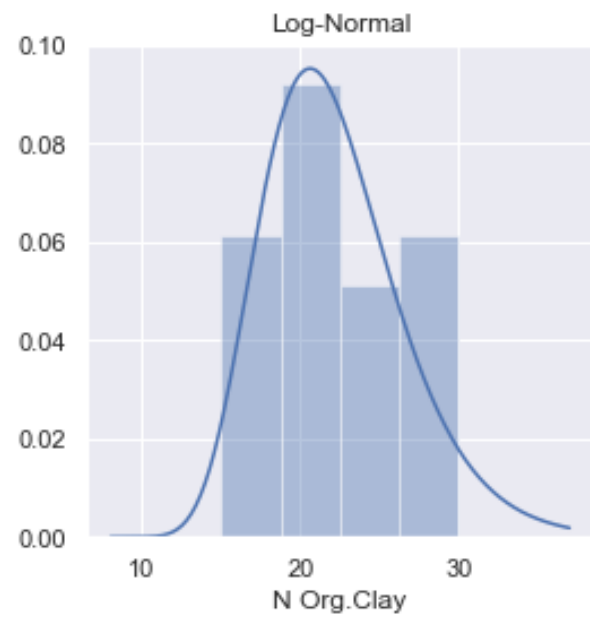
Figure B 20 Histogram and PDF database organic content Organic Clay
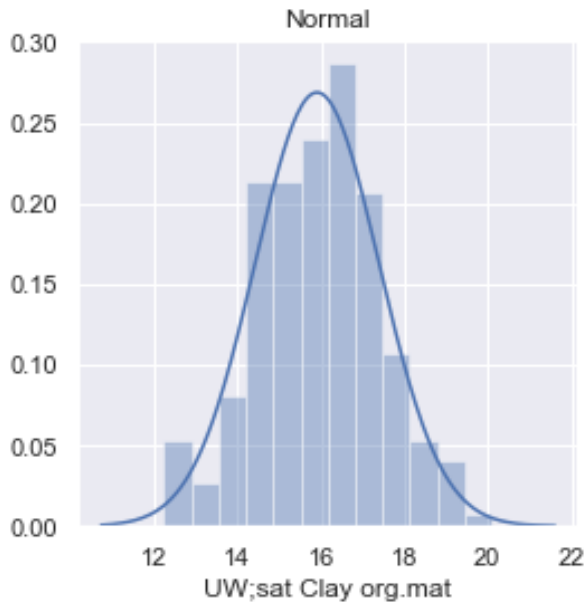
Figure B 21 Histogram and PDF database unit weight Clay with organic matter
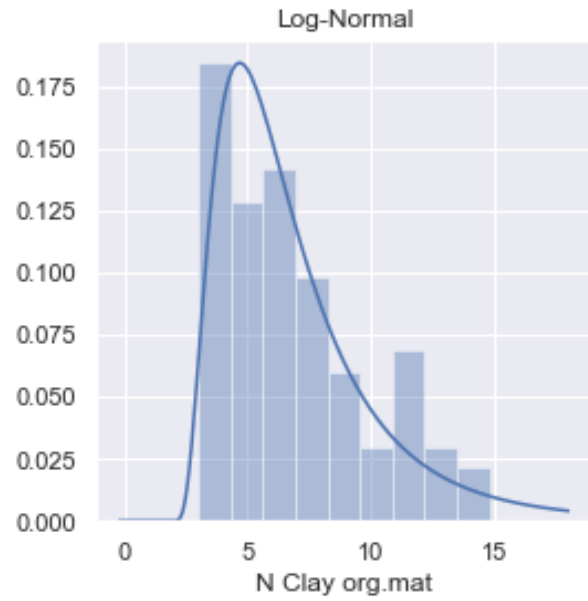
Figure B 22 Histogram and PDF database organic content Clay with organic matter
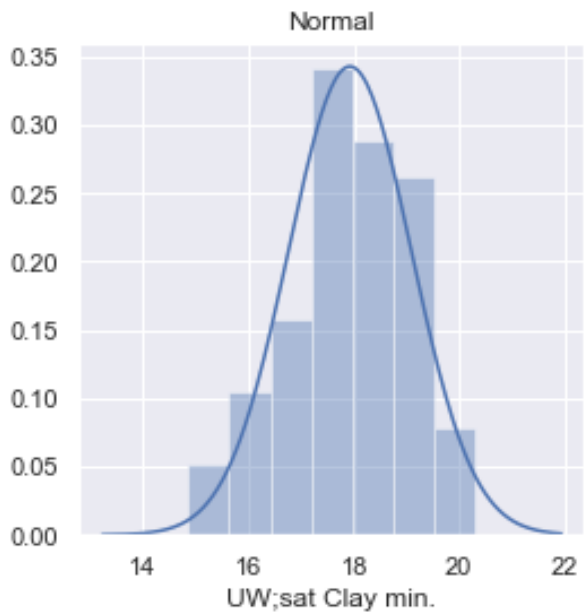
Figure B 23 Histogram and PDF database unit weight mineral clay
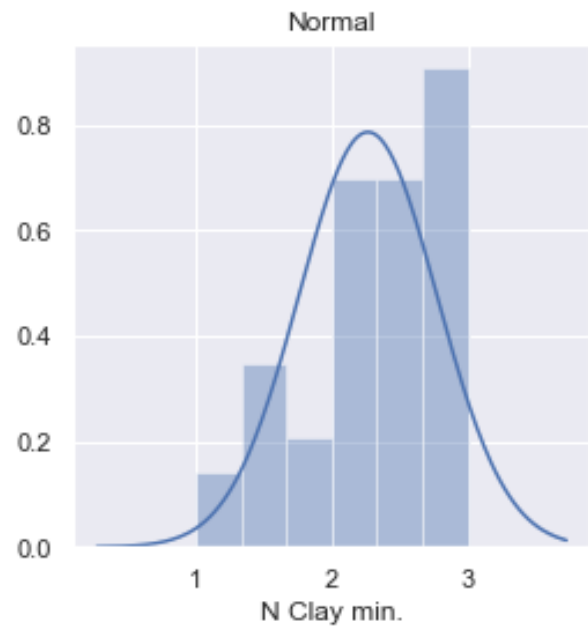
Figure B 24 Histogram and PDF database organic content mineral clay

APPENDIX C   CAUC TEST RESULTS KULHAWY AND MAYNE (1990)

Table C 1 Reported Triaxial test undrained normalized undrained shear strength, critical state friction angle and plastic volumetric strain ratio (Kulhawy and Mayne, 1990)

SOIL	TYPE TEST	S_u/σ'_{vnc}	ϕ_{nc}'	Λ	REFERENCE
Guanabara Bay	CK₀UC	0.254	25.0°	0.600	Ramalho-Ortigao (1983)
Drammen (P&H)	CK₀UC	0.39	32.6°	0.619	Prevost & Hoeg (1977)
Lilla Mellosa	CK₀UC	(0.400)a	33.2°	0.623	Larsson (1964)
Olav Kyrres, Oslo	CK₀UC	0.309	24.6°	0.65	Karlsrad & Myrvoll (1967)
Khor-Al-Zubair	CK₀UC	0.355	32.4°	0.654	Hanzawa (1977a)
Haney Clay	CK₀UC	0.268	21.4°	0.688	Vaid & Campanella (1974)
Oslo Clay	CAUC	0.317	27.0°	0.689	Simons (1960)
Weald Clay(H&S)	CK₀UC	0.256	25.0°	0.696	Wade (1966)
Taranto	CK₀UC	0.23	28.0°	0.70	Jamiolkowski et al (1982)
Buckshot	CAUC (Ko=0.50)	0.320	24.9°	0.703	Donaghe & Townsend (1978)
Sydney	CK₀UC	0.410	30.7°	0.704	Poulos (1978)
Boston Blue	CK₀UC	0.33	26.5°	0.716	Kinner & Ladd (1973), Ladd et al. 1977; D'Appolonia et al. (1971)
Onegai	CK₀UC	0.315	27.0°	0.725	Mitachi & Fujiwara (1987)
Buckshot	CAUC (Ko=0.67)	0.305	22.1°	0.730	Donaghe & Townsend (1978)
Plastic Holocene	CK₀UC	0.322	35.0°	0.757	Koutsoftas & Fisher (1976)
Hokkaido A	CK₀UC	0.400	35.1°	0.764	Mitachi & Kitago (1976)
North Sea	CK₀UC	0.309	23.9°	0.786	Hight, Gens, Jardine (1985)
Hokkaido C	CK₀UC	0.360	34.0°	0.786	Mitachi & Kitago (1976)
Haga Clay (A&S)	CAUC	(0.442)a	38.2°	0.787	Anderson & Stenhamer (1982)
Soft Bangkok	CAUC	0.442	43.9°	0.791	Holmberg (1977)
Hokkaido B	CK₀UC	0.361	34.9°	0.795	Mitachi & Kitago (1976)
Hayakita	CK₀UC	0.335	29.0°	0.804	Mitachi & Fujiwara (1987)
Silty Holocene	CK₀UC	0.325	29.2°	0.809	Koutsoftas (1981)
London (HGJ)	CK₀UC	0.258	19.7°	0.817	Hight, Gens, Jardine (1985)
Kawasaki K-30	CK₀UC	0.389	38.6°	0.828	Kamei & Nakase (1989)
Natsushima	CK₀UC	0.360	36.0°	0.860	Hanzawa (1983)
Hackensack Valley (Sax)	CK₀UC	0.232	19.0°		Saxena et al (1978)
Connecticut Valley (Sax)	CK₀UC	0.250	20.5°		Saxena et al (1978)
Goose Lake	CAUC	0.351	22.1°		Khera Krizek (1976)
Higgins Clay	CAUC	0.295	23.1°		Lee & Morrison (1970)
Kimola	CK₀UC	0.42	23.2°		Kankare (1968)
Vicksburg	CAUC	0.28	23.5°		Ladd (1965)
Chicago	CK₀UC	0.225	23.8°		Finno et al (1989)
Portsmouth	CAUC	0.248	23.9°		Ladd (1972)
Trieste Clay	CK₀UC	0.320	24.0°		Battaglio et al (1981)

Wallaceburg	CAUC	0.31	25.0°		DeLory & Salvas
Whitefish Falls	CAUC	0.330	26.0°		DeLory & Salvas
Ellingsrud (D&S)	CAUC	0.281	26.4°		DiBagio & Stenhamar (1976)
Rissa, Norway	CK$_O$UC	0.316	26.4°		Gregersen (1980)
Skabo	CAUC	0.32	26.5°		Landva
Evanston, Ill.	CK$_O$UC	0.33	26.9°		Finno (1989)
Postgirotomten	CK$_O$UC	0.319	27.3°		Aas (1980)
Louisville	CK$_O$UC	0.311	27.4°		Hagerty & Garlanger
Sapporo	CK$_O$UC	0.309	28.1°		Mitachi & Kitago (1979, 1983)
Belfast	CK$_O$UC	0.355	28.2°		Crooks (1981)
Porto Tolle	CK$_O$UC	0.320	30.0°		Battaglio et al (1981)
Lean Drammen	CK$_O$UC	0.340	30.0°		Berre & Bjerrum (1973)
Nagoya	CK$_O$UC	0.386	30.9°		Nakase & Kamei (1988)
Gloucester, Ottawa	CAUC	0.470	31.9°		Bozozuk & Leonards (1972)
Hokkaido	CK$_O$UC	0.321	32.0°		Mitachi & Kitago (1979, 1980)
Kyoto	CK$_O$UC	0.451	32.5°		Akai & Adachi (1965)
Kawasaki	CK$_O$UC	0.445	33.0°		Ladd (1965)
LaRoche Chalais	CAUC	0.386	33.0°		Darve et al (1979)
Kobe	CK$_O$UC	0.354	33.1°		Nakase & Kamei (1988)
Baastad, Norway	CK$_O$UC	0.344	33.7°		Gregerson & Loken (1979)
Firfani, Turkey	CAUC	0.414	33.7°		Lowe & Karafiath
Drammen Clay	CK$_O$UC	(0.239)a	33.8°		Berre (1976)
San Francisco Bay Mud	CK$_O$UC	0.350	35.6°		Duncan & Seed (1966)
Fao Clay, Iraq	CK$_O$UC	0.423	36.4°		Hanzawa (1977b)
Ariake Clay (Y)	CAUC	0.450	39.2°		Yasuhara et al (1982)
Mixed M-10	CK$_O$UC	0.402	39.2°		Kamei & Nakase (1989)
Kawasaki M10	CK$_O$UC	0.375	39.3°		Nakase & Kamei (1983)
Laval	CAUC	0.458	39.3°		Tavenas (1981)
Kawasaki M20	CK$_O$UC	0.394	40.1°		Nakase & Kamei (1983)
Kawasaki M15	CK$_O$UC	0.385	40.1°		Nakase & Kamei (1983)
Niigata	CK$_O$UC	0.416	40.4°		Nakase & Kamei (1988)
Kawasaki M-50	CK$_O$UC	0.393	40.5°		Nakase & Kamei (1988)
Aomori	CK$_O$UC	0.416	40.5°		Nakase & Kamei (1988)
Toyama	CK$_O$UC	0.408	40.9°		Nakase & Kamei (1988)
Kawasaki M30	CK$_O$UC	0.405	41.0°		Nakase & Kamei (1983)
Ohita	CK$_O$UC	0.401	41.0°		Nakase & Kamei (1988)
Sakaiminato	CK$_O$UC	0.388	41.3°		Nakase & Kamei (1988)

APPENDIX D EXAMPLE CSR MODEL RECONSTITUTED OOSTVAARDERSPLASSEN CLAY

The OVP clay can be classified as a highly plastic clay. The clay has liquid limit of 166% and plasticity index of 110%. The main soil properties are: φ'=40.0, m=(1-CR/RR)=0.87, CR=0.30 and e_0=2.51.

Table D 1 OVP clay: State dependent parameters CSR model.

Test	1	2	3	4	5	6
OCR (-)	1.00	1.00	3.00	6.05	12.00	20.00
s'_{vy} (kPa)	200	100	150	121	150	200
s'_{v0} (kPa)	200	100	50	20	13	10
K_0 (-)	0.36	0.36	0.68	1.18	2.14	3.44
p'_0 (kPa)	114	57	39	22	22	26
$s_{u,test}$ (kPa)	63	33	43	29	33	45
$s_{u,EPP}$ (kPa)	94	47	32	18	18	21
$s_{u,CSR}$ (kPa)	66	33	43	31	35	44
s_u/σ'_{vy} (-)	0.33	0.33	0.28	0.26	0.24	0.22
s_u/σ'_{vo} (-)	0.33	0.33	0.85	1.56	2.83	4.40
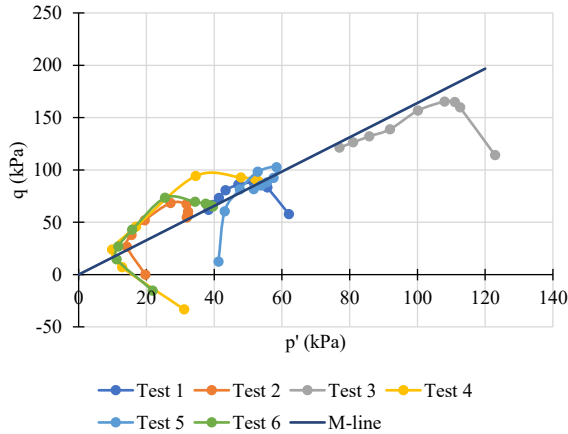
Figure D 1 OVP clay: q-p-diagram normalized by the vertical preconsolidation stress.
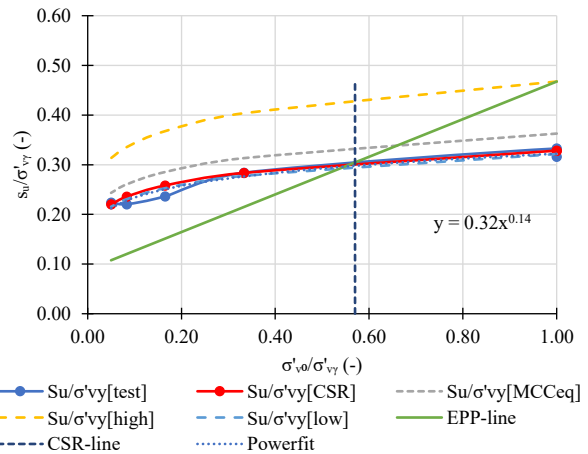
Figure D 2 OVP clay: Undrained shear strength versus vertical consolidation stress, both normalized by the vertical preconsolidation stress.

175

Table D 2 OVP clay: Model constants and calculation steps CSR model.

Step	Equation	Output
	CSR model:	
1	$M_c = \frac{6\sin\phi'}{3-\sin\phi'}$	1.64
2	$K_{nc} = 1 - \sin\phi'$	0.36
3	$OCR_{K:1} = \left(\frac{1}{K_{nc}}\right)^{\left(\frac{1}{\sin\phi'}\right)}$	4.96
4	$\Delta K_{ur,K:1} = K_{nc}\frac{OCR - OCR^{\sin\phi'}}{OCR-1}$	0.19
5b	$K_0 = OCR_{K:1}\left(K_{nc} - \Delta K_{ur,K:1}\right) + \Delta K_{ur,K:1}$	var
6b	$s_{u,EPP} = \left(\frac{M_c}{2}\right)p'_0$	var
7b	CSR (fit based on graph)	1.75
8b	$m \cong 1 - \frac{RR}{CR}$ (fit based on graph)	0.87
9b	$K_x = CSR\left(K_{nc} - \Delta K_{ur,K:1}\right) + \Delta K_{ur,K:1}$	0.48
10	$s_{u,CAUC,CSR} = \sigma'_{v0}\left(\frac{1+2K_x}{3}\right)\left(\frac{M_c}{2}\right)\left(\frac{OCR}{CSR}\right)^m$	var
11	$S_{CAUC,CSR} = \left(\frac{1+2K_x}{3}\right)\left(\frac{M_c}{2}\right)\left(\frac{1}{CSR}\right)^m$	0.33
	MCC model:	
12	$\nu_{K:1} = \frac{\Delta K_{ur,K:1}}{1+\Delta K_{ur,K:1}}$	0.16
13	$c_{K:1} = \frac{\log(OCR_{K:1})}{\log\left(\frac{OCR_{K:1}(1+2K_{nc})}{3}\right)}$	1.54
14	$\Lambda = 1 - c_{K:1}(1-m)$	0.80
15	$\lambda = \frac{(1+e_0)CR}{\ln(10)}$	0.457
16	$\kappa_{oed} = \kappa \cdot c_{K:1} = \frac{c_{K:1}(1+e_0)RR}{\ln(10)}$	0.094
17b	$M_{c,MCC,eq} \approx M_c\frac{s_{u,test}}{s_{u,CAUC,CSR}}$ and CSR based on method A	1.45

APPENDIX E   SCHEMES   FOR   CONSTITUTIVE   MODEL PARAMETER DETERMINATION

The following figure presents the procedure to determine the equivalent Mohr-Coulomb effective strength parameters to match SHANSEP undrained shear strength envelope

1 Check NC s_u and determine φ', φ'$_{cs}$

K_{nc} consolidation:
$$K_{nc} = 1 - \sin(\phi_{cs}')$$

if $s_{u,Num} < s_{u,lab}$:
\>\> φ'

if $s_{u,Num} > s_{u,Lab}$:
\<\< φ'

2 Check OC s_u based on OCR (σ'$_{v,y}$)

K_{oc} consolidation:
$$K_{oc} = K_{oc} OCR^{\sin(\phi_{cs}')}$$

if $s_{u,Num} > s_{u,Lab}$:
check \<\< OCR
\<\< c'

if $s_{u,Num} < s_{u,Lab}$
check \>\> OCR
\>\> c' (step 3)

3 Update OC and NC s_u and determine c'

if $s_{u,Num} < s_{u,Lab}$:
determine maximum cohesion i.c.w. tension cut-off (TCO)
$$c'_{max} = \frac{s_u(1 - \sin(\phi'))}{\cos(\phi')}$$

iterate φ' and c' to fit NC and OC strength (SHANSEP envelope)
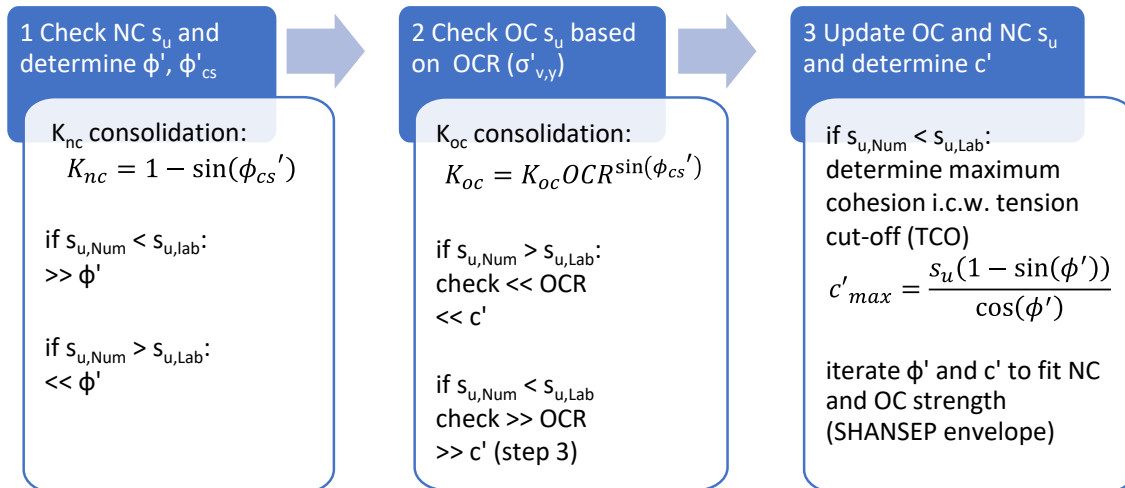
Figure E 1 Procedure to determine the equivalent Mohr-Coulomb effective strength parameters to match SHANSEP undrained shear strength envelope

The following figures schematically show the applied procedure to derive the model parameters from the laboratory tests for various Plaxis constitutive soil models. The green boxes are the input parameters, where the stiffness is based on K_0CRS tests and strength is based on DSS and CAUC tests. The blue boxes are the model parameters. The black arrows represent a direct relation. The grey arrows represent an indirect relation or influence, which require numerical simulations. The grey shaded parameters are auxiliary parameters, not part of the constitutive model.
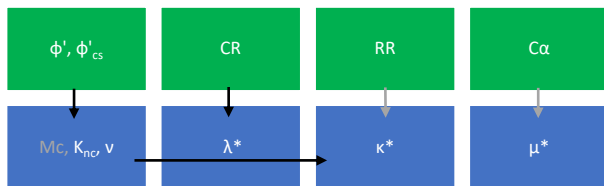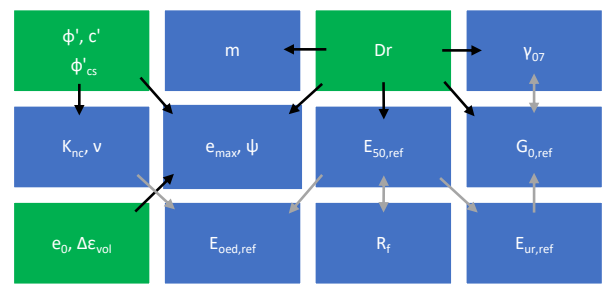
Figure E 2 SS(C)-model parameter determination procedure for fine grained soils. The earth pressure ratio, Poisson's ratio and the correction for the recompression index are based on the critical state friction angle as elaborated on in Chapter 3. The Mc parameter is not an input parameter. The Recompression index is increased for the SSC model and the Creep index is reduced for the SSC model based on numerical simulations.
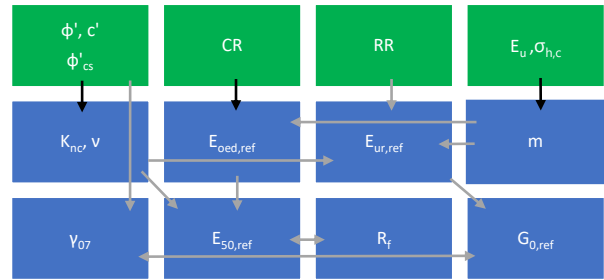
Figure E 3 HS(S)-model parameter determination procedure for fine grained soils. The earth pressure ratio and Poisson's ratio are based on the critical state friction angle as elaborated on in Chapter 3. The stiffness parameters require corrections for the reference stress, drained versus undrained behavior, 1D versus 2D conditions and the stress exponent (m). Final corrections require numerical simulations.
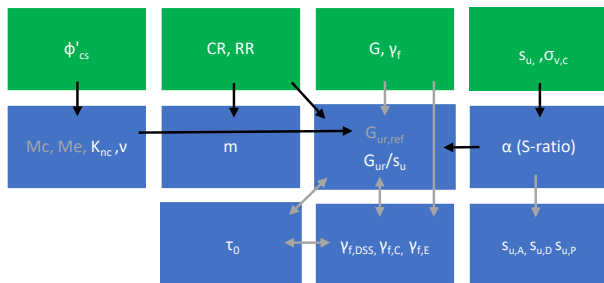
Figure E 4 SHANSEP-model parameter determination procedure for fine grained soils. The scheme is based on a DSS test, but can also be based on a CAUC or CAUE test or all tests. The earth pressure ratio and Poisson's ratio are based on the critical state friction angle as elaborated on in Chapter 3. The ratios between the strains at failure and undrained shear strength for DSS, CAUC and CAUE require numerical simulations.
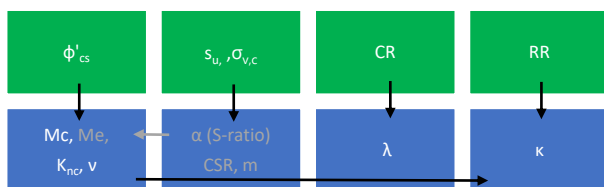
Figure E 5 MCC model parameter determination procedure for fine grained soils. The earth pressure ratio and Poisson's ratio are based on the critical state friction angle as elaborated on in Chapter 3. The Mc can be optimized by the CSR model verification as shown in chapter 3 or by numerical simulations. The Me is not an input parameter for the MCC model implemented in Plaxis.
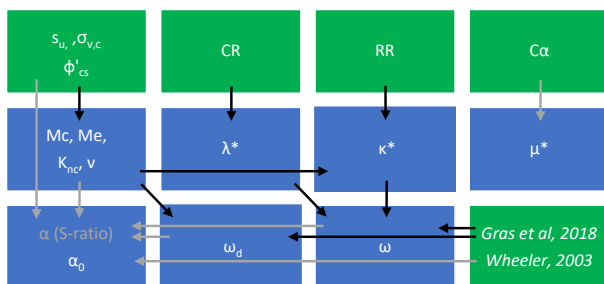
Figure E 6 CSC1S-model parameter determination procedure for fine grained soils. The earth pressure ratio and Poisson's ratio are based on the critical state friction angle as elaborated on in Chapter 3. The parameter α_0, ω and ω_d are based on literature, where for ω a lower bound is used and α_0 is optimized by numerical simulations. The Creep index is reduced for too as in the SSC model. No de-structuration parameters are taken into account for these soft organic soils.

Figure E 7 HS(S)-model parameter determination procedure for coarse grained soils. The earth pressure ratio and Poisson's ratio are based on the critical state friction angle as elaborated on in Chapter 3. The stiffness parameters require corrections for the reference stress. Final corrections require numerical simulations.

APPENDIX F COMPARISON NUMERICAL SIMULATIONS WITH LABORATORY TESTS

Table F 1 DSS undrained shear strength results organic clay layer 3 and soft clay layer 3a

borehole	sample	layer	level (m NAP)	σ'_{vc} (kPa)	state	$s_{u,pk}$ (kPa)	$s_{u,ult}$ (kPa)	G at γ_s=1% (MPa)	γ_s at τ_{pk} (%)
B35	234	3	-1.50	70	NC	28.1	27.9	0.70	35
B36	272	3	-1.50	72	NC	27.9	27.3	0.66	34
B31	6	3	-1.70	75	NC	35.5	35.0	0.82	32
B31	11	3	-2.60	72	NC	29.9	29.1	0.79	20
B36	270	3	-1.10	12	OC	10.4	10.3	0.38	34
B35	232	3	-1.13	12	OC	9.6	9.5	0.29	35
B41	196	3	-1.40	10	OC	7.4	7.4	0.21	40
B38	153	3	-1.45	13	OC	11.0	11.0	0.30	40
B42	214	3a	-1.65	70	NC	24.3	24.2	0.70	38
B33	254	3a	-1.75	70	NC	22.0	21.9	0.60	36

Table F 2 DSS undrained shear strength results peat layer 4

borehole	sample	layer	level (m NAP)	σ'_{vc} (kPa)	state	$s_{u,pk}$ (kPa)	$s_{u,ult}$ (kPa)	G at γ_s=1% (MPa)	γ_s at τ_{pk} (%)
B38	158	4	-2.3	40	NC	21.6	21.6	0.38	40
B40	52	4	-2.7	90	NC	42.3	41.8	0.55	35
B31	14	4	-3.0	79	NC	43.0	43.0	0.53	40
B37	104	4	-3.0	54	NC	25.2	25.1	0.38	39
B27	75	4	-3.8	40	NC	18.9	18.9	0.31	40
B39	32	4	-2.7	17	OC	20.1	20.1	0.37	40
B31	16	4	-3.4	15	OC	22.1	20.8	0.43	23
B25	145	4	-3.4	17	OC	13.9	13.9	0.21	40
B40	56	4	-3.8	16	OC	20.9	17.5	0.42	28
B31	21	4	-4.1	15	OC	21.5	20.6	0.30	25

Table F 3 CAUC undrained shear strength results organic clay layer 3 and soft clay layer 3a

borehole	sample	layer	σ'$_{vc}$ (kPa)	σ'$_{hc}$ (kPa)	state	stress path at failure	s$_{u,pk}$ (kPa)	s$_{u,ult}$ (kPa)	ε$_{ult}$ (%)	Eu at ε=1% (MPa)	ε at q$_{max}$
B40	49	3	91	34	NC	contractive	42.1	34.6	15	1.80	4.5
B27	65	3	50	14	NC	contractive	25.8	20.6	15	1.12	3.1
B31	8	3	129	53	NC	contractive	70.1	56.1	15	3.21	6.1
B38	152	3	13	8	OC	dilative	17.1	11.9	15	0.68	25.0
B35	233	3	13	9	OC	intermediate	10.6	7.7	15	0.58	21.9
B41	194	3	9	5	OC	contractive	9.3	7.0	5	0.79	5.4
B38	151	3	12	8	OC	dilative	22.3	14.4	5	1.58	25.0
B42	215	3a	15	10	OC	contractive	8.7	6.6	15	0.74	5.9
B33	252	3a	12	7	OC	contractive	9.8	6.4	5	0.66	24.7

Table F 4 K0CRS stress conditions Soiltest numerical simulations all layers

K0CRS	Step	σ'v,start (kPa)	σ'v,end (kPa)	σ'v,end (kPa)	days
OED	1	20	200	200	1
OED	2	200	20	20	1

Organic clay layer 3

Table F 5 CAUC and DSS stress conditions Soiltest numerical simulations

Layer	Test	Condition	σ'v (kPa)	σ'vy (kPa)	K0 (-)	σ'h (kPa)	days
3	CAUC	OC	10	25	0.67	6.7	1
3	CAUC	NC	90	90	0.38	34.0	1
3	DSS	OC	10	25	0.67	6.7	1
3	DSS	NC	70	70	0.38	26.4	1
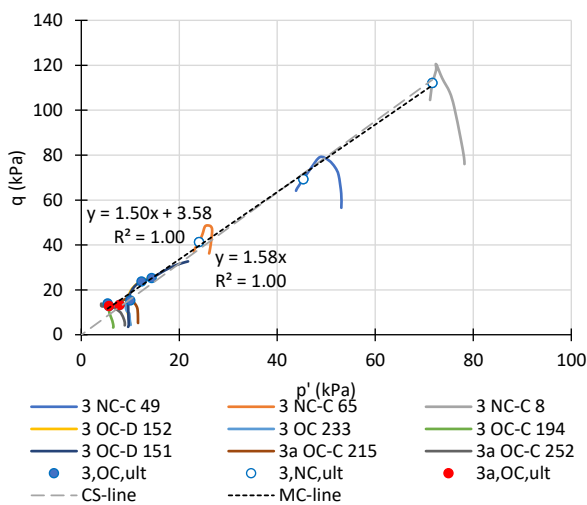
Figure F 1 Organic clay layer 3: CAUC laboratory tests, stress path
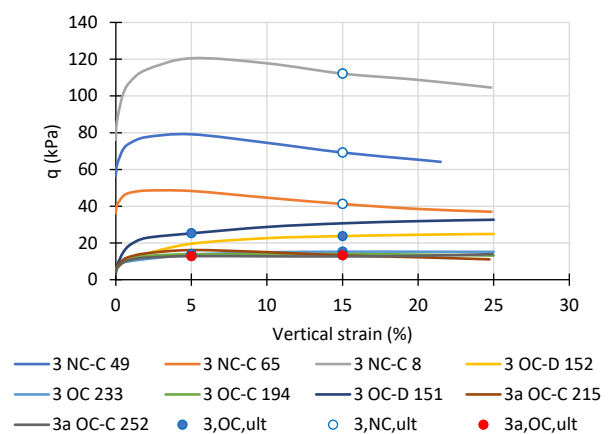
Figure F 2 Organic clay layer 3: CAUC laboratory tests, stress-strain curve
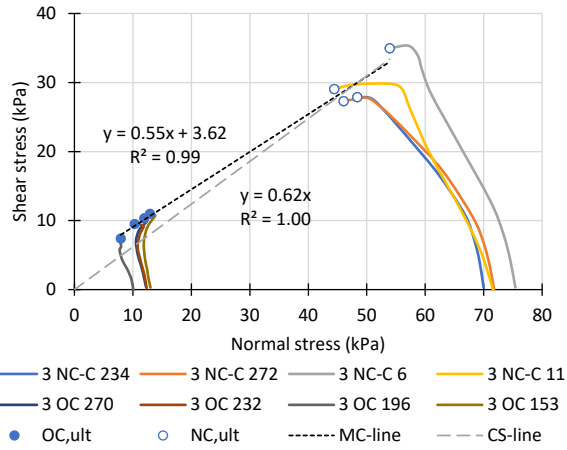
Figure F 3 Organic clay layer 3: DSS laboratory tests, stress path
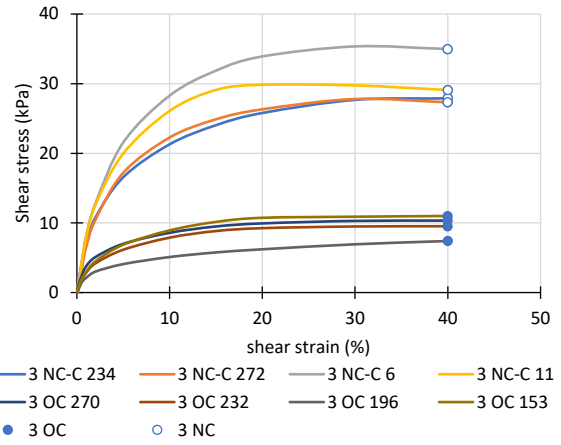
Figure F 4 Organic clay layer 3: DSS laboratory tests, stress-strain curve
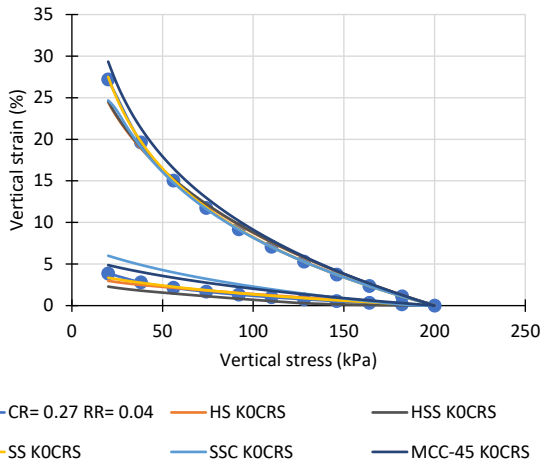
Figure F 5 Organic clay layer 3: K0CRS simulation, stress-strain curve
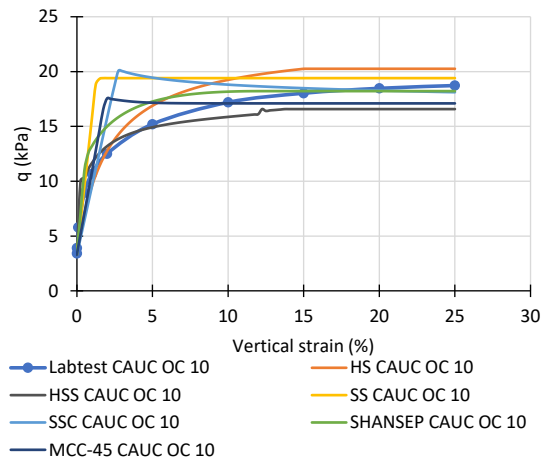
Figure F 6 Organic clay layer 3: OC CAUC simulation (ultimate strength), stress-strain curve
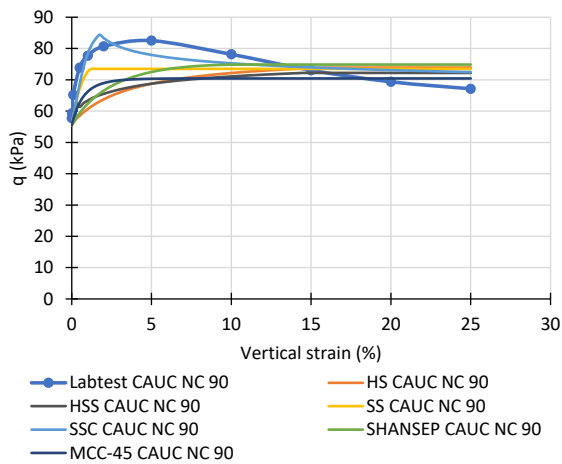
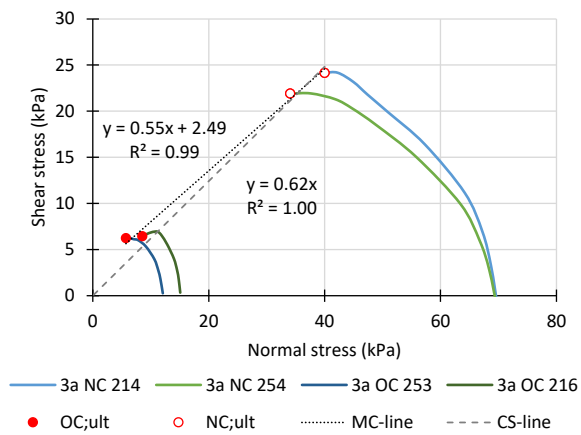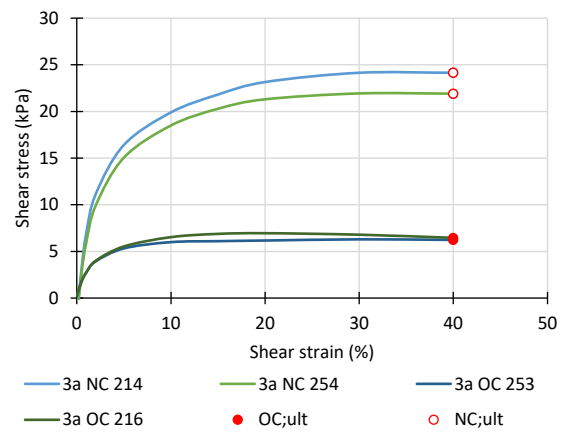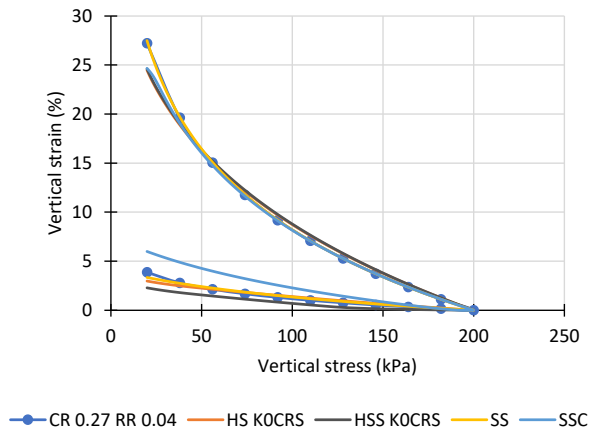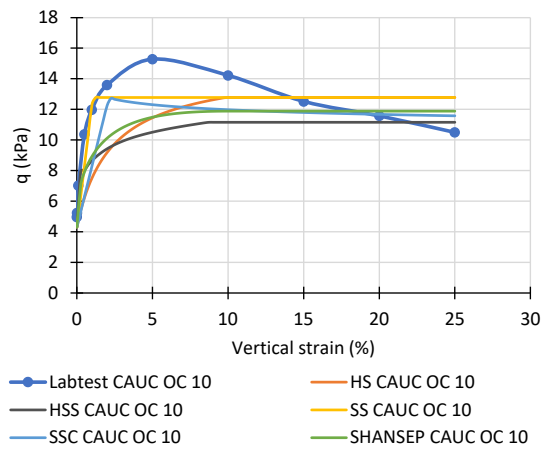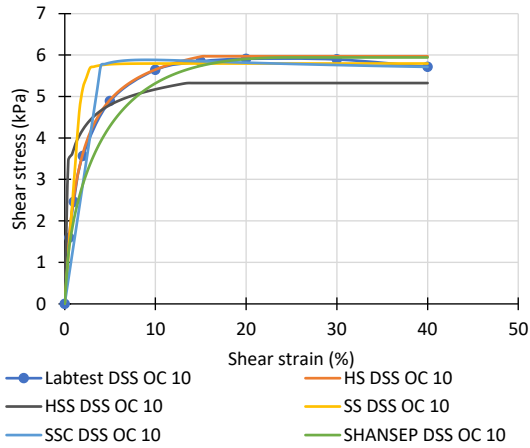Figure F 7 Organic clay layer 3: NC CAUC simulation (ultimate strength), stress-strain curve
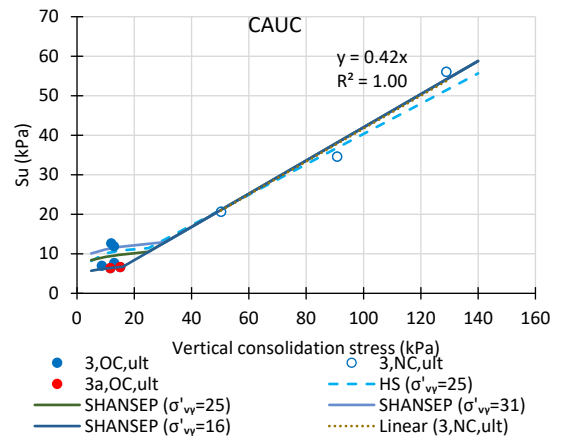
Figure F 8 Organic clay layer 3: CAUC simulation (ultimate strength), SHANSEP failure envelope
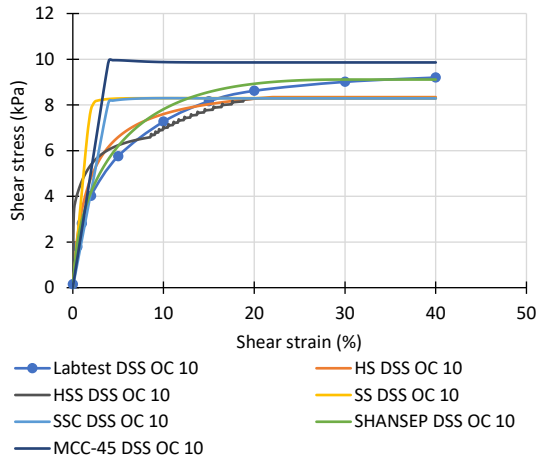
Figure F 9 Organic clay layer 3: OC DSS simulation (ultimate strength), stress-strain curve
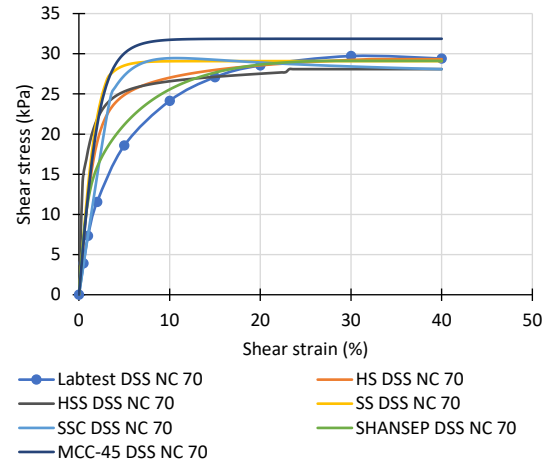
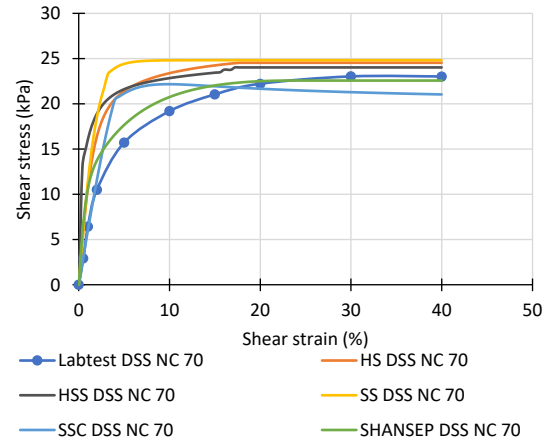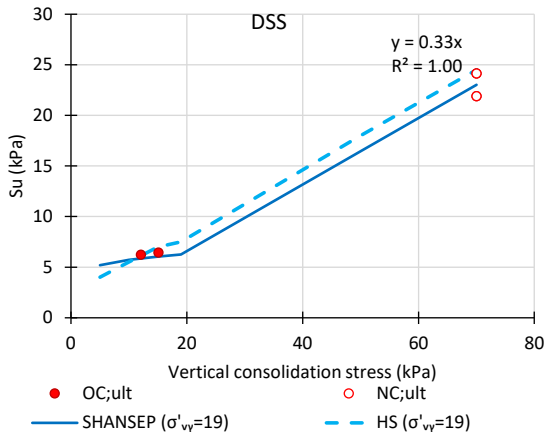Figure F 10 Organic clay layer 3: NC DSS simulation (ultimate strength), stress-strain curve
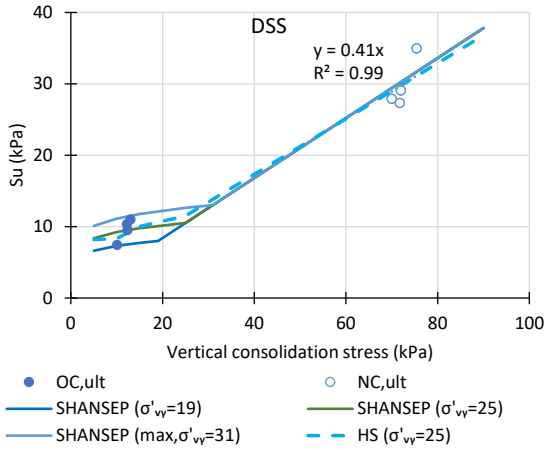
Figure F 11 Organic clay layer 3: DSS simulation (ultimate strength), SHANSEP failure envelope

## Organic clay layer 3 anisotropic models and no geometrical correction
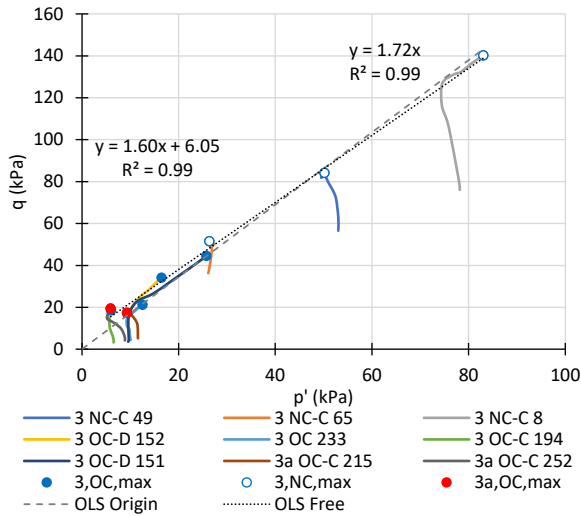
Figure F 12 Organic clay layer 3: CAUC laboratory tests without geometrical correction, stress path
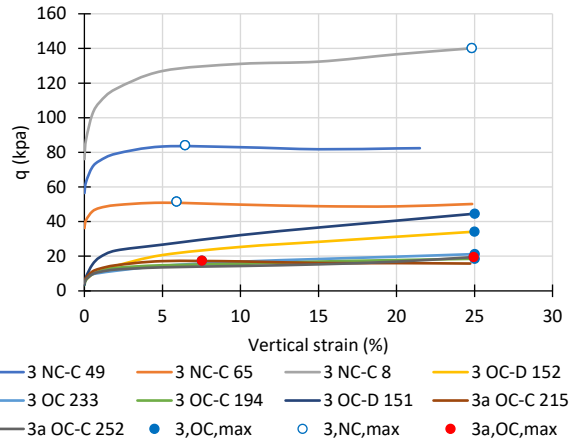
Figure F 13 Organic clay layer 3: CAUC laboratory tests without geometrical correction, stress strain curve
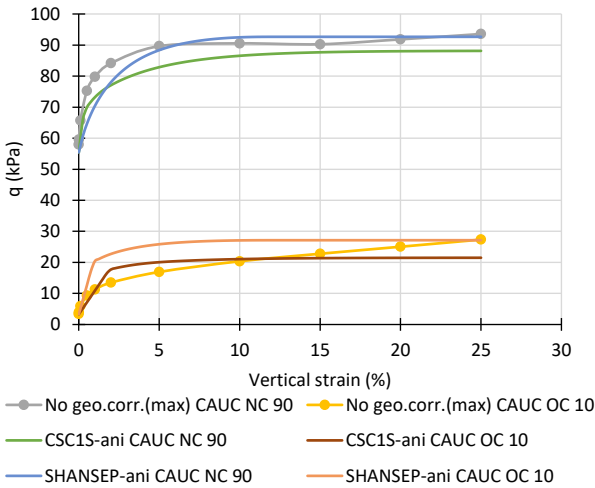
Figure F 14 Organic clay layer 3 (without geometrical correction): CAUC simulation anisotropic strength models, stress strain curve
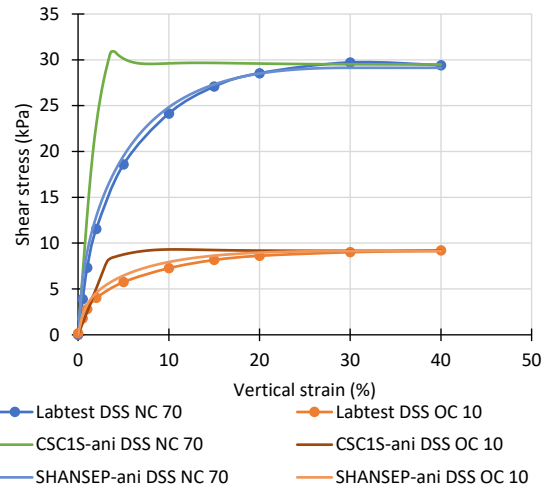


Figure F 15 Organic clay layer 3: DSS simulation anisotropic strength models, stress strain curve
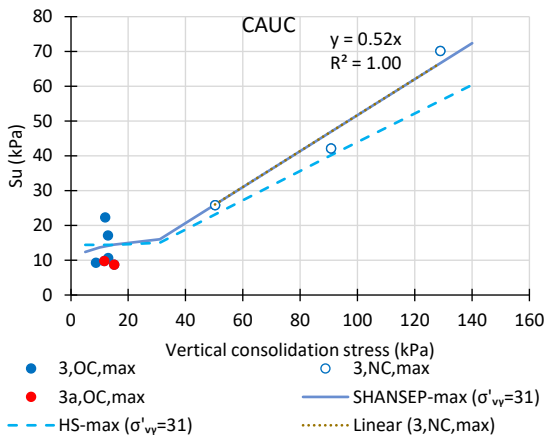
Figure F 16 Organic clay layer 3 (without geometrical correction): CAUC simulation without geometrical correction, SHANSEP failure envelope

Soft clay layer 3a

Table F 6 CAUC and DSS stress conditions Soiltest numerical simulations

Layer	Test	Condition	σ'v (kPa)	σ'vy (kPa)	K0 (kPa)	σ'h (kPa)	days
3a	CAUC	OC	15	19	0.44	6.6	1
3a	CAUC	NC	70	70	0.38	26.6	1
3a	DSS	OC	10	19	0.57	5.7	1
3a	DSS	NC	70	70	0.38	26.6	1

Figure F 17 Soft clay layer 3a: DSS laboratory tests, stress path

Figure F 18 Soft clay layer 3a: DSS laboratory tests, stress-strain curve

Figure F 19 Soft clay layer 3a: K0CRS simulation, stress-strain curve

Figure F 20 Soft clay layer 3a: OC CAUC simulation (ultimate strength), stress-strain curve

Figure F 21 Soft clay layer 3a: OC DSS simulation (ultimate strength), stress-strain curve
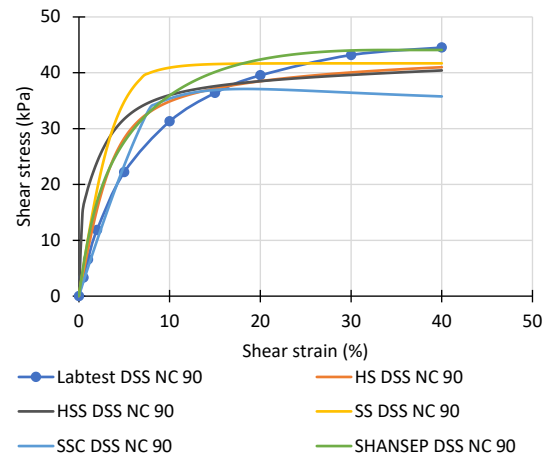

Figure F 22 Soft clay layer 3a: NC DSS simulation (ultimate strength), stress-strain curve

Figure F 23 Soft clay layer 3a: DSS simulation (ultimate strength), SHANSEP failure envelope

Soft clay layer 3a anisotropic models and no geometrical correction
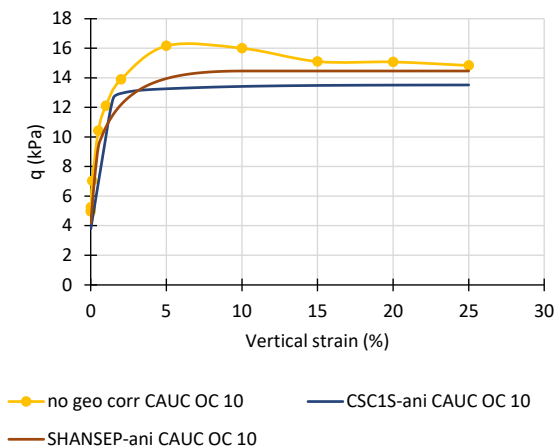
Figure F 24 Soft clay layer 3a (no geometrical correction): OC CAUC simulation anisotropic strength models, stress strain curve
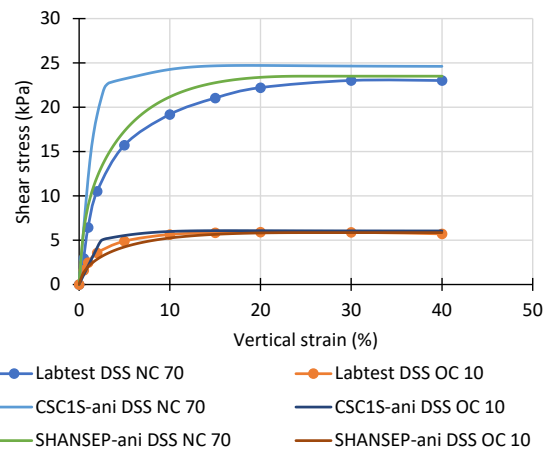
Figure F 25 Soft clay layer: OC DSS simulation anisotropic strength models, stress strain curve

185

Peat layer 4

Table F 7 CAUC and DSS stress conditions Soiltest numerical simulations Peat layer 4

Layer	Test	Condition	σ'v (kPa)	σ'vy (kPa)	K0 (kPa)	σ'h (kPa)	days
4	CAUC	OC toe GD	15	43	0.65	9.7	1
4	CAUC	NC	90	90	0.32	28.4	1
4	DSS	OC toe GD	15	43	0.65	9.7	1
4	DSS	NC	90	90	0.32	28.4	1
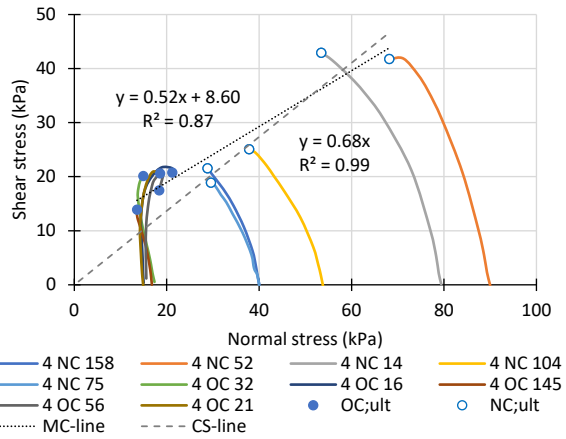
Figure F 26 Peat layer 4: DSS laboratory tests, stress path
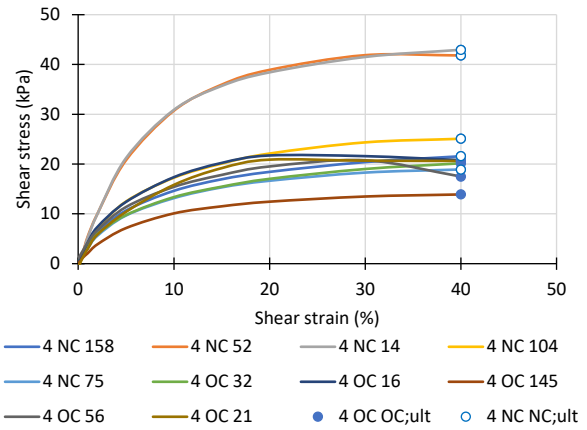
Figure F 27 Peat layer 4: DSS laboratory tests, stress-strain curve
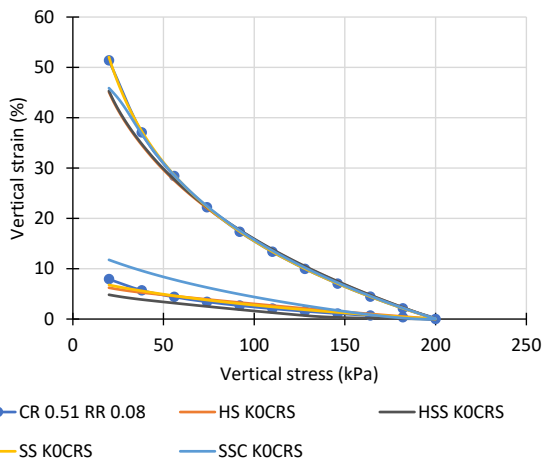
Figure F 28 Peat layer 4: K0CRS simulation, stress-strain curve

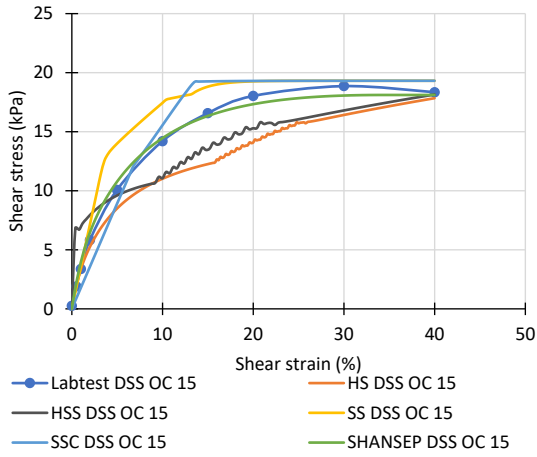*Figure F 29 Peat layer 4: NC DSS simulation (ultimate strength), stress-strain curve*

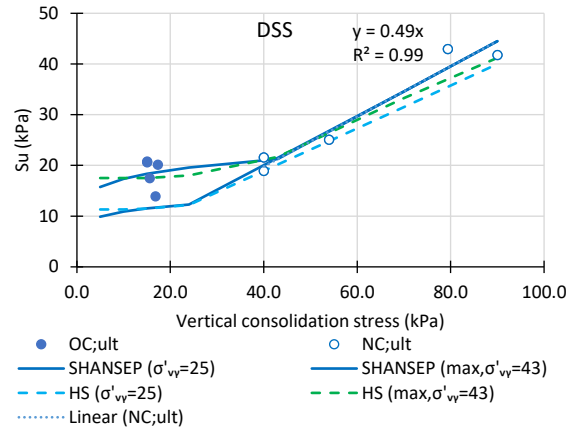Figure F 30 Peat layer 4: OC DSS simulation (ultimate strength), stress-strain curve

Figure F 31 Peat layer 4: DSS simulation (ultimate strength), SHANSEP failure envelope

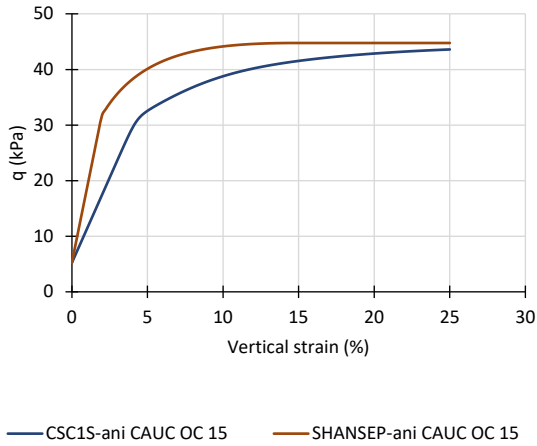## Peat layer 4 anisotropic models and no geometrical correction

Figure F 32 Peat layer 4 (no geometrical correction): OC CAUC simulation anisotropic strength models, stress strain curve (no CAUC laboratory test available for comparison)
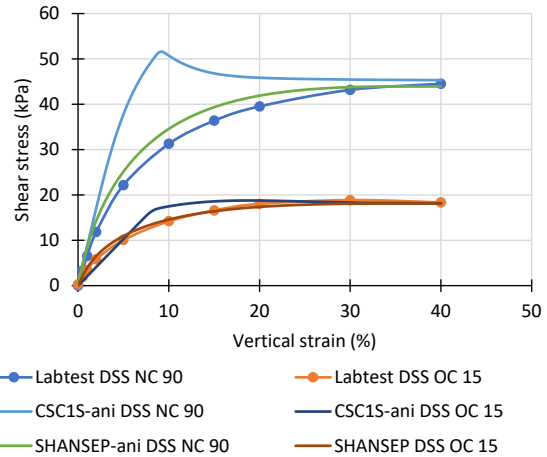

Figure F 33 Peat layer 4: DSS simulation anisotropic strength models, stress strain curve

Sand embankment layer 1a

Table F 8 Embankment Sand layer 1a: CIDC laboratory test conditions and results

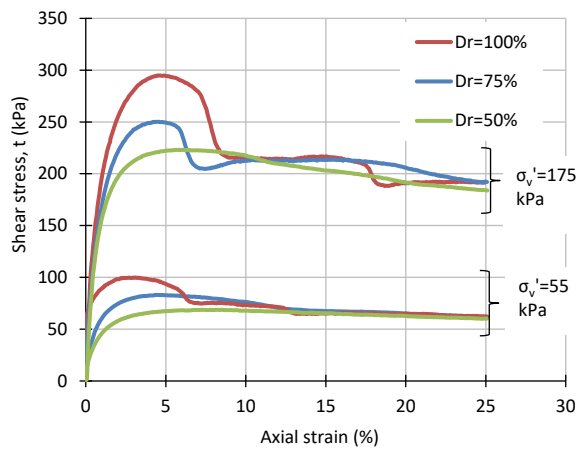|	Dr (%)	σ'vc (kPa)	σ'hc (kPa)	t peak (kPa)	s'peak (kPa)	t ult (kPa)	s'ult (kPa)
Test 1	50	55	55	69	124	60	116
Test 4	50	175	175	223	398	184	358
Test 2	75	55	55	83	138	62	117
Test 5	75	175	175	250	426	192	367
Test 3	100	55	55	100	156	65	118
Test 6	100	175	175	295	472	191	368

Figure F 34 Embankment Sand layer 1a: CIDC stress strain curves for 50%, 75% and 100% relative density at two stress levels
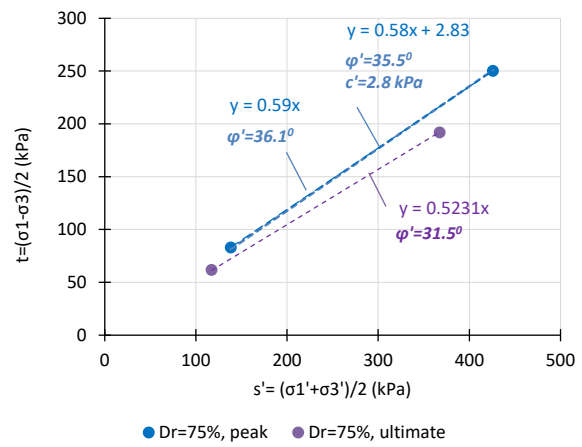

Figure F 35 Embankment Sand layer 1a: CIDC laboratory tests, peak and ultimate strength for 75% relative density
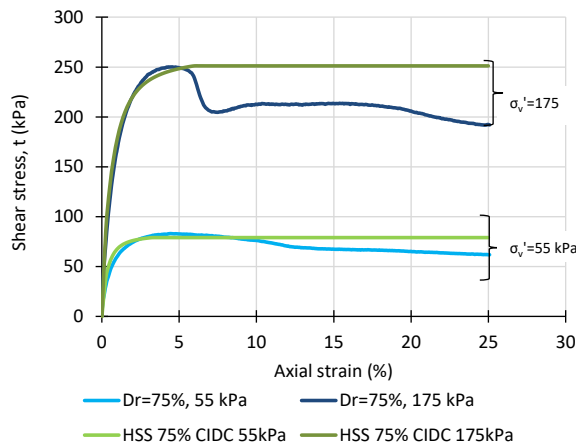

Figure F 36 Embankment Sand layer 1a: CIDC simulation 75% relative density, stress-strain curve
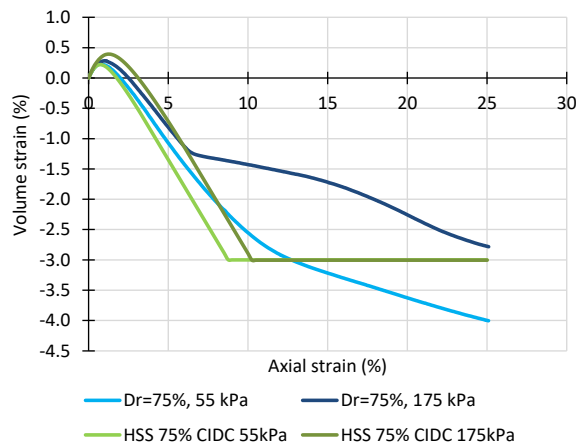

Figure F 37 Embankment Sand layer 1a: CIDC simulation 75% relative density, volume versus axial strain diagram

APPENDIX G VALIDATION OF CPT-BASED CLASSIFICATION AND CORRELATIONS AT EEMDIJK

This appendix presents the results of validation of the new CPT-based classification and correlations as presented in Chapter 2, based on the soil investigations at Eemdijk.

Table G 1 presents two sets of Figures side by side for comparison of the existing Robertson (2010) SBT classification and the proposed changes. The first comparison is based on a CPT at the toe of the ground dike, to verify the identification of a soft clay layer 3a. From this comparison it can be concluded that the new classifications perform better as it identifies the thin, soft clay layer at 1.5 m depth, whereas in the original classification it is classified as peat due to the low cone resistance despite the low friction ratio. The second comparison is based on CPT performed after placing the embankment at the crest of the sheet pile dike. From this comparison it can be concluded that the new classification performs better as it captures the compressed peat layer, whereas in the existing classification it is partly identified as clay due to the high cone resistance, despite the high friction ratio.

Table G 1 Comparison of existing Robertson (2010) SBT classification and proposed adjustments for organic soils
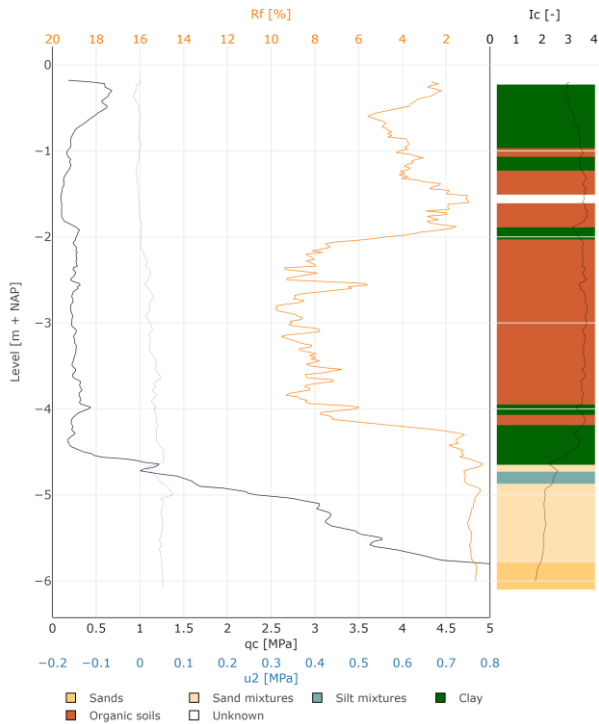
Robertson 2010   Update R2010 for organic soils
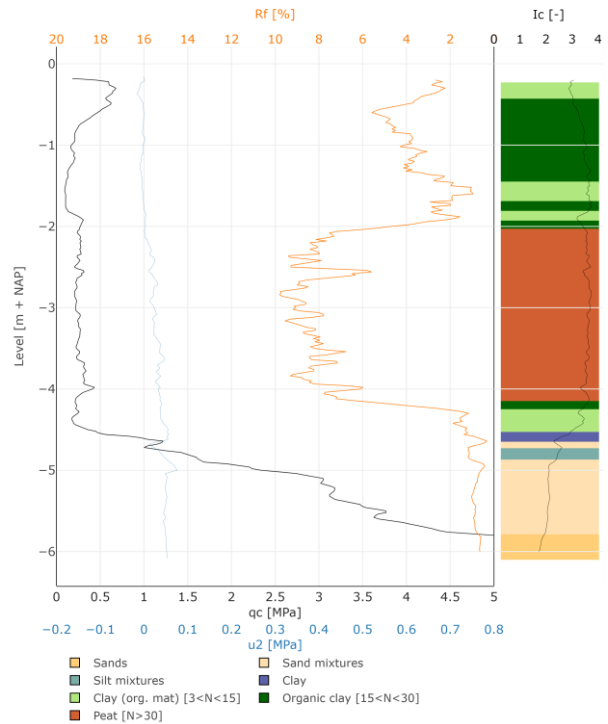

Figure G 1 CPT LKMP33 R2010

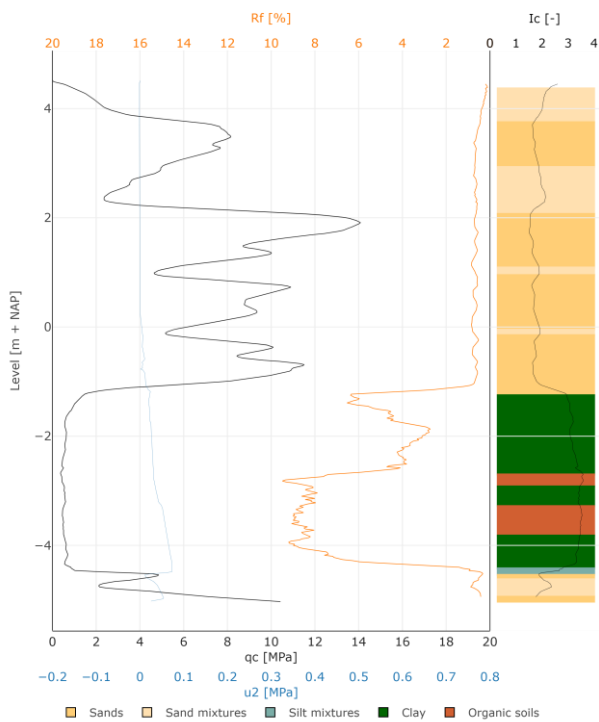*Figure G 2 CPT LKMP33 R2010-ORG-NL*

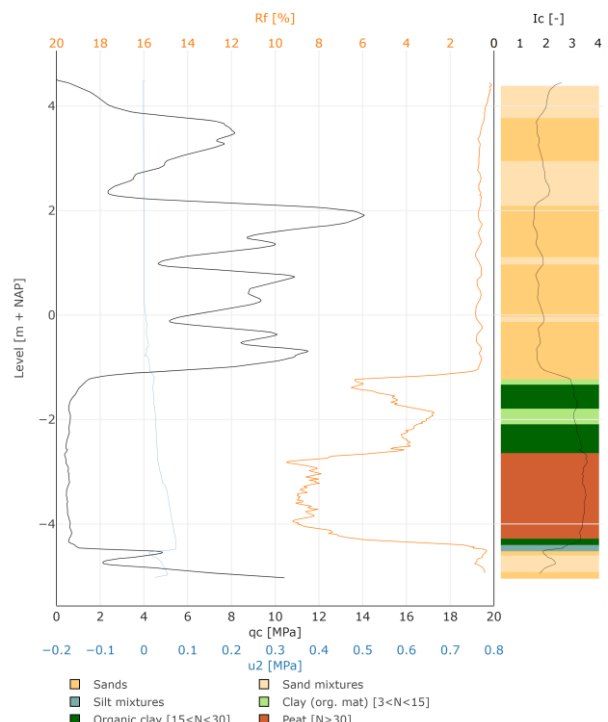*Figure G 3 CPT LKMP38C R2010*

Figure G 4 CPT LKMP38C R2010-ORG-NL

Figure G 5 to Figure G 9 present a selection of graphs based on the pairs of CPT data and laboratory data as presented in Chapter 4. These data are plotted together with the 90% confidence interval of the regional correlations developed for the whole range of organic soils in the Netherlands, as reported in Chapter 3. The following conclusions can be drawn, although it should be noted that the number of observations is limited:

- The compression ratio matches well with the regional correlation
- The correlation for preconsolidation stress shows a lower trend, but is still within the confidence interval. The corresponding cone factor k_p is 0.08, which is 50% lower.
- The correlation for CAUC undrained shear strength shows a lower trend, but is still within the confidence interval. The corresponding cone factor N_{kt} is 20, which is 33% higher.
- The correlation for DSS undrained shear strength shows a slightly lower trend.
- The correlation for DSS undrained shear strength shows a similar trend with minor bias.

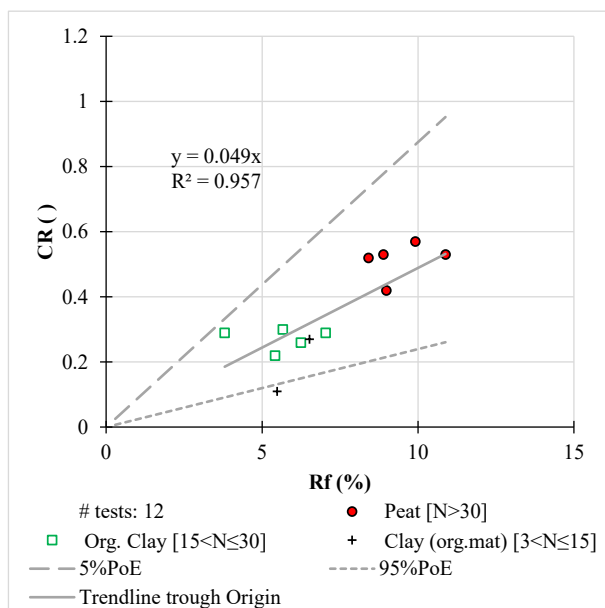Figure G 5 Eemdijk K0CRS results: Compression ratio stress friction ratio
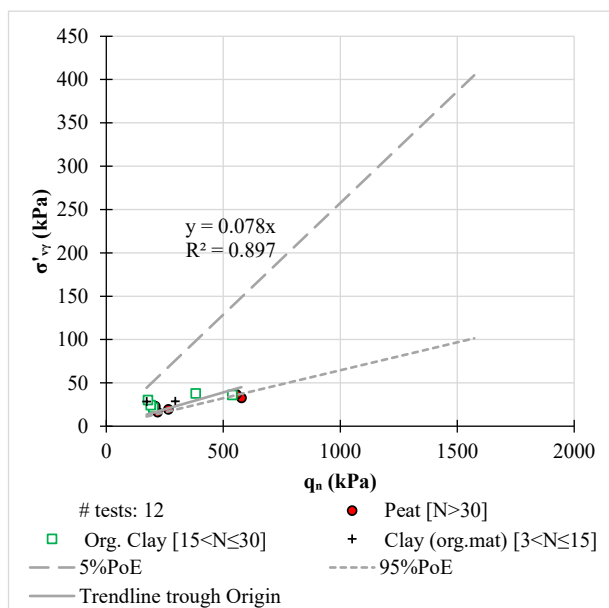
Figure G 6 Eemdijk K0CRS results: Preconsolidation stress versus net cone resistance
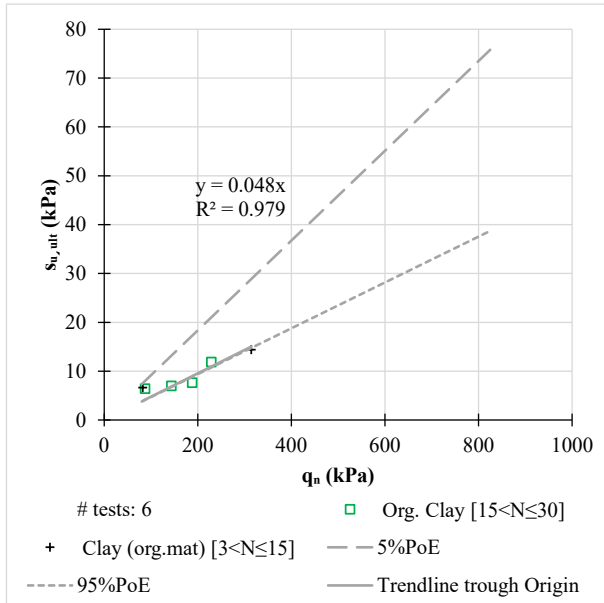
Figure G 7 Eemdijk OC CAUC results: Undrained shear strength versus net cone resistance
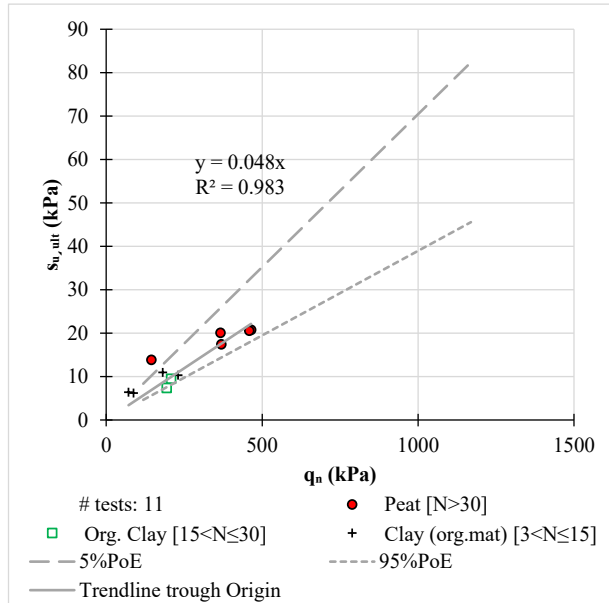

Figure G 8 Eemdijk OC DSS results: Undrained shear strength versus net cone resistance
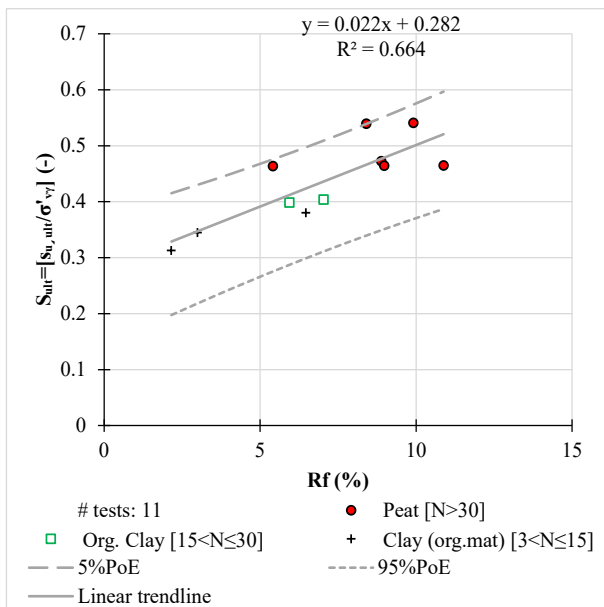
Figure G 9 Eemdijk NC DSS results: S-ratio versus friction ratio

APPENDIX H VALIDATION OF CSR MODEL FOR EEMDIJK ORGANIC CLAY

This appendix presents the performance of the CSR model for Eemdijk organic clay. The effective strength parameters in terms of friction angle and S-ratio are high for a clayey material. The peak values (sin(φ')=0.67, S-ratio=0.52) and ultimate value (sin(φ')=0.60, S-ratio=0.42) are presented in Figure H 1. From this figure it is concluded that the peak value for the S-ratio is relatively high which can be explained by the fact that this is not a critical state value. The ultimate value is in line with the average and higher than the theoretical value following the MCC model. Despite that the Eemdijk organic clay shows high strength parameters, they seem to be consistent and match well with values reported clays by Kulhawy and Mayne (1990) for mineral soils.

The CSR model parameters require the preconsolidation stress and CAUC tests results, assuming that the test conditions correspond to oedometric consolidation. The parameter determination following method B is described in Chapter 2. The results are presented in following tables and figures.
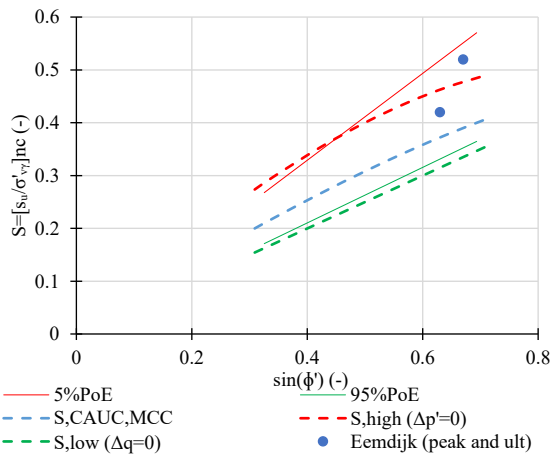
Figure H 1 Undrained shear strength ratio versus sine of friction angle. Comparison of Eemdijk organic clay layer 3 with boundary values for mineral clays.
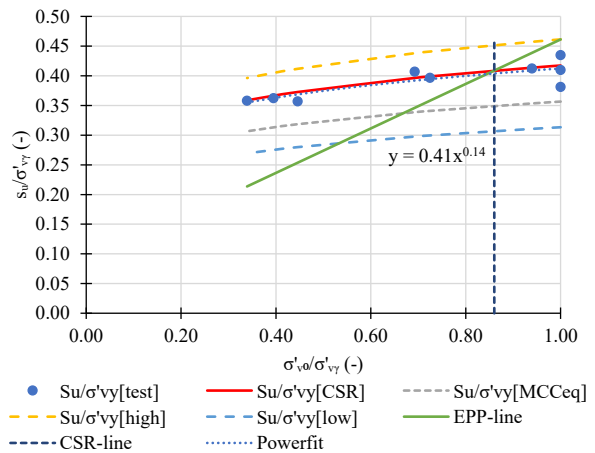
Figure H 2 Eemdijk organic clay layer 3: Undrained shear strength versus vertical consolidation stress, both normalized by the vertical preconsolidation stress

Table H 1 Eemdijk organic clay layer 3: State dependent CAUC test parameters CSR model

| Test	8	49	65	215	252	194	233	152	151
s'_{vy} (kPa)	129	91	50	16	16	19	20	33	35
s'_{v0} (kPa)	129	91	50	15	12	13	9	13	12
OCR (-)	1.00	1.00	1.00	1.06	1.38	1.44	2.24	2.53	2.95
$s_{u,test}$ (kPa)	56	35	21	7	6	8	7	12	13
$s_{u,EPP}$ (kPa)	59	42	23	7	6	7	5	8	8
$s_{u,CSR}$ (kPa)	54	38	21	7	6	7	7	12	13
s_u/σ'_{vy} (-)	0.42	0.42	0.42	0.41	0.40	0.40	0.37	0.37	0.36
s_u/σ'_{v0} (-)	0.42	0.42	0.42	0.44	0.55	0.57	0.84	0.93	1.06

The CSR model results in similar values for the S-ratio and exp-m as the SHANSEP model, although these are determined based on the M-line and not directly. Figure H 2 presents the undrained shear strength versus vertical consolidation stress, both normalized by the vertical preconsolidation stress. The value for CSR is 1.16, which means that at an OCR as low as 1.16 the undrained shear strength is neither contractive (NC0 nor dilative (OC) and yields to the same undrained shear strength as in an elastic perfectly plastic model. With the MCC model this would occur at an OCR equal to 1.50, hence the undrained shear strength of the MCC model is significant lower. To derive similar strength with the MCC the strength increased by about 16 % to Mc=1.84, corresponding to an equivalent friction angle of 45 degrees.

Table H 2 Eemdijk organic clay layer 3: Model constants and calculation steps CSR model

Step	Equation	Output
	CSR model:	
1	$M_c = \frac{6 \sin \phi'}{3 - \sin \phi'}$	1.58
2	$K_{nc} = 1 - \sin \phi'$	0.37
3	$OCR_{K:1} = \left(\frac{1}{K_{nc}}\right)^{\left(\frac{1}{\sin \phi'}\right)}$	4.82
4	$\Delta K_{ur,K:1} = K_{nc} \frac{OCR - OCR^{\sin \phi'}}{OCR - 1}$	0.21
5b	$K_0 = OCR_{K:1}\left(K_{nc} - \Delta K_{ur,K:1}\right) + \Delta K_{ur,K:1}$	var
6b	$s_{u,EPP} = \left(\frac{M_c}{2}\right) p'_0$	var
7b	CSR (fit based on graph)	1.16
8b	$m \cong 1 - \frac{RR}{CR}$ (fit based on graph)	0.86
9b	$K_x = CSR\left(K_{nc} - \Delta K_{ur,K:1}\right) + \Delta K_{ur,K:1}$	0.40
10	$s_{u,CAUC,CSR} = \sigma'_{v0} \left(\frac{1+2K_x}{3}\right)\left(\frac{M_c}{2}\right)\left(\frac{OCR}{CSR}\right)^m$	var
11	$S_{CAUC,CSR} = \left(\frac{1+2K_x}{3}\right)\left(\frac{M_c}{2}\right)\left(\frac{1}{CSR}\right)^m$	0.42
	MCC model:	
12	$\nu_{K:1} = \frac{\Delta K_{ur,K:1}}{1 + \Delta K_{ur,K:1}}$	0.17
13	$c_{K:1} = \frac{\log(OCR_{K:1})}{\log\left(\frac{OCR_{K:1}(1+2K_{nc})}{3}\right)}$	1.52
14	$\Lambda = 1 - c_{K:1}(1 - m)$	0.79
15	$\lambda = \frac{(1+e_0)CR}{\ln(10)}$	0.435
16	$\kappa_{oed} = \kappa \cdot c_{K:1} = \frac{c_{K:1}(1+e_0)RR}{\ln(10)}$	0.093
17b	$M_{c,MCC,eq} \approx M_c \frac{s_{u,test}}{s_{u,CAUC,CSR}}$ and CSR based on method A	1.84

APPENDIX I   EEMDIJK GD AND SPD CONSTRUCTION MONITORING RESULTS

Table I-1 Overview of construction phasing in time, layer thickness (ΔH), settlements (ΔUv) and embankment level.

| phase	project day	duration (days)	ΔH (m)	ΔUv (m)	Level (m NAP)
fill 1	0	1	1.2		-0.2
consolidation 1	1	15		0.1	0.9
fill 2	16	1	1		
consolidation 2	17	18		0.1	1.8
fill 3	35	1	0.6		
consolidation 3	36	34		0.1	2.3
fill 4	70	1	0.6		
consolidation 4	71	30		0.1	2.8
fill 5	101	1	0.6		
consolidation 5	102	17		0.1	3.3
fill 6	119	1	0.6		
consolidation 6	120	15		0.1	3.8
fill 7	135	1	0.6		
consolidation 7	136	20		0.1	4.3
fill 8	156	1	0.6		
consolidation 8	157	57		0.1	4.8
fill 9	214	1			
consolidation 9	215	11		0.1	4.7
start GD-test	226	7			
consolidation 10	233	23			
SP installation	256	1			6.0
consolidation 11	257	9			
fill 12	266	1	0.9		
consolidation 12	267	6		0.1	5.5
start SPD-test	273	6			
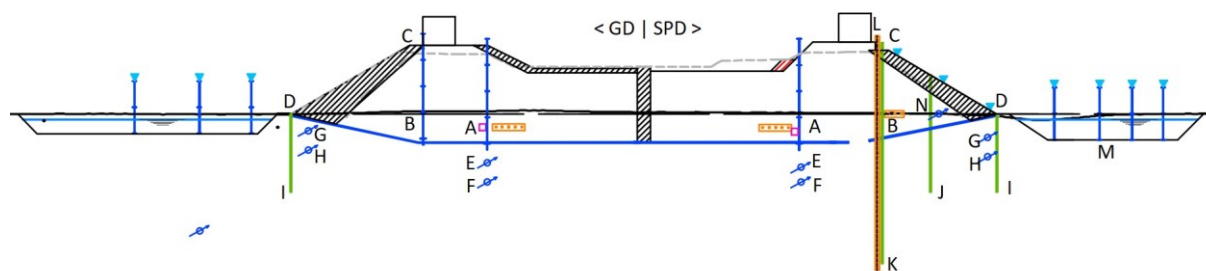
Figure I 1 Locations of monitoring at GD and SPD

196

Table I-2 Coordinates of measurement points in back-analysis model

Dike	GD			SPD		
Phase	Initial	Initial	Failure test	Initial	Initial	Failure test
Coordinate	x (m from center)	y (m NAP)	y' (m NAP)	x (m from center)	y (m NAP)	y' (m NAP)
A	12.0	0.0	-0.5	12.0	0.0	-0.8
B	20.0	0.0	-0.7	20.0	0.0	-0.8
C	18.0	6.0	5.3	18.9	5.6	4.7
D	27.0	0.0	-0.2	27.3	0.0	-0.2
E	12.0	-1.5	-1.9	12.0	-1.5	-2.1
F	12.0	-3.0	-3.2	12.0	-3.0	-3.3
G	26.8	-1.5	-1.7	26.8	-1.5	-1.7
H	26.8	-3.0	-3.1	26.8	-3.0	-3.1
I	27.0	-6.0	-6.0	27.0	-7.0	-7.0
J				22.5	-8.0	-8.0
K				18.1	-12.0	-12.0
L				18.1	6.0	6.0
M				33.3	-2.0	-2.0
N				20.0	0.7	-0.1
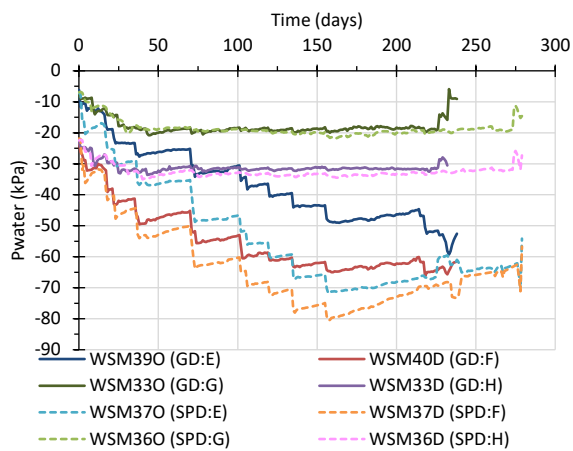
Figure I 2 Measured pore pressures during construction, below crest and toe of GD and SPD at -1.5 m and -3.0 m NAP
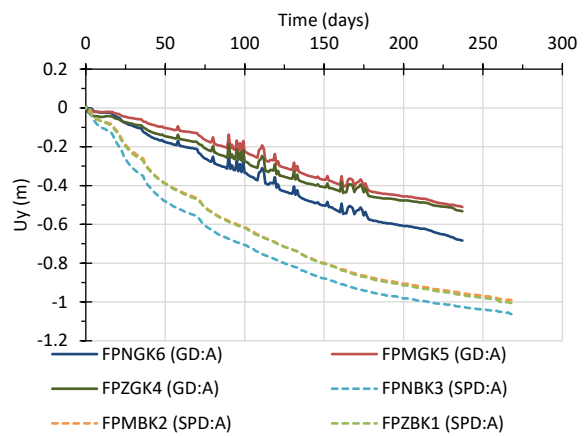
Figure I 3 Measured vertical displacement below crest of GD and SPD during construction

APPENDIX J EEMDIJK GD FULL-SCALE FAILURE TEST MONITORING RESULTS

GD-test time-lapse during failure (7-hour duration)

a) 2018-01-30; 09:00:00
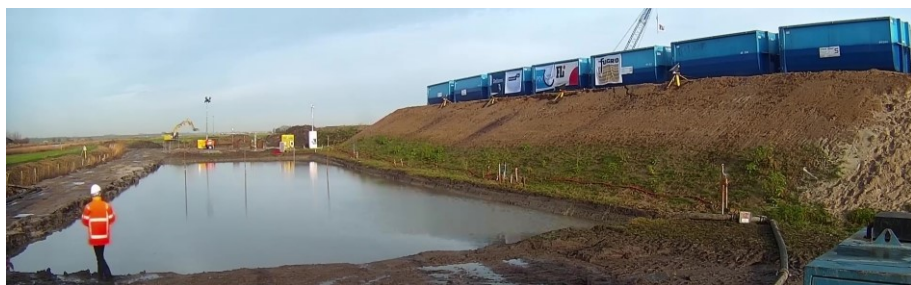
b) 10:00:00

c) 10:20:00

d) 10:50:00

e) 11:30:00

f) 12:20:00

g) 13:40:00
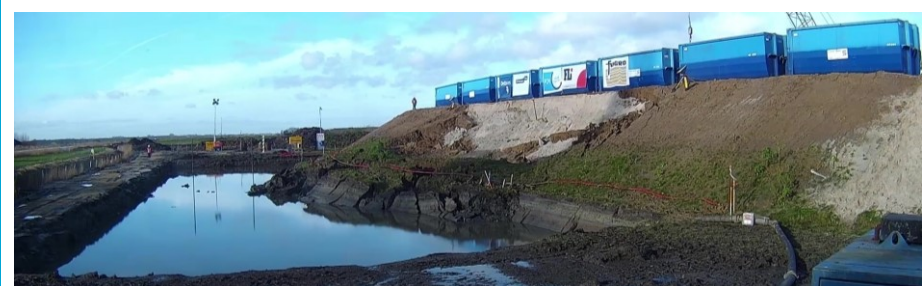
h) 16:00:00

Figure J 1 Time-lapse (photo a to h) during failure of GD

GD: total prism displacements during failure test

a)

b)

c)

d)
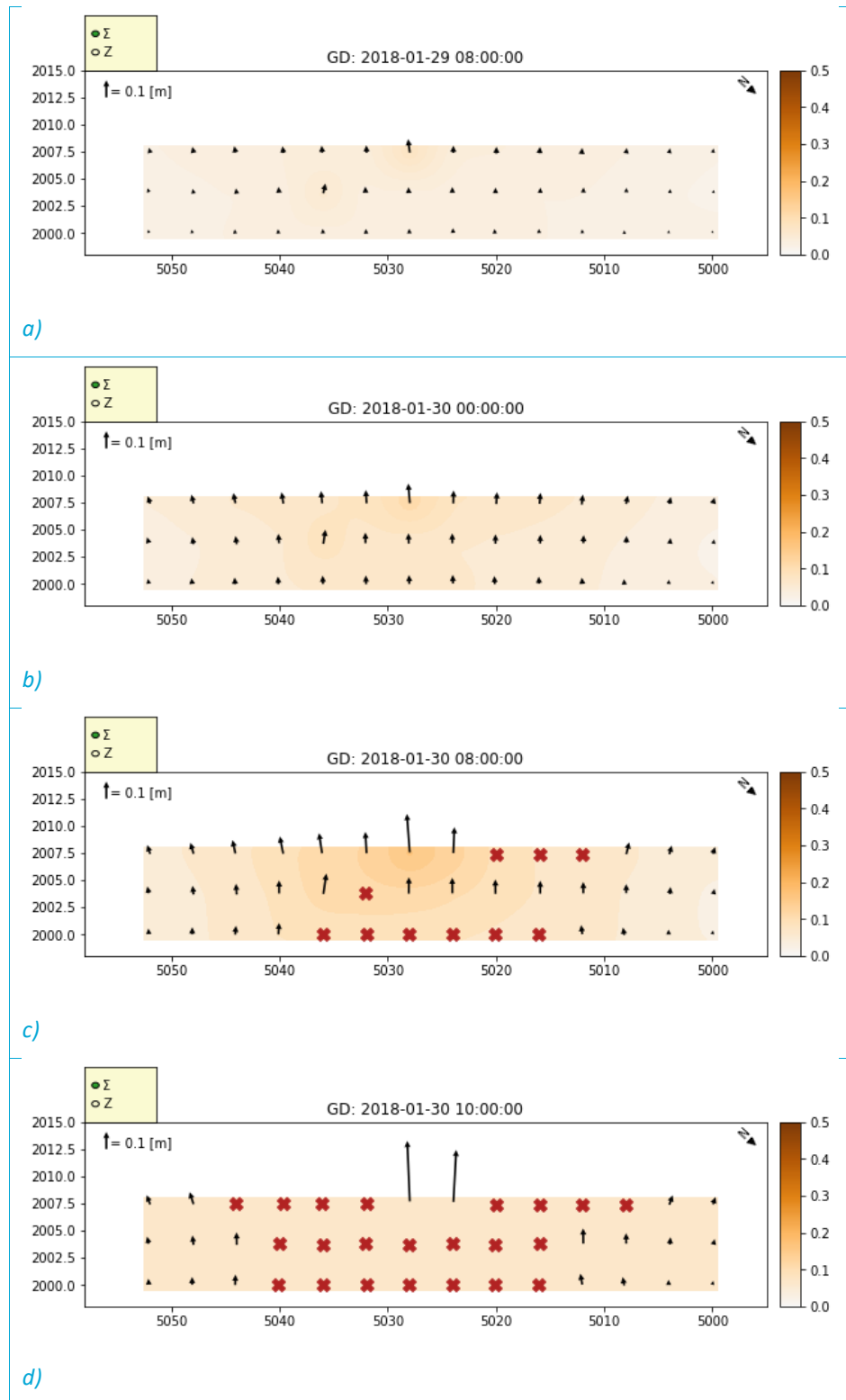
Figure J 2 Total GD prism displacement at four moments (a to d). Top of graph is the toe, bottom is the crest.
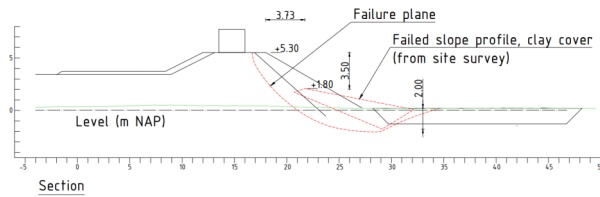
Figure J 3 Reconstructed failure mode of GD based on monitoring and post failure survey
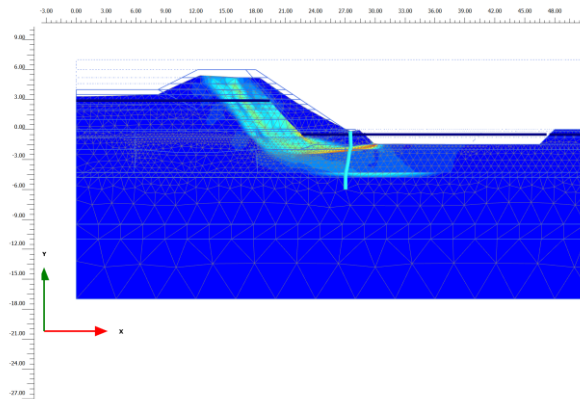
Figure J 4 Ground dike, phase shear strains prior to failure. The failure surface of the back analysis is located in soft clay layer 3a at 2 m depth. In addition, shear strain occurs just below the peat layer due to very low stresses associated with uplift conditions.
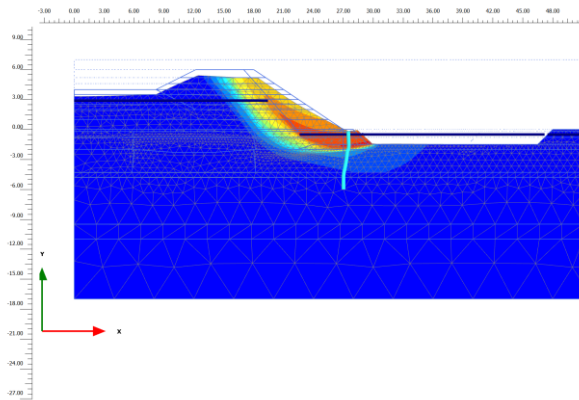
Figure J 5 Ground dike, phase displacements prior to failure. The failure surface of the back analysis is located in soft clay layer 3a at 2 m depth and extends in the fill just behind the clay cover.
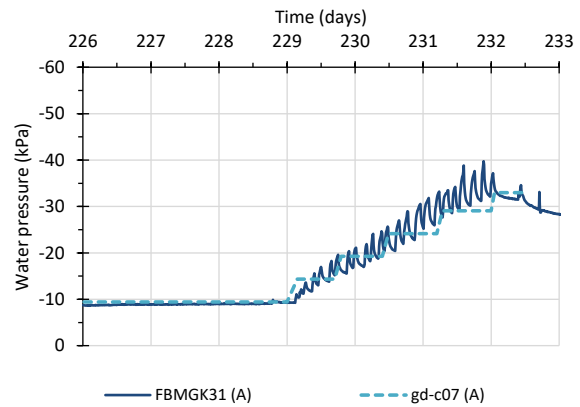
Figure J 6 Ground dike, measurements (FB..) and back analysis (gdc07) of pore pressure, at original surface level in the embankment fill, below the crest (location A). The modelled pore pressures following the back analysis match well with the measurements during the field test. The maximum water level during the test is 2.9 m NAP.

203
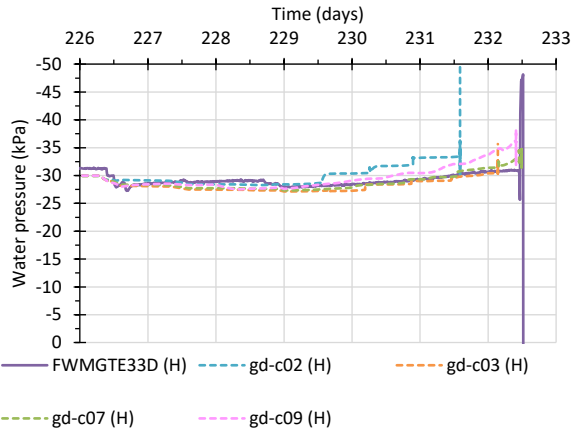
Figure J 7 Ground dike, measurements (FW..) and back analysis (gd..) of pore pressure, at 3.0 m depth in the peat at the toe (location H). The pore pressures following the back analysis models match well with the measurements during the field test. Model gd-c02 deviates due to early failure following the relative lower strength.
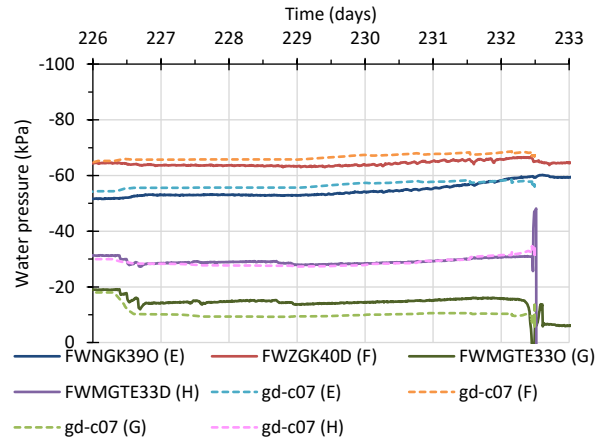
Figure J 8 Ground dike, measurements (FW..) and back analysis (gd-c07) of pore pressure, at 1.5 m depth in the clay and 3.0 m depth in the peat, at the toe and crest. The pore pressures following the back analysis match well with the measurements during the field test, although the response of the shallow piezometer near the ditch (G) is less prone in the field than in the models. This figure only shows back analysis model gd-c07.
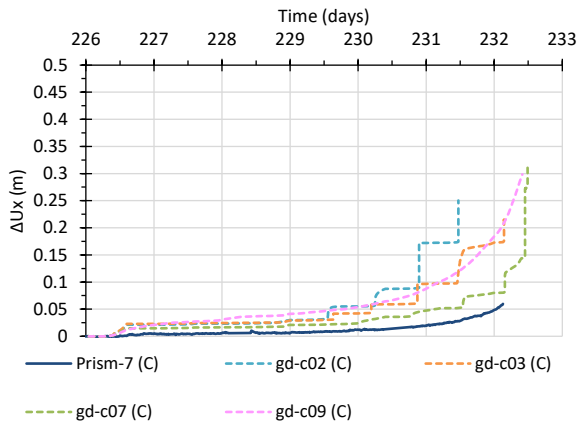
Figure J 9 Ground dike, measurements (Prism..) and back analysis (gd..) of horizontal displacements, at the crest (location C). The horizontal displacements following the back analysis models are all larger than the measurements during the field test. Model gd-c02 deviates the most due to early failure following the relative lower strength. Model gd-c07 performs best with no early failure and slightly larger displacements.
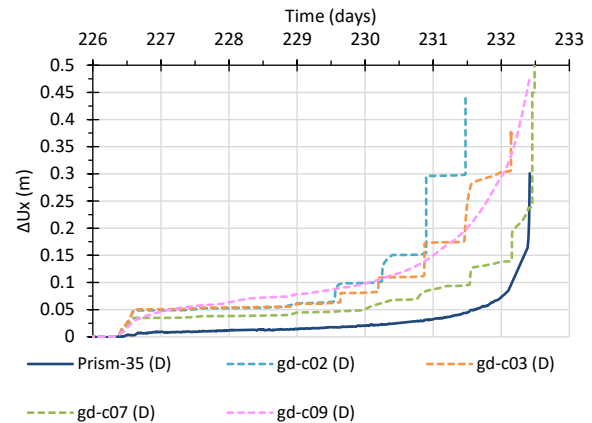
Figure J 10 Ground dike, measurements (Prism..) and back analysis (gd..) of horizontal displacements, at the toe (location D). The horizontal displacements following the back analysis models are all larger than the measurements during the field test. Model gd-c02 deviates the most due to early failure following the relative lower strength. Model gd-c07 performs best with no early failure and slightly larger displacements.
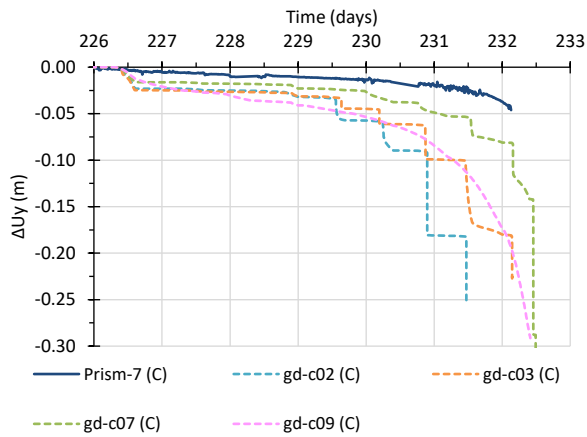
Figure J 11 Ground dike, measurements (Prism..) and back analysis (gd..) of vertical displacements, at the crest (location C). The vertical displacements (settlement) following the back analysis models are all larger than the measurements during the field test. Model gd-c02 deviates the most due to early failure following the relative lower strength. Model gd-c07 performs best with no early failure and slightly larger displacements.
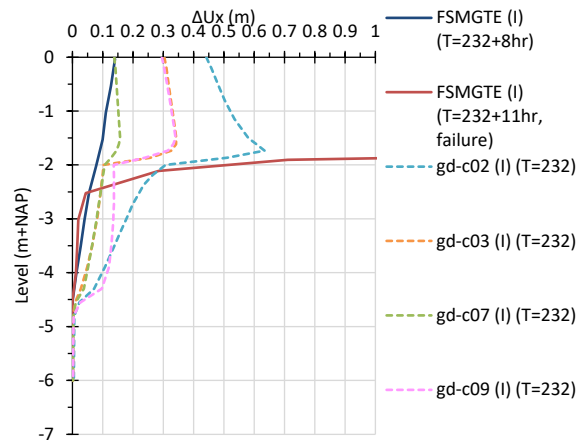
Figure J 12 Ground dike, inclinometer measurements (FS..) and back analysis (gd..) of horizontal displacements over depth, at the toe (SAAF location I). Last loading stage prior to failure with water level +2.5 m NAP. The location of the main sliding plane at -2 m NAP is well captured by the back analysis models. Model gd-c02 deviates the most due to early failure following the relative lower strength. Model gd-c07 performs best with no early failure and slightly larger displacements.

APPENDIX K   EEMDIJK   SPD   FULL-SCALE   FAILURE   TEST MONITORING RESULTS

SPD-test time-lapse during failure (7 minutes duration)

a) 2018-3-17; 15:56:09

b) 15:58:11

c) 15:58:45

d) 15:59:09

e) 15:59:30

f) 16:00:00

g) 16:00:30

h) 16:02:30

Figure K 1 Time-lapse (photo a to h) during failure of sheet pile and collapse of SPD

SPD total prism displacements during failure test
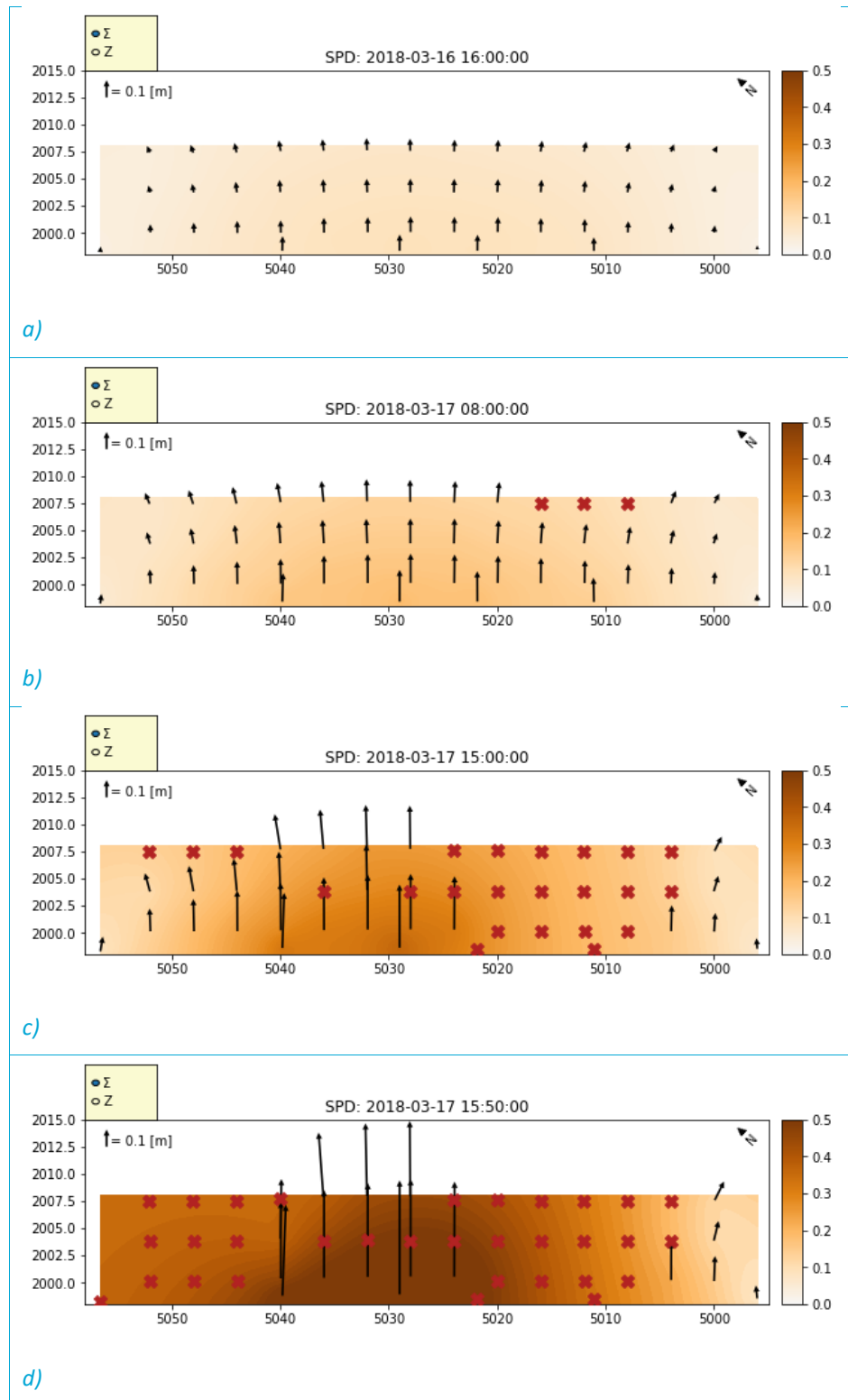
Figure K 2 Total SPD prism displacement at four moments (a to d). Top of graph is the toe, bottom is the crest.

SPD inclinometer results during failure test

e)

f)

g)

h)
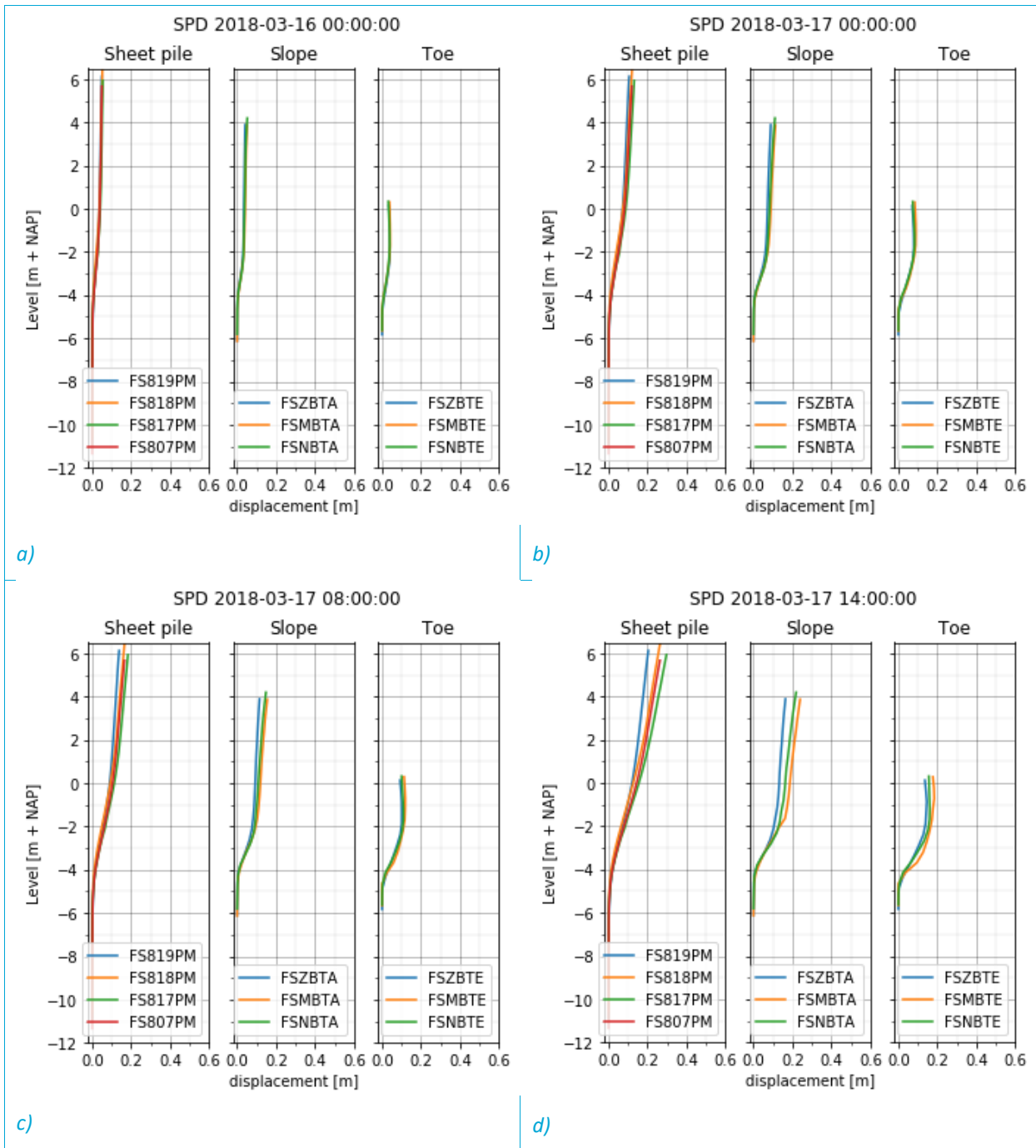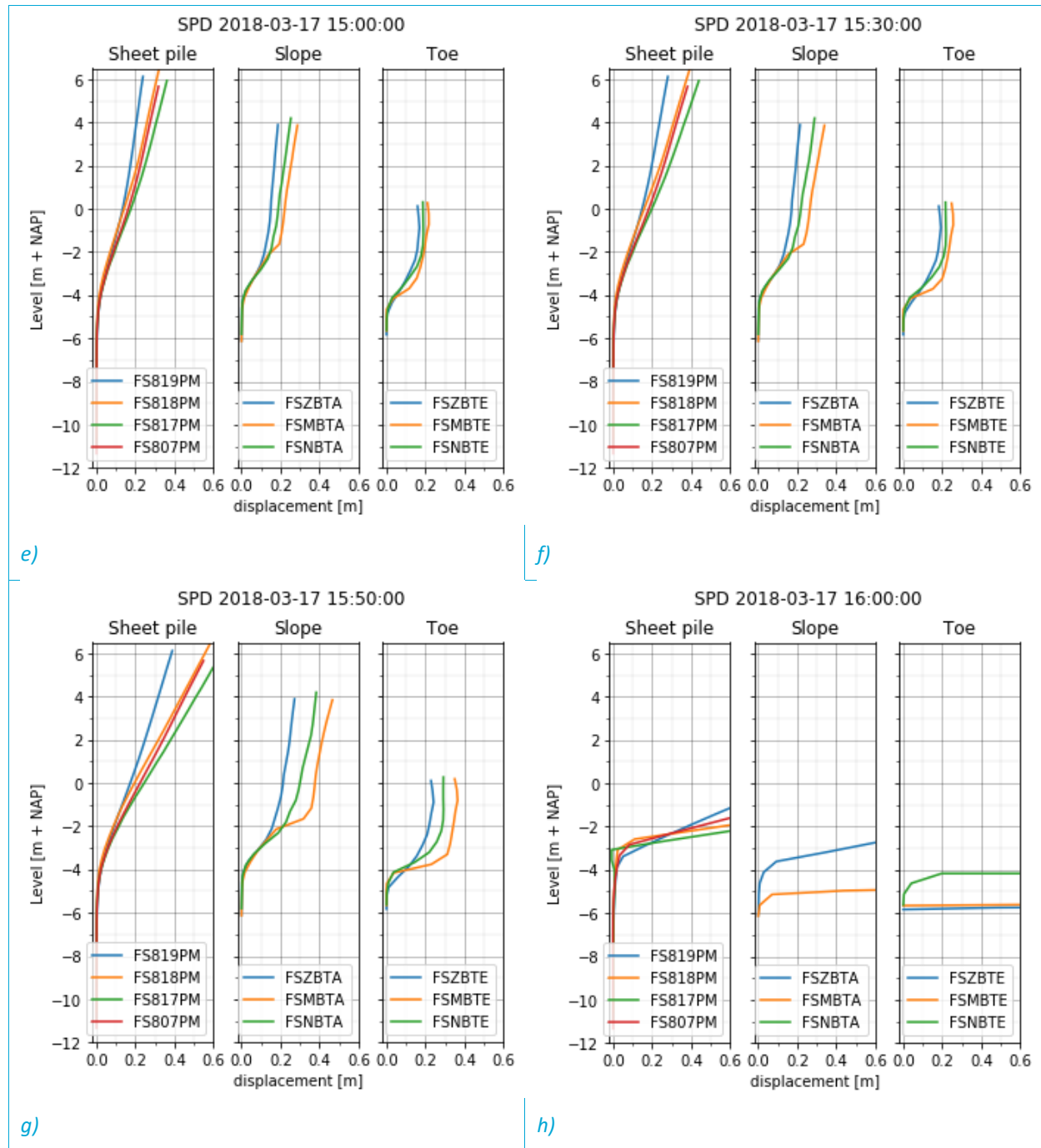
Figure K 3Horizontal displacements SPD at eight moments (a to h). Left graph SAAF at sheet pile, middle SAAF at slope, right SAAF at toe
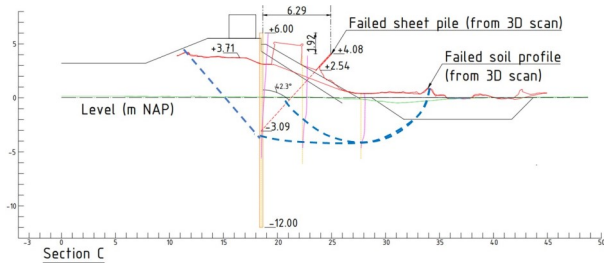
Figure K 4 Reconstructed failure mode of SPD based on monitoring and post failure survey and 3D-scans
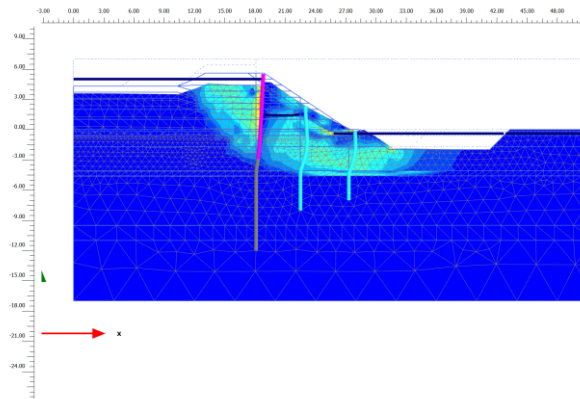
Figure K 5 Sheet pile dike, phase shear strains prior to failure. The failure plane of the back analysis is located at the base of peat layer 4 at 4 m depth associated with uplift conditions. In addition, shear strains occur behind the sheet pile in the active wedge starting from the plastic hinge at -3.5 m NAP.
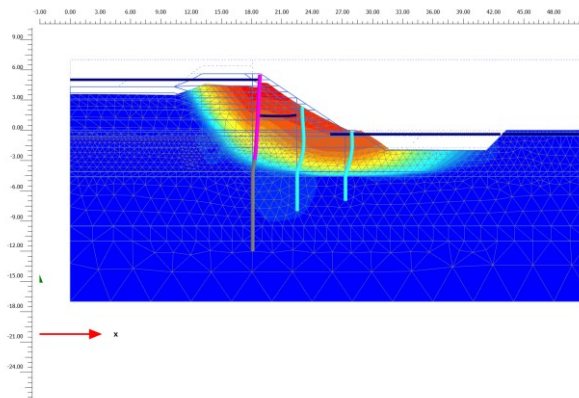
Figure K 6 Sheet pile dike, phase displacements prior to failure. Near the toe, the failure plane of the back analysis is located at the base of peat layer 4 at 4 m depth. Below the slope in front of the sheet pile, the failure plane changes to a failure zone over the height of the peat layer 4. Behind the sheet pile an active wedge occurs.
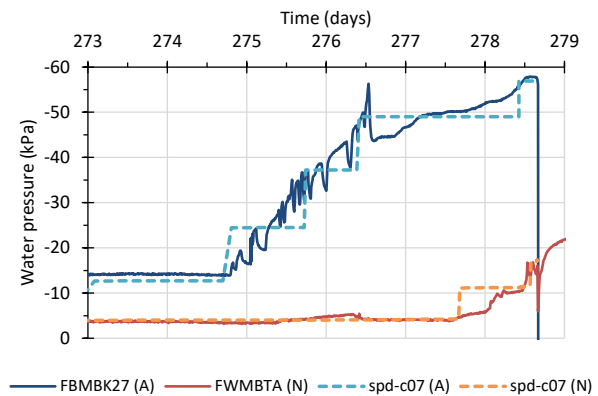
Figure K 7 Sheet pile dike, measurements (FB..) and back analysis (spd-c07) of pore pressure, at original surface level in the embankment fill, below the crest and on the slope side of the sheet pile. The modelled pore pressures following the back analysis match well with the measurements during the field test. The pore pressures at location in the center (A) and below the slope (B) are different due to the impermeable sheet pile. The maximum water level during the test is 5.0 m NAP at (A) and 1.5 m NAP at (N).

213
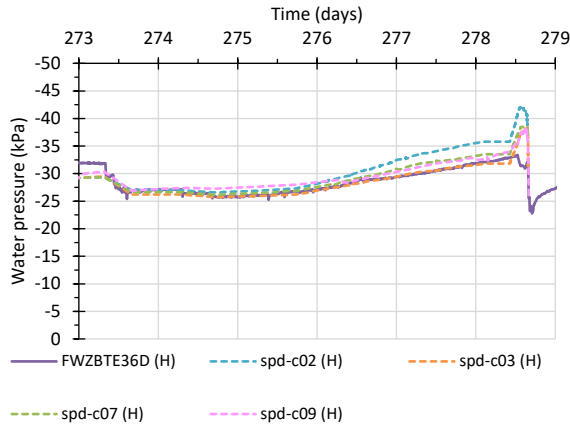
Figure K 8 Ground dike, measurements (FW..) and back analysis (spd..) of pore pressure, at 3.0 m depth in the peat at the toe (location H). Model spd-c02 deviates slightly due to near failure following the relative lower strength.
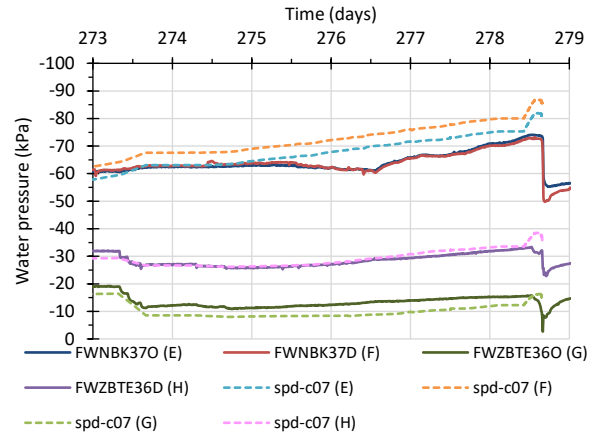
Figure K 9 Sheet pile dike, measurements (FW..) and back analysis (spd-c07) of pore pressure, at 1.5 m depth in the clay and 3.0 m depth in the peat, at the toe and crest. The pore pressures following the back analysis match well with the measurements during the field test, although the response of the shallow piezometer near the ditch (G) is less prone in the field than in the models. This figure only shows back analysis model spd-c07.
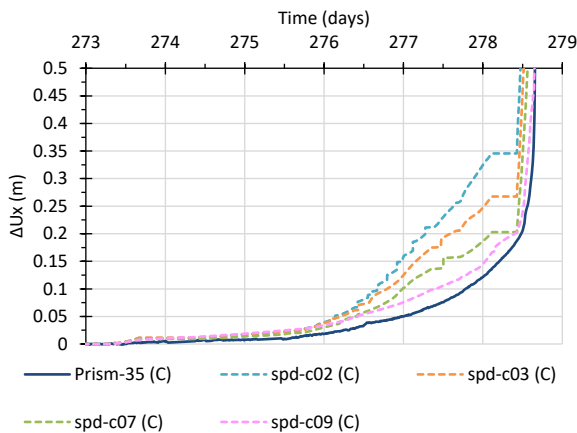
Figure K 10 Sheet pile dike, measurements (Prism..) and back analysis (spd..) of horizontal displacements, at the crest (location C). The horizontal displacements following the back analysis models are all larger than the measurements during the field test. The performance of model spd-c07 and spd-c09 is the best. The performance of the models is better than for the ground dike without sheet pile.
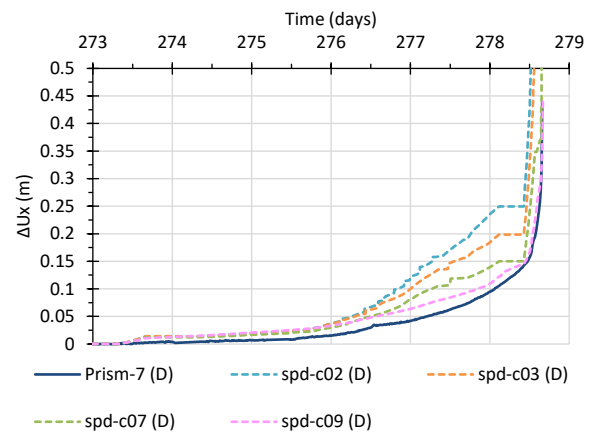
Figure K 11 Sheet pile dike, measurements (Prism..) and back analysis (spd..) of horizontal displacements, at the toe (location D). The horizontal displacements following the back analysis models are all larger than the measurements during the field test. The performance of model spd-c07 and spd-c09 is the best. The performance of the models is better than for the ground dike without sheet pile.
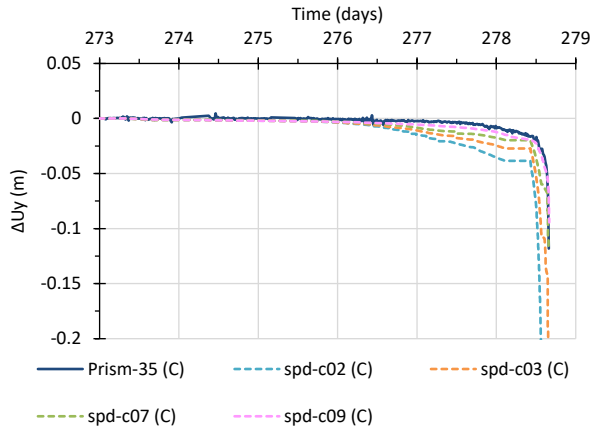
Figure K 12 Sheet pile dike, measurements (Prism..) and back analysis (spd..) of vertical displacements, at the crest (location C). The vertical displacements (settlement) following the back analysis models are all slightly larger than the measurements during the field test. The performance of the models is better than for the ground dike without sheet pile.
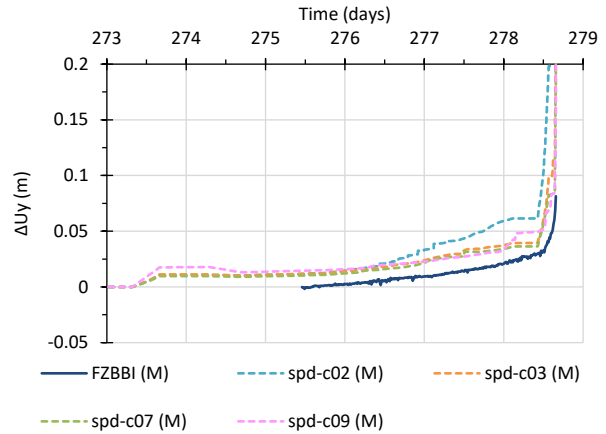
Figure K 13 Sheet pile dike, measurements (Prism..) and back analysis (spd..) of vertical displacements, at 2 m depth in the ditch (location M). The vertical displacements (heave) following the back analysis models are all slightly larger than the measurements during the field test.
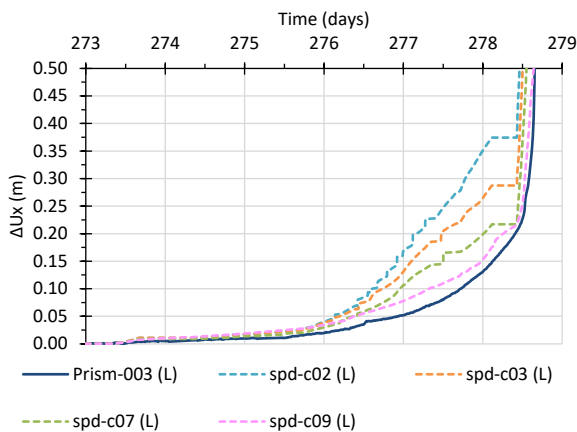
Figure K 14 Sheet pile dike, measurements (Prism..) and back analysis (spd..) of horizontal displacements, at the top of the sheet pile (location L). The horizontal displacements following the back analysis models are all larger than the measurements during the field test. The performance of model spd-c07 and spd-c09 is the best. The performance of the models is better than for the ground dike without sheet pile.
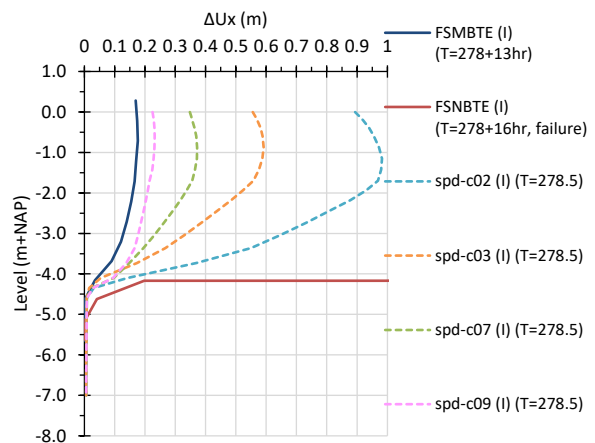
Figure K 15 Sheet pile dike, inclinometer measurements (FS..) and back analysis (spd..) of horizontal displacements over depth, at the toe (SAAF location I). Last loading stage prior to failure with water level +5.0 m NAP. The location of the main sliding plane at -4 m NAP is well captured by the back analysis models. Model spd-c02 deviates the most due to near failure following the relative lower strength. Model spd-c07 and spd-c09 performs best with no early failure and slightly larger displacements.

215
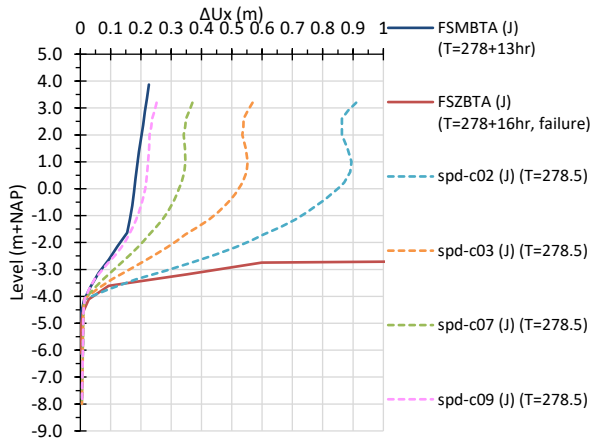
Figure K 16 Sheet pile dike, inclinometer measurements (FS..) and back analysis (spd..) of horizontal displacements over depth, at the slope (SAAF location J). Last loading stage prior to failure with water level +5.0 m NAP. The location of the main sliding plane just above -4 m NAP is well captured by the back analysis models. Model spd-c02 deviates the most due to near failure following the relative lower strength. Model spd-c07 and spd-c09 performs best with no early failure and slightly larger displacements.
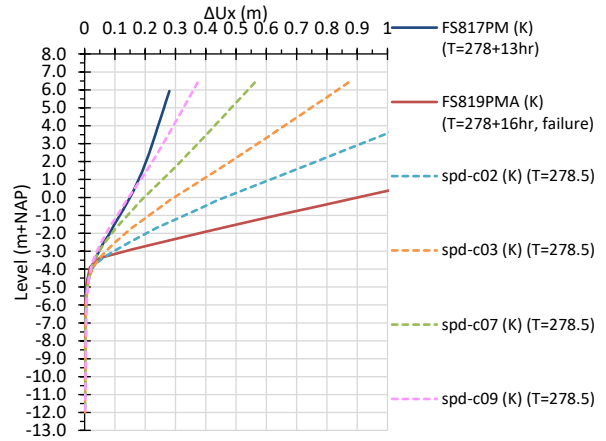
Figure K 17 Sheet pile dike, inclinometer measurements (FS..) and back analysis (spd..) of horizontal displacements over depth, at the sheet pile (SAAF location K). Last loading stage prior to failure with water level +5.0 m NAP. The location of the plastic hinge in the sheet pile at about -3.5 m NAP is well captured by the back analysis models. Model spd-c02 deviates the most due to near failure following the relative lower strength. Model spd-c07 and spd-c09 performs best with no early failure and slightly larger displacements.
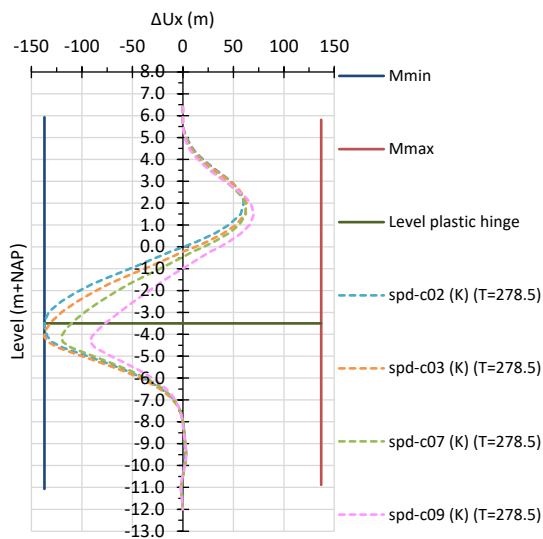
Figure K 18 Sheet pile dike, back analysis (spd..) of Bending moments over depth at the sheet pile (location K). Last loading stage prior to failure with water level +5.0 m NAP. Maximum and minimum bending moment are indicated and the approximate level where the plastic hinge occurred based on the post failure survey. The location of the plastic hinge in the sheet pile at about -3.5 m NAP is well captured by the back analysis models. Model spd-c02 and spd-c03 show full plasticity already in the stage prior to the final loading stage.

APPENDIX L PARAMETERS CONSTITUTIVE MODELS BACK-ANALYSIS

Identification all FEA		1a;cs;emb.sand:Gs:20 Dr:70 Phi:36.1 Phi,cs:31.5 HS	1a;mc;emb.sand:Gs:20 Dr:70 Phi:35.5 Phi,cs:31.5 HS	5;cs;boxtel.sand:Gs:20.5 Dr:80 Phi40 Phi,cs:32.5 HS	5a;mc;top.boxtel.sand:Gs:19.5 Dr40 Phi:30 Phi,cs:30 HS	7;cs;eem.sand:Gs:19.5 Dr:40 Phi:35 Phi,cs:30 HS
Material model		Hardening soil	Hardening soil	Hardening soil	Hardening soil	Hardening soil
Drainage type		Drained	Drained	Drained	Drained	Drained
Colour		RGB 171, 159, 140	RGB 243, 194, 89	RGB 231, 249, 67	RGB 144, 153, 77	RGB 229, 211, 133
γ_unsat	kN/m³	18.00	18.00	18.50	17.50	17.50
γ_sat	kN/m³	20.00	20.00	20.50	19.50	19.50
Dilatancy cut-off		Yes	Yes	Yes	Yes	Yes
e_init		0.59	0.59	0.51	0.67	0.67
e_min		0.54	0.54	0.47	0.65	0.65
e_max		0.64	0.64	0.56	0.69	0.69
E_50^{ref}	kN/m²	4.20E+04	4.20E+04	4.80E+04	2.40E+04	2.40E+04
E_oed^{ref}	kN/m²	3.71E+04	3.71E+04	4.18E+04	2.16E+04	2.12E+04
E_ur^{ref}	kN/m²	1.26E+05	1.26E+05	1.44E+05	7.20E+04	7.20E+04
power (m)		0.48	0.48	0.45	0.58	0.58
c_ref	kN/m²	0.10	2.80	0.10	5.00	0.10
φ (phi)	°	36.10	35.50	40.00	30.00	35.00
ψ (psi)	°	10.37	9.35	18.00	0.00	7.00
v_ur		0.24	0.24	0.23	0.25	0.25
p_ref	kN/m²	100	100	100	100	100
K_0^{nc}		0.48	0.48	0.46	0.50	0.50
R_f		0.95	0.95	0.95	0.95	0.95
Tension cut-off		Yes	Yes	Yes	Yes	Yes
K_0,x		0.48	0.48	1.00E+10	1.00E+10	1.00E+10
K_0,z		0.48	0.48	1.00E+10	1.00E+10	1.00E+10
OCR		1	1	1	1	1
POP	kN/m²	0	0	30	30	30
k_x	m/day	20	20	20	20	20
k_y	m/day	10	10	10	10	10
c_k		1.00E+15	1.00E+15	1.00E+15	1.00E+15	1.00E+15

Identification all FEA		1a;cs;emb.loose.sand: Gs:20 E:5000 MC	1b;mc;clay.cover Gs:17 E:5000 MC	2a;mc;top.clay Gs:15 E:500 MC
Material model		Mohr-Coulomb	Mohr-Coulomb	Mohr-Coulomb
Drainage type		Drained	Drained	Drained
γ_unsat	kN/m³	18.00	17.00	14.40
γ_sat	kN/m³	20.00	17.00	15.00
Dilatancy cut-off		No	No	No
e_init		0.59	1.00	2.00
e_min		0.54	0.00	0.00
e_max		0.64	999.00	999.00
E	kN/m²	5000	5000	500
ν (nu)		0.33	0.33	0.33
G	kN/m²	1875	1875	187.5
E_oed	kN/m²	7491	7499	749.9
c_ref	kN/m²	0.10	5.00	5.00
ϕ (phi)	°	31.50	30.00	30.00
ψ (psi)	°	0	0	0
Tension cut-off		Yes	Yes	No
K_0,x		0.48	0.50	0.50
K_0,z		0.48	0.50	0.50
k_x	m/day	20	0.1	0.1
k_y	m/day	10	0.1	0.1
c_k		1.00E+15	1.00E+15	1.00E+15

Identification all FEA		2;mc;top.clay: Gs:15 Phi:38.5 CR:0.27 Knc:0.38 S:0.42 SSC	3;mc;clay: Gs:13.1 Phi:38.5 CR:0.27 Knc:0.38 S:0.42 SSC	4;mc;peat: Gs:10.3 Phi:45 CR:0.51 Knc:0.32 S:0.49 SSC	6;cs;clay: Gs:17 Phi:33 CR:0.1 Knc:0.46 S:0.32 SSC
Material model		Soft soil creep	Soft soil creep	Soft soil creep	Soft soil creep
Drainage type		Undrained (A)	Undrained (A)	Undrained (A)	Undrained (A)
γ_unsat	kN/m³	14.40	12.69	10.17	16.20
γ_sat	kN/m³	15.00	13.10	10.30	17.00
Dilatancy cut-off		No	No	No	No
e_init		1.99	2.68	10.20	1.19
e_min		0.00	0.00	0.00	0.00
e_max		999.00	999.00	999.00	999.00
λ^* (lambda*)		1.18E-01	1.18E-01	2.23E-01	4.34E-02
κ^* (kappa*)		5.10E-02	5.10E-02	1.07E-01	2.02E-02
μ^*		3.96E-03	3.96E-03	1.18E-02	7.20E-04
c_ref	kN/m²	4.00	4.00	5.00	0.10
ϕ (phi)	°	38.50	38.50	45.00	33.00
ψ (psi)	°	0	0	0	0
v_ur		0.18	0.18	0.14	0.22
K_0^{nc}		0.38	0.38	0.32	0.46
M		1.91	1.91	2.11	1.63
OCR		1	1	1	1
POP	kN/m²	13	13	12	150
k_x	m/day	8.10E-03	1.62E-02	6.40E-02	1.00E-02
k_y	m/day	8.10E-04	1.62E-03	6.40E-03	1.00E-03
c_k		0.31	0.31	1.52	0.11

Identification GD FEA		2b;mc;top.clay: Gs:15 Phi:38.5 CR:0.27 Knc:0.38 S:0.42 SSC	3a;mc;soft.clay: Gs:12.6 Phi:30 CR:0.27 Knc:0.5 S:0.33 SSC	3b;mc;clay: Gs:13.1 Phi:38.5 CR:0.27 Knc:0.38 S:0.42 SSC	4b;mc;peat: Gs:10.3 Phi:45 CR:0.51 Knc:0.32 S:0.49 SSC
Material model		Soft soil creep	Soft soil creep	Soft soil creep	Soft soil creep
Drainage type		Undrained (A)	Undrained (A)	Undrained (A)	Undrained (A)
γ_unsat	kN/m³	14.40	12.24	12.69	10.17
γ_sat	kN/m³	15.00	12.60	13.10	10.30
Dilatancy cut-off		No	No	No	No
e_init		1.99	4.01	2.68	10.20
e_min		0.00	0.00	0.00	0.00
e_max		999.00	999.00	999.00	999.00
λ^* (lambda*)		1.18E-01	1.18E-01	1.18E-01	2.23E-01
κ^* (kappa*)		2.55E-02	4.74E-02	2.55E-02	5.35E-02
μ^*		3.96E-03	3.96E-03	3.96E-03	1.18E-02
c_ref	kN/m²	4.00	2.00	4.00	8.00
ϕ (phi)	°	38.50	30.00	38.50	45.00
ψ (psi)	°	0	0	0	0
v_ur		0.18	0.25	0.18	0.14
K_0^nc		0.38	0.50	0.38	0.32
M		2.01	1.54	2.01	2.24
OCR		1	1	1	1
POP	kN/m²	35	7	35	35
k_x	m/day	4.00E-03	1.62E-02	8.10E-03	1.60E-02
k_y	m/day	4.00E-04	1.62E-03	8.10E-04	1.60E-03
c_k		0.31	0.31	0.31	1.52

Identification c02 FEA		2;cs;top.clay: Gs:15 Phi:38.5 CR:0.27 Knc:0.38 S:0.42 Iso SHANSEP	3;cs;clay: Gs:13.1 Phi:38.5 CR:0.27 Knc:0.38 S:0.42 Iso SHANSEP	3a;cs;soft.clay: Gs:12.6 Phi:38.3 CR:0.27 Knc:0.38 S:0.33 Iso SHANSEP	4;cs;peat: Gs:10.3 Phi:43.2 CR:0.51 Knc:0.32 S:0.49 Iso SHANSEP
Model in DLL		NGI-ADP-S	NGI-ADP-S	NGI-ADP-S	NGI-ADP-S
Drainage type		Undrained (A)	Undrained (A)	Undrained (A)	Undrained (A)
γ_unsat	kN/m³	14.40	12.69	12.24	10.17
γ_sat	kN/m³	15.00	13.10	12.60	10.30
Dilatancy cut-off		No	No	No	No
e_init		1.99	2.68	4.01	10.20
e_min		0.00	0.00	0.00	0.00
e_max		999.00	999.00	999.00	999.00
G/s_u^A		56	56	71	25
γ_f^C	%	18	18	15	21
γ_f^E	%	36	36	30	42
γ_f^DSS	%	30	30	25	35
vert_ref	m	0	0	0	0
s_u^A_inc	kN/m²/m	0	0	0	0
s_u^P/s_u^A		1.00	1.00	1.00	1.00
τ_0/s_u^A		0.50	0.50	0.50	0.50
s_u^DSS/s_u^A		1.00	1.00	1.00	1.00
v		0.18	0.18	0.18	0.14
v_u		0.495	0.495	0.495	0.495
alpha		0.42	0.42	0.33	0.49
power		0.86	0.86	0.86	0.85
s_u,min	kN/m²	4.20	4.20	3.30	4.90

Identification c03 FEA		2;csa;top.clay : Gs:15 Phi:38.5 CR:0.27 Knc:0.38 S:0.53 Ani SHANSEP	3;csa;clay: Gs:13.1 Phi:38.5 CR:0.27 Knc:0.38 S:0.52 Ani SHANSEP	3a;csa;soft.clay : Gs:12.7 Phi:33 CR:0.27 Knc:0.46 S:0.41 Ani SHANSEP	4;csa;peat: Gs:10.3 Phi:43.2 CR:0.51 Knc:0.32 S:0.61 Ani SHANSEP
Model in DLL		NGI-ADP-S	NGI-ADP-S	NGI-ADP-S	NGI-ADP-S
Drainage type		Undrained (A)	Undrained (A)	Undrained (A)	Undrained (A)
γ_unsat	kN/m³	14.40	12.69	12.33	10.17
γ_sat	kN/m³	15.00	13.10	12.70	10.30
Dilatancy cut-off		No	No	No	No
e_init		1.99	2.68	4.01	10.20
e_min		0.00	0.00	0.00	0.00
e_max		999.00	999.00	999.00	999.00
G/s_u^A		45	45	52	20
γ_f^C	%	18	18	15	21
γ_f^E	%	36	36	30	42
γ_f^{DSS}	%	30	30	25	35
$vert\_ref$	m	0	0	0	0
$s\_u^A\_inc$	kN/m²/m	0	0	0	0
s_u^P/s_u^A		0.67	0.67	0.67	0.67
τ_0/s_u^A		0.50	0.50	0.50	0.50
s_u^{DSS}/s_u^A		0.80	0.80	0.80	0.80
v		0.18	0.18	0.22	0.14
v_u		0.495	0.495	0.495	0.495
alpha		0.525	0.52	0.4125	0.6125
power		0.86	0.86	0.86	0.85
s_u,min	kN/m²	5.25	5.20	4.13	6.13

Identification c07 FEA		2;cs;top.clay: Gs:15 Phi:38.5 CR:0.27 Knc:0.38 S:0.42 Iso SHANSEP	3;cs;clay: Gs:13.1 Phi:38.5 CR:0.27 Knc:0.38 S:0.42 Iso SHANSEP	3a;cs;soft.clay: Gs:12.6 Phi:38.3 CR:0.27 Knc:0.38 S:0.33 Iso SHANSEP	4;cs;peat: Gs:10.3 Phi:43.2 CR:0.51 Knc:0.32 S:0.49 Iso SHANSEP
Model in DLL		NGI-ADP-S	NGI-ADP-S	NGI-ADP-S	NGI-ADP-S
Drainage type		Undrained (A)	Undrained (A)	Undrained (A)	Undrained (A)
γ_unsat	kN/m³	14.40	12.69	12.24	10.17
γ_sat	kN/m³	15.00	13.10	12.60	10.30
Dilatancy cut-off		No	No	No	No
e_init		1.99	2.68	4.01	10.20
e_min		0.00	0.00	0.00	0.00
e_max		999.00	999.00	999.00	999.00
G/s_u^A		56	56	71	25
γ_f^C	%	18	18	15	21
γ_f^E	%	36	36	30	42
γ_f^{DSS}	%	30	30	25	35
vert_ref	m	0	0	0	0
s_u^A_inc	kN/m²/m	0	0	0	0
s_u^P/s_u^A		1.00	1.00	1.00	1.00
τ_0/s_u^A		0.50	0.50	0.50	0.50
s_u^{DSS}/s_u^A		1.00	1.00	1.00	1.00
v		0.18	0.18	0.18	0.14
v_u		0.495	0.495	0.495	0.495
alpha		0.48	0.48	0.38	0.56
power		0.86	0.86	0.86	0.85
s_u,min	kN/m²	4.20	4.20	3.30	4.90

Identification c09 FEA		2;csa;top.clay : Gs:15 Phi:38.5 CR:0.27 Knc:0.38 S:0.53 Ani CSC1S	3;csa;clay: Gs:13.1 Phi:38.5 CR:0.27 Knc:0.38 S:0.52 Ani CSC1S	3a;csa;soft.clay : Gs:12.7 Phi:33 CR:0.27 Knc:0.46 S:0.41 Ani CSC1S	4;csa;peat: Gs:10.3 Phi:43.2 CR:0.51 Knc:0.32 S:0.61 Ani CSC1S
Model in DLL		Creep-SClay1S	Creep-SClay1S	Creep-SClay1S	Creep-SClay1S
Drainage type		Undrained (A)	Undrained (A)	Undrained (A)	Undrained (A)
γ_unsat	kN/m³	14.40	12.69	12.33	10.17
γ_sat	kN/m³	15.00	13.10	12.70	10.30
Dilatancy cut-off		No	No	No	No
e_init		1.99	2.68	4.01	10.20
e_min		0.00	0.00	0.00	0.00
e_max		999.00	999.00	999.00	999.00
Rayleigh α		0	0	0	0
Rayleigh β		0	0	0	0
κ^*		0.026	0.026	0.024	0.054
ν		0.18	0.18	0.22	0.14
λ^*		0.118	0.118	0.118	0.223
M_c		1.57	1.57	1.33	1.77
M_e		1.03	1.03	0.92	1.12
w		22	22	21	12
w_d		1.02	1.02	0.89	0.97
x		0	0	0	0
x_d		0	0	0	0
OCR >=1		1	1	1	1
POP >=0	kN/m²	13	13	7	12
e_0		1.99	2.68	4.01	10.20
α_0		-0.05	-0.05	0.30	-0.25
c_0		0	0	0	0
τ	day	1	1	1	1
μ*		3.96E-03	3.96E-03	3.96E-03	1.18E-02
K_0^NC		0.38	0.38	0.46	0.32

Identification all FEA Plates		GU8N-cont	GU8N-discont	Saaf1
Material type		Elastoplastic	Elastoplastic	Elastic
Isotropic		No	No	Yes
EA_1	kN/m	2.17E+06	1.08E+06	1.00E-03
EA_2	kN/m	1.08E+05	2.71E+04	1.00E-03
EI	kN m²/m	2.30E+04	1.15E+04	1.00E-03
d	m	0.36	0.36	3.46
w	kN/m/m	0.81	0.40	0.00
v (nu)		0.00	0.00	0.00
M_p	kN m/m	229	137	1.00E+15
N_p,1	kN/m	1.00E+06	1.00E+06	1.00E+10
N_p,2	kN/m	1.00E+06	1.00E+06	1.00E+10
Rayleigh α		0	0	0
Rayleigh β		0	0	0
Prevent punching		Yes	Yes	No
Identification number		1	2	3

BIBLIOGRAPHY

Andersen, C.F., Battjes, J.A., and Daniel, D.E. 2007. The New Orleans hurricane protection system: what went wrong and why. American Society of Civil Engineers. Hurricane Katrina External Review Panel ISBN-13: 978-0-7844-0893-3, ASCE.

Andrejko, M.J., Fiene, F., and Cohen, A.D. 1983. Comparison of Ashing Techniques for Determination of the Inorganic Content of Peats. *In* Testing of Peats and Organic Soils. *Edited by* P.M. Jarrett. ASTM International, West Conshohocken, PA. pp. 5-5-16.

Baligh, M.M., and Azzouz, A.S. 1975. End Effects on Stability of Cohesive Slopes. Journal of the geotechnical engineering division, **101**(11): 1105-1117. doi:10.1061/ajgeb6.0000210.

Been, K., and Jefferies, M.G. 1993. Towards systematic CPT interpretation. *In* Predictive soil mechanics. Thomas Telford Publishing. pp. 121-134.

Begemann, H.K. 1965. The friction jacket cone as an aid in determining the soil profile. Proc. 6th Int. Conf. on SMFE, **1**: 17-20.

Bjerrum, L. 1967. Engineering Geology of Norwegian Normally-Consolidated Marine Clays as Related to Settlements of Buildings. Géotechnique, **17**(2): 83-118. doi:10.1680/geot.1967.17.2.83.

Boulanger, R.W., and Idriss, I.M. 2016. CPT-Based Liquefaction Triggering Procedure. Journal of Geotechnical and Geoenvironmental Engineering, **142**(2): 04015065. doi:10.1061/(asce)gt.1943-5606.0001388.

Boulanger, R.W., Arulnathan, R., Harder, L.F., Torres, R.A., and Driller, M.W. 1998. Dynamic Properties of Sherman Island Peat. Journal of Geotechnical and Geoenvironmental Engineering, **124**(1): 12-20. doi:10.1061/(asce)1090-0241(1998)124:1(12).

Bourne-Webb, P.J., Potts, D.M., König, D., and Rowbottom, D. 2011. Analysis of model sheet pile walls with plastic hinges. Géotechnique, **61**(6): 487-499. doi:10.1680/geot.9.P.061.

Breedeveld, J. 2018. POVM Eemdijkproef, Geotechnisch Basisrapport, Product F (In Dutch). Nederland.

Breedeveld, J., Zwanenburg, C., Van, M.A., and Lengkeek, H.J. 2019. Impact of the Eemdijk full-scale test programme. *In* European Conference on Soil Mechanics and Geotechnical Engineering, ECSMGE 2019, Reykjavik. p. 8.

Breedeveld, J., Post, M., de Bruijn, H., Lengkeek, A., and Naves, T. 2018a. POVM Eemdijkproef, Eindrapport proefprogramma, Product V (In Dutch). Nederland.

Breedeveld, J., Post, M., de Bruijn, H., Lengkeek, A., and Naves, T. 2018b. Beschrijving en conclusies Eemdijkproef (in Dutch), Conclusions on the Eemdijk full-scale test. *In* Geotechniek. Educom. pp. 56-59.

Brinkgreve, R.B.J. 2019. Automated Model And Parameter Selection: Incorporating Expert Input into Geotechnical Analyses. Geo-Strata—Geo Institute of ASCE, **23**(1): 38-45.

Calle, E.O.F., Kanning, W., and Schweckendiek, T. 2021. Characteristic values of soil properties in Dutch codes of practice - Theretical backgrounds and assumptions. Deltares, Delft.

Chang, M.-F., Teh, C.I., and Cao, L. 1999. Critical state strength parameters of saturated clays from the modified Cam clay model. Canadian Geotechnical Journal, **36**(5): 876-890.

Cheng, X.H., Ngan-Tillard, D.J.M., and Den Haan, E.J. 2007. The causes of the high friction angle of Dutch organic soils. Engineering Geology, **93**(1-2): 31-44. doi:10.1016/j.enggeo.2007.03.009.

Cola, S., and Cortellazzo, G. 2005. The Shear Strength Behavior of Two Peaty Soils. Geotechnical and Geological Engineering, **23**(6): 679-695. doi:10.1007/s10706-004-9223-9.

Dafalias, Y.F. 1986. An anisotropic critical state soil plasticity model. Mechanics Research Communications, **13**(6): 341-347.

Dafalias, Y.F., Manzari, M.T., and Papadimitriou, A.G. 2006. SANICLAY: simple anisotropic clay plasticity model. International Journal for Numerical and Analytical Methods in Geomechanics, **30**(12): 1231-1257. doi:10.1002/nag.524.

De Gast, T., Hicks, M.A., Van den Eijnden, A.P., and Vardon, P.J. 2021. On the reliability assessment of a controlled dyke failure. Géotechnique, **71**(11): 1028-1043. doi:10.1680/jgeot.19.SiP.003.

Den Haan, E.J. 1996. A compression model for non-brittle soft clays and peat. Géotechnique, **46**(1): 1-16. doi:10.1680/geot.1996.46.1.1.

Den Haan, E.J. 1997. An overview of he mechanical behaviour of peats and organic soils and some appropriate construction techniques. *In* Conference on Recent Advances in Soft Soil Engineering, 5-7 March 1997, Kuching, Serawak. Geodelft.

Den Haan, E.J., and Kruse, G.A.M. 2007. Characterisation and engineering properties of Dutch peats. *In* Characterisation and engineering properties of natural soils. Taylor & Francis Group, London. pp. 2101-2133.

Douglas, B.J. 1981. Soil classification using electric cone penetrometer. *In* Symp. on Cone Penetration Testing and Experience, Geotech. Engrg. Div. ASCE. pp. 209-227.

Edil, T.B., and Wang, X. 2000. Shear strength and Ko of peats and organic soils. *In* Geotechnics of High Water Content Materials. *Edited by* T.B. Edil and P.J. Fox. ASTM International, West Conshohocken, PA. pp. 209-209-217.

EN1990. 2002. Eurocode 0: Basis of structural design. European Committee for Standardization.

EN1993-5. 2007. Eurocode 3: Design of steel structures - Part 5: Piling. European Committee for Standardization.

EN1997-1. 2005. Eurocode 7: Geotechnical design - part 1: General rules. European Committee for Standardization.

EN1997-2. 2007. Eurocode 7: Geotechnical Design - Part 2: Ground investigation and testing. European Committee for Standardization.

EN10248-1. 2006. Eurocode: Hot-rolled steel sheet piling - Part 1 : Technical delivery conditions. European Committee for Standardization.

Eslami, A., and Fellenius, B.H. 1997. Pile capacity by direct CPT and CPTu methods applied to 102 case histories. Canadian Geotechnical Journal, **34**(6): 886-904. doi:10.1139/t97-056.

Gaba, A.R., Hardy, S., Doughty, L., Powrie, W., Selemetas, D., Construction Industry, R., and Information, A. 2017. Guidance on embedded retaining wall design. CIRIA Report ; C760. CIRIA, London. pp. xxvi, 441 pages : illustrations (black and white, and colour) ; 30 cm.

Gens, A. 1982. Stress-strain and strength characteristics of a low plasticity clay. Doctoral, Imperial College, London.

Grimstad, G., Andresen, L., and Jostad, H.P. 2012. NGI-ADP: Anisotropic shear strength model for clay. International Journal for Numerical and Analytical Methods in Geomechanics, **36**(4): 483-497. doi:10.1002/nag.1016.

Hartlén, J., and Wolski, W. 1996. Embankments on Organic Soils, Developments in Geotechnical Engineering. Elsevier.

Hayashi, H., Yamazoe, N., Mitachi, T., Tanaka, H., and Nishimoto, S. 2012. Coefficient of earth pressure at rest for normally and overconsolidated peat ground in Hokkaido area. Soils and Foundations, **52**(2): 299-311.

Head, K.H. 1998. Manual of soil laboratory testing. Volume 3: effective stress tests. No. Ed. 2. John Wiley & Sons.

Hicks, M.A., Varkey, D., van den Eijnden, A.P., de Gast, T., and Vardon, P.J. 2019. On characteristic values and the reliability-based assessment of dykes. Georisk: Assessment and Management of Risk for Engineered Systems and Geohazards, **13**(4): 313-319. doi:10.1080/17499518.2019.1652918.

Hobbs, N.B. 1986. Mire morphology and the properties and behaviour of some British and foreign peats. Quarterly Journal of Engineering Geology and Hydrogeology, **19**(1): 7-80. doi:10.1144/gsl.Qjeg.1986.019.01.02.

Huang, P.-T., Patel, M., Santagata, M.C., and Bobet, A. 2009. Classification of organic soils. Joint Transportation Research Program, Indiana Department of Transportation and Purdue University, West Lafayette, Indiana, FHWA/IN/JTRP-2008/02.

ISO14475-1. 2016. Geotechnical investigation and testing - Sampling methods and groundwater measurements - Part 1: Technical principles for execution. International Organization for Standardization.

ISO14688-1. 2017. Geotechnical investigation and testing - Identification and classification of soil - Part 1: Identification and description. International Organization for Standardization.

ISO14688-2. 2017. Geotechnical investigation and testing - Identification and classification of soil - Part 2: Principles for a classification. International Organization for Standardization.

ISO22476-1. 2012. Geotechnical Investigation and Testing - Field Testing - Part 1: Electrical Cone and Piezocone Penetration Test. International Organization for Standardization.

Jaky, J. 1944. The coefficient of earth pressure at rest. J. of the Society of Hungarian Architects and Engineers: 355-358.

Jardine, R.J., Potts, D.M., Fourie, A.B., and Burland, J.B. 1986. Studies of the influence of non-linear stress–strain characteristics in soil–structure interaction. Géotechnique, **36**(3): 377-396. doi:10.1680/geot.1986.36.3.377.

Jarrett, P.M. 1983. Testing of Peats and Organic Soils. ASTM International, West Conshohocken, PA.

Jonkman, S.N., and Schweckendiek, T. 2015. Developments in levee reliability and flood risk analysis in the Netherlands. *In* Geotechnical safety and risk V. IOS press. pp. 50-60.

Jorissen, R., Kraaij, E., and Tromp, E. 2016. Dutch flood protection policy and measures based on risk assessment. E3S Web Conf., **7**: 20016. Available from https://doi.org/10.1051/e3sconf/20160720016 [accessed.

Karstunen, M., and Koskinen, M. 2008. Plastic anisotropy of soft reconstituted clays. Canadian Geotechnical Journal, **45**(3): 314-328.

Karstunen, M., and Yin, Z.-Y. 2010. Modelling time-dependent behaviour of Murro test embankment. Géotechnique, **60**(10): 735-749.

Kort, D.A. 2002. Rotterdam sheet pile wall field test. CUR publication 207, Civieltechnisch Centrum Uitvoering Research en Regelgeving, Gouda.

Ku, T., and Mayne, P.W. 2015. In Situ Lateral Stress Coefficient (K0) from Shear Wave Velocity Measurements in Soils. Journal of Geotechnical and Geoenvironmental Engineering, **141**(12): 06015009. doi:10.1061/(asce)gt.1943-5606.0001354.

Kulhawy, F.H., and Mayne, P.W. 1990. Manual on estimating soil properties for foundation design. ; Electric Power Research Inst., Palo Alto, CA (USA); Cornell Univ., Ithaca, NY (USA). Geotechnical Engineering Group EPRI-EL-6800 United States Research Reports Center, Box 50490, Palo Alto, CA 94303 TIC English.

Ladd, C.C., and Foott, R. 1974. New design procedure for stability of soft clays. Journal of Geotechnical and Geoenvironmental Engineering (ASCE), **100 (GT7)**: 763-786.

Ladd, C.C., and DeGroot, D.J. 2003. Recommended practice for soft ground site characterization: Arthur Casagrande Lecture. *In* Soil & Rock America (Proc. 12th Pan American Conference on Soil Mechanics and Geotech Engrg., MIT), Verlag Glückauf, Essen. pp. 3-57.

Laera, A., Sarathchandran, A., and Brinkgreve, R.B.J. 2018. The Creep-SCLAY1S model 2018. Delft, The Netherlands.

Landva, A.O. 2007. Characterization of Escuminac peat and construction on peatland. *In* 2nd International Workshop on Characterisation and Engineering Properties of Natural Soils. CRC Press, Singapore.

Landva, A.O., and Pheeney, P.E. 1980. Peat fabric and structure. Canadian Geotechnical Journal, **17**(3): 416-435.

Landva, A.O., and La Rochelle, P. 1983. Compressibility and shear characteristics of Radforth peats. Testing of peats and organic soils. ASTM International.

Landva, A.O., Korpijaakko, E.O., and Pheeney, P.E. 1983. Geotechnical Classification of Peats and Organic Soils. Testing of Peats and Organic Soils. ASTM International, West Conshohocken, PA. pp. Stp37333s.

Law, K.T., and Holtz, R.D. 1978. A note on Skempton's A parameter with rotation of principal stresses. Géotechnique, **28**(1): 57-64. doi:10.1680/geot.1978.28.1.57.

Leclercq, V.J.F. 2020. Residual strength and profile of the Eemdijk full-scale test. Master of Science, Delft University of Technology.

Lehtonen, V., Meehan, C., Länsivaara, T., and Mansikkamäki, J. 2015. Full-scale embankment failure test under simulated train loading. Géotechnique, **65**(12): 961-974.

Lengkeek, H.J. 2022. CPT-based classification and correlations for organic soils. 4TU.ResearchData. doi:https://doi.org/10.4121/19139651.v2.

Lengkeek, H.J., and Bouw, R. 2011. Triaxial, DSS, CRS tests and numerical simulations of soft soils at river dike. *In* 15th European Conference on Soil Mechanics and Geotechnical Engineering, ECSMGE 2011, Athens. pp. 427 - 434.

Lengkeek, H.J., and Brinkgreve, R.B.J. 2022a. CPT-based classification of soft organic clays and peat. *In* CPT'22, Bologna. p. 6.

Lengkeek, H.J., and Brinkgreve, R.B.J. 2022b. CPT-based unit weight estimation extended to soft organic clays and peat: an update. *In* CPT'22, Bologna. p. 6.

Lengkeek, H.J., and Breedeveld, J. 2022. Eemdijk full-scale test on dike reinforced by sheet pile. 4TU.ResearchData. doi:https://doi.org/10.4121/19213890.v1.

Lengkeek, H.J., de Greef, J., and Joosten, S. 2018. CPT based unit weight estimation extended to soft organic soils and peat. *In* 4th International Symposium on Cone Penetration Testing (CPT'18), Delft. pp. 389-394.

Lengkeek, H.J., Jonkman, S.N., and Kanning, W. 2021. Application of geo-statistics and pairwise established CPT-based correlations for line infrastructure. *In* 6th International Conference on Geotechnical and Geophysical Site Characterization:"Toward synergy at site characterisation". p. 10.

Lengkeek, H.J., Jonkman, S.N., and Hauth, M. 2022. Application of statistics to CPT-based parameter selection. *In* 20th International Conference on Soil Mechanics and Geotechnical Engineering: a geotechnical discovery downunder (In-Press). (in-Press), Sydney. p. 6.

Lengkeek, H.J., Naves, T., Post, M., and Breedeveld, J. 2019a. Eemdijk full-scale field test programme: sheet pile pullover tests. *In* European Conference on Soil Mechanics and Geotechnical Engineering, ESCMGE 2019, Reykjavik. p. 8.

Lengkeek, H.J., Post, M., Breedeveld, J., and Naves, T. 2019b. Eemdijk full-scale field test programme: ground dike and sheet pile dike failure test. *In* European Conference on Soil Mechanics and Geotechnical Engineering, ESCMGE 2019, Reykjavik. p. 8.

Leroueil, S., Kabbaj, M., Tavenas, F., and Bouchard, R. 1985. Stress–strain–strain rate relation for the compressibility of sensitive natural clays. Géotechnique, **35**(2): 159-180. doi:10.1680/geot.1985.35.2.159.

Lindenberg, J., Van, M.A., Koelewijn, A.R., Zwanenburg, C., Lambert, J.W.M., van der Meer, M.T., and Teunissen, P.A.A. 2002. Bergambacht field test evaluation. Delft Cluster.

Lunne, T., Powell, J.J., and Robertson, P.K. 2002. Cone penetration testing in geotechnical practice. CRC Press.

MacFarlane, I. 1969. Muskeg Engineering Handbook. Canadian building series ; 3. University of Toronto Press, Toronto. pp. 297.

Mayne, P.W. 2006. In-situ test calibrations for evaluating soil parameters. *In* Characterisation and Engineering Properties of Natural Soils–Proceedings of the Second International Workshop on Characterisation and Engineering Properties of Natural Soils: Taylor & Francis. pp. 1601-1652.

Mayne, P.W. 2008. Piezocone profiling of clays for maritime site investigations. *In* Proceedings of the 11th Baltic Sea Geotechnical Conference, Gdansk, Poland. Citeseer. pp. 15-18.

Mayne, P.W. 2014. Interpretation of geotechnical parameters from seismic piezocone tests. *In* Proceedings, 3rd International Symposium on Cone Penetration Testing. pp. 47-73.

Mayne, P.W. 2017. Stress history of soils from cone penetration tests. 34th Manual Rocha Lecture, Soils and Rocks, **40**: 203-218.

Mayne, P.W., and Kulhawy, F.H. 1982. Ko- OCR Relationships in Soil. Journal of the Soil Mechanics and Foundations Division, **108**(6): 851-872.

Mayne, P.W., Agaiby, S.S., and Dasenbrock, D. 2020. Piezocone Identification of Organic Clays and Peats. *In* Geo-Congress 2020. pp. 541-549.

Meijer, F.L.E. 2019. Evaluation of sheet pile behavior based on Eemdijk monitoring data. Master of Science, Delft University of Technology.

Mesri, G., and Hayat, T.M. 1993. The coefficient of earth pressure at rest. Canadian Geotechnical Journal, **30**(4): 647-666. doi:10.1139/t93-056.

Mesri, G., and Ajlouni, M. 2007. Engineering Properties of Fibrous Peats. Journal of Geotechnical and Geoenvironmental Engineering, **133**(7): 850-866. doi:doi:10.1061/(ASCE)1090-0241(2007)133:7(850).

Michalowski, R.L. 2010. Limit Analysis and Stability Charts for 3D Slope Failures. Journal of Geotechnical and Geoenvironmental Engineering, **136**(4): 583-593. doi:10.1061/(asce)gt.1943-5606.0000251.

Mitchell, J.K., and Soga, K. 2005. Fundamentals of Soil Behavior 3rd ed., JohnWiley &Sons. Inc. Foundation failure.

Muir Wood, D. 1990. Soil behaviour and critical state soil mechanics. Cambridge University Press, Cambridge [England].

NEN5104. 1989. Classificatie van onverharde grondmonsters (In Dutch), Classification of unconsolidated soil samples. Nederlands Normalisatie-instituut.

O'Kelly, B.C. 2016. Briefing: Atterberg limits and peat. Environmental Geotechnics, **3**(6): 359-363. doi:10.1680/envgeo.15.00003.

Ohta, H., Nishihara, A., and Morita, Y. 1985. Undrained stability of Ko-consolidated clays. *In* International conference on soil mechanics and foundation engineering. 11. pp. 613-616.

Panagoulias, S., and Brinkgreve, R.B.J. 2017. SHANSEP NGI-ADP. Delft, The Netherlands.

Pestana, J.M., Whittle, A.J., and Gens, A. 2002. Evaluation of a constitutive model for clays and sands: Part II - clay behaviour. International Journal for Numerical and Analytical Methods in Geomechanics, **26**(11): 1123-1146. doi:10.1002/nag.238.

POVM. 2020a. POVM Langsconstructies - PPL (In Dutch). Nederland.

POVM. 2020b. POVM Eindige-elementenmethode - PPE (In Dutch). Nederland.

Remmerswaal, G., Vardon, P.J., and Hicks, M.A. 2021. Evaluating residual dyke resistance using the Random Material Point Method. Computers and Geotechnics, **133**: 104034. doi:10.1016/j.compgeo.2021.104034.

Rijkswaterstaat. 2017. Handreiking ontwerpen met overstromingskansen, Veiligheidsfactoren en belastingen bij nieuwe overstromingskansnormen - OI2014v4 (In Dutch). Ministerie van infrastructuur en Milieu, WVL.

Rijkswaterstaat. 2021. Schematiseringshandleiding macrostabiliteit - WBI 2017 (In Dutch). Ministerie van Infrastructuur en Milieu, WVL.

Robertson, P.K. 1990. Soil classification using the cone penetration test. Canadian Geotechnical Journal, **27**(1): 151-158. doi:10.1139/t90-014.

Robertson, P.K. 2009. Interpretation of cone penetration tests — a unified approach. Canadian Geotechnical Journal, **46**(11): 1337-1355. doi:10.1139/t09-065.

Robertson, P.K. 2010. Soil behaviour type from the CPT: an update. *In* 2nd international symposium on cone penetration testing, USA. pp. 9-11.

Robertson, P.K. 2012. The James K. Mitchell Lecture: Interpretation of in-situ tests–some insights. *In* Proc. 4th Int. Conf. on Geotechnical and Geophysical Site Characterization–ISC. pp. 3-24.

Robertson, P.K. 2016. Cone penetration test (CPT)-based soil behaviour type (SBT) classification system — an update. Canadian Geotechnical Journal, **53**(12): 1910-1927. doi:10.1139/cgj-2016-0044.

Robertson, P.K., and Wride, C.E. 1998. Evaluating cyclic liquefaction potential using the cone penetration test. Canadian Geotechnical Journal, **35**(3): 442-459. doi:10.1139/t98-017.

Robertson, P.K., and Cabal, K.L. 2010. Estimating soil unit weight from CPT. *In* 2nd International symposium on cone penetration testing. pp. 2-40.

Robertson, P.K., Campanella, R.G., Gillespie, D., and Greig, J. 1986. Use of piezometer cone data. *In* Use of in situ tests in geotechnical engineering. ASCE. pp. 1263-1280.

Roscoe, K.H., and Burland, J.B. 1968. On the generalized stress-strain behaviour of wet clay.

230

Roscoe, K.H., Schofield, A.N., and Thurairajah, A. 1963. Yielding of Clays in States Wetter than Critical. Géotechnique, **13**(3): 211-240. doi:10.1680/geot.1963.13.3.211.

Rowe, R.K., Gnanendran, C.T., Valsangkar, A.J., and Landva, A.O. 2001. Performance of a test embankment constructed on an organic clayey silt deposit. Canadian Geotechnical Journal, **38**(6): 1283-1296.

Schmertmann, J.H. 1978. Guidelines for cone penetration test: performance and design. United States. Federal Highway Administration Report FHWA-TS-78-209.

Schneider, J.A., Randolph, M.F., Mayne, P.W., and Ramsey, N.R. 2008. Analysis of Factors Influencing Soil Classification Using Normalized Piezocone Tip Resistance and Pore Pressure Parameters. Journal of Geotechnical and Geoenvironmental Engineering, **134**(11): 1569-1586. doi:10.1061/(asce)1090-0241(2008)134:11(1569).

Schofield, A., and Wroth, P. 1968. Critical state soil mechanics. McGraw-hill.

Seed, R.B., Bea, R.G., Athanasopoulos-Zekkos, A., Boutwell, G.P., Bray, J.D., Cheung, C., Cobos-Roa, D., Ehrensing, L., Harder, L.F., Pestana, J.M., Riemer, M.F., Rogers, J.D., Storesund, R., Vera-Grunauer, X., and Wartman, J. 2008. New Orleans and Hurricane Katrina. II: The Central Region and the Lower Ninth Ward. Journal of Geotechnical and Geoenvironmental Engineering, **134**(5): 718-739. doi:10.1061/(asce)1090-0241(2008)134:5(718).

Sivasithamparam, N., Karstunen, M., and Bonnier, P. 2015. Modelling creep behaviour of anisotropic soft soils. Computers and Geotechnics, **69**: 46-57. doi:10.1016/j.compgeo.2015.04.015.

Skempton, A.W. 1954. The pore-pressure coefficients A and B. Géotechnique, **4**(4): 143-147. doi:10.1680/sposm.02050.0010.

Skempton, A.W., and Petley, D.J. 1970. Ignition Loss and other Properties of Peats and Clays from Avonmouth, King's Lynn and Cranberry Moss. Géotechnique, **20**(4): 343-356. doi:10.1680/geot.1970.20.4.343.

Stochino, F., Bedon, C., Sagaseta, J., and Honfi, D. 2019. Robustness and Resilience of Structures under Extreme Loads. Advances in Civil Engineering, **2019**: 1-14. doi:10.1155/2019/4291703.

Tashiro, M., Nguyen, S.H., Inagaki, M., Yamada, S., and Noda, T. 2015. Simulation of large-scale deformation of ultra-soft peaty ground under test embankment loading and investigation of effective countermeasures against residual settlement and failure. Soils and Foundations, **55**(2): 343-358. doi:10.1016/j.sandf.2015.02.010.

Van Berkom, I.E., Brinkgreve, R.B.J., Lengkeek, H.J., and De Jong, A.K. 2022. An automated system to determine constitutive model parameters from in situ tests. *In* 20th International Conference on Soil Mechanics and Geotechnical Engineering. *Edited by* ICSMGE, Sydney. p. 6.

Van, M.A., Koelewijn, A.R., and Barends, F.B. 2005. Uplift Phenomenon: Model, Validation, and Design. International Journal of Geomechanics, **5**(2): 98-106. doi:10.1061/(ASCE)1532-3641(2005)5:2(98).

Vanmarcke, E.H. 1977. Reliability of earth slopes. Journal of the geotechnical engineering division, **103**(11): 1247-1265.

Von Post, L. 1922. Sveriges Geologiska Undersöknings torvinventering och några av dess hittills vunna resultat (In Swedish). SGU peat inventory and some preliminary results. **36**.

Wheeler, S.J., Näätänen, A., Karstunen, M., and Lojander, M. 2003. An anisotropic elastoplastic model for soft clays. Canadian Geotechnical Journal, **40**(2): 403-418.

Wroth, C.P. 1984. The interpretation of in situ soil tests. Géotechnique, **34**(4): 449-489. doi:10.1680/geot.1984.34.4.449.

Wüst, R.A.J., Bustin, R.M., and Lavkulich, L.M. 2003. New classification systems for tropical organic-rich deposits based on studies of the Tasek Bera Basin, Malaysia. Catena, **53**(2): 133-163. doi:10.1016/s0341-8162(03)00022-5.

Yamaguchi, H., Ohira, Y., Kogure, K., and Mori, S. 1985. Undrained Shear Characteristics of Normally Consolidated Peat Under Triaxial Compression and Extension Conditions. Soils and Foundations, **25**(3): 1-18. doi:10.3208/sandf1972.25.3_1.

Yin, J.-H., and Graham, J. 1994. Equivalent times and one-dimensional elastic viscoplastic modelling of time-dependent stress–strain behaviour of clays. Canadian Geotechnical Journal, **31**(1): 42-52. doi:10.1139/t94-005.

Yin, J.-H., and Feng, W.-Q. 2016. A new simplified method and its verification for calculation of consolidation settlement of a clayey soil with creep. Canadian Geotechnical Journal, **54**(3): 333-347. doi:10.1139/cgj-2015-0290.

Yu, H.S. 1998. CASM: a unified state parameter model for clay and sand. International Journal for Numerical and Analytical Methods in Geomechanics, **22**(8): 621-653. doi:10.1002/(sici)1096-9853(199808)22:8<621::Aid-nag937>3.0.Co;2-8.

Zhang, G., Robertson, P.K., and Brachman, R.W.I. 2002. Estimating liquefaction-induced ground settlements from CPT for level ground. Canadian Geotechnical Journal, **39**(5): 1168-1180. doi:10.1139/t02-047.

Zwanenburg, C., and Jardine, R.J. 2015. Laboratory, in situ and full-scale load tests to assess flood embankment stability on peat. Géotechnique, **65**(4): 309-326. doi:10.1680/geot.14.P.257.

Zwanenburg, C., Den Haan, E.J., Kruse, G.A.M., and Koelewijn, A.R. 2012. Failure of a trial embankment on peat in Booneschans, the Netherlands. Géotechnique, **62**(6): 479-490. doi:10.1680/geot.9.P.094.

CURRICULUM VITAE

Henri John Lengkeek

25 May 1973   born in Raesfeld, Germany

Education

1991 - 1997   MSc Civil Engineering and Geosciences, Hydraulic Engineering, Delft University of Technology, Delft, The Netherlands

1986 - 1991   VWO, pre-university secondary Education, GSR, Rotterdam, The Netherlands

Employment

2022 - present   geotechnical expert practice board ProRail, stability assessment railway embankments.

2020 - present   geotechnical expert on sheet pile reinforced dikes, Dutch Water Authorities for flood defenses 'Adviesteam Dijken'

2017 - present   PhD researcher, Hydraulic Structures and Flood Risk section, Civil Engineering and Geosciences, Delft University of Technology

2017 - 2018   geotechnical expert, full-scale failure test ('Eemdijk damwandproef') of a dike with sheet pile sheet pile reinforcement; Eemdijk

2008 - present   geotechnical expert, dikes reinforcement projects; The Netherlands

2005 - present   tutor postgraduate course: parameter determination, innovative dike reinforcement, Eurocode 7, retaining structures and anchorage, PAO, Delft

2002 - 2020   geotechnical expert, design of manmade islands, foundations, retaining structures, breakwaters and ice protection structures, ice-basin model tests; North Caspian Sea, Kazakhstan

1997 - 2012   geotechnical engineer Noord/Zuidlijn Metro, Amsterdam. Geotechnical parameters determination, building pits, bored tunnel, full-scale diaphragm wall test, detailed design immersed tunnel

1997 - present   geotechnical engineer at consultancy and engineering firm Witteveen+Bos

Committees

2019 - present   ISSMGE TC102 committee on In-Situ Testing

2018 - present   IOGP TC67/SC7/WG10 & API/SC2/RG7. Geotechnical representative for Ice & Arctic engineering.

2017 - 2018   NPR 9998 committee, development of national annex to Eurocode 8 for seismic design and liquefaction analysis.

2017 - 2018   TC67/SC7/WG8/TP4. Geotechnical lead for Foundations and Manmade islands of ISO 19906 Arctic offshore structures.

2015 - 2020   POVM committee FEM stability assessment of dikes. Contributions to publications 'POVM Eindige-elementenmethode' (FEM) and 'POVM Langsconstructies' (reinforcement walls)

2014 - 2020   board member of geotechnical section of The Royal Netherlands Society of Engineers (KIVI).

2013 - 2014   STOWA committee on undrained stability analysis on regional dikes.

2010 - 2011   SBW committee of actual strength assessment of dikes.

2005 - 2007   CUR C219: development of dike soil nailing (INSIDE).

2005 - 2006   CIRIA committee: Rock Manual 2nd Ed. Author of physical conditions and structural response related to Ice.

2003 - 2011   CUR committees C126, C127, C135, C152, C219, C236: parameter determination, retaining structures and anchorage.

1997 - 2001   COB committees K100, L520, F210: underground construction and tunneling.

LIST OF PUBLICATIONS

Related to this thesis

- Breedeveld, J., Zwanenburg, C., Van, M.A., and Lengkeek, H.J. 2019. Impact of the Eemdijk full-scale test programme. In European Conference on Soil Mechanics and Geotechnical Engineering, ECSMGE 2019, Reykjavik. p. 8.
- Breedeveld, J., Post, M., de Bruijn, H., Lengkeek, A., and Naves, T. 2018b. POVM Eemdijkproef, Eindrapport proefprogramma, Product V (In Dutch). Nederland.
- Lengkeek, H.J. 2022. CPT-based classification and correlations for organic soils. 4TU.ResearchData. doi:https://doi.org/10.4121/19139651.v2.
- Lengkeek, H.J., and Breedeveld, J. 2022. Eemdijk full-scale test on dike reinforced by sheet pile. 4TU.ResearchData. doi:https://doi.org/10.4121/19213890.v1.
- Lengkeek, H.J., and Brinkgreve, R.B.J. 2022a. CPT-based classification of soft organic clays and peat. In CPT'22, Bologna. p. 6.
- Lengkeek, H.J., and Brinkgreve, R.B.J. 2022b. CPT-based unit weight estimation extended to soft organic clays and peat: an update. In CPT'22, Bologna. p. 6.
- Lengkeek, H.J., de Greef, J., and Joosten, S. 2018. CPT based unit weight estimation extended to soft organic soils and peat. In 4th International Symposium on Cone Penetration Testing (CPT'18), Delft. pp. 389-394.
- Lengkeek, H.J., Jonkman, S.N., and Kanning, W. 2021. Application of geo-statistics and pairwise established CPT-based correlations for line infrastructure. In 6th International Conference on Geotechnical and Geophysical Site Characterization:"Toward synergy at site characterisation". p. 10.
- Lengkeek, H.J., Jonkman, S.N., and Hauth, M. 2022. Application of statistics to CPT-based parameter selection. In 20th International Conference on Soil Mechanics and Geotechnical Engineering: a geotechnical discovery downunder (In-Press). (in-Press), Sydney. p. 6.
- Lengkeek, H.J., Naves, T., Post, M., and Breedeveld, J. 2019a. Eemdijk full-scale field test programme: sheet pile pullover tests. In European Conference on Soil Mechanics and Geotechnical Engineering, ESCMGE 2019, Reykjavik. p. 8.
- Lengkeek, H.J., Post, M., Breedeveld, J., and Naves, T. 2019b. Eemdijk full-scale field test programme: ground dike and sheet pile dike failure test. In European Conference on Soil Mechanics and Geotechnical Engineering, ESCMGE 2019, Reykjavik. p. 8.

Other

- Bakker, K.J., Lengkeek, H.J., and Bonnier, P.G. 1997. Interface elements to model subgrade reactions for tunnel design. In Numerical Models in Geomechanics - Numog VI. Edited by S. Pietruszczak and G.N. Pande, Montreal. pp. 507-512.
- Besseling, F., and Lengkeek, A. 2012. Plaxis as a Tool for Soil-Structure Interaction Modelling in Performance-Based Seismic Jetty Design. In Plaxis Bulletin. pp. 10-15.
- Besseling, F., Lengkeek, H.J., de Waard, H., and Nieuwenhuis, K. 2019. Ice actions for hydraulic structures of primary flood defense Afsluitdijk-"Applying ISO 19906 at home". In 25th International Conference on Port and Ocean Engineering under Arctic Conditions, POAC 2019, Delft.
- Bouzoni, E., Besseling, F., Bosman, E., and Lengkeek, H.J. 2017. Insight into dynamic soil-pile-structure interaction analysis of an industrial facility. In 3rd International Conference on Performance-based Design in Earthquake Geotechnical Engineering, PBD-III, Vancouver.
- De Greef, J., and Lengkeek, H.J. 2018. Transition-and thin layer corrections for CPT based liquefaction analysis. In 4th International Symposium on Cone Penetration Testing (CPT'18). CRC Press, Delft. pp. 317-322.
- De Greef, J., Lengkeek, H.J., Brunetti, M., and Besseling, F. 2017. Liquefaction susceptibility underneath a large storage tank: a CPT based methodology. In 3rd International Conference on Performance-based Design in Earthquake Geotechnical Engineering, PBD-III, Vancouver.

- De Wit, J.C.W.M., and Lengkeek, H.J. 2002. Full scale test on environmental impact of diaphragm wall trench installation in Amsterdam-the final results. In International symposium on geotechnical aspect of underground construction in soft ground., Toulouse, France. pp. 433-440.
- Kwast, E.A., Lengkeek, H.J., Aukema, E.J., and Bos, R.M. 2001. Swell investigation by the Sophia railway tunnel, Betuwelijn, the Netherlands. In XVth ICSMGE International Conference on Soil Mechanics and Geotechnical Engineering, ICSMGE 2001. Balkema, Istanbul. pp. 2203-2206.
- Lengkeek, A. 2006. Slot voor damwand (In Dutch), Interlock for sheet-pile. In De Ingenieur, De vernufteling. KIVI. p. 45.
- Lengkeek, A., and Peters, M. 2006. Simulation of soil nail in large scale direct shear test. In Plaxis Bulletin. pp. 12-14.
- Lengkeek, A., and Brunetti, M. 2015. Interpretation of TA and DSS test on organic soft soil to derive strength parameters for dike design. In Geotechniek. Educom. pp. 10-17.
- Lengkeek, H.J. 2003. Estimation of sand stiffness parameters from cone resistance. In Plaxis Bulletin. pp. 15-20.
- Lengkeek, H.J. 2008. Kunstmatige eilanden in de Kaspische zee onder ijsbelasting (in Dutch, Artificial islands in ice invested waters of the North Caspian Sea. In Geotechniek. Educom. pp. 28-32.
- Lengkeek, H.J., and Bruijn, E. 2009. Soil nailing in clay for dike reinforcement. In 17th International Conference on Soil Mechanics and Geotechnical Engineering, ICSMGE 2009. pp. 1586-1589.
- Lengkeek, H.J., and Bouw, R. 2011. Triaxial, DSS, CRS tests and numerical simulations of soft soils at river dike. In 15th European Conference on Soil Mechanics and Geotechnical Engineering, ECSMGE 2011, Athens. pp. 427 - 434.
- Lengkeek, H.J., and Besseling, F. 2013. Combined translational and rotational sliding of gravity based structures loaded by ice. In 22nd International Conference on Port and Ocean Engineering under Arctic Conditions, POAC'2013, Helsinki.
- Lengkeek, H.J., and Besseling, F. 2014. Verification of deck on piles quay wall structures for operational and seismic load conditions. In Soil-Structure Interaction, Underground Structures and Retaining Walls. Edited by V.M. Ulitsky and M.B. Lisyuk and A.G. Shashkin, Saint Petersburg. pp. 296-301.
- Lengkeek, H.J., Croasdale, K.R., and Metge, M. 2003. Design of Ice Protection Barrier in Caspian Sea. In Volume 3: Materials Technology; Ocean Engineering; Polar and Arctic Sciences and Technology; Workshops, Cancun, Mexico. pp. 831-837.
- Lengkeek, H.J., Brunetti, M., and de Jong, A.K. 2014. the Use of Anisotropically Consolidated Triaxial, Direct Simple Shear and Constant Rate of Strain Tests in Determining the Strength Parameters of Organic Soft Soil. In Proceedings of Soft Soils.
- Lengkeek, H.J., Besseling, F., and Wang, Z. 2015. Ultimate foundation capacity analysis for an arctic drilling unit with ring-shaped skirted shallow foundation. In 23rd International Conference on Port and Ocean Engineering under Arctic Conditions, POAC'2015, Trondheim.
- Marzouk, I., Tschuchnigg, F., Paduli, F., Lengkeek, H.J., and Brinkgreve, R.B.J. Determination of fine-grained soil parameters using an automated system. In CPT'22, Bologna.
- Sluis, J., Besseling, F., Stuurwold, P., and Lengkeek, H.J. 2013. Validation and application of the embedded pile row-feature in PLAXIS 2D. In Plaxis Bulletin. pp. 10-13.
- Van Berkom, I.E., Brinkgreve, R.B.J., Lengkeek, H.J., and De Jong, A.K. 2022. An automated system to determine constitutive model parameters from in situ tests. In 20th International Conference on Soil Mechanics and Geotechnical Engineering. Edited by ICSMGE, Sydney. p. 6.
- Van Elsäcker, W.A., Besseling, F., Lengkeek, H.J., Brinkgreve, R.B.J., De Gijt, J.G., and Jonkman, S.N. 2017. Evaluation of performance of analytical and numerical methods to account for liquefaction effects on the seismic response of anchored quay walls. In 3rd International Conference on Performance-based Design in Earthquake Geotechnical Engineering, PBD-III, Vancouver.
- Yogatama, B.A., and Lengkeek, H.J. 2017. Comparison of several non-linear soil models in a ground response analysis for a typical sand and clay profile. In 3rd International Conference on Performance-based Design in Earthquake Geotechnical Engineering, PBD-III, Vancouver.